LEED AND AB INITIO STUDY OF RARE EARTH METALS ON SILICON AND GERMANIUM

by

Christopher Eames

A thesis submitted for the degree of Doctor of Physics

University of York

Department of Physics

December 2006

Abstract

Low Energy Electron Diffraction (LEED) and *ab initio* calculations have been used to investigate the structure and properties of surfaces formed when thin layers of rare earth metals are deposited on the (111) surfaces of silicon and germanium.

A quantitative LEED I-V and *ab initio* study of the two-dimensional (2D) holmium silicide surface has been carried out. LEED I-V data has been obtained and this has been compared to that simulated for over twenty thousand structural models. This process has refined the structural parameters that have been obtained in earlier LEED and MEIS studies. Vibrations have been shown to be particularly important in this system and it has been shown how the electronic structure influences the atomic structure.

A novel nanorod structure has been observed using STM for holmium on the Ge(111) surface by other workers in the York Surface Physice group and a structural model has been proposed. In this work this model has been qualitatively validated using *ab initio* methods. The stability of the structure has been verified and the calculated STM profiles are in good agreement with those observed in experiment. The calculated local density of states supports the experimental observation that the nanorod has conducting properties.

LEED I-V has been used to investigate the growth of Ho on the Fe-covered Si(111) surface and of Fe on the 2D holmium silicide surface. Each of these surfaces reveals similar I-V curves. The surface does not appear to be composed of separate domains of Fe silicide and 2D Ho silicide but no conclusive evidence has been found that a novel mixed phase has been formed.

The growth of both the 1×1 and the 3×2 phases of samarium on the silicon (111) surface has been studied using quantitative LEED I-V analysis and total energy calculations. The 1×1 phase is shown to be disordered and to possess no unique structure. The honeycomb-channel chain structure of the 3×2 phase is believed to be common to many metal atoms on the Si(111) surface. In this work this model is quantitatively verified using a combination of LEED I-V structure fitting and *ab initio* calculations. The discrepancy between the 3×2 unit cell observed in STM experiments and the 3×1 LEED pattern is shown to be due to the relative electron scattering strengths of the honeycomb chain and the samarium atom.

Contents

List of Figures **5**

List of Tables **14**

Acknowledgements **16**

1 Introduction **19**

1.1 Techniques used in the study of surfaces 20

1.1.1 Experimental Techniques 20

1.1.2 Theoretical techniques 23

1.2 Metal-Semiconductor Surfaces 26

1.2.1 Rare Earth-Semiconductor Surfaces 27

1.2.2 Nanowires 29

1.2.3 Honeycomb-Chain Channel Surfaces 30

1.3 Overview of research. 32

2 Low Energy Electron Diffraction **34**

2.1 History 34

2.2 Theoretical Discussion of Low Energy Electron Diffraction 36

2.3 Experimental Details of Low Energy Electron Diffraction 49

3 The Calculation of Surface Structure and Properties **55**

3.1 Electronic Structure 55

3.1.1 Density Functional Theory 55

3.1.2 Solution of the Kohn-Sham Hamiltonian 60

3.1.3 Practical Electronic Minimisation 64

3.2 Atomic Relaxation 69

3.3 Surface Properties 71

3.4 Simulated Scanning Tunneling Microscopy 71

3.4.1 Theoretical Approximation 72

3.4.2 Limitations 74

4 *Ab Initio* Study of Holmium on Silicon and Germanium 76
4.1 Introduction . . . 76
4.2 *Ab Initio* Study of 2D Holmium Silicide . . . 77
4.2.1 Convergence of Parameters . . . 77
4.2.2 The effect of spin polarisation . . . 80
4.2.3 Geometry optimisation . . . 82
4.2.4 Investigation of the top silicon bilayer . . . 84
4.2.5 Electronic Structure of 2D Si(111)-1×1-Ho . . . 87
4.2.6 Discussion . . . 89
4.3 Holmium nanowires on Ge(111) . . . 90
4.3.1 Experimental STM observations . . . 91
4.3.2 *Ab initio* Validation of the Structural Model . . . 95
4.3.3 Discussion . . . 101
4.4 Chapter 4 Conclusions . . . 103

5 LEED and Ab-Initio Study of Iron and Holmium on Si(111) 104
5.1 Introduction: The Interface of Iron and Silicon . . . 104
5.2 Iron and Holmium on Si(111) . . . 106
5.2.1 Low Energy Electron Diffraction Experiments . . . 106
5.2.2 Mixed phase investigation . . . 119
5.2.3 STM study of 1ML Fe on Si(111)-1×1-Ho . . . 126
5.2.4 Discussion . . . 127
5.3 Re-evaluation of Si(111)-1×1-Ho . . . 128
5.3.1 LEED I-V Structure fit . . . 128
5.3.2 Thermal vibrations . . . 132
5.3.3 Comparison of Experimental and Ab-initio Structures. . . . 134
5.3.4 Discussion . . . 136
5.4 Chapter 5 Conclusions . . . 137

6 LEED and ab initio Study of Samarium Silicide on Si(111) 138
6.1 Introduction . . . 138
6.2 Experimental Preparation of Samarium Overlayer Structures . . . 140
6.3 LEED I-V and *ab initio* Study of the Si(111)-1x1-Sm Phase . . . 145
6.4 LEED I-V and *ab initio* Study of the Si(111)-3×2-Sm Phase . . . 152
6.5 Chapter 6 Conclusions . . . 172

References 173

List of Figures

1.1 The major branches of surface science cover a huge range of subjects of both fundamental and technological interest. 19

1.2 The bulk terminated (111) surface of silicon (or germanium) seen in schematic view from above and from the side. Three possible adsorbtion sites are labelled T4, H3 and T1. Smaller circles indicate perspective. . 26

1.3 The AlB_2 type structure of the bulk RE silicides in (a) top view and (b) perspective view has a good lattice match to the bulk terminated Si(111) surface. This means that an ordered structure like the one in (c) can be grown. RE atoms are darker and larger spheres. 27

1.4 Schematic showing the structure of a 2D RE silicide on the Si(111) surface. Smaller circles indicate perspective. Six characteristic vertical spacings are defined; three silicon bilayer rumpling amplitudes R1, R2, R3 and three interlayer spacings L1, L2, L3. 28

1.5 The unit cell of the 3×2 HCC structure seen from above (a) and from the side (b). The metal atom is large and black. 30

1.6 The unit cell of the 3×1 and the 3×2 structures showing their reciprocal lattices both with and without the extra spots introduced by rotational domains. 31

2.1 Composite LEED pattern formed by a square lattice substrate and an overlayer with a square unit cell with lattice vectors twice those of the substrate. 39

2.2 Distortion of a LEED I(V) curve away from the Bragg condition (a) as the effects of (b) phase shifts, (c) finite penetration depth and (d) multiple scattering are included. 41

2.3 A cross section of the 'muffin tin' potential that is used to approximate the ion cores. The horizontal axis is normal to the surface plane and the surface barrier is shown on the left. 43

2.4 In the renormalised forward scattering perturbation scheme the beam is propagated into the crystal until the amount reflected (labelled r) falls below some tolerance. A beam reflected just once becomes the first order beam. Successive orders are built up until their contribution becomes negligible. 46
2.5 Schematic view from above of the relevant parts of the diffractometer main chamber. The labelled components correspond to M; manipulator, QCM; quartz crystal microbalance, H; electron beam heater, P; sample preparation position, W; pyrometry window, S; deposition source, C; carousel, V; gate valve, D; diffractometry position, G; electron gun. . . 50

3.1 Showing the relative performance of the steepest descents (a) and the conjugated gradients (b) methods of generating search directions for a two-dimensional narrow valley energy landscape. Steepest descents requires many steps and follows an oscillatory path to the minimum with slow convergence. Conjugated gradients reaches the minimum in two steps (assuming a quadratic form for the energy landscape). 62
3.2 Side view of ten supercells of the Si(100)-2×1 surface with a vertical vacuum gap of 9 Å. Hydrogen atoms (black) are used to passivate dangling bonds on the last bulk layer. 66
3.3 Outside of the core radius r_c the pseudowavefunction Ψ_{PP} and pseudopotential V_{PP} match the full wavefunction Ψ and potential Z/r and the environment presented to the valence electrons remains unchanged. Inside r_c both Ψ_{PP} and V_{PP} are much smoother and this significantly reduces the number of plane waves required in the basis set. 67
3.4 The line minimisation proceeds by choosing the optimal step length $\lambda = 1$ for a perfectly quadratic energy landscape and computing the total energy and force. If at this point the force $\boldsymbol{F}$ is not orthogonal to the search direction $\Delta\boldsymbol{S}$ another step length is chosen and the method proceeds until the optimal step length λ_{min} is found at which $\boldsymbol{F} \cdot \Delta\boldsymbol{S} = 0$ 70
3.5 Sample (left, S) and STM tip (right, T) energy level diagram. When far apart **(a)** each has a distinct Fermi level ε_F and work function ϕ_F. When the tip is close enough for tunneling to occur **(b)** sample electrons tunnel into the tip (in this example) and equalise the local Fermi level in the two materials, causing a barrier to develop that prevents further tunneling. A bias voltage V will introduce an effective electric field and an energy shift $\delta\varepsilon$ that will act to restore sample-tip tunneling **(c)**. . . 72

3.6 The bias voltage V shifts the density of states in the sample by an amount $+eV$ and makes tunnelling unidirectional. **(Left)** the first fermi overlap term in Equation 3.31 allows tunnelling from filled sample states within an energy eV below the Fermi level into empty tip states within eV above the Fermi level. **(Right)** there is no significant overlap of empty sample states and filled tip states. The second fermi overlap term in Equation 3.31 is effectively zero and tip to sample tunnelling does not occur. 73

4.1 Variation of the singlepoint energy, which is the calculated energy for a given configuration of the atomic positions, with the cutoff energy and with the number of k-points at which the wavefunction is sampled in reciprocal space for the 2D Si(111)-1×1-Ho system. 78
4.2 The variation of the mean force and the singlepoint energy with the vacuum gap thickness for the Si(111)-1×1-Ho system. 79
4.3 The variation of the mean force with the number of bulk-like silicon layers for the Si(111)-1×1-Ho system. 79
4.4 Variation of the total energy of a Si(111)-1×1-Ho supercell during electronic minimisation compared for the spin polarised and the non-spin polarised case. 80
4.5 Variation of the total energy of a Si(111)-1×1-Ho supercell during electronic minimisation compared for various initial spin states. All spin states were allowed to relax after 8 steps except the spin free state which was relaxed after 9 steps. 81
4.6 Convergence of the total energy (top) and logarithmic convergence of the forces (bottom) during the geometry optimisation of the Si(111)-1×1-Ho supercell for the spin polarised and non spin polarised cases. Only the last few steps are shown in the energy convergence for the spin polarised case since the relative energy of earlier steps would dominate the figure. 83
4.7 Initial (left) and final (right) atomic configurations of three structures for the Si(111)-1×1-Ho surface that have been geometry optimised. The shortened names are defined in the text. 85
4.8 Convergence of the total energy and the maximum force on any atom during the geometry optimisation of Si(111)-1×1 supercells with three different top bilayer structures. RS is a reverse buckled 2D silicide that is observed during experiment. BB has buckling in the same sense as in the bulk and BS is BB but with the top bilayer laterally shifted. 86

4.9 3D isosurface plot showing those regions that have a density difference of 0.44 (e) near to the holmium atom in 2D reverse buckled holmium silicide. The unit cell is shown in a dashed outline. The holmium atom sits at the centre of a triangle formed by both the three dangling bonds in the layers above and below it. These triangles of dangling bonds are rotated 180° with respect to one another to prevent their interaction. This dictates the orientation of the top bilayer. 87
4.10 Electron density difference (δQ) plot along a vertical slice through the supercell showing the regions that have gained charge during electronic minimisation. In plane holmium atoms are marked + and those out of plane ×. Most of the deep black areas are covalent bonds between silicon atoms but there are two regions, marked 1 and 2, that represent charge transfer to saturate dangling bonds in the silicon layers immediately above and below the holmium layer. 88
4.11 Two overview experimental STM images of the nanorods formed with a low (0.1 ML) coverage of Ho. (Left) Large area (59 × 75 nm) filled states image taken with a sample bias of − 2.0 V and a tunneling current of 2 nA. (Right) 14 × 33 nm empty states image taken with sample bias + 2.0 V and a tunneling current of 2 nA showing the surrounding clean Ge(111)-c(2×8) substrate. Reproduced with the permission of C. Bonet. 91
4.12 Filled states (a) and empty states (b) experimental STM images for the Ge(111)-5×1-Ho system. The tunneling current in both images was 2 nA. In the filled states image the sample bias was − 2.0 V and in the empty states image it was + 1.50 V. The dimensions of both images are 4.2 × 3.3 nm. The left half of both images has been contrast adjusted to determine of the holmium atoms within the top layer of the nanorod can be more clearly discerned. Reproduced with the permission of C. Bonet. 92
4.13 Two views of the Ge(111)5×1-Ho system whose structure has been suggested by C. Bonet; (a) top view in which the 5×1 unit cell is outlined in black (b) side view. Holmium atoms are large and black, reconstructed germanium atoms are coloured dark grey and bulk-like germanium atoms are light grey. 94
4.14 Labelling of the top two layers in the optimised Ge(111)5×1-Ho structure. The holmium and germanium atoms in the top nanorod layer are labelled in figure (a) and in (b) the germanium atoms in the second layer, that is bulk-like, are labelled. 96

4.15 Measured (a) and simulated (b) filled states STM images for the Ge(111)5×1-Ho system. Both images correspond to a sample bias of -2.0 V and have dimensions of 4.2 × 3.3 nm. 97
4.16 Measured (a) and simulated (b) empty states STM images for the Ge(111) 5×1 Ho system. Both images correspond to a sample bias of $+1.50$ V and have dimensions of 4.2 × 3.3 nm. The left half of (a) has been contrast adjusted so that the Ho atoms within the top layer of the nanorod can be more clearly discerned. 98
4.17 Electron density within a slice taken (a) horizontally in the plane of the surface through the flat layer of germanium atoms labelled 1-6 and (b)/(c) vertically through the two holmium atoms (labelled Ho 1 and Ho 2) to show the bonding to the layer below. 99
4.18 Calculated local density of states for the Ge(111)-5×1-Ho structure. . . 100
4.19 (Original in colour) Experimental Scanning Tunneling Spectroscopy data showing the conducting properties of the nanorod. Data taken from the germanium substrate, with its large bandgap at the Fermi level, is included for reference. Reproduced with permission of Dr. C. Bonet . . 100

5.1 Experimental LEED spot pattern formed by Ho on the Si(111)-1×1-Fe surface shown at (a), (b) 40 eV and (c), (d) 80 eV and (e), (f) 150 eV for two separate experiments. 108
5.2 Experimental LEED I-V curves for the 1×1 surface formed by Ho on Si(111)-1×1-Fe for all five degenerate spot groups. For a given spot group experiments performed on different days starting from a clean substrate are compared. 109
5.3 Experimental LEED spot pattern formed by Fe on the Si(111)-1×1-Ho surface shown at (a) 40 eV and (b) 80 eV and (c) 150 eV. 110
5.4 Experimental LEED I-V curves for the 1×1 surface formed by Fe on Si(111)-1×1-Ho for all five degenerate spot groups. For a given spot group experiments performed on different days starting from a clean substrate are compared. 112
5.5 A comparison of the averaged experimental LEED I-V curves for the surface formed by Fe on Si(111)-1×1-Ho with those for the surface formed by Ho on Si(111)-1×1-Fe. The R-factor beside each curve indicates the level of agreement. 113
5.6 Experimental LEED spot pattern for the Si(111)-1×1-Fe surface shown at (a) 40 eV and (b) 80 eV and (c) 150 eV. 114

5.7 Experimental LEED I-V curves for the Si(111)-1×1-Fe for all five degenerate spot groups. For a given spot group experiments performed on different days starting from a clean substrate are compared. 116
5.8 Experimental LEED spot pattern for the Si(111)-1×1-Ho surface shown at (a), (b) 40 eV and (c), (d) 80 eV and (e), (f) 150 eV for two separate experiments. 117
5.9 Experimental LEED I-V curves for the Si(111)-1×1-Ho for all five degenerate spot groups. For a given spot group experiments performed on different days starting from a clean substrate are compared. 118
5.10 A comparison of the averaged experimental LEED I-V curves for the Si(111)-1×1-Fe surface with those for the surface formed by Fe on Si(111)-1×1-Ho and the surface formed by Ho on Si(111)-1×1-Fe. 120
5.11 A comparison of the averaged experimental LEED I-V curves for the Si(111)-1×1-Ho surface with those for the surface formed by Fe on Si(111)-1×1-Ho and the surface formed by Ho on Si(111)-1×1-Fe. 121
5.12 Pendry R-factors for linear combinations of the Si(111)-1×1-Fe and Si(111)-1×1-Ho experimental I-V curves when compared with (left) the averaged experimental LEED I-V curves for the Fe on Si(111)-1×1-Ho surface and (right) the averaged experimental LEED I-V curves for the Ho on Si(111)-1×1-Fe surface. 122
5.13 Experimental LEED spot pattern for the Si(111)-1×1-Ho surface shown at (a), (b) 40 eV and (c), (d) 80 eV and (e), (f) 150 eV for two separate experiments. 123
5.14 Experimental LEED I-V curves for the surface formed by 1.5 ML of Fe on Si(111)-1×1-Ho for all five degenerate spot groups. For a given spot group experiments performed on different days starting from a clean substrate are compared. 124
5.15 A comparison of the averaged experimental LEED I-V curves for the Si(111)-1×1-Ho surface with those for the surface formed by 1.5 ML Fe on Si(111)-1×1-Ho and the surface formed by Ho on Si(111)-1×1-Fe. . 125
5.16 Two 200 × 200 nm^2 STM images of the surface formed by 1ML of Fe on Si(111)-1×1-Ho taken during different experiments. 126
5.17 The effect upon the r-factor of the variation of each structural parameter in the coarse search. For each curve one parameter only is varied and the other parameters are fixed at their optimum values. 129
5.18 The effect upon the r-factor of the variation of each structural parameter in the fine search. For each curve one parameter only is varied and the other parameters are fixed at their optimum values. 130

5.19 Variation of the Pendry R-factor with interlayer spacing 2 showing how the standard error was used to determine the error in the structural parameter. 131
5.20 Variation of the Pendry R-factor with the Debye temperature for the atomic species in each of the three top layers. The bulk Debye temperatures for silicon and holmium are 645K and 190K respectively. 133
5.21 Best fit theoretical I-V curves for the five degenerate spots groups in the LEED pattern of Si(111)-1×1-Ho compared with experiment. The effects of enhanced vibrations are included in the calculated curves. The Pendry R-factor that was used to compare each pair of curves is included. The overall R-factor was 0.29 ± 0.02. 135

6.1 Experimental LEED spot pattern for the Si(111)-1×1-Sm surface shown at (a), (b) 40 eV and (c), (d) 80 eV and (e), (f) 150 eV for two separate experiments. 140
6.2 Experimental 3×1 LEED spot pattern for the Si(111)-3×2-Sm surface shown at (a), (b) 40 eV and (c), (d) 80 eV for two separate experiments. 142
6.3 Labelled spots in the 3×1 LEED pattern produced by the Si(111)-3×2-Sm surface as it appears at 40 eV. The degeneracies of the spots are indicated by the pattern used to fill each spot. 142
6.4 Experimental LEED I-V curves for the Si(111)-1×1-Sm surface for all five degenerate spot groups. For a given spot group experiments performed on different days starting from a clean substrate are compared. 143
6.5 Experimental LEED I-V curves for the Si(111)-3×2-Sm surface for all thirteen degenerate spot groups. For a given spot group experiments performed on different days starting from a clean substrate are compared.144
6.6 Variation of the singlepoint energy, which is the calculated energy for a given configuration of the atomic positions, with the cutoff energy and with the number of k-points at which the wavefunction is sampled in reciprocal space for the Si(111)-1×1-Sm system. 146
6.7 Variation of the energy with the total spin for the Si(111)-1×1-Sm system. The figure on the left shows the convergence of the electronic minimisation for each spin state and the figure on the right shows the final singlepoint energy as a function of the net spin state imposed on the system. 147
6.8 Showing the structure of the surface layers of each of the Si(111)-1×1-Sm structures that have been geometry optimised. 148

6.9 Calculated coarse-fit LEED I-V curves for the bulk terminated silicon (111) surface (left) and the 2D silicide with the samarium atoms in a T4 site (right) compared with experiment for the Si(111)-1×1-Sm surface. 150
6.10 Variation of the singlepoint energy, which is the calculated energy for a given configuration of the atomic positions, with the cutoff energy and with the number of k-points at which the wavefunction is sampled in reciprocal space. 153
6.11 Convergence of the total energy (top) and logarithmic convergence of the forces (bottom) during the geometry optimisation of the T4 and H3 structures. The T4 structure has a lower energy than the H3 structure and the maximum force on any atom is lower. 154
6.12 Optimised structures for the HCC model showing the H3 model from above (a) and in side view (b) and the T4 model from above (c) and in side view. Silicon atoms here are grey, samarium is black and the hydrogen atoms are white. The first and second interlayer spacings are labelled L1 and L2 respectively. 155
6.13 A comparison of the I-V curves calculated for the integer spots for the structures suggested by the *ab initio* calculations in this study and elsewhere with those obtained experimentally. The R-factor beside each curve indicates the level of agreement with experiment. 157
6.14 Coarse search Pendry R-factor landscape for a range of values of the interlayer spacings in the (a) H3 and (b) T4 structure for the fractional spots. The step size was 0.05 Å. The cross indicates the *ab initio* energy minimum. 159
6.15 Fine search Pendry R-factor landscape for a range of values of the interlayer spacings in the (a) H3 and (b) T4 structure for the fractional spots. The step size was 0.005 Å. 160
6.16 Variation of the Pendry R-factor with interlayer spacing 1 showing how the standard error was used to determine the error in the structural parameter. 161
6.17 Variation of the Pendry R-factor with interlayer spacing 2 showing how the standard error was used to determine the error in the structural parameter. 161
6.18 Variation of the spacing between layers three and four in the Si(111)-3x2-Sm H3 (left) and T4 (right) structures. The bulk value for this interlayer spacing is 3.14 Å 162

6.19 Pendry R-factors for various linear combinations of the H3 and T4 structures in various mixing ratios for two different vibrational regimes. In the figure on the left the Debye temperature for the samarium atom is $119K$ and in the figure on the right it is $84K$. In both cases the Debye temperatures of the top silicon honeycomb layer, the first silicon bulk-like layer and the repeated bulk layer are $215K$, $323K$ and $645K$ respectively. 164
6.20 Calculated LEED I-V curves for the integer spots (left) and fractional spots (right) of the H3 unit cell with and without the samarium atom in place. Bulk Debye temperatures were used throughout. 165
6.21 Calculated I-V curves for the HCC structure showing the difference in the intensity (typically an order of magnitude) between the half order spots and a representative spot that is visible in the LEED pattern during an experiment. 166
6.22 Best fit I-V curves for the integer LEED spots produced by a linear combination of the H3 and the T4 structures in a 40: 60 ratio. 170
6.23 Best fit I-V curves for the fractional spots produced by a linear combination of the H3 and the T4 structures in a 40: 60 ratio. 171

List of Tables

4.1 Interlayer spacings (L) and rumpling amplitudes (R) in the Si(111)-1×1-Ho system determined by LEED and DFT in this work compared with the results from other studies. The parameters were defined in figure 1.4 in Chapter 1 and those marked with an asterisk have not been optimised. 82

4.2 Tabulated atomic coordinates (in Å), forces ($|\boldsymbol{F}|$), electronic configuration, total charge (Q) and charge depletion δ Q of each atom in the geometry optimised Ge(111)5×1-Ho supercell. The lattice parameters are $\boldsymbol{a}$=4.000457 Å, $\boldsymbol{b}$=20.002283 Å, $\boldsymbol{c}$=26.532718 Å with $\alpha = \beta = 90°$ and $\gamma = 120°$. 96

5.1 The range of interrun R-factors for each spot in the 1×1 LEED pattern of the surface formed by Ho on Si(111)-1×1-Fe. 108

5.2 The range of interrun R-factors for each spot in the 1×1 LEED pattern of the surface formed by Fe on Si(111)-1×1-Ho. 111

5.3 The range of interrun R-factors for each spot in the 1×1 LEED pattern of the Si(111)-1×1-Fe surface. 114

5.4 The range of interrun R-factors for each spot in the 1×1 LEED pattern of the Si(111)-1×1-Ho surface. 115

5.5 The range of interrun R-factors for each spot in the 1×1 LEED pattern of the surface formed by 1.5 ML of Fe on Si(111)-1×1-Ho. 123

5.6 The range of values and the step sizes for each parameter that was varied in the coarse structural fit for the Si(111)-1×1-Ho system. 129

5.7 The range of values and the step sizes for each parameter that was varied in the fine structural fit for the Si(111)-1×1-Ho system. 130

5.8 Errors in the four structural parameters that have been optimised for the Si(111)-1×1-Ho system. The method shown in figure 5.21 for interlayer spacing 2 was repeated for each parameter. 131

5.9 Interlayer spacings (L) and rumpling amplitudes (R) in the Si(111)-1×1-Ho system determined by LEED and DFT in this work compared with the results from other studies. The parameters were defined in figure 1.4 in Chapter 1 and those marked with an asterisk have not been optimised. 134

6.1 The energy and the maximum force on any atom tabulated for all of the Si(111)-1×1-Sm structures that have been geometry optimised. 148
6.2 Pendry R-factors resulting from a comparison of the candidate structures for the Si(111)-1×1-Sm surface with averaged experimental data. 149
6.3 Pendry R-factors resulting from a comparison of a coarse fit of the seven candidate structures for the Si(111)-1×1-Sm surface with averaged experimental data. 150
6.4 Variation of the Debye temperature for the samarium atom, silicon honeycomb layer and first bulk like layer and the effect upon the Pendry R-factors for the H3 structure. The naming scheme here is Sm=samarium atom, Si1=silicon honeycomb atoms, Si2=first silicon bulk-like layer. A Debye temperature of B indicates the bulk unoptimised value for that atomic species. Similar data is available for the T4 structure. 163
6.5 Pendry R-factors for the fractional spots (R_P^{FRAC}), integer spots (R_P^{INT}) and for all spots (R_P^{ALL}) for the various optimised structures in this work. All of the calculated I-V curves used optimised vibrations. The interlayer spacings are shown in columns five and six and the midpoint of layer 1 is defined as the midpoint of the honeycomb layer; for this table only the height of the samarium atom has not been included to determine the midpoint. 167
6.6 Tabulated atomic coordinates (in Å) for each atom in the top three layers in the geometry optimised Si(111)-3×2-Sm supercells in the T4 and H3 arrangements. The deepest layer is bulk-like silicon and the coordinates of two atoms are listed. The lattice parameters are $\boldsymbol{a}$=7.68 Å, $\boldsymbol{b}$=11.52 Å, $\boldsymbol{c}$=17.096832 Å with $\alpha = 120°$ and $\beta = \gamma = 90°$. 168

Acknowledgements

"*The job of a scientist is to listen carefully to nature, not to tell nature how to behave.*"
R. P. Feynman

I would especially like to thank both of my supervisors, Dr. Steve Tear and Dr. Matt Probert, for their constant support, advice, guidance and patience.

Dr. Chris Bonet has acted as my mentor during this project, particularly with respect to the LEED experiments and analysis. From Chris I learned the practicalities of how to do surface science. Thankyou Chris for giving so much of your time with good humour.

The technical and support staff in the Department of Physics have been essential in the smooth running of the experimental and bureaucratic apparatus associated with this project.

My regards also go out to the other members of the surface physics and condensed matter theory groups with whom I have shared the journey. In particular; Ed Perkins, Andy Pratt, Alex Roskoss, Ian Scott, Tim Wood, Luke Abraham, Phil Hasnip, Matt Farrow, Dave Quigley and Maff Glover.

I would also like to thank my friends and family who have helped me to balance my PhD studies with the wider scope of my life.

Declaration

I declare that the work presented in this thesis, except contributions acknowledged explicitly in the text or by reference, is based on my own research. No part of this work has previously been submitted for any award or qualification.

The material presented in Chapter 4 on nanowires is based, in part, upon work accepted for publication in Physical Review B., **74**, 193318, (2006). All of the experimental STM and STS investigations were carried out by C. Bonet and E. Perkins. The structural model was suggested by C. Bonet.

The STM investigation of Fe on Si(111)-1×1-Ho that is discussed in Chapter 5 was performed by C. Bonet with the author in partial attendence.

The initial atomic coordinates of the structure of the Si(111)-3×2-Sm honeycomb-chain channel unit cell were provided by F. Palmino.

Publications

The following publications have arisen from this work;

STM and ab initio study of holmium nanowires on a Ge(111) surface.
Physical Review B., **74** 193318 (2006).

Quantitative LEED I-V and ab initio study of the Si(111)-3×2-Sm surface structure and the missing half order spots in the 3×1 diffraction pattern.
Submitted to Physical Review B.

Chapter 1

Introduction

The most fundamental defect found in a solid is a surface. Any body that wishes to enter the bulk of a solid must pass through the surface and when two bodies make contact it is the surfaces that physically meet. It is important to know the chemical and physical properties of a surface and such knowledge benefits the many areas of science and engineering that involve the surface (see Figure 1.1).

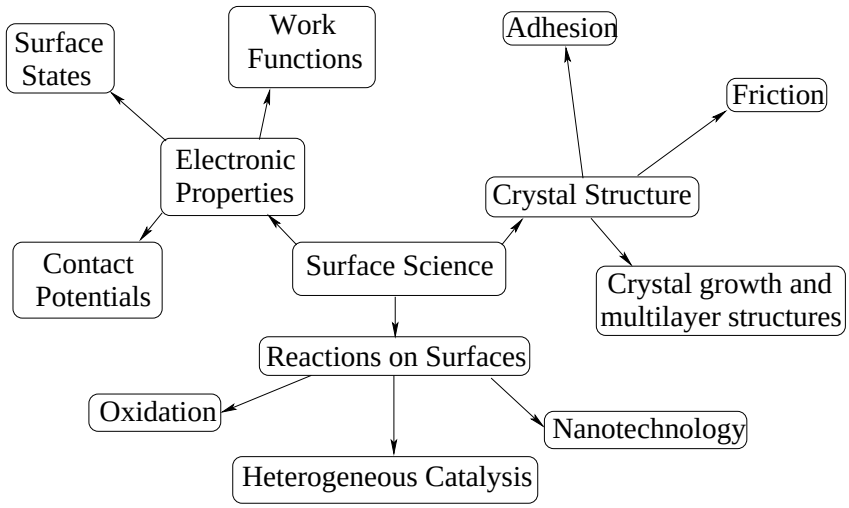

Figure 1.1: The major branches of surface science cover a huge range of subjects of both fundamental and technological interest.

At a surface the absence of bonding in one direction means that atoms near to the surface have uncompensated electric charge and this increase in energy introduces strain into the system. The need to reduce this strain and saturate uncompensated bonds can involve surface atoms forming a periodic structure that is very different to that in the bulk. To begin a determination of the properties of a surface on the nanoscale the atomic positions and chemical character of the ordered surface regions are needed. In the next section the major theoretical and experimental techniques for obtaining these properties are outlined.

1.1 Techniques used in the study of surfaces

1.1.1 Experimental Techniques

A clean surface is crucial to any surface science experiment. Ambient air molecules and other airborne contaminants are in constant contact with the surface. If we assume that each particle that collides with the surface sticks to it then the time taken to accumulate one layer (one monolayer or 1ML) depends exponentially upon the ambient air pressure. It can be shown that this pressure must be roughly ** if the surface is to stay clean for several hours in which experiments can be performed.

The major breakthrough in experimental surface science that came in the early 1960s was the commercial availability of apparatus that could be used to generate a reliable vacuum (see [1–3] for an interesting set of review articles that cover the major historical developments). Since that time a vast number of techniques have become feasible. In the rest of this section the main techniques are summarised.

Low Energy Electron Diffraction

If the atoms in a surface are arranged periodically then they may diffract incident photons and particles if these have the right energy. Electrons with energies in the range $30 - 400$ eV have a de Broglie wavelength of a few Angstroms which makes them a candidate for surface diffraction. Electrons with these energies have inelastic mean free paths that are typically less than 10Å and so any electrons which emerge from the crystal having been diffracted cannot have penetrated to a depth greater than a few atomic layers. This surface sensitivity makes Low Energy Electron Diffraction (LEED) a central tool in surface science.

Electrons which have been elastically backscattered from a periodic surface give rise to a pattern of bright spots on a dark background. The nature of the diffraction process means that this pattern is the fourier transform of the of the two dimensional real space surface lattice. The periodicity of the reconstructed surface with respect to the underlying substrate is readily apparent in a LEED pattern and the size of the LEED spots and the background of incoherently scattered electrons indicate the degree of order on the surface. In most surface science experiments the LEED spot pattern is used as a quick method of determining if the surface is clean and well ordered before more extensive experiments are carried out with another technique.

It is also possible to use the variation in intensity of each spot in the LEED pattern with the energy of the electrons in the incident beam to determine the atomic positions in the surface region. This is discussed in detail in Chapter 2.

Scanning Tunneling Microscopy

In the mid-1980's a new technique emerged that was to revolutionise surface science. The Scanning Tunneling Microscope (STM) allows imaging of surface details on the atomic scale. The idea is simple; a sharp tip (preferably with a single atom forming the tip) is held close ($\sim$ 5 Å) to a surface. A bias voltage between the tip and the surface encourages electrons to tunnel between the surface and the tip or vice-versa, depending upon the direction of the applied electric field. The tunneling current is exponentially sensitive to the distance between the tip and the sample. If the tip is rastered over the surface the tip height must be adjusted vertically to maintain a constant tunneling current. A record of the height of the tip during the rastering process allows a topographic map of the surface to be generated. Alternatively, the tip height can be kept fixed and the variations in the tunneling current can be recorded.

Since we are sampling electron density STM can reveal a wealth of spectroscopic detail. If electrons are tunneling from the states in the surface into the tip we can map the filled states in the surface. Tunneling from the tip into the available states in the surface provides us with information about the distribution of empty states across the surface. Much more spectroscopic information can be gained from the STM but a discussion of this is outside the scope of this work. STM is limited in that only the top exposed layer can be imaged.

Medium Energy Ion Scattering

In Medium Energy Ion Scattering (MEIS) a beam of hydrogen ions with an energy of $\sim 100keV$ is directed into the surface at some angle. The energy and the yield of ions scattered into a given direction is recorded. These two distributions give two types of information about the species in the surface. The energy of a scattered ion is used to establish which particular atomic species within the surface was responsible for it being scattered. If the species within the surface have a large difference in mass (for example, silicon and holmium) the scattered ions will have a significant energy difference and for this reason MEIS can give elemental sensitivity. The energy of the scattered ions also varies with the depth of the scatterer in the surface and a picture can be assembled of the distribution of elemental species. If the incident ion beam is carefully aligned with the crystal then each incident ion will be scattered off an atom within the surface region and no ions will be able to reach the bulk. As the ion leaves the crystal there will be certain scattering angles in which it will meet an atom in one of the layers above. The yield of scattered ions will reflect this in that there will be a trough in the scattered ion intensity for this particular scattering angle. Thus, by a process of triangulation the positions of atoms in the top few layers can be determined.

Spectroscopic Techniques

All surface spectroscopic techniques attempt to determine the electronic structure of the surface and the local chemical environment. In **Auger Electron Spectroscopy** a core level electron is removed from the surface using incident electrons with energies of around 3-5keV. A surface electron with a higher energy than the removed electron then moves to occupy the vacant core state. The energy gained during this drop to a lower state is imparted to yet another core electron which is ejected from the surface. The energy of the ejected core electron is characteristic of the energy levels that were involved in the initial Auger process. The spectrum of all Auger electrons thus contains a number of peaks which are characteristic of the particular elements present in the surface. The attenuation length of the ejected Auger electron makes it possible for only those Auger electrons emitted from within the top few atomic layers to leave the crystal without being inelastically scattered and this gives the technique surface sensitivity.

The various **Photoelectron Spectroscopy** techniques use a photon to remove an electron from the surface. The energy of the removed electron, with the photon energy subtracted, indicates the chemical environment within the surface. If an X-Ray photon is used the technique (**XPS**) removes a core level electron and indicates the binding energy of core level electrons. With an ultraviolet photon the (**UPS**) technique samples the valence states in the surface. UPS can determine the change in these valence states as material is adsorbed and indicate which features of the bonding environment are due to the adsorbate and its bonding to the surface.

The **Metastable Deexcitation Spectroscopy** technique is novel in that it uses a beam of laser-cooled metastable helium atoms to sample the electronic states in a surface with no bulk contribution to the signal. The slowly moving metastable helium atom approaches the surface until it is close enough for an electron within the surface valence region to tunnel into the helium atom. The resulting cascade of electrons causes many electrons to be emitted with characteristic energies. This non-destructive technique can provide a sample of the local density of states in the top surface layer and it can also, with modification, determine the energy of any spin polarised states that the surface might possess.

Spectroscopic techniques are of particular use as a diagnostic tool. They can reveal the presence of contaminant atoms and indicate the level of cleanliness of a surface. These techniques are also complementary to structural techniques. If a surface model requires dangling bonds on the surface then their absence, as inferred from spectroscopy, can allow the immediate rejection of that particular model from the time consuming structural fitting process.

1.1.2 Theoretical techniques

Over the past two decades theoretical calculations have moved to occupy a central position in surface science. This has been due to improvements in the efficiency of the algorithms involved and, more importantly, advances in computing technology and the widespread availability of parallel computing resources to the physics community. It is now commonplace for published work to contain a theoretical prediction of surface structure or properties alongside the reports of experimental observations.

Early theoretical prediction of surface structure involved a simple discussion of the likely bonding environment based upon the needs of each atom and a suggested structure that would satisfy these bonding needs at the lowest energy cost. The first computational calculations of surface properties used empirical potentials and did not include electronic effects in any way.

Tight Binding Methods

In the 1960s computational codes that included the electronic structure began to emerge. The most prominent of these used the so-called Tight Binding approximation [4]. In this the interactions in the system are not explicitly calculated. The elements of the Hamiltonian are left as adjustable parameters and fitted to high symmetry points in the first Brillouin zone in the bulk such as photoemission and band gap data obtained experimentally or the results of studies that calculate all of the interactions from first principles.

The method relies on the assumption that the parameterised matrix elements can be extrapolated from the bulk to the surface. That is, that the electron charge density at the surface is similar to that in the bulk. Despite this questionable approximation the tight binding method has been responsible for a wide range of total energy calculations for semiconductor surfaces. Its computational simplicity means that it can be applied to systems containing large numbers of atoms and this has meant that traditionally it has been this method that has first obtained theoretical semiconductor surface structures. The method is justifed on the basis of its speed and its good agreement with more expensive first principles calculations.

This method is not suitable for use in conjunction with LEED as it relies on the pre-existence of experimentally obtained data or calibration against more rigorous calculations. For LEED we require a method of suggesting trial surface reconstructions that is independent of experiment.

Ab-Initio Methods

In the mid 1980s it became possible to calculate the electronic structure and the total energy of a system from first principles. Such *ab-initio* methods use Density Functional Theory (DFT) and a number of approximations to transform the solution of the Schrödinger equation for a large system into a much more computationally tractable problem.

DFT emerged as a formal framework in the 1960s but the determination of the eigenvalues from the large matrices that it presents prevented the application of the method to systems of any real size and most early work was with clusters or the simulation of small parts of the surface. The use of iterative methods to diagonalise the matrices that was employed by Carr and Parrinello in 1985 was a major step forward in algorithmic efficiency that was quickly adopted as the natural way forward [5].

A schism was to emerge early on with respect to the way that the electronic wavefunction was to be represented in a computer. One approach uses plane waves as a basis set (eg `CASTEP`, `VASP`). Another type of basis set that is used predominantly in the chemistry community is the linear combination of atomic orbitals (LCAO). This method, like the TB method, uses the independent atomic orbitals as a basis set. However, whereas the TB method adjusts the combination coefficients so as to fit the final result to bulk experimental data the LCAO method uses the expansion coefficients as a variational parameter for *ab-initio* determination of the electronic structure. A notable implementation of the DFT LCAO method is in the Spanish Initiative for Electronic Simulations with Thousands of Atoms (`SIESTA`) code [6]. A review of both the Tight Binding and the LCAO method and their applications to surface structure and properties until 1992 is available [7] and for an excellent review of all of the material discussed in this section the reader is referred to the book by Martin [8].

There are many codes that use DFT and a plane wave basis set. The calculations in this work were performed with the `CASTEP` code [9]. This uses an iterative search method to relax the atomic and electronic coordinates. Another notable implementation is the Vienna *Ab-Initio* Simulation Package (`VASP`) which uses molecular dynamics as its relaxation method [10].

Two independent pieces of work in surface structure determination warrant specific mention. In 1990 Payne et al (using an early version of the `CASTEP` code) and Brommer et al (using an early version of the molecular dynamics implementation within `CASTEP`) were able to obtain the Si(111)-7x7 Takayanagi surface structure from first principles and independent of experimental data [11, 12]. This marked the arrival of theoretical methods alongside experiment in the surface science canon.

Molecular Dynamics

This method is very similar to the *ab-initio* method outlined in the last subsection. The crucial difference is that the nuclear motion and the electronic structure are evolved together (see Martin [8] for full details). This readily allows for finite temperature analysis of the thermal properties of a surface. The method has been very successfully applied to the problems of adsorbtion and subsequent diffusion of gas molecules on surfaces and the determination of the vibrational properties of a surface.

Molecular dynamics is not suitable for the optimisation of the atomic structure of a surface if the initial structure is not close to that which has the minimum energy. When this is the case then the time required to anneal the surface into the minimum energy configuration is computationally prohibitative.

Quantum Monte Carlo Methods

The solution of the many body hamiltonian can also be achieved by the use of the Quantum Monte Carlo (QMC) method [13]. There are many varieties of this but in essence they all use the same principle. The system is sampled in a number of random configurations and then statistical methods are applied to extrapolate the sampled properties to describe the system as a whole. The method allows the determination of the same basic properties as the plane wave pseudopotential method and it gives a greater accuracy. It includes no approximation in its treatment of many body effects, scales well in a parallel computational environment, has low storage requirements and does not contain the basis set errors inherent in plane wave methods.

However, there are costs. Forces are computationally very expensive to calculate and although the determination of the electronic structure is more accurate with little change in the computational cost the optimisation of the atomic positions is significantly more expensive using QMC. Also, some modification of the established QMC methods for bulk materials is required to extend the method to surface analysis. It is perhaps for these reasons that QMC has not yet become an established tool for the surface scientist (See Schattke et al [14] for a recent review).

1.2 Metal-Semiconductor Surfaces

The study of the interface between metals and semiconductors is of great technological interest because such metal-semiconductor contacts are crucial to integrated circuits and electronic devices. The atomic structure and quality of the interface will determine the electronic properties of the interface. A knowledge of the surface reconstruction formed when a few layers of a metal are deposited onto a semiconducting substrate and the system is annealed will indicate the quality of the epitaxy. This can be used to make interfaces with more controllable and reliable electronic properties and to prolong the life of electronic components.

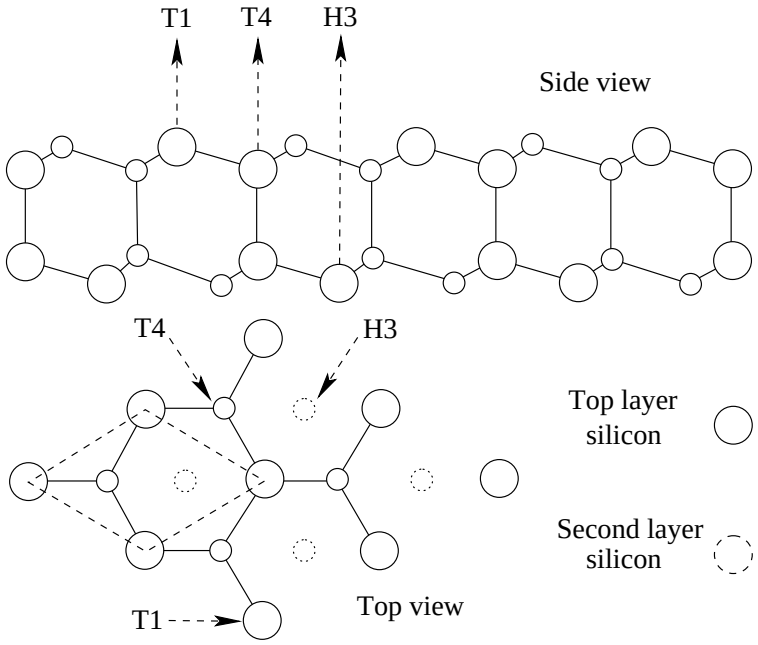

Figure 1.2: The bulk terminated (111) surface of silicon (or germanium) seen in schematic view from above and from the side. Three possible adsorbtion sites are labelled T4, H3 and T1. Smaller circles indicate perspective.

When discussing the deposition of material onto a surface it is customary to define certain unique sites in which the deposited atoms might sit in a regular array. In this work it is the (111) surfaces of silicon and germanium on which material has been deposited. In Figure 1.2 the (111) surface is shown together with three common adsorbtion sites. The sites refer to the atoms in the silicon bilayer above which the deposited atom sits. In the T1 site the adsorbate sits directly above an 'up' atom in the silicon bilayer. In the H3 site the adsorbate sits in the centre of the triangle formed by three 'up' atoms in the silicon bilayer and there is no 'down' atom immediately below it. The T4 site has the adsorbate sitting above the centre of the triangle formed by three silicon 'up' atoms in which there is a 'down' atom immediately below it in the silicon bilayer.

1.2.1 Rare Earth-Semiconductor Surfaces

The interface between rare earth (RE) metals and silicon is known to have a low Schottky barrier on n-type silicon [15, 16] and a high Schottky barrier on p-type silicon [17]. This has potential applications in devices and there have been studies that characterise such device structures [18–24]. This has generated interest in the study of the surface structure and properties of reconstructions formed by RE metals on silicon. Netzer [25] has reviewed progress up to 1995.

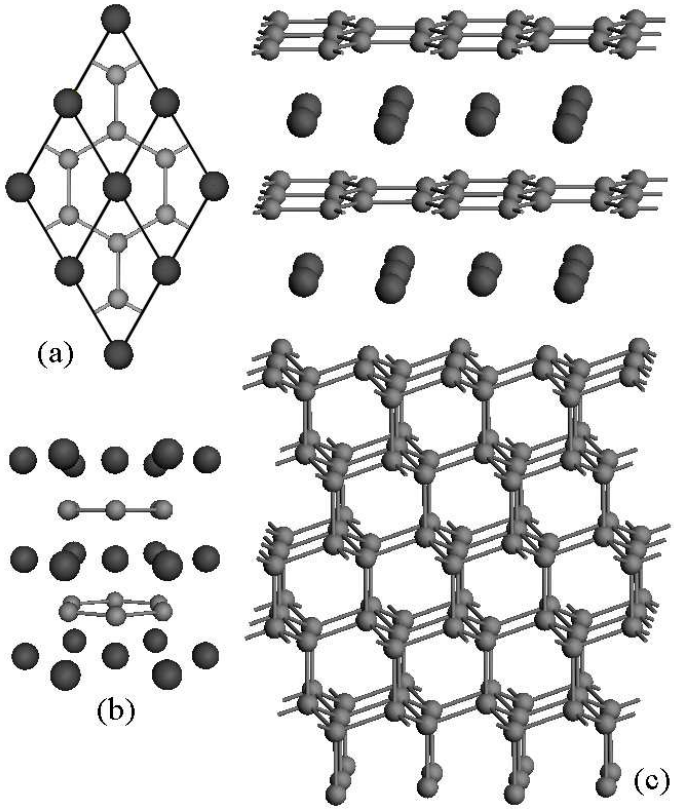

Figure 1.3: The AlB_2 type structure of the bulk RE silicides in (a) top view and (b) perspective view has a good lattice match to the bulk terminated Si(111) surface. This means that an ordered structure like the one in (c) can be grown. RE atoms are darker and larger spheres.

The RE silicides are also of fundamental interest because the bulk RE silicides have a good lattice match to silicon and well ordered surface reconstructions might be expected [26, 27]. The lattice mismatch ranges from about -2.5% for lutetium silicide to $+1\%$ for gadolinium silicide. Figure 1.3 shows a bulk RE crystal and its fit onto the bulk-terminated silicon lattice. Such a good match to the substrate confers a great deal of order and stability to the RE silicide surfaces and such multilayer structures have been shown to grow epitaxially ([26, 28, 29] and therein). Their structure has been characterised using a variety of techniques (see [30] and therein for a full list of

references) and it has been shown that there are vacancies in the graphitic silicon layers.

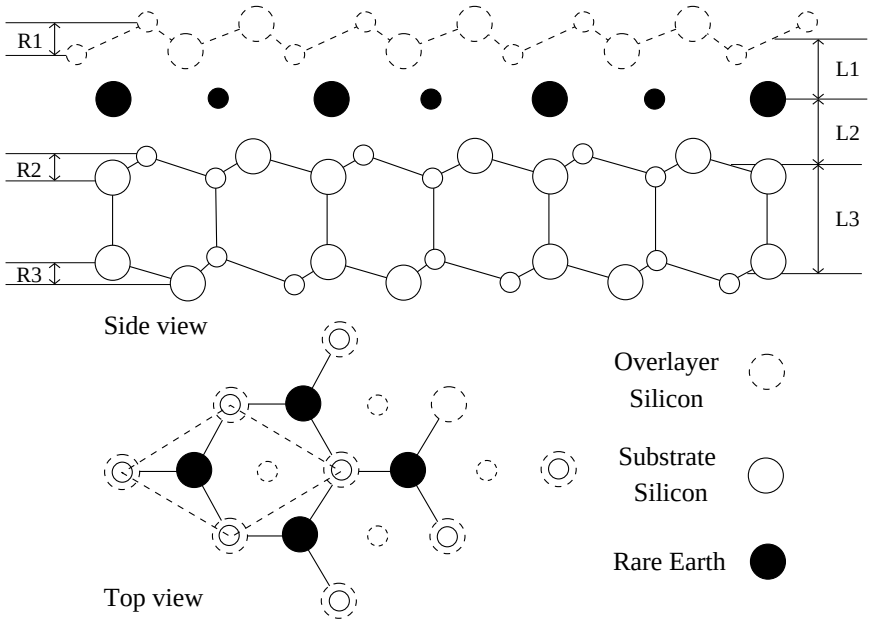

Figure 1.4: Schematic showing the structure of a 2D RE silicide on the Si(111) surface. Smaller circles indicate perspective. Six characteristic vertical spacings are defined; three silicon bilayer rumpling amplitudes R1, R2, R3 and three interlayer spacings L1, L2, L3.

Such a structure is termed a 3D RE silicide since there is more than one RE layer. For just one monolayer (ML) of RE metal the structure shown in Figure 1.4 is formed, which is termed a 2D RE silicide. In the 3D RE silicides the silicon layers above the flat RE metal layers are flat but here the silicon overlayer is rumpled almost to the same degree as in the silicon bulk. Another interesting feature is present. The direction of the rumpling is in the opposite sense to that in the bulk. The top bilayer is the equivalent to a bulk layer that has been rotated 180° about an axis normal to the surface plane.

The 2D RE silicides have been extensively studied with LEED, MEIS, STM, *ab-initio* calculations and spectroscopic studies [29,31–50] and the structure shown in figure 1.4 is well established. A similar structure has also been reported for RE germanides [37, 51]. Some remaining open issues are why the top bilayer is reverse buckled, what are the vibrational modes on the surface (LEED and MEIS structure fits both require enhanced vibrations) and whether the surface has other novel properties such as optical properties.

1.2.2 Nanowires

In systems with reduced dimensions quantum effects cause the electronic and magnetic properties of certain materials to be very different from those in the bulk. This may lead to new applications in optoelectronic and microelectronic devices. One class of materials that are attracting attention are so-called nanorods, which comprise a chain of atoms limited to one dimension or a group of such chains in close parallel proximity. A natural medium on which to grow nanorods is a surface and some novel properties have already been reported for nanorods grown on surfaces [52–54].

There are many systems in which the reconstruction adopted by the deposited material can be considered a nanorod. On semiconductor surfaces most of the work has involved silicon as a substrate. On the Si(100) surface differences in the energy of binding sites cause the group III-IV metals Al, Ga, In, Sn, Pb [55, and references therein] to form anisotropic nanorod structures. The rare-earth (RE) metals Dy, Er, Gd, Ho, Sc, Sm, Y and Yb also form nanorods on this surface [56–59, and therein] due to a good lattice match between the adsorbate and the substrate in the direction in which the nanorod is grown and a poor lattice match in the perpendicular direction. The RE nanorods on Si(100) are distinct because they form a chemically incorporated silicide surface whereas the other structures consist of isolated metal atoms in some site of the reconstructed substrate. On Ge(100) no nanowires involving RE metals have been reported but it is assumed that the anisotropy in the matching of the lattice constants may yield nanorod structures akin to those on Si(100).

The Si(111) surface has three fold symmetry and is not as favourable a host to nanorod growth. Gd and Pb nanorods have been grown in the lee of step edges along the [110] direction [60, 61]. On the terraced regions the way forward is to deposit an adsorbate on a prestructured adsorbate/Si(111) surface. In this way Pb nanorods have recently been grown on the Sm/Si(111) surface [62]. Other systems involving Si(111) could also more loosely be considered as hosting nanorods; the Si(111)$5\times n$-Au surfaces [53,54], Si(111)4×1-In [52] and the family of $3\times n$ structures formed by Ag and alkali metals (such as Li, Na, K and Rb) and alkali earth metals (such as Mg, Ca and Ba) and rare earth metals (Yb and Sm) on Si(111). It is to these $3\times n$ structures that we now turn our attention.

1.2.3 Honeycomb-Chain Channel Surfaces

The prospect of creating an ordered one-dimensional system has lead to the extensive study of chain structures grown on surfaces. The alkali metals (AM) form such a chain structure as part of a 3×1 reconstruction with an AM coverage of 1/3ML [63, 64, and therein]. At a coverage of 1/6 ML the alkali earth metals (AEM) and the rare earth metals (REM) form a 3×2 reconstruction [65–68, and therein]. There is a wealth of experimental evidence from STM, LEED and spectroscopic techniques to suggest that in these 3× structures there is a common structure for the reconstructed silicon [63–73, and therein]. The honeycomb-chain channel model (HCC) is now regarded by many as the most plausible of the candidate structures [74–76]. In the HCC model there are parallel ordered one-dimensional lines of metal atoms sited in a silicon free channel. These are separated by almost flat honeycomb layers of silicon. The 3×2 unit cell of the HCC model is shown in figure 1.5.

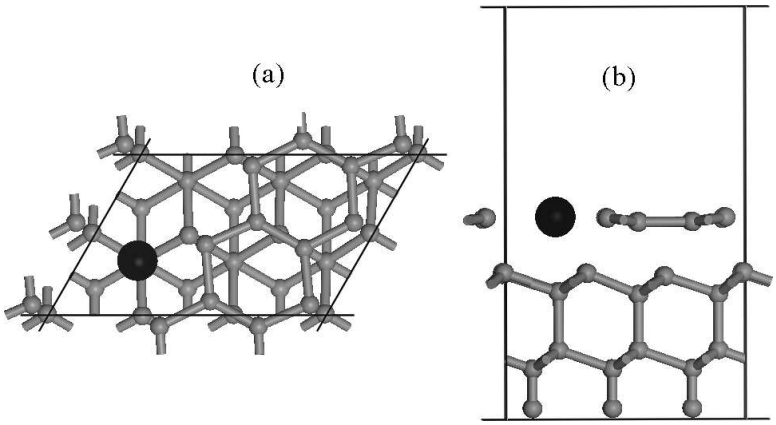

Figure 1.5: The unit cell of the 3×2 HCC structure seen from above (a) and from the side (b). The metal atom is large and black.

There are still important questions to answer about this family of 3× metal surfaces. There has been no quantitative structural validation using MEIS or LEED for any of the 3× structures. Good qualitative agreement has been obtained between the experimental and theoretical STM images for Ba and Sm [65, 67]. Fan and Ignatiev have also qualitatively compared the I-V curves for the 3×1 structures with Ag, Li and Na as the deposited metal atoms [73] but they have not attempted a full structural fit.

A major open question concerns the level of disorder in the system. There is no evidence from STM experiments to suggest that the samarium atoms are in random sites in the channel. STM images reveal large 120° rotational domains in which the samarium atoms are evenly spaced in the ×2 direction. We might expect this since electrostatic repulsion between the metal atoms would act to space them evenly along the one-dimensional chain.

Despite this, many workers have used disorder in the positions of the samarium atoms to explain why the 3×2 surface seen in STM produces a 3×1 LEED pattern. Figure 1.6 shows the difference between the 3×1 and 3×2 unit cells in real and reciprocal space. If the periodicity is halved in the ×2 direction then the 3×2 unit cell becomes a 3×1 unit cell. The honeycomb chain of silicon atoms is almost mirror symmetric about a line drawn perpendicular to it and it is the metal atom that makes the unit cell of ×2 periodicity in this direction. It is reasonable to suggest, therefore, that disorder in the location of the metal atom is responsible for the apparent 3×1 unit cell.

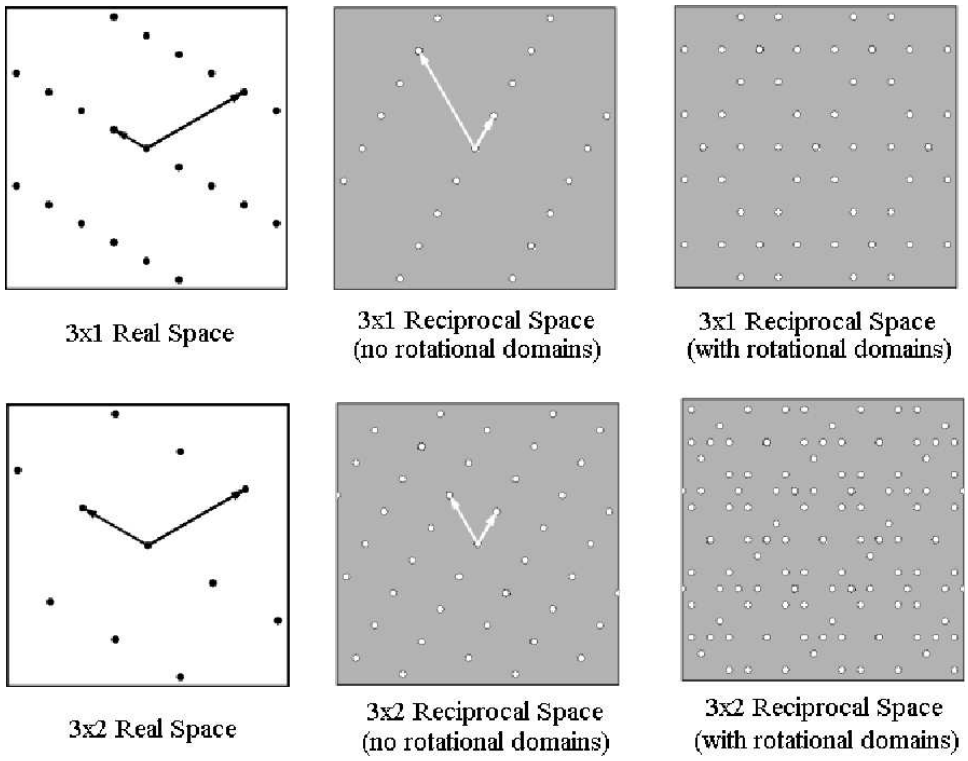

Figure 1.6: The unit cell of the 3×1 and the 3×2 structures showing their reciprocal lattices both with and without the extra spots introduced by rotational domains.

Fan and Ignatiev [73] showed that the 3×1 structures formed by Ag, Li and Na have similar I-V curves and the authors suggest that the reconstructions that are formed are largely independent of the species of metal atom present and that there is a common reconstruction of silicon atoms that is responsible for the LEED I-V curves. In another study a Fourier analysis of a random tesselation of a large sample of registry shifted unit cells has been carried out by Schäfer et al [73]. They show that this simulation of long range disorder in the position of the metal atom does produce a unit cell with a 3×1 periodicity in reciprocal space. Alternatively, Over et al [77] have suggested that the substrate and silicon adatoms could be acting as the dominant scattering unit with the metal atoms sitting in 'open sites'. It is clear that a full LEED I-V structural investigation is needed to attempt a resolution of this STM-LEED discrepancy.

1.3 Overview of research.

The overall aim of this work was to compare LEED I-V analysis with the results of DFT calculations to determine the usefulness of the latter for suggesting trial structures for LEED I-V analysis. A second main aim was to determine the electronic and structural properties of the RE silicides and to compare these to those determined from other experimental techniques. Collaborative projects with the experimental efforts of other members of the surface physics group at York arose as the merits of the *ab-initio* technique became apparent within the group.

In Chapter 4 of this work *ab-initio* calculations of the structure of 2D Si(111)-1×1 Ho and a nanowire structure Ge(111)-5×1 Ho are described. The 2D Si(111)-1×1 Ho structure has previously been studied using LEED and MEIS in the surface physics group at York. The aim of this study was to calculate the optimum atomic arrangement for this surface and to compare this with that obtained by experiment. The second half of Chapter 4 concerns a novel nanowire structure that was observed by E. Perkins and C. Bonet using the York STM instrument. Using the dimensions obtained from the STM images C. Bonet has been able to suggest a structural model. The work reported in this section attempts to optimise the atomic coordinates in this large unit cell that contains two holmium atoms and thus to determine if the suggested structure is stable. The electronic properties thus obtained are compared to those determined from STM and STS data taken from this surface.

In Chapter 5 a LEED I-V investigation of the structure formed when both iron and holmium are deposited onto the Si(111) surface is reported. Iron is known to form many phases on Si(111) with a good degree of disorder. The aim was to determine whether a mixed holmium-iron overlayer would benefit from the structural order of the Si(111)-1×1-Ho surface and at the same time retain the technologically interesting properties of the Si(111)-Fe surface. In the course of this work reference I-V data taken from the Si(111)-1×1-Ho surface was found to differ from that reported in the literature and to bear a closer resemblance to that obtained from Si(111)-1×1-Dy in other work. A new LEED I-V structural fit was obtained to this new experimental data and compared to that obtained previously from MEIS, LEED and the *ab-initio* calculations reported in Chapter 4.

The RE metal samarium was not known to form a 2D structure on Si(111) akin to that described in §1.2.1. In Chapter 6 we describe details of the experimental characterisation and an attempted structure fit for a 1×1 structure that has been observed on this surface. LEED I-V curves have been recorded for this 1×1 surface and several structures are suggested and compared with one another through LEED I-V R-factor analysis and their relative energies obtained from *ab-initio* calculations. The second

half of Chapter 6 descibes work on the Si(111)-3×2-Sm surface that has previously been studied using STM and an *ab-initio* calculation. The structural model suggested in the literature has been quantitatively tested using LEED I-V analysis working in tandem with *ab-initio* structural optimisations. This surface is part of a family of metal silicides that give a 3×1 LEED pattern but in STM experiments show a 3×2 unit cell. In this chapter the reasons for this discrepancy are suggested from the results of LEED I-V analysis.

Chapter 2

Low Energy Electron Diffraction

2.1 History

Bragg and others studying the diffraction of X-Rays by crystals were confounded by their behaviour. Some of their interactions with matter could be explained by ascribing to them wave properties but others demanded that they be considered as particles. In 1912, William Bragg remarked that 'the problem becomes not to decide between theories of X-Rays, but to find one theory which possesses the capacities of both' [78]. One experimentalist who worked extensively with X-Rays was Maurice de Broglie. He introduced the problem to his younger brother Louis, a theorist. In 1924 in his doctoral work the younger de Broglie suggested that there was an 'impossibility of considering an isolated fragment of energy without assigning a certain frequency to it' [78]. The idea was placed on a sound theoretical basis rooted in special relativity and was generalised beyond X-Rays to predict that particles such as electrons might display wave-like behaviour. The thesis was published in 1925 and during his oral examination de Broglie was asked how his ideas might be tested. He suggested that since his electrons would have wavelengths that are of the order of the atomic and interplanar spacings in a crystal then they should be diffracted from a crystal lattice if they are given the right energy. This effect would not occur if electrons were purely particles and its observation would provide clear validation of the de Broglie theory.

In fact, this experiment had already been carried out. Between 1919 and 1929, at the Bell telephone laboratories in New York, Clinton Davisson and various co-workers (principally L. Germer) carried out a comprehensive series of investigations into electron scattering, looking at the properties of secondary electrons. As a 'sideline' the team also looked at bombardment of clean and oxidised metal surfaces by electrons. The first sample that they used was polycrystalline nickel. The electron beam was incident upon the sample at some angle and the distribution of secondary electrons was recorded

as a function of scattering angle. One day a liquid air flask exploded and cracked the vacuum tube. The group had to rebuild the apparatus and clean the nickel surface by heating it to a high temperature. In subsequent experiments the angular distribution of the scattered electrons was drastically altered. The effect was traced to the introduction of order into the crystal. During the cleaning process large single crystal domains were introduced into the polycrystalline nickel sample. Further experiments in which the angle of collection was made equal to the angle of incidence revealed a set of maxima in the electron intensity as their energy was increased. In 1926 Davisson heard of the de Broglie theory and the experiments came into focus. Working on the assumption that his electrons were being diffracted by the crystal they used the energies at which the maxima occured to determine the wavelengths of the electron. They were found to be in good agreement with those suggested by the theory of de Broglie [79].

Another electron diffraction effect analogous to X-Ray powder diffraction was observed in 1927 by G. P. Thompson, a Cambridge fellow working in Aberdeen. Inside a pumped discharge tube electrons were passed through a thin ($\sim$ 10nm) polycrystalline sample and their positions recorded on a photographic film. The result was a series of concentric rings similar to those seen with X-Ray powder diffraction. The radii of these rings suggested an electron wavelength that was in good agreement with that suggested by de Broglie [80].

These independent experiments were amongst the first to ratify the predictions of the new quantum mechanics and Davisson and Thomson were awarded the joint Nobel Prize in 1937. The work of Davisson was much more akin to modern LEED experiments than that of Thompson. The Bell group looked at the overall intensity of electrons diffracted into a given direction (in effect a single spot in the LEED pattern, with off-normal incidence) as a function of the energy. From the discrepancy between the energies at which diffraction maxima occured and those that they expected from the Bragg condition they were able to postulate that the spacings between the outer few layers of the crystal were relaxed from their bulk value which was the first ever quantitative surface structure determination. They also observed extra diffraction maxima when the surface was coated with a thin oxide layer.

The experiments at Bell labs suggested that electron diffraction might be used to determine surface crystal structure. It was not until the advent of effective and economical ways to produce a sufficient vacuum in the early 1960's that this became a realistic proposition [81–83]. Then there came a flurry of LEED experiments on a variety of surfaces. In the 1970's LEED was positioned as a central quantitative tool in surface science by the work of J. B. Pendry [84] and others who developed a theoretical means to calculate the properties of electrons diffracted by a given surface. We will now take an overview of LEED theory, starting with a discussion of the LEED spot pattern.

2.2 Theoretical Discussion of Low Energy Electron Diffraction

What follows is a discussion of the LEED spot pattern and I(V) curves that concentrates on the mechanisms involved. For the full detail the reader is referred to the standard LEED theory literature [84, 85]. Where appropriate extra references have been added.

The LEED Diffraction Pattern

Electrons that are elastically scattered from a crystal surface form a series of spots when they are subsequently allowed to illuminate a phosphorescent screen. In this section we will attempt to explain why the allowed directions for scattering are quantised.

Bragg scattering and LEED spots

A one-dimensional array of scatterers that are equally spaced at intervals of d will scatter incoming waves of de Broglie wavelength λ. Constructive interference between the waves scattered from each point in the array will occur when the angle of scattering θ_n satisfies the condition

$$sin\theta_n = \frac{n\lambda}{d} \tag{2.1}$$

where n is an integer. The diffraction maxima form lines where each line is at an angle to the normal given by equation 2.1. Now consider a second array perpendicular to the first with array spacing b. Diffraction maxima now satisfy

$$sin\theta_y = \frac{m\lambda}{b} \tag{2.2}$$

where m is an integer and the new angles θ_n each trace out a line that defines a diffraction maximum. If we expand our array into two dimensions we effectively have two orthogonal one dimensional arrays and the conditions for a diffraction maximum have to satisfy the conditions for both *simultaneously* - the maxima in the diffraction pattern form a series of spots where the allowed lines for the two orthogonal directions overlap.

We can see from equations 2.1 and 2.2 that as the energy of a monochromatic beam of incident electrons is increased and the de Broglie wavelength of the electrons is decreased the spots in the LEED pattern will contract in both directions parallel to the surface as the angles θ_n and θ_m are decreased. The spots in the LEED pattern contract towards the centre of the pattern as the energy of the incident electrons increases.

Another consequence of our diffraction conditions is that if the spacings d and b of the features in either direction in the array are changed then the spacings of the spots in the LEED pattern will also change. In fact, there is a reciprocal relationship between the spacings of features in real space and their spacing in the LEED pattern. This relationship is better understood if we look at the full quantum mechanical analysis of the diffraction pattern.

The Laue condition and parallel momentum exchange

In our conceptual picture the angle of the allowed state with respect to the normal for a de Broglie wavelength λ was given by equations 2.1 and 2.2. We can recast these equations. The wavevector of the electron is a propagation direction and it is related to the wavelength by

$$\lambda = \frac{2\pi}{|\,\boldsymbol{k}_0|} \tag{2.3}$$

Equations 2.1 and 2.2 become

$$|\,\boldsymbol{k}_0| sin\theta_n = \frac{2\pi}{d}\, n \tag{2.4}$$

$$|\,\boldsymbol{k}_0| sin\theta_m = \frac{2\pi}{b}\, m \tag{2.5}$$

The de Broglie wavelength is related to the momentum p of the particle by

$$\lambda = \frac{h}{p} \tag{2.6}$$

where h is the Planck constant. This means that we can use the wavevector $|\,\boldsymbol{k}_0|$ as a measure of the momentum of the electron since the two are directly proportional

$$|\,\boldsymbol{k}_0| = \frac{2\pi}{h}\, p \tag{2.7}$$

We can see that in equations 2.4 and 2.5 the term on the left is a measure of the momentum of the electron parallel to the surface. It is quantised by the term on the right into units of 2π/spacing. In the two dimensional picture the spots in the LEED pattern correspond to scattered states in which the parallel momentum of the electron is quantised in the two orthogonal directions. The spots form a lattice

$$\boldsymbol{g} = \frac{2\pi}{d}\, n + \frac{2\pi}{b}\, m \tag{2.8}$$

In this lattice each point corresponds to an allowed component of parallel momentum

for an elastically scattered electron. The manifestation of the momentum state space lattice in real space is called the reciprocal lattice because of the reciprocal relationship between spacings of features in the real space lattice and the allowed parallel momentum lattice. An incident beam normal to the surface and with no initial parallel component of momentum can only be elastically scattered into a state where its component of parallel momentum has changed by a discrete amount. The integers in equation 2.8 can be used to label the spots in the diffraction pattern. Electrons incident along the normal that do not gain a parallel component of momentum would be diffracted to form the (0,0) spot and so on.

Only a finite number of beams emerge from the crystal. The largest allowed value of parallel momentum is that for which the z component of momentum is almost zero and the electrons are travelling almost parallel to the surface. This places a restriction upon the parallel component of momentum for a given spot $\boldsymbol{g}$

$$|\boldsymbol{k}_{0||} + \boldsymbol{g}|^2 \leq 2E \tag{2.9}$$

where $\boldsymbol{k}_{0||}$ is the component of parallel momentum in the incident beam which extends the condition in equation 2.9 to cases of off-normal incidence. As the primary energy is increased the parallel momentum of more beams satisfy (2.9) and there are more spots on the screen. The existing beams contract towards the centre to accomodate the new beams.

For a general real space lattice with lattice vectors (a, b) the diffraction pattern will represent the reciprocal lattice of the real space lattice formed by taking the fourier transform of the real space lattice. The reciprocal relationship of the real space lattice vectors $\boldsymbol{a}$ and $\boldsymbol{b}$ and the reciprocal lattice vectors $\boldsymbol{a^*}$ and $\boldsymbol{b^*}$ can be formally stated as

$$\boldsymbol{a^*} = 2\pi \frac{\boldsymbol{b} \times \hat{\boldsymbol{n}}}{\boldsymbol{a} \cdot (\boldsymbol{b} \times \hat{\boldsymbol{n}})} \tag{2.10}$$

$$\boldsymbol{b^*} = 2\pi \frac{\boldsymbol{a} \times \hat{\boldsymbol{n}}}{\boldsymbol{a} \cdot (\boldsymbol{b} \times \hat{\boldsymbol{n}})} \tag{2.11}$$

In summary, the effect of the periodic potential in real space is to form a series of discrete beams each with a different value of momentum parallel to the surface which is incremented by a reciprocal lattice vector. Quantum mechanics places a restriction upon the spatial distribution of the allowed states for elastic scattering.

Overlayers, Domains and Defects

Consider two parallel layers of material in which the spacings of features in the top layer are two times greater than those in the second layer. If we record the diffraction pattern formed by this composite layer stack then the deeper layer will form a series of points on the screen. The top layer will form its own set of spots but these will be spaced two times closer together than the second layer spots. The process is illustrated in figure 2.1.

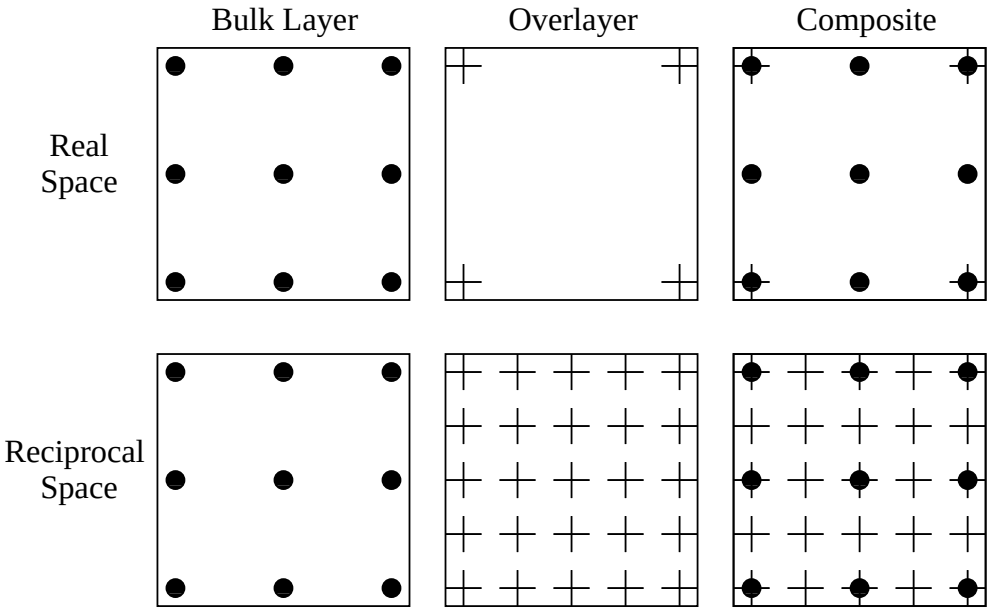

Figure 2.1: Composite LEED pattern formed by a square lattice substrate and an overlayer with a square unit cell with lattice vectors twice those of the substrate.

In a surface reconstruction where the top layer of material is arranged periodically upon an infinite bulk substrate the diffraction pattern will reveal the relative periodicity of the overlayer and the repeated bulk. For example, if an overlayer of Fe is deposited onto the silicon (111) surface and after annealing there is one Fe atom sat in every three-fold hollow site then we would call the reconstruction Si(111)-1x1 Fe because the Fe overlayer lattice is the same size and has the same periodicity as the substrate. Samarium deposited onto Si(111) and found to sit in every third three-fold hollow site along one lattice vector direction and every second three-fold site along the second lattice vector direction would be termed Si(111)-3x2 Sm.

Spot Intensity as a Function of Incident Electron Energy

The Bragg interference model is a useful tool that aids the understanding of the appearance of spots in the LEED diffraction pattern and their behaviour. We will now

look at the variation of the intensity of a given spot in the LEED pattern with the energy of the incident electrons and see how well the Bragg model explains the features in the curves.

First, a simple model for the positions of the Bragg peaks. For normal incidence of an electron beam of wavelength λ upon layers separated by a distance d the constructive interference condition is

$$n\,\lambda = 2d \tag{2.12}$$

where n is an integer. The de Broglie wavelength of the electron is

$$\lambda^2 = \frac{B}{E} \tag{2.13}$$

where B is a constant and E is the energy. Intensity maxima are thus expected at energies

$$E = \frac{B}{4d^2}\,n^2 \tag{2.14}$$

which means that we get a sharp peak at energies of 1, 4, 9 and so on in units of energy given by $B/4d^2$.

For a real surface there is a finite flux of electrons and the intensities of the Bragg peaks are not infinite. Also, in a surface region the interlayer spacings become relaxed (and sometimes expanded) so that there are a distribution of spacings around the value d. We have to relax the Bragg condition and the peak are smeared out a little (see figure 2.2 a).

The electron is also affected by the electrostatic melée inside the crystal produced by other electrons and ions. As the electron enters the crystal the electrostatic attraction of the ion cores lowers its energy. This 'inner potential' increases the kinetic energy of the electron to conserve energy in the diffraction process. The same inner potential holds all the other electrons inside the crystal. The incident electron with its extra kick of kinetic energy will meet the Bragg condition at a lower initial energy and the peaks will become shifted in energy.

The inner potential is a background potential provided by all ion cores. The electrons are also affected by individual ion cores as they pass near to them. The electrostatic attraction causes the electron to momentarily speed up which lowers its de Broglie wavelength. As the electron moves away from the atom it loses energy and it's original wavelength is restored but there is an overall change in phase. The complex electrostatic object that an atom is affects only the phase of the electron and not the net energy. A similar effect occurs when a particle moves over a square well potential

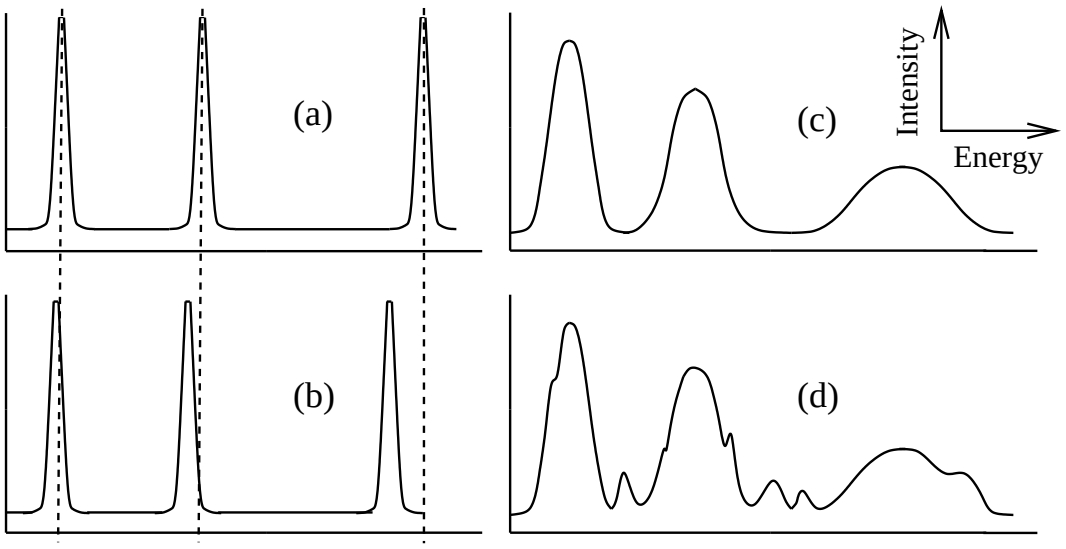

Figure 2.2: Distortion of a LEED I(V) curve away from the Bragg condition (a) as the effects of (b) phase shifts, (c) finite penetration depth and (d) multiple scattering are included.

and simple potentials such as this are used to approximate the ion cores (more about this later). The interaction of the electrons with the ion cores shifts the peaks to lower energies (see figure 2.2 b), typically by a few eV. The exact shift depends upon the species present and their exact geometry and it is thus difficult.

It is not only the positions of the maxima that are affected. The peak widths are also sensitive to the scattering properties of the composite crystal. The minimum width of an intensity peak is determined by the uncertainty principle. The majority of the flux in an incident beam is inelastically scattered. The electron wavefunction must contain a large damping term V_{0i}, a complex number that will remove electron flux from the elastic part of the wavefunction. It is shown in Pendry [84] that V_{0i} is in inverse proportion to the mean lifetime τ of an electron in the crystal. If an electron is to be elastically diffracted this process must occur before a time τ has elapsed. The uncertainty principle requires that this restriction upon the time frame be repaid by a given diffraction maximum being widened to a minimum width given by

$$E \geq 2|V_{0i}| \tag{2.15}$$

This defines the minimum width of a Bragg peak. The peaks are smeared to become wider than this by two other effects; absorption and elastic reflection. The effect of both processes is due to their impact on the depth of penetration of the electron into the crystal. In a simple double slit diffraction experiment we see two maxima. If we add more slits to make a grating the maxima become narrower and more closely spaced. The same effect occurs with Bragg scattering from a set of stacked layers. The more

layers that scatter electrons the narrower the Bragg peaks, tending towards a minimum peak width given by equation 2.15. If absorption is low then the electron will penetrate deep into the crystal and the peaks will narrow. Conversely, if the top two layers are strong elastic scatterers then very little of the incident flux penetrates deep into the crystal and the Bragg peaks will widen. Peak broadening is shown in figure 2.2 (c).

In comparison with X-Ray diffraction the scattering of the incident particles is strong. Electrons do not penetrate deep into the crystal which is of benefit because it makes LEED surface sensitive. It also makes the process complex because multiple scattering can occur. An electron that emerges from the crystal without loss of energy will generally have travelled a very complicated path into and back out of the crystal. It is possible for an electron to be scattered in a given direction and on the way out of the crystal be again elastically scattered in a different direction by another layer. This new multiply scattered beam will satisfy the Bragg condition for a different energy than the rest of the flux in that spot in the LEED pattern and we will see a subsidiary maximum (see figure 2.2 d).

If the layer structure is comprised of many different species of material in different intralayer geometrical arrangements or even if there is a simple overlayer then complex interference effects that vary with the species present, their geometrical arrangment and with the energy occur. It is difficult to extend our simple conceptual discussion of the shape of I(V) curves to include any effects as complicated as these. Multiple scattering and the many factors that compete for electron flux mean that it is simpler to just calculate the I(V) curve and observe the result. In the next section we will take an overview of the theory that underlies such LEED calculations.

Diffraction by a single atom - muffin tins and phase shifts

To describe the scattering properties of an atom we must first determine the form of the potential that can be used to accurately represent the ion core and the electrons. LEED electrons are insensitive to small changes in the potential caused by the valence electrons and we can assume a constant potential between ion cores to model their effect. The ion core, with its core state electrons, is modelled by a spherically symmetric 'muffin-tin' potential centered on each atom. Figure 2.3 below shows the form of the potential

The effect of this potential is to introduce a phase shift into the electron wave. In spherical coordinates we can express the scattered wave for an electron with momentum ℓ as being

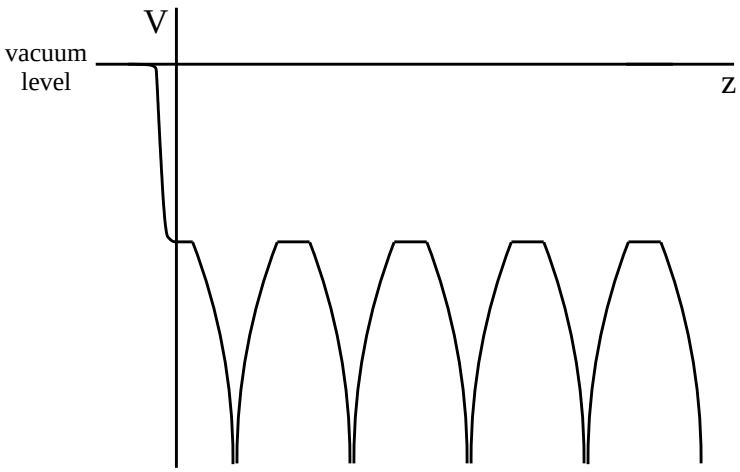

Figure 2.3: A cross section of the 'muffin tin' potential that is used to approximate the ion cores. The horizontal axis is normal to the surface plane and the surface barrier is shown on the left.

$$\Psi_\ell^S \;=\; \mathcal{C}_\ell^0 h_\ell \left[e^{2\imath\delta_\ell} - 1\right] \tag{2.16}$$

$\mathcal{C}_\ell^0$ is the amplitude of the unscattered wave, h_ℓ is a spherical Hankel function which determines the angular distribution of the scattered wave and δ_ℓ is the phase shift. To represent the scattering properties of the atom we must determine the phase shifts for all of the composite spherical waves with angular momentum values that are affected by the potential. As the electron energies are increased spherical wave components with greater angular momenta come under the influence of the atomic potential and are scattered. At 300 eV a strong scatterer might require the inclusion of electron spherical wave components with angular momenta up to $\ell = 15$ or more.

In this work the `DLPHASE` [86] program was used to calculate the phase shifts for each angular momentum channel included and for each electron energy over which I(V) curves were to be simulated for each type of inequivalent atom. The program uses a library of atomic densities calculated using density functional theory to model the 'muffin-tin' potentials.

Diffraction by a single layer

The probability for an incident plane wave $\exp(i\,\boldsymbol{k_g}\cdot\boldsymbol{r})$ to emerge in the direction $\exp(i\,\boldsymbol{k_{g'}}\cdot\boldsymbol{r})$ after an elastic interaction with a layer of atoms is given by the appropriate element in the layer diffraction matrix $\mathrm{M}^{\pm\pm}_{\boldsymbol{g'g}}$. There are four such matrices that we can construct;

$\mathbf{M}^{+-}$ The wave is incident from above the layer and is reflected into the opposite direction.

$\mathbf{M}^{-+}$ The wave is incident from below the layer and is reflected into the opposite direction.

$\mathbf{M}^{++}$ The wave is incident from above the layer and is transmitted.

$\mathbf{M}^{--}$ The wave is incident from below the layer and is transmitted.

Each element in these matrices depends upon the energy of the incident beam and upon the angular momentum dependent phase shifts for each atom in the layer that describes the electron-atom elastic scattering. If the layers correspond to a Bravais-lattice then symmetry considerations mean that $\mathrm{M}^{+-} = \mathrm{M}^{-+}$ and $\mathrm{M}^{++} = \mathrm{M}^{--}$ and we need only calculate a reflection matrix and a transmission matrix. As the incident energy increases the incident electron wavelength decreases and the number of scattered beams from a given layer increases. This means that the number of beams used in the basis set $\sum_{\boldsymbol{g}}\exp(i\,\boldsymbol{k}^{\pm}_{\boldsymbol{g}}\cdot\boldsymbol{r})$ to represent the incident and scattered beams is energy dependent and the reflection and transmission matrices must be separately calculated for each primary energy for which the I(V) curves are to be determined.

If the scattering is strong then the flux of waves incident upon the ion core of some atom $\jmath$ within the layer will contain a significant contribution arriving from other atoms within the layer. If we consider the incident wave amplitude incident upon atom $\jmath$ in a spherical wave basis set we can write for the amplitude

$$A_{\ell m\jmath} = A^{(s)}_{\ell m\jmath} + A^{(0)}_{\ell m\jmath} \tag{2.17}$$

The suffixes ℓ and m describe the angular dependence. $A^{(0)}_{\ell m\jmath}$ is the amplitude incident from outside the layer and $A^{(s)}_{\ell m\jmath}$ is that scattered from other ion cores within the layer. This depends upon $A^{(0)}_{\ell m\jmath}$ and it must be evaluated self consistently. Now, the electron flux is slightly absorbed by the inner potential as it makes it's journey between the ion cores. For our atom $\jmath$ there are a limited number of nearby atoms whose scattered electron wavefield arrives at atom $\jmath$ with any significant amplitude. A truncated summation over nearby atoms eases the self consistent evaluation of $A_{\ell m\jmath}$.

Having determined $A_{\ell m_J}$ for all of the atoms in the unit cell and after application of the relevant phase shifts to the incident spherical waves it is possible to construct the total set of diffracted spherical waves. These can readily be used to form an overall layer diffraction matrix $\mathrm{M}^{\pm\pm}_{\boldsymbol{g'g}}$. Determination of the scattering matrices for each layer in the system is a significant part of any LEED calculation and in turn the most time consuning part of their determination is in the self consistent evalution of the intralayer scattering matrices.

Layer Stacking

Having determined the scattering properties of each type of scatterer in the system and the scattering properties of each individual layer we are almost ready to calculate the electron scattering properties of the surface as a whole. The user chooses a number of layers to represent the surface region and the layers are stacked parallel to one another with user defined separations. The last layer provided must have the same structure as the bulk substrate as it is repeated ad infinitum in the event that the incident electron penetrates deep into the crystal. The change in an electronic wavefunction during propagation between layers is easily represented by an imaginary component in the energy that acts as a damping term.

Renormalised Forward Scattering

Perturbation theory is used to approximate the propagation of the incident beamset at a given energy through the layer stack. In the `CAVLEED` program [87] the default scheme used is Renormalised Forward Scattering (RFS hereafter). The scheme is illustrated in figure 2.4 below

In the RFS scheme [88] the beams that are transmitted without being scattered and the beams that are scattered forwards are considered as the unperturbed basis set. Reflection by a layer is then treated as a weak perturbation of this beamset. The total reflectivity can be expanded into a series of passes into and out of the crystal each requiring the electron to undergo a greater number of reflection events in order to emerge from the crystal. The first order perturbation is for an electron to emerge after having being reflected just once. The second order perturbation is for an electron to emerge after undergoing two reflection events and so on.

Increasing orders of perturbation contribute less and less to the reflected wavefield. The process is repeated until the addition to the reflected amplitude by the next order of perturbation falls below some tolerance. However, if one pair of successive layers both have strong reflections then multiple scattering can result in the wavefield becoming trapped between these layers. Many orders of perturbation would be needed in order

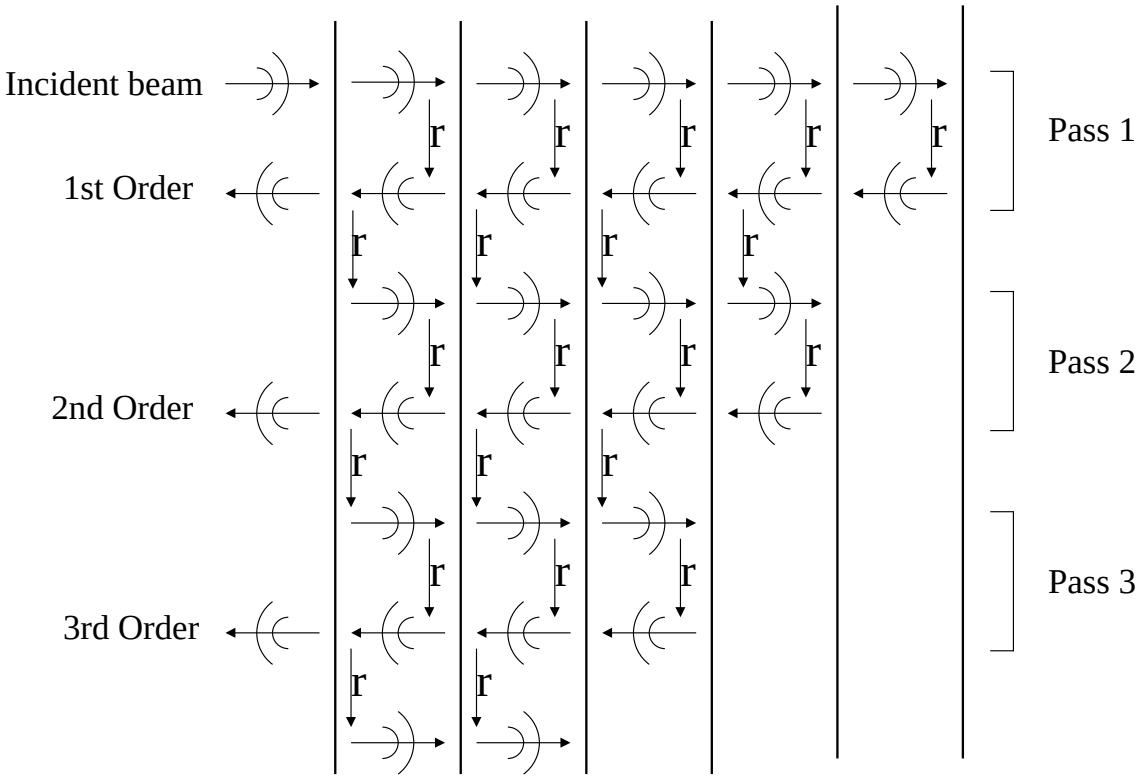

Figure 2.4: In the renormalised forward scattering perturbation scheme the beam is propagated into the crystal until the amount reflected (labelled r) falls below some tolerance. A beam reflected just once becomes the first order beam. Successive orders are built up until their contribution becomes negligible.

to converge RFS and it will fail. If the layers are very close together many evanescent waves are needed to describe the wavefield and this can cause convergence problems. In these cases where RFS fails to converge `CAVLEED` will default to Layer Doubling, its second layer stacking perturbation scheme.

Layer Doubling

In this scheme two layers of the crystal are first tested to determine if the electron beam propagation converges. The slab is then doubled in thickness at each subsequent iteration until the penetration depth is spanned. This method is very efficient for deep electron penetration but for typical penetration depths of about eight layers Renormalised Forward Scattering requires less storage space for the scattering matrices and is quicker to attain convergence.

Thermal Effects

The effect of temperature is to reduce the intensity of peaks and it is more pronounced at higher energies. This is because small random displacements in the atomic positions mean that the waves that are scattered from them are not as coherent even when the Bragg condition is met. The positive interference effect is diluted and peak intensities dim. At higher energy the electron has a shorter wavelength and the phase shifts are much more sensitive to discord in the diffraction process.

Mathematically, the problem is how do we model the heat capacity for a material for which there might be no data available? The codes used in this work make use of the Debye approximation. In this atomic vibrations are treated as phonons in a box (in an almost identical manner electromagnetic waves are treated like photons in a box to obtain the Planck law of black body radiation). The true dispersion of the waves is ignored and instead it is assumed that

$$\omega = v_s k \tag{2.18}$$

where ω is the frequency, k is the wavevector and v_s is the local speed of sound. We assume that this runs up to some cutoff frequency ω_D, above which there are no allowed phonon modes. Integrating over all frequencies up to the Debye frequency gives a rough approximation of the total number of modes which must of course be equal to the 3N lattice vibration modes possible in a crystal of N atoms. From this it is possible to produce expressions for the lattice vibration energy and the specific heat capacity as a function of temperature. In LEED calculations the user parameterises the species in the material by their Debye temperature, which is a measure of the phonon mode with highest energy that is present.

In diffraction studies the Debye temperature manifests in the Debye-Waller correction to the amplitude of the scattering by the ion core by a factor $\exp(-M)$ where M is given by

$$M = \frac{3|\triangle \boldsymbol{k}|^2 T}{2mk_B\Theta_D^2} \tag{2.19}$$

and where $\triangle \boldsymbol{k}$ is the momentum change that occurs during the scattering event and Θ_D is the Debye temperature.

Finite temperature and lattice vibrations are not an obstacle to the theoretical simulation of LEED I(V) curves because they do not affect peak positions but their effect must be taken into account by correcting the phase shifts for each atom type in the calculation. In this work the phase shifts were first generated using the `DLPHASE` program [86] and then temperature corrected using the `pt2` extension program. The temperature

at which the experiment was carried out was included as an input parameter. The Debye temperature, which is also used as an input parameter, can be varied to investigate the presence of intrinsic vibrational modes that are of greater amplitude than ambient temperature might bestow. Θ_D is a measure of how hard or soft a material is to vibration. As we lower Θ_D we place the requirement that all possible phonon modes occupy a narrower range of frequencies; we effectively offer a greater density of vibrational states to the crystal and enhance the vibrations. If the real crystal in the experiment has many phonon modes which are affecting the I(V) curves in the manner described by equation 2.19 then allowing the simulated material to explore these modes will bring better agreement with experiment. This will be demonstrated in more detail in chapters 5 and 6.

Domains and Defects

A surface is never a pristine single domain crystal. STM experiments reveal surfaces to have patches of crystal order which are blighted by crevices which open up to relieve strain, missing atoms, steps from one crystal layer down to the next and sometimes even contaminant gas atoms. Since LEED is sensitive to order the effect of disorder is to produce a uniform background intensity in the LEED pattern. This is associated with elastic scattering in random directions by defects. A LEED pattern with a low background intensity indicates a clean, well ordered surface.

One type of defect has a major impact upon the comparison of theoretically generated I(V) curves to those obtained from the LEED pattern. These are domains, patches of the surface that have the same crystal structure but a different spatial orientation. On a hexagonal surface lattice we might see three types of domain with relative orientations of 120°. Each will be represented in a given LEED spot. If spots in the LEED pattern that are rotationally separated by 120° have the same I(V) profile then this indicates that either the surface is three fold symmetric or that there are three 120° domains on the surface. If the corresponding I(V) curves generated theoretically are not degenerate then they must be manually combined (first in equal proportion and then in other ratios) to simulate the effect of domains.

2.3 Experimental Details of Low Energy Electron Diffraction

After our discussion of the effects that produce the LEED spot pattern and its variation with incident electron energy we are now ready to look at the practical details of a LEED experiment. The following general steps are involved in making a surface and extracting I(V) curves from it;

1. Prepare the sample substrate surface and check the LEED pattern to ensure a clean and ordered surface is present.
2. Deposit the requisite amount of material from a pre-calibrated source.
3. Check the LEED pattern. A dim and diffuse pattern indicates the presence of the deposited material in a disordered state.
4. Anneal the sample to overcome local energy barriers and induce a surface reconstruction.
5. Check the LEED pattern and if it is clean and bright check that the electron beam is at normal incidence.
6. Acquire an image of the LEED pattern at each primary energy.
7. Generate I(V) curves from the I(V) images.

LEED at York

Figure 2.5 shows a schematic diagram of the main chamber of the York [89–92] LEED instrument.The chamber is surrounded by a large frame housing three perpendicular Helmholtz coils. The current through these is adjusted so that the magnetic field within the frame is zero. This allows the potentially significant effect of the magnetic field of the earth upon the path of the low energy electrons to be nullified.

The base pressure in the chamber is typically in the high 10^{-10} mbar range. It is maintained by an oil diffusion pump backed by a roughing pump and these are assisted by a titanium sublimation pump. The pressure is monitored by Pirani gauges on both the main chamber and the backing line for higher pressure ranges and by an Ion gauge in the ultra-high vacuum regime.

Samples are both prepared and analysed in the main chamber. The working sample is mounted onto the end of the manipulator which is driven by a stepper motor controlled by an instrument dedicated computer. The stepper motor can be used to

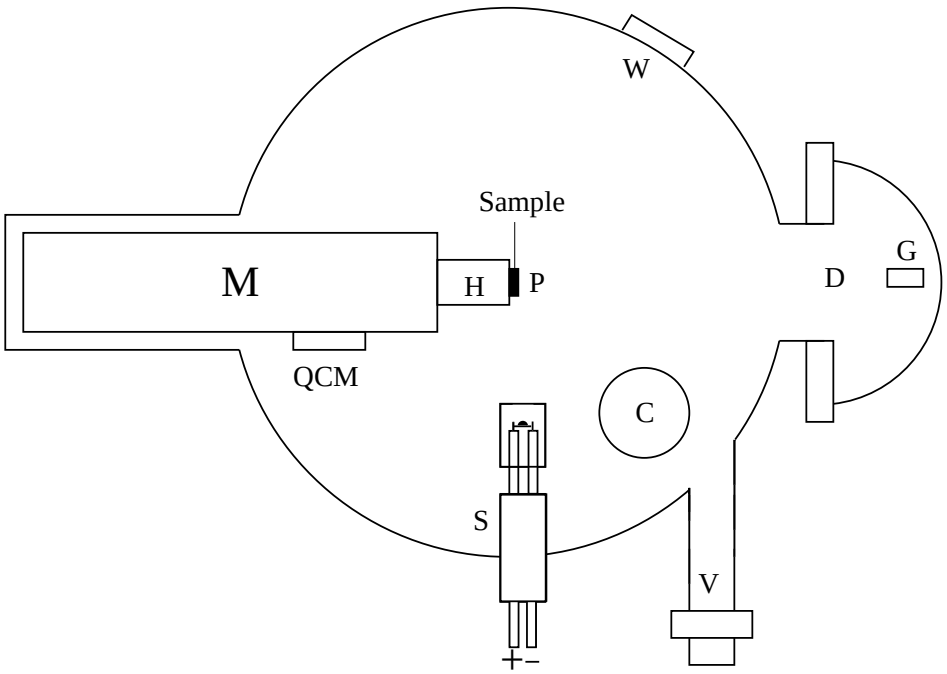

Figure 2.5: Schematic view from above of the relevant parts of the diffractometer main chamber. The labelled components correspond to M; manipulator, QCM; quartz crystal microbalance, H; electron beam heater, P; sample preparation position, W; pyrometry window, S; deposition source, C; carousel, V; gate valve, D; diffractometry position, G; electron gun.

translate the sample over a 30 cm range along the direction of the manipulator axis (the 'z-direction') from the sample preparation position to the diffractometry position. Translations of ± 5mm in the two directions perpendicular to the z-direction and rotation of the crystal about the polar axis and the z-direction are also possible. These allow for fine adjustment of the sample in the diffractometry position to ensure that the electron beam is at normal incidence to the sample. When the sample is in the preparation position it can be rotated to face the deposition source S or the pyrometry window.

Up to five spare samples can be stored in a carousel that can be reloaded under vacuum using a transfer trolley coupled to the main chamber via a gate valve. The working sample in the manipulator can be exchanged with a stored sample using a wobble stick which enters through the top of the chamber.

The controlled deposition of material onto the sample is achieved using sources bolted onto the side of the chamber and a quartz crystal microbalance (QCM). Each source consists of two hollow copper rods, closed at the vacuum end, which protrude from the exterior of the system into the chamber. The material to be deposited is attached between the end of the copper rods. In the Fe source this is a coil of Fe wire but wire made of RE metals is very expensive and so a piece of RE metal is wrapped

in a piece of tantalum. The RE metal is held in place by the tantalum but most of its surface area is left exposed so that, when a current passes through the tantalum and the RE is resistively heated, material can evaporate from the source (the tantalum does not evaporate at these temperatures) and freely pass towards the silicon sample. The end of the copper rods and the source material are housed in a copper shroud which has a small aperture facing the sample that serves to collimate the flux onto the sample. Cooling water is fed through the hollow copper tubes in order to prevent the chamber walls from heating up and degassing due to thermal conduction from the source. The QCM is used to calibrate the deposition rate onto the sample. It is located further back on the manipulator than the sample such that when the sample is moved forward the QCM is in the sample deposition position. The quartz crystal resonates at a frequency of about 6MHz but as material is deposited onto it this oscillation frequency decreases. The frequency change is proportional to the density per unit area of material that has been deposited onto the surface. The QCM has been calibrated such that for a given source a given frequency change indicates the deposition of a monolayer of material. The time taken for a monolayer deposit can be adjusted by varying the source current.

Sample heating is provided by two methods; radiative heating and electron beam bombardment if higher temperatures are desired. The temperature of the sample can be monitored using an infra-red pyrometer fitted with a set of neodymium filters to extend the range of temperatures that can be measured. The sample is rotated to face the pyrometer window during heating and the aperture of the pyrometer is aligned to receive the radiation from the sample through this window. The measurement of sample temperatures during lower temperature annealing (< 700C) is somewhat difficult because at these temperatures silicon is transparent to the particular wavelength (1.6 μm) of the infra-red light that the pyrometer responds to and the glow from the filament located behind the sample plate causes the pyrometer to tend to overestimate the sample temperature.

An electron gun acts as an electron source in these experiments. In the diffractometry position the sample is at the centre of a hemispherical glass screen coated with a semi-transparent phosphorescent film. The screen is set at a potential of 6-7kV so that electrons diffracted from the surface are accelerated towards it, causing it to glow when struck. Between the electron gun and the screen are a series of three grids which act to filter out inelastically scattered electrons. The main central grid is set at a potential which is offset from the electron gun potential by about 10V so that only electrons with energies within 10eV of the primary energy can reach the screen. A grid between the main central grid and the sample shields the electron gun and the sample from the potential of the main central grid. A third grid between the main central grid and the screen shields the main central grid from the large potential on the screen.

The instrument control computer is used to control the stepper motors for sample translation and rotation and also controls the electronics needed to vary the primary energy of the incident electrons. A third function is its synchronisation to the image acquisition computer which controls the Photonic Science CV12 CCD camera via the Media Cybernetics Image Pro Plus software. In-house [92] modifications to this software have made it possible to automate the LEED I(V) image capture process. The energy range and energy step size are set and once the process is initiated the instrument control computer varies the primary energy as the image acquisition computer takes I(V) images.

The diffraction pattern must be carefully optimised before acquisition such that the intensity of energetically degenerate beams is the same at all energies. The electron beam must be at normal incidence to achieve this. The top-to-bottom symmetry can be corrected by rotating the polar angle of the sample such that the (0,0) normal spot, which is in the electron gun shadow at normal incidence, is now visible. Variation in the primary energy should not cause this spot to change position. The left to right symmetry can be maximised by varying the polar angle.

The image control computer contains software that can follow the trajectory of a beam in the LEED image and measure its intensity as a function of the primary energy to generate I(V) curves.

Relating Theory and Experiment - (1) The Pendry R-Factor

The method of comparing the experimentally observed I(V) curves and those produced by the trial structure is crucial. We must focus our comparison upon those aspects of the I(V) curves that are the most sensitive to structure. In this work the Pendry R-Factor [93] is used to achieve this.

The derivative of a function will highlight those regions where the value of the curve is changing the most - such as where the function is rising to form a peak or descending after the formation of a peak.

The second derivative might be even more sensitive to changes because it measures changes in the change of a curve. However, the second derivative introduces extra calculation and might be more sensitive to noise and poor levels of smoothing. One smoothes curves to remove random noise but is restricted by the need to keep small but significant peaks (peak positions are the key and not their intensity).

If we take the first derivative of our function $f(E)$ and divide it by itself we have a function L defined by

$$L = \frac{f'}{f} \tag{2.20}$$

The chain rule reveals this to be the logarithmic derivative of the function f. This will be sensitive to peak positions and will not be biased towards peak heights since they are scaled out. Every time a peak is reached the amplitude of L will flip from its positive to its negative extreme.

However, there is a problem. It is entirely possible with multiple scattering to cancel out all of the elastically scattered electrons which can zero the function so that $f = 0$ and $L \to \infty$. The logarithmic function is biased towards zeroes in the I(V) curve. We do not want to reject zeroes as they are just as important in the scattering theory as maxima. We need a way to introduce equality between zeroes and maxima. In the Pendry R-factor this is achieved by use of the so-called Y function. This is based upon the logarithmic derivative but the amplitude of the Y function makes a $\pm$ excursion whenever a peak or a zero is encountered.

After the transformation of a given I(V) curve into a form that emphasises the structurally sensitive aspects the curves for theory and experiment must be compared for a given LEED spot. The Pendry R-factor is given by

$$R_p = \frac{\int (Y_{theory} - Y_{experiment})^2 dE}{\int (Y_{theory}^2 + Y_{experiment}^2) dE} \tag{2.21}$$

If there is good correlation between Y_{theory} and $Y_{experiment}$ the Pendry R-factor will tend towards zero and for poor correlation the denominator will act so as to normalise R_p to a value of 1.

Relating Theory and Experiment - (2) Structure Fitting

Multiple scattering processes make the electron paths within a surface during LEED so complex that it is not possible to reverse engineer a set of experimental I(V) curves to determine the structure that is responsible even if we are working with an elemental surface and we know the periodicity of the surface region with respect to the bulk. Instead an educated guess must be made to suggest possible structures. This will rely upon the periodicity revealed in the LEED pattern, knowledge of similar systems and any information gleaned from experiments that use other techniques.

The phase shifts are first calculated for the input structure. Next a Debye temperature must be decided upon for each layer in the calculation. This is not crucial at this stage since temperature will not shift I(V) peaks and so it is independent of structural parameters. After the calculation of the I(V) curves for all spots in the LEED pattern and comparison with experimental data the input model must be changed to try and optimise the level of agreement between the structural model and the experimental data.

The variation of structural parameters can be automated using an optimisation technique such as a genetic algorithm to efficiently search the many variable landscape for minima in the Pendry R-factor. In this work the parameter space was investigated manually. This is less efficient but with modern parallel computational resources it is not excessively time consuming.

The structural parameters that are varied are usually related to vertical aspects of the structure such as intralayer buckling distances and interlayer separations since LEED I(V) curves are very sensitive to these. Phase shifts do not need to be recalculated each time a parameter is varied since they are not expected to change much with small structural variations. A range of values for each parameter is decided upon along with a step size. This step size must be small enough so that minima in the R-factor landscape do not fall between grid points but not so small that the number of calculations required is not computationally tractable. Local minima identified in this coarse search can be mapped in more detail using a fine search using a smaller range in the structural parameters and a smaller step size.

Chapter 3

The Calculation of Surface Structure and Properties

An outline of the method that is used in this work to calculate the structure and properties of a surface naturally falls into three parts. The main task in any such calculation is to first determine the electronic structure. This is the most computationally challenging aspect and when it has been accomplished other properties that derive from it or from the total energy are readily available. The first section in this chapter is devoted to the determination of electronic structure. In §3.2 the ideas and methodology behind obtaining the lowest energy atomic arrangement from the calculated total energy are outlined. Section 3.3 is a bried outline of the properties that can be derived from the methods outlined in §3.1 and §3.2 and in §3.4 one particular property that is of special relevance to the work in this thesis, namely the calculation of the expected STM profile of a surface, is outlined in detail.

3.1 Electronic Structure

In this section DFT is discussed and the basic framework of practical algorithms that optimise the atomic and electronic structure is described, specifically with respect to the CASTEP code.

3.1.1 Density Functional Theory

The determination of the many body wavefunction for a system containing many atoms is made difficult by two fundamental obstacles;

Storage Requirements Consider the division of space into ten grid points in each direction. At each point we are to store the value of the many body wavefunc-

tion. For one electron there are 10^3 pieces of information to store. For 5 electrons (neglecting spin which increases the storage requirements) the many body wavefunction is the product of the single particle wavefunctions and there are 10^{3N} numbers to store which would require a million Gigabytes of storage space (assuming 1 byte at each grid point). It is not practical to work with the full many body wavefunction because we cannot store it.

Dimensionality It is clear that approximation methods must be used. In the variational theorem some parameter of the system is varied until the total energy is minimised. For our 5 electron system this means working with a function of 15 coordinates and for a typical calculation in this thesis working with 100 electrons we would have a function of at least 300 coordinates.

Density Functional Theory uses the total electronic density of a system as the working parameter. This is a function of three coordinates and for a system of any size we would require 1 kb of storage space to describe the system on the $10 \times 10 \times 10$ grid used in the simplified example above.
Thomas and Fermi used the density as the working parameter in a simple semi-classical method for the determination of the total energy in 1927 [94, 95]. A full framework was to emerge in the 1960's due to the efforts of Hohenberg, Kohn and Sham. In 1964 Hohenberg and Kohn [96] proposed two theorems

1. A group of ions and associated electrons possesses a unique ground state charge density $n_0(\boldsymbol{r})$ that is produced by the unique potential $V(\boldsymbol{r})$ of the system. It is not possible for any other potential $V'(\boldsymbol{r})$ to be responsible for this ground state charge density.

2. The ground state energy is solely determined by the ground state charge density and it can be found by minimising an energy functional $E[n(\boldsymbol{r})]$ with respect to the charge density $n(\boldsymbol{r})$.

To determine the ground state energy and charge density the energy functional $E[n(\boldsymbol{r})]$ must be constructed. The Born-Oppenheimer approximation is employed in which electrons are considered to respond essentially instantaneously to forces. This allows the nuclei to be treated adiabatically, leading to a separation of electronic and nuclear co-ordinates. The nuclei can now be considered as being fixed in place and the problem is reduced to the solution of the dynamics of the electron motion.

$$E[\rho] = E_{II} + \int V_{ion}(\boldsymbol{r}) n(\boldsymbol{r}) \boldsymbol{d}^3\boldsymbol{r} + F[n(\boldsymbol{r})] \boldsymbol{d}^3\boldsymbol{r} \tag{3.1}$$

E_{II} is the ion-ion interaction energy, $V_{ion}(\boldsymbol{r})$ is the electron-ion potential and the remaining functional $F[n(\boldsymbol{r})]$ can be separated into three components

$$F[n(\boldsymbol{r})] = T[n(\boldsymbol{r})] + U[n(\boldsymbol{r})] + E_{XC}[n(\boldsymbol{r})] \tag{3.2}$$

$$= -\frac{1}{2}\sum_{j=1}^{N} \boldsymbol{\nabla}^2\psi_j + \frac{1}{2}\int\int \frac{n(\boldsymbol{r})n(\boldsymbol{r'})}{\mid \boldsymbol{r} - \boldsymbol{r'} \mid}\boldsymbol{d}^3\boldsymbol{r}\boldsymbol{d}^3\boldsymbol{r'} + E_{XC}[n(\boldsymbol{r})] \tag{3.3}$$

$T[n(\boldsymbol{r})]$ is the kinetic energy of a system of non-interacting particles of density $n(\boldsymbol{r})$. It neglects any effects of interaction on the kinetic energy. The second term in equation 3.2 is the Hartree term which represents the classical electrostatic energy due to interelectron Coulomb interactions. The one remaining term in equation 3.2 is the Exchange-Correlation energy functional $E_{XC}[n(\boldsymbol{r})]$ which includes the many-body contributions to the total energy, the exchange and correlation energies.

The Exchange-Correlation Energy Functional

The total wavefunction for a many electron system must be antisymmetric. A consequence of this is that if two electrons are placed in the same state the wavefunction will collapse. This effective repulsion between electrons in the same state lowers their Coulomb energy and the correction to the total energy that it demands is called the **Exchange energy**.

Electrons are not independent particles that move in a fixed potential provided by the ions and the other electrons in the system. Each electron will affect the other electrons via Coulomb repulsion. We have included the energy of this Coulomb interaction in the functional in equation 3.2 but the complex many body effect that it produces has not been included. As the electrons move around they avoid one another to lower their Coulomb energy which gives rise to a correction known as the **Correlation energy**.

Exchange and Correlation are complex many body effects that act to lower the total energy of a system of electrons. We will now discuss the two main methods of their approximation.

The Local Density Approximation (LDA)

The exchange correlation energy of a homogenous electron gas can be exactly calculated using Quantum Monte-Carlo methods for any given electron density and we can tabulate values of $\varepsilon_{XC}^{HEG}[n]$. In the LDA an element of charge at position $\boldsymbol{r}$ that has a charge density n is ascribed the same exchange correlation energy of a charge element in a homogeneous electron gas that has the same density n. The total exchange correlation energy of the system can be found by integration

$$E_{XC}^{LDA} = \int \varepsilon_{XC}^{HEG}[n(\boldsymbol{r})]\ \ n(\boldsymbol{r})d\boldsymbol{r} \tag{3.4}$$

At first sight this method should not work since the electron density in any atomic system is non-uniform, especially near to the atoms. In fact, it works surprisingly well. Two main reasons have been suggested to explain this

- The errors in the exchange and correlation energy tend to cancel one another out.
- Each electron makes a hole for itself in the surrounding charge density. The electron-electron interactions depend only upon the spherically averaged properties of these *exchange correlation holes*. The LDA suggests properties for a given region of charge that match those of the spherical average over the exchange correlation hole. See the review by Jones and Gunnarsson for more detail [97].

The Generalised Gradient Approximation (GGA)

The LDA, despite being such a coarse approximation, has been shown to be remarkably robust over the past 40 years. However, there are situations where it does not perform well. We would not expect it to perform well for systems in which there is a high variation in the density. Exchange-Correlation approximation functions that include a correction for the effects of variation in the density are called Generalised Gradient Approximations (GGAs) [98–100]. The details of the gradient correction are complex but essentially the lookup table for the exchange correlation energy now depends upon two variables, the density and the gradient of the density

$$E_{XC}^{GGA} = \int \varepsilon_{XC}^{GGA}[n(\boldsymbol{r}), \bigtriangledown n(\boldsymbol{r})]\ \ n(\boldsymbol{r})d\boldsymbol{r} \tag{3.5}$$

The LDA tends to overbind materials and the GGA has been shown to correct this (even if it sometimes overcorrects). The GGA has been shown to be more effective than the LDA in materials where there is a high variation in the density and for magnetic systems or complex metals (see [99] and therein). The materials in this work contain Rare-Earth metals that contain d and f electrons and these are possibly magnetised. The GGA has been used in all calculations in this work and of those available the Perdew Burke Ernzerhoff (PBE) form was chosen [99]. This GGA attempts to keep the features of the LDA that work and combine them with those features of existing GGAs that affect the energy the most. As a result PBE is much simpler than other GGAs and has been shown to yield essentially the same results (see, for example, [101]).

The Kohn-Sham Equations

To recap, DFT has provided a way to determine the ground state total energy and the ground state charge density for a system of ions and associated electons. We have made the Born-Oppenheimer approximation to separate ionic and electronic energies and expressions have been given for the ion-ion, ion-electron and electron-electron interaction energies, with suitable approximations for the latter. It may seem that the only thing left to do is to determine a density function $n(\boldsymbol{r})$ that will minimise equation 3.2. There are problems;

- How is the kinetic energy to be calculated? It is not possible to calculate the kinetic energy of a charge distribution. A wavefunction is needed.
- Which useful properties can be determined from the charge density? It is very difficult to determine simple properties from the density such as whether the material is a metal or an insulator.

In 1965 Kohn and Sham [102] transformed the problem of equation 3.2 into one that explicitly includes orbitals. They introduced a set of wavefunctions, the Kohn-Sham orbitals, to describe the particles in the system as being independent. The effects of the other particles in the system are accounted for by interaction terms that have a functional form and are represented by an effective potential V_{eff} that bathes the independent particle

$$V_{eff} = V_{XC} + V_{ion} + V_{Hartree} \tag{3.6}$$

The states in the system are determined by solving a set of n Schrödinger-like **Kohn-Sham equations** for the n non-interacting electrons

$$(-\frac{1}{2}\boldsymbol{\nabla}^2 + V_{eff})\psi_j = \epsilon_j \psi_j \tag{3.7}$$

These must be solved self consistently;

1. They are solved for a given V_{eff}
2. The eigenfunctions ψ_j are used to construct the charge density
3. The potential produced by this charge density is compared with V_{eff}. If self-consistency has not been obtained return to (1) and generate a new set of eigenfunctions ψ_i
4. The process is repeated until these potentials are self consistent

We can restate the Kohn-Sham ansatz in terms of the Kohn-Sham Hamiltonian from equation 3.7.

$$E = \sum_{j=1}^{N} < \psi_j \mid H_{KS} \mid \psi_j > \tag{3.8}$$

This must be diagonalised to give the Kohn-Sham eigenfunctions from which the ground state density and other properties can be determined.

3.1.2 Solution of the Kohn-Sham Hamiltonian

In this section we will discuss the practical methods used to solve the H_{KS} hamiltonian matrix and obtain the Kohn-Sham groundstate electron density function $n(\boldsymbol{r})$. The emphasis is upon the approximations that are made, their effect upon the accuracy of the final answer and the effect that user controlled parameters can have upon the final solution.

Direct Diagonalisation of H_{KS}

The Kohn-Sham Hamiltonian matrix can be directly solved by diagonalisation to obtain the eigenvalues of the system. There are two reasons why such direct methods are not employed in practice;

- We do not require all of the available eigenstates in the system. Typically only a few percent of these are occupied to make up the ground state of the system which is the object of our calculation.
- Matrix diagonalisation is a computationally expensive process. For an $n \times n$ matrix the computational time required for diagonalisation scales as n^3. Typical systems present matrices with billions of elements. To diagonalise such a matrix just once would require many tens of hours of computational time and such an operation would have to be carried out hundreds of times during a typical calculation in this work.

Iterative Diagonalisation of H_{KS}

The iterative solution of H_{KS} involves the variational minimisation of the total energy E with respect to the trial wavefunctions ψ.

$$E = \sum_{j=1}^{N} < \psi_j \mid H_{KS} \mid \psi_j > \tag{3.9}$$

When this has been achieved the total energy is at its minimium value $E = E_0$. The Hohenberg-Kohn theorem tells us that the charge density

$$n(\boldsymbol{r}) = \sum_{j=1}^{N} |< \psi_j \mid \psi_j >|^2 \tag{3.10}$$

will be the ground state charge density and that we have obtained our ground state electronic structure.

Let us concentrate upon a single state. The key problem is how to vary the trial wavefunction ψ such that it will lower the total energy towards $E = E_0$. Suppose we start with a trial wavefunction $\mid \psi >$. If we differentiate equation 3.9 we can determine the gradient of the energy with respect to the wavefunction

$$\frac{\delta E}{\delta \mid \psi >} = H_{KS} \mid \psi >= \bigtriangledown \tag{3.11}$$

This gives us the direction in which the energy increases most rapidly and if we move in the opposite direction $-\bigtriangledown$ we will head for the energy minimum. Now, starting from our initial point ψ we can move to a new point ψ' that is closer to the minimum by taking a step of length λ in the direction $-\bigtriangledown$

$$\mid \psi' >=\mid \psi > -\lambda \mid \bigtriangledown > \tag{3.12}$$

The optimum step length λ is found by interpolation along the direction $-\bigtriangledown$. There are two further constraints that must be applied before the method will work. First, the wavefunctions must be normalised so that we occupy each state with exactly one electron. Second, the search for the next eigenstate must ensure that we search only for eigenstates that are orthogonal to those already discovered.

It so happens that there is a more efficient search direction to choose than the direct in which the function is decreasingly most rapidly. To understand why we need to refer to figure 3.1 which compares the performance of the steepest descents search direction algorithm with that of the conjugated gradients method for a two-dimensional narrow valley energy landscape.

The search directions in a conjugate gradients search [5,103,104] are made α-orthogonal or conjugate to one another. This ensures that there is no component of a search direction that lies upon a direction that has already been searched. If the two dimensional energy landscape in figure 3.1 was stretched in the vertical direction to make it a circular energy landscape then the conjugate directions would be orthogonal. The steepest descents algorithm would then become identical to the conjugate gradients method and both would converge in the same number of steps. In this sense the method of conjugated gradients can be considered as a means of searching unsymmetrical energy

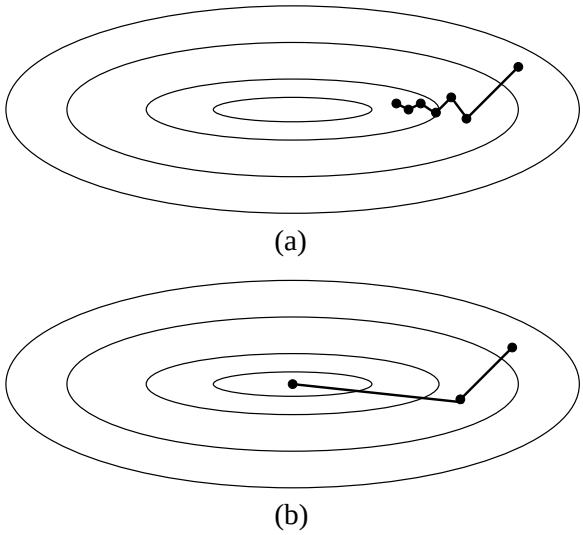

Figure 3.1: Showing the relative performance of the steepest descents (a) and the conjugated gradients (b) methods of generating search directions for a two-dimensional narrow valley energy landscape. Steepest descents requires many steps and follows an oscillatory path to the minimum with slow convergence. Conjugated gradients reaches the minimum in two steps (assuming a quadratic form for the energy landscape).

landscapes and never repeating a search along any given direction.

Stability in Metallic Systems and Charge Sloshing

A question arises here concerning self consistency. One could perform many wave-function updates and only check for self consistency once at the end. These non-self-consistent methods save time even though they usually require an extra algorithm to drive them towards the minimum. However, they can be unstable for metallic systems where the algorithm can fail to converge.

In a metallic system where the band gap is small and the energy bands are very close together it is possible that by fully occupying the bands below the Fermi level we can change the density such that a band B slightly above the Fermi level is now lower in energy than a fully occupied band A just below the Fermi level. In the next update of the occupancies band B is occupied and band A is emptied whereupon band A will now return to being lower in energy than band B. The system will repeat this ad-infinitum and will never converge. This is known as a sloshing instability and it was observed for early calculations in this work involving Rare Earth metals where a non-self consistent method was used.

Ensemble Density Functional Theory and Metallic Systems

The calculations in this work use Ensemble Density Functional Theory (EDFT) [105]. It was shown by Mermin in 1965 [106] that for each argument in the Hohenberg-Kohn theorem for the ground state density there is a corresponding argument that can be used for the density of a system that is in thermal equilibrium. A new functional, the Mermin finite temperature functional was introduced

$$A[T, \psi_i, f_{ij}] \tag{3.13}$$

The functional is now dependent upon the Kohn-Sham orbitals ψ_i, the band occupancy matrix f_{ij} and the temperature T. The density must be constructed so that it corresponds with the thermal ensemble

$$n(\boldsymbol{r}) = \sum_{i,j}^{Nbands} f_{ij} \ \ \psi_i^*(\boldsymbol{r})\psi_j(\boldsymbol{r}) \tag{3.14}$$

This allows a smearing of the Fermi surface and partial occupancies which is effectively like heating up the system. The occupancies and the wavefunctions can be updated independently and in turn. The method requires that the wavefunctions for all bands be determined simultaneously so that the occupancies can be assigned whilst conserving the total number of electrons.

The EDFT code written into `CASTEP` is a fully self-consistent method in which the electron density is calculated after each wavefunction update. It is fully variational in that the energy always decreases during electronic minimisation and the number of steps for convergence is usually much lower than for non-self consistent methods although the total time is usually greater.

Sloshing instabilities are avoided because at each stage the density and the wavefunctions remain self-consistent. The partial occupancies ensure that the density does not change as much after each wavefunction/occupancy update and the relative energy of the bands near to the Fermi level does not undergo such large discrete changes.

Spin Polarised Density Functional Theory

It is relatively straightforward to extend DFT to include magnetisation of the electrons (see [107], §IV). The total energy functional is generalised to include two types of density, the total density $n(\boldsymbol{r})$ and the spin density $s(\boldsymbol{r})$

$$E[n] \ \Rightarrow \ E[n, s] \tag{3.15}$$

$$n(\boldsymbol{r}) \ = \ n(\boldsymbol{r}, \uparrow) + n(\boldsymbol{r}, \downarrow) \tag{3.16}$$

$$s(\boldsymbol{r}) \quad = \quad n(\boldsymbol{r},\uparrow) - n(\boldsymbol{r},\downarrow) \tag{3.17}$$

Care must be taken when minimising a system with a net spin. For each spin configuration there is a different energy landscape. It is possible for the spin to change during electronic minimisation so that a local energy minimum can be reached, even though this might have an unfavourable spin conifguration. The calculation should be repeated several times with a different initial spin in each case and with the net spin specified as fixed in value for the duration of the calculation. These different runs can be compared in energy and the spin configuration with the lowest energy can be taken as the true local minimum in both density and spin density space.

3.1.3 Practical Electronic Minimisation

In this section the implementation of the electronic minimisation method is outlined with specific reference to the inputs that the user must decide upon.

The Plane Wave Basis Set

A plane wave basis set is used to represent the wavefunctions in the `CASTEP` code. Blochs theorem tells us that in a periodic potential the electronic wavefunction is composed of a wavelike part multiplied by a function ϕ with the periodicity of the potential

$$\psi(\boldsymbol{r}) = e^{i\boldsymbol{k}\cdot\boldsymbol{r}}\phi(\boldsymbol{r}) \tag{3.18}$$

The function with the periodicity of the potential can be constructed from a linear combination of plane waves.

$$\phi(\boldsymbol{r}) = \sum_{\boldsymbol{G}} C_{\boldsymbol{G}} e^{i\boldsymbol{G}\cdot\boldsymbol{r}} \tag{3.19}$$

The summation indices $\boldsymbol{G}$ are the reciprocal lattice vectors of the system. The total electronic wavefunction is now composed of a sum of plane waves

$$\psi(\boldsymbol{r}) = \sum_{\boldsymbol{k},\boldsymbol{G}} C^{\boldsymbol{k}}_{\boldsymbol{G}} e^{i(\boldsymbol{k}+\boldsymbol{G})\cdot\boldsymbol{r}} \tag{3.20}$$

The wavefunction can be varied by altering the coefficients $C_{\boldsymbol{G}}$ (in fact the search algorithms use the coefficients as the variable parameter). The accuracy of the representation of the wavefunction is increased by including more plane waves in the basis set. However, plane waves must be stored and their multiplication, although computationally inexpensive, still scales with the detail that we require in our wavefunction.

The beauty of a plane wave basis set is that the size of the basis set can be limited by specifying a single parameter, the cutoff energy E_C. This is defined as the greatest energy possessed by any plane wave in the basis set

$$E_C = \frac{\hbar^2|\boldsymbol{k}+\boldsymbol{G}|^2}{2m} \tag{3.21}$$

In real space this is the wave with the shortest wavelength and it is used to represent features with a fine spatial separation. The user can decide to limit the number of plane waves included to save computational time but the system must be converged with respect to the cutoff energy. E_C is a variational parameter and as the number of plane waves in the basis set is increased the total energy of the system should decrease towards the true energy of the system.

In this work the basis set has been checked before any major calculation has begun. The electronic structure is optimised for a given configuration of the atoms and a given cutoff energy so that the total energy may be determined. This process is repeated using the same structure with all of the other parameters fixed except for the cutoff energy which is raised slightly. The total energy should now be lower. The process is repeated until the total energy does not change with repect to a small increase in the cutoff energy. See the results chapters for examples of this convergence test.

Sampling of the Wavefunction

It is not feasible to sample the wavefunction at each point in space. If a finite 3-dimensional grid of sampling points is made fine enough the wavefunction will not change very much from one point to the next. Such a sampling grid is used in `CASTEP`. In this work the Monkhorst-Pack scheme [108] for generating a sampling grid was used which is a means of generating a symmetrical and evenly spaced grid of sampling points for a unit cell of any shape or size.

As with the cutoff energy, the calculation must be converged with respect to the sampling grid density. A series of total energy calculations is performed each with the same parameters. The difference between subsequent calculations is the sampling grid density. As this increases the energy will change and when the energy is not changing by any significant amount then the calculation has been converged with respect to the basis set. The sampling grid density is not a variational parameter and the energy does not necessarily have to decrease each time the sampling grid density is increased.

Supercells

A plane wave basis set makes it very easy for periodic systems to be represented. The smallest repeating unit cell is chosen and the calculation is only carried out for the

atoms within this 'supercell'. The effect of the other atoms is represented by periodic boundary conditions and the plane wave basis set allows this to be readily implemented.

A surface is aperiodic in the direction perpendicular to the surface. However, the potential from the uncompensated surface charges is known to decrease exponentially with the distance from the surface. In the supercell approach a vacuum gap is included in the vertical direction perpendicular to the surface between adjacent supercells so that there is no interaction between the top atoms in the lower supercell and the bottom atoms in the upper supercell. To ensure convergence the calculation must be repeated with increasing vacuum gap until the total energy does not change.

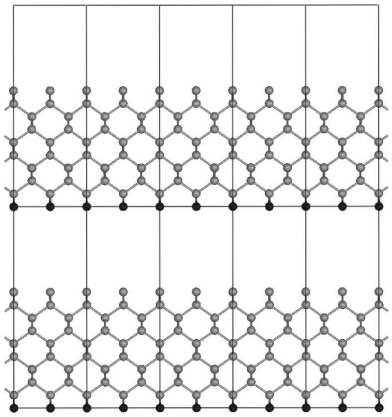

Figure 3.2: Side view of ten supercells of the Si(100)-2×1 surface with a vertical vacuum gap of 9 Å. Hydrogen atoms (black) are used to passivate dangling bonds on the last bulk layer.

Figure 3.2 shows a side view of a supercell and its periodic images for the Si(100)-2x1 surface. In the plane of the surface the supercell has to be of suffcient area to enclose the expected reconstruction. This prevents the modelling of surface features which have periodicity over large length scales such as step edges and rifts. The supercell has two surfaces, the one under consideration and another surface which is occupied by the last layer of bulk-like atoms included.

Enough bulk like layers must be added so that interaction between atoms with uncompensated charges on the top and bottom surfaces within a supercell is negligible. In practice a symmetrical arrangement with two identical supercells joined bottom to bottom can be used. The two inner bulk-like layers are frozen into their bulk-like positions and bonded with their symmetrically equivalent partners so that the charges from their dangling bonds are compensated. The drawback to this approach is that the number of atoms in the supercell is doubled. An alternative technique is to add a layer of hydrogen atoms to bond with the inner bulk layer to compensate the charges.

Pseudopotentials

Near to the atomic cores where the wavefunction has its greatest curvature an intractably large number of plane waves would be needed to represent the electronic wavefunction. In the pseudopotential approximation ([8] Ch. 11 and therein) the many body wavefunction and the ionic potential inside some critical radius associated with the core electrons is replaced by a much weaker, approximate potential called a pseudopotential (PP) (see figure 3.3).

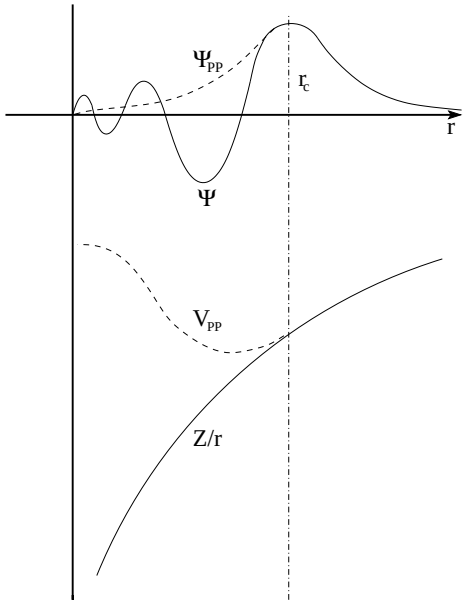

Figure 3.3: Outside of the core radius r_c the pseudowavefunction Ψ_{PP} and pseudopotential V_{PP} match the full wavefunction Ψ and potential Z/r and the environment presented to the valence electrons remains unchanged. Inside r_c both Ψ_{PP} and V_{PP} are much smoother and this significantly reduces the number of plane waves required in the basis set.

After the approximation of the exchange-correlation potential the use of PPs is the second major source of innaccuracy due to approximation in the application of DFT to surface reconstructions. The user must take extreme care when selecting a PP to use and be prepared to test its validity and even construct their own PP.

The Calculation of Forces

The force on an ion i in our system is given by

$$\boldsymbol{F_i} = -\frac{\partial E}{\partial \boldsymbol{R_i}} = -\frac{\partial < \Psi|\hat{H}|\Psi >}{\partial \boldsymbol{R_i}} \tag{3.22}$$

This can be evaluated using first order perturbation theory

$$\boldsymbol{F_i} = -<\frac{\partial\Psi}{\partial\boldsymbol{R_i}}|\hat{H}|\Psi> -<\Psi|\hat{H}|\frac{\partial\Psi}{\partial\boldsymbol{R_i}}> -<\Psi|\frac{\partial\hat{H}}{\partial\boldsymbol{R_i}}|\Psi> \quad (3.23)$$

$$= -E\{\frac{\partial}{\partial\boldsymbol{R_i}}<\Psi|\Psi>\} -<\Psi|\frac{\partial\hat{H}}{\partial\boldsymbol{R_i}}|\Psi> \quad (3.24)$$

Since $<\Psi|\Psi>=0$ we have the final expression for the perturbation expansion

$$\boldsymbol{F_i} = -<\Psi|\frac{\partial\hat{H}}{\partial\boldsymbol{R_i}}|\Psi> \quad (3.25)$$

Forces depend only upon those parts of the hamiltonian that depend explicitly upon the ionic positions $\boldsymbol{R}_i$. Referring to equation 3.1 we can see that the force does not require computation of electron-electron effects or the kinetic energy. It can be shown that the force is given by a sum of the classical attractive force on nucleus i from the ground state electronic density and the classical repulsive force on nucleus i due to all of the other nuclei. This is the Hellmann-Feynman force theorem [109].

It is computationally inexpensive to calculate forces once the ground state density has been determined. With an accurate basis set the state determined during electronic minimisation will correspond closely to the true eigenstate Ψ and the force as determined from the theorems above will be accurate. The force is sensitive to second order to errors in the wavefunction and it is crucial that the basis set is accurate enough to represent the variational minimum. This is particularly important in the optimisation of atomic structure which is discussed in the next section.

The Plane Wave Basis Set

In summary, the plane wave basis set offers

Advantages

1. Periodic systems are efficiently represented
2. Forces and stresses are easy to calculate
3. Easy to code and numerically efficient
4. The atoms do not drag a local basis set with them

Disadvantages

1. The system must be periodically represented

2. Regions near to atomic cores require many basis functions

3. Empty space must be represented

3.2 Atomic Relaxation

The total energy of any configuration of atoms and their associated electrons can now be determined. This can be used to perform structural optimisation. The atomic coordinates are sequentially varied and the total energy is checked. When the energy has reached a minimum and the forces have reached zero then the structure can be considered as a local minimum or a metastable minimum if the forces are at a minimum.

In CASTEP the Broyden-Fletcher-Goldfarb-Shannon (BFGS) method [103,104,110] is used to generate the search directions in the $3N$-dimensional energy landscape defined by the co-ordinates of the ions in our N-atom system. At some point $E(\boldsymbol{S})$ near to our current point $E(\boldsymbol{S}_i)$ Taylor expand the energy function

$$\boldsymbol{E(S) = E(S_i) + E(S_i) \cdot (S - S_i) + \frac{1}{2}(S - S_i) \cdot A \cdot (S - S_i)} \tag{3.26}$$

If we take the derivative of this function and set this equal to zero we define a point for which the energy is at a minimum

$$\nabla E(\boldsymbol{S}) = \nabla E(\boldsymbol{S}_i) + \boldsymbol{A} \cdot (\boldsymbol{S} - \boldsymbol{S}_i) \tag{3.27}$$

Here $\boldsymbol{A}$ is the Hessian matrix that contains the second derivatives of the energy with respect to the $3N$ coordinates. We have truncated the expansion to second order and we are approximating the energy landscape as quadratic along the search direction. If the energy landscape is quadratic then the search direction that will yield point $\boldsymbol{S}$ at which the total energy is at a minimum in one step is

$$\boldsymbol{S} - \boldsymbol{S}_i = -\boldsymbol{A}^{-1} \nabla E(\boldsymbol{S}_i) \tag{3.28}$$

However, the matrix $\boldsymbol{A}$ is not known. In practice it is approximated at first and then this approximation is successively refined as more steps are taken and more information about the Hessian can be accumulated. It can be shown that the BFGS technique will generate a set of conjugate search directions and will converge with an efficiency similar to that of the conjugate gradients technique used in electronic minimisation. BFGS allows the use of forces in the generation of search directions and it also allows the calculation of stress and the variation of the unit cell vectors for a supercell.

Having determined a search direction $\Delta \boldsymbol{S}_i$ using BFGS it remains to perform a line minimisation. The set of ionic position vectors $\boldsymbol{S}$ are updated as a unit according to

$$\boldsymbol{S}_{i+1} = \boldsymbol{S}_i + \lambda \Delta \boldsymbol{S}_i \tag{3.29}$$

λ is the step length in the multidimensional energy landscape defined by the set of ionic position vectors $\boldsymbol{S}$. The subscript i refers to the iteration number and not any individual ion. An initial step of length $\lambda = 1$ is chosen since in a truly quadratic energy landscape this should define the minimum. A line search is then performed which allows any step length that does not require too significant a distortion of the structure (see figure 3.4).

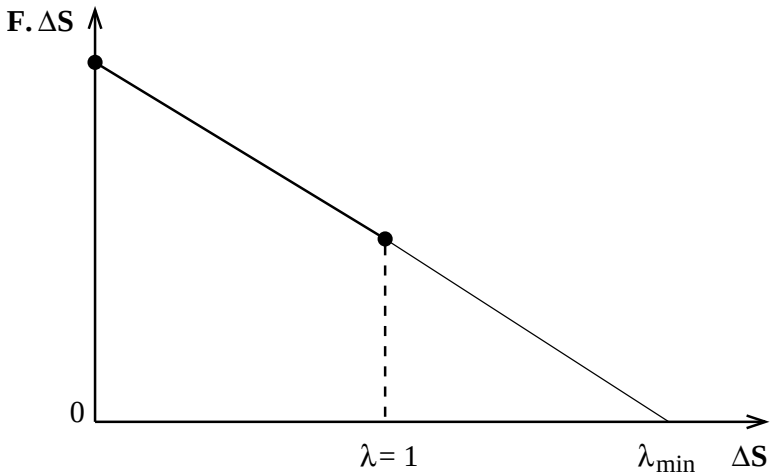

Figure 3.4: The line minimisation proceeds by choosing the optimal step length $\lambda = 1$ for a perfectly quadratic energy landscape and computing the total energy and force. If at this point the force $\boldsymbol{F}$ is not orthogonal to the search direction $\Delta \boldsymbol{S}$ another step length is chosen and the method proceeds until the optimal step length λ_{min} is found at which $\boldsymbol{F} \cdot \Delta \boldsymbol{S} = 0$

The forces drive the search directions and this is why errors in the forces caused by an innaccurate basis set are to be avoided. At the energy minimum the force vector $\boldsymbol{F}$ should be orthogonal to the search direction $\Delta \boldsymbol{S}_i$. If such a condition cannot be found along the search direction the hessian matrix is rejected and another search direction is generated. If there is no search direction in which the energy can be found to decrease then uphill steps are allowed to overcome shallow energy barriers that might be presented if the system is in a local energy minimum.

3.3 Surface Properties

The following is a summary of some of the properties of a surface that can be determined using the *ab-initio* method that has been outlined in this chapter.

Forces and Atomic Structure

The force acting on each ion in the system can be determined to show where the likely relaxation directions in a surface are. These forces can be used to drive a minimisation algorithm to optimise the atomic positions with respect to the total energy. The total energy of similar structures can be compared provided that the same basis set and pseudopotentials were used in both cases and provided that both systems contain the same number of atoms of each element present. This allows discrimination between competing surface structures.

Electronic Structure

For a given structure the **electron density** distribution that corresponds to the minimum energy can be determined. The eigenstates determined from the plane wave calculation can be projected onto localised orbitals and a **population analysis** [111] can be performed to determine the nature of the bonds between the atoms.

A **density of states** plot of the relative number of electrons in a given energy range (and their spin resolution, if any) is an extremely useful way to look at the electron bonding environments and it allows the results of theoretical calculations to be compared with spectroscopic surface techniques such as MDS (see Appendix A).

The knowledge of the equilibrium electron distribution and the energy of each region allows a map to be built of which electrons are likely to tunnel out of the surface under given bias conditions to determine the expected **STM profile** of the surface. This calculated property is of particular relevance to the work in this thesis and it is outlined in more detail in the next section.

3.4 Simulated Scanning Tunneling Microscopy

The electron states in a surface are distributed so as to minimise the energy of the system which usually involves shielding the ionic core. Topographic features can be interpreted as atomic positions because in most cases the electron density contours correspond to the atomic positions. However, it is possible that the electron charge distribution follows a more complex pattern than the atomic envelope. It is crucial to the interpretation of experminetal STM images that they be compared with some form

of theoretical electronic structure simulation. In the literature an STM investigation of a surface is often now accompanied with theoretical simulations of the appearance of the expected STM profile produced by the model surface. It is the calculation of the expected STM image of a model surface and its comparison with experiment that we must now turn our attention to. An introduction to the mathematical detail can be found in Kaxiras [112] and the recent review by Gottlieb and Wesoloski [113].

3.4.1 Theoretical Approximation

Figure 3.5 shows the potential energy for electrons in a surface sample and a tip as the two are brought together and a bias voltage is applied.

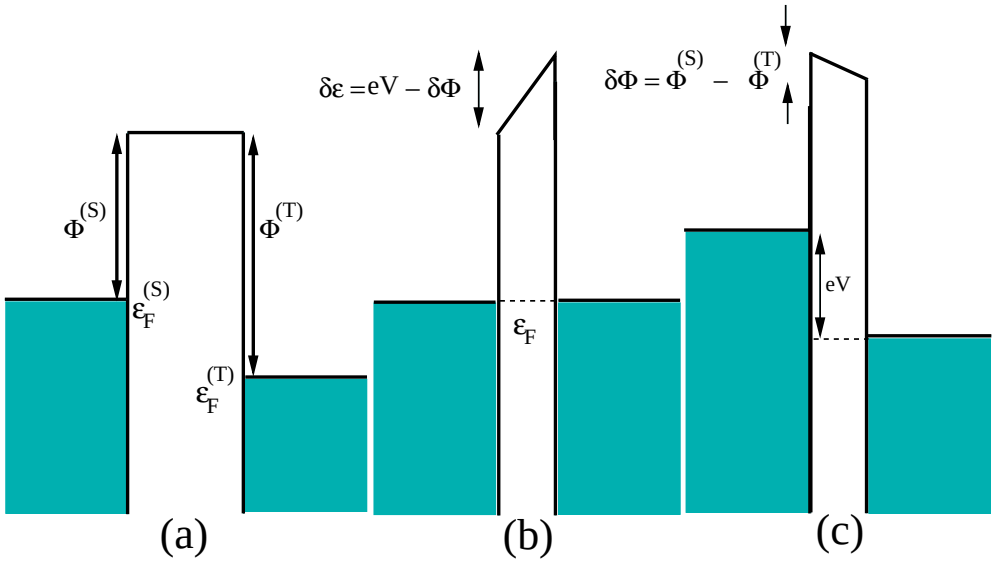

Figure 3.5: Sample (left, S) and STM tip (right, T) energy level diagram. When far apart **(a)** each has a distinct Fermi level ε_F and work function ϕ_F. When the tip is close enough for tunneling to occur **(b)** sample electrons tunnel into the tip (in this example) and equalise the local Fermi level in the two materials, causing a barrier to develop that prevents further tunneling. A bias voltage V will introduce an effective electric field and an energy shift $\delta\varepsilon$ that will act to restore sample-tip tunneling **(c)**.

The probability that an electron in a state ψ_T will tunnel into a state ψ_S is given by Fermi's Golden Rule

$$P = \frac{2\pi}{\hbar}|M_{TS}|^2\delta(E_T - E_S) \tag{3.30}$$

where M_{TS} is a tunnelling matrix element and the delta function ensures energy conservation. The tunnelling current is determined by introducing occupancies into 3.30

$$I = \frac{2\pi}{\hbar} \int |M_{TS}|^2 (f^S(E)[1 - f^T(E)] - f^T(E)[1 - f^S(E)])\delta(E_T - E_S)dE \qquad (3.31)$$

where $f^T(E)$ and $f^S(E)$ are the Fermi filling factors for states in the tip and the sample. In figure 3.5 we established a bias voltage **V** between tip and sample that was to encourage tip-sample tunneling. Figure 3.6 shows the effect of this upon the fermi distributions of the tip and the sample

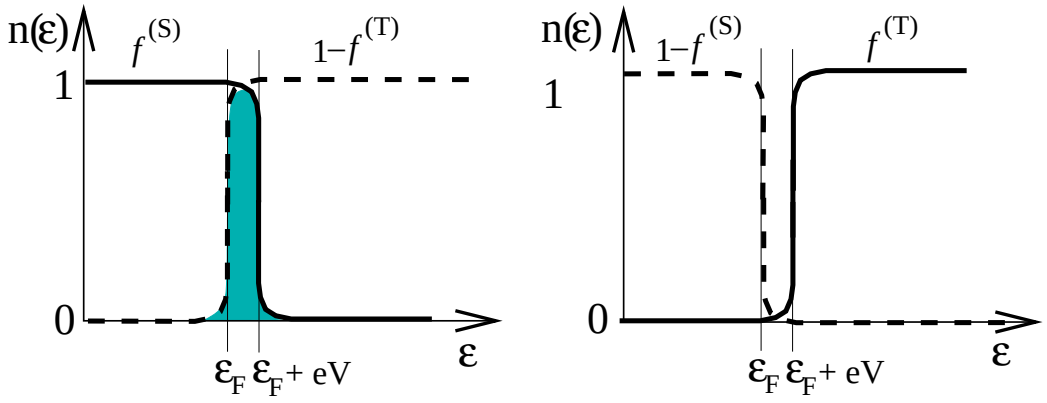

Figure 3.6: The bias voltage V shifts the density of states in the sample by an amount $+eV$ and makes tunnelling unidirectional. **(Left)** the first fermi overlap term in Equation 3.31 allows tunnelling from filled sample states within an energy eV below the Fermi level into empty tip states within eV above the Fermi level. **(Right)** there is no significant overlap of empty sample states and filled tip states. The second fermi overlap term in Equation 3.31 is effectively zero and tip to sample tunnelling does not occur.

Only states within an energy eV of the Fermi level can take part in tunnelling and only into states of equal energy. Equation 3.31 now becomes

$$I = \frac{2\pi}{\hbar} \int |M_{TS}|^2 (f^S(E)[1 - f^T(E)])\delta(E_T - E_S)dE \qquad (3.32)$$

This equation is fundamental to any theory of Scanning Tunneling Microscopy.

Tersoff-Hamann Theory

In the Tersoff-Hamann theory [114] the Bardeen approximation for the matrix elements is used. This approximation [115] uses time dependent perturbation theory to show that if the potential from the tip is approximately zero in the region of the sample and vice-versa then the tunnelling matrix element can be written as a surface integral

$$M_{TS} = \frac{\hbar^2}{2m} \int (\psi_S \nabla \psi_T^* - \psi_T^* \nabla \psi_S) dS \tag{3.33}$$

The integral is over a surface that divides the regions where the tip potential is non-zero and the sample potential is non-zero.

All that remains is to approximate the wavefunctions for the tip and the sample. Tersoff and Hamann approximated an s-state for the tip wavefunction and a point source tip and showed that these approximations reduce the tunneling current to the form

$$I \propto \sum_S |\psi_S(\boldsymbol{r}_T)|^2 \delta(E_S - E_F) \tag{3.34}$$

where $|\psi_S(\boldsymbol{r}_T)|^2$ is the value of the sample charge density *at the position of the tip*. Equation 3.34 reveals that the tunneling current in STM is the local density of states of the sample at the Fermi level evaluated at the tip centre. The wavefunctions of the surface states decay exponentially as we move away from the surface which explains the observed exponential sensitivity of the tunnelling current to the tip-sample separation.

3.4.2 Limitations

The Tersoff-Hamann model is widely used and has been very successful but it does have limitations. Bardeen's scheme (equation 3.33) assumes that despite the close proximity of the tip and the sample there is no mutual distortion of their wavefunctions. In experiments the tip and the sample are typically 5 Å apart which means that the Bardeen method is an approximation.

The other main assumption is of a point source tip with s-states taking part in tunneling. STM tips are usually made of tungsten or platinum because these metals are durable. The electrons in W and Pt overwhelmingly reside in d-states.

Chen has extended the Tersoff-Hamann theory to include distortion of the wavefunctions in the Bardeen approximation and the use of d-states to represent the tip [59]. The main modification is that the tunneling current is now proportional to the magnitude of the derivatives of the surface state wavefunctions. This has been shown to be important in certain metal surfaces where the Tersoff-Hamann theory underestimates the degree of atomic corrugation.

The theoretical STM images in this work were generated using the `Materials Studio` package from `Accelrys` [116]. The limitations of the software must be made clear. The tunneling current is never explicitly calculated and instead it is the spatial distribution of the electron density for those electrons in the right energy range (ie within eV_B of E_F) that is determined. We assume that this is proportional to the

tunneling current.

Also, there is no explicit height information contained in the images. The STM image is represented as an isosurface of a given electron density for electrons within eV_B of E_F. It is possible to project other properties onto the isosurface such as the charge density but the software does not include the functionality to project the height and the user must rely on the relative heights in the isosurface. It is also possible to look at the electron density within eV_B of E_F on a two-dimensional slice taken parallel to the surface. This is akin to constant height mode STM but it can only be applied to atoms that lie exactly within the plane since the pixels that represent no tunneling current obscure any potential view onto a slice below (there is no option to make these obstructive pixels transparent).

Chapter 4

Ab Initio Study of Holmium on Silicon and Germanium

4.1 Introduction

The two-dimensional rare earth silicides (2D RE Si) have a novel structure in which the RE atoms sit in a subsurface layer below a reverse buckled silicon overlayer. These surfaces, which were discussed in the introductory chapter, have attracted interest due to the good epitaxy of bulk RE silicides with the Si(111) surface and the low Schottky barrier of RE metals on Si(111) means that there are potential technological applications. They have been extensively studied using a variety of experimental techniques but theoretical studies have not been as numerous. Stauffer et al. [43] have used a semiempirical technique to determine the band structure for a variety of top layer orientations in 2D Si(111)-1×1-Er, although they have not geometry optimised the system. They have shown that the reverse buckled top layer gives the best match with the experimentally obtained band structure. They suggest that each trivalent erbium atom saturates a dangling bond in the silicon bilayer below it by direct bonding and saturates two dangling bonds in the silicon overlayer, one by a direct bond and the other by charge transfer. Rogero et al. [38] have used the `SIESTA` code to geometry optimise the 2D Si(111)-1×1-Y structure and they have found a good level of agreement with the structural parameters as obtained by LEED. Palmino et al. [117] have shown that there is a favourable comparison between the calculated and experimental STM images for 2D Si(111)-1×1-Er. In the first half of this chapter *ab initio* geometry optimisation studies of the 2D Si(111)-1×1-Ho system is described and the the effects of spin polarisation of the electrons upon the atomic geometry has been characterised. The geometry optimisation has been repeated with various configurations of the top silicon bilayer to determine their relative energetics.

One dimensional nanorod structures are of fundamental and technological interest. As discussed in the introductory chapter such structures have been grown on the Si(100) surface, making use of the anisotropy of the lattice parameter in the two perpendicular directions. On the Si(111) surface nanorods have not been observed that do not require defects or prepatterning of the surface. Workers in the Surface Physics Group at York have observed and characterised a nanorod structure on the Ge(111) surface using STM and MEIS. These can be formed in isolation or as part of a 5×1 reconstruction at higher coverage. A model structure has been proposed but there is a need to validate both the stability of this model structure and the properties of its electronic structure. In the second half of this chapter the model 5×1 unit cell has been studied using an *ab initio* calculation. This work has provided a qualitative validation of the structure and the calculated STM profile and the predicted conducting properties of the nanorod are in good agreement with experiment. Analysis of the forces remaining within the system and of the chemical bonds formed in the top few layers allow the general principles by which the system is stabilised to be discussed.

4.2 *Ab Initio* Study of 2D Holmium Silicide

The *ab-initio* geometry optimisation calculations were performed using the `CASTEP` code [9]. The code was run in a parallel computing environment on a Beowulf cluster of 33 machines, each with dual Intel Pentium 4 Xeon processors running at 1.7 GHz in the Department of Physics at York. A typical geometry optimisation calculation used 18 processors and required around 200 hours.

4.2.1 Convergence of Parameters

Before proceeding with the geometry optimisation the input parameters were carefully checked (see [118] and Chapter 3 of this work for a discussion of the importance of this). Figure 4.1 shows how the calculated energy varies with the number of plane waves included in the calculation as the cutoff energy is raised for three increasingly dense Monkhorst-Pack [108] reciprocal space sampling grids. A cutoff energy of $400eV$ yields a total energy near to the variational minimum and will allow accurate calculation of the energy and the forces within the system. A reciprocal space sampling grid with 18 k-points was used in the geometry optimisation since in figure 4.1 it is apparent that increasing the sampling grid size to 32 k-points does not significantly change the energy. The Perdew-Burke-Ernzerhof [99] generalised gradient approximation was used to represent exchange and correlation effects.

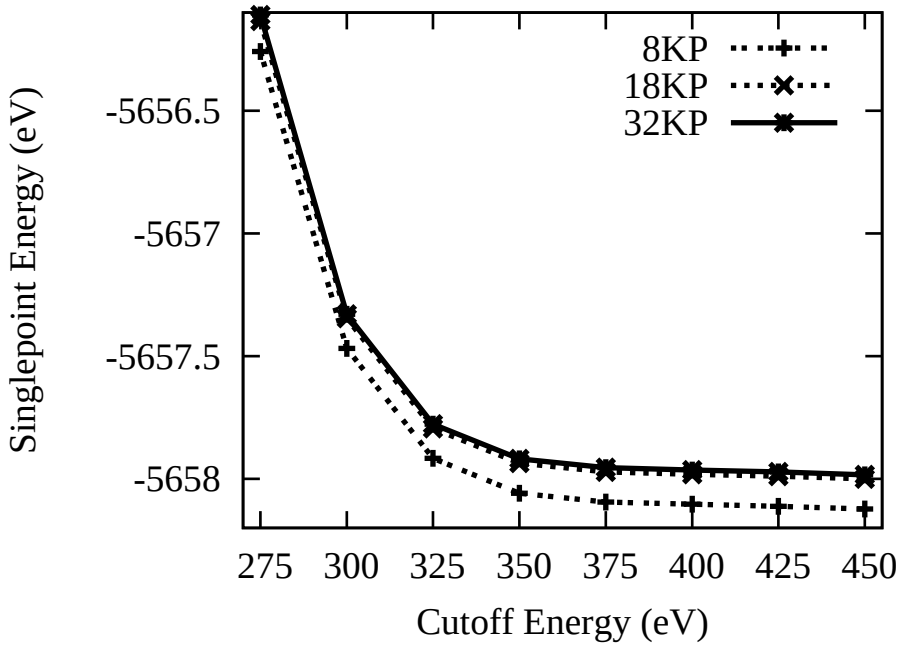

Figure 4.1: Variation of the singlepoint energy, which is the calculated energy for a given configuration of the atomic positions, with the cutoff energy and with the number of k-points at which the wavefunction is sampled in reciprocal space for the 2D Si(111)-1×1-Ho system.

The vacuum gap must be of sufficient thickness to prevent interaction between the top surface in one supercell and the bottom surface in the supercell above. For a fixed atomic geometry and basis set the energy and the mean force on all of the atoms in the supercell was calculated as a function of the thickness of the vacuum gap. This is shown in figure 4.2. There are two competing effects here. As the vacuum gap thickness is increased the interactions across it are reduced to a minimum when it reaches a value of around 8 Å. As the vacuum gap is increased further the energy begins to increase. This can be explained by dilution of the basis set. As the supercell increases in size the effective number of plane waves per unit volume is reduced. This is effectively like reducing the cutoff energy which is why the total energy increases. Even with this secondary effect it is clear that a vacuum gap of 9 Å is sufficicent to minimise interactions across this expanse.

The number of bulk-like silicon layers must be sufficient to minimise interactions through the supercell between uncompensated charge in the top and bottom layers. The bottom bulk like silicon layer has been hydrogen passivated to quench dangling bonds and to reduce the number of layers needed in the slab (this also reduces the thickness of the vacuum gap that is needed). Figure 4.3 shows the reduction in the mean force per atom in the supercell as the number of bulk-like silicon layers is increased. The energy has not been plotted since it is not valid to compare two supercells that do contain

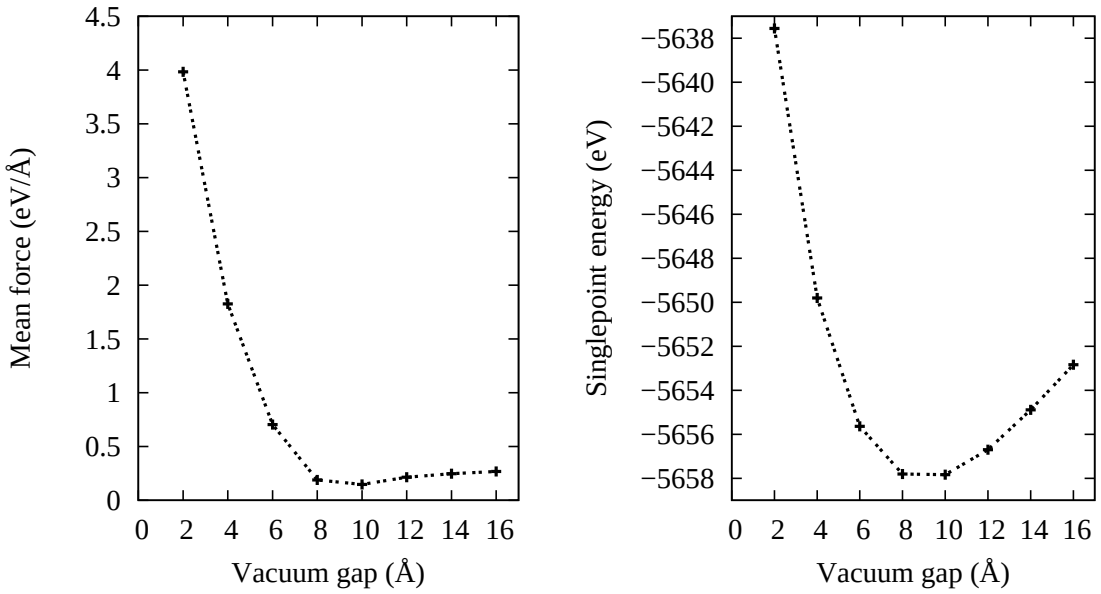

Figure 4.2: The variation of the mean force and the singlepoint energy with the vacuum gap thickness for the Si(111)-1×1-Ho system.

the same ratio of atomic species. Less than three bulk-like silicon layers do not prevent interactions through the slab but increasing the number of layers beyond three does not significantly reduce the interactions. The force does not seem to converge and it would appear that there is some persistent residual force in the supercell that is being diluted in the averaging process. Four bulk-like silicon layers have been used in the geometry optimisations in this section.

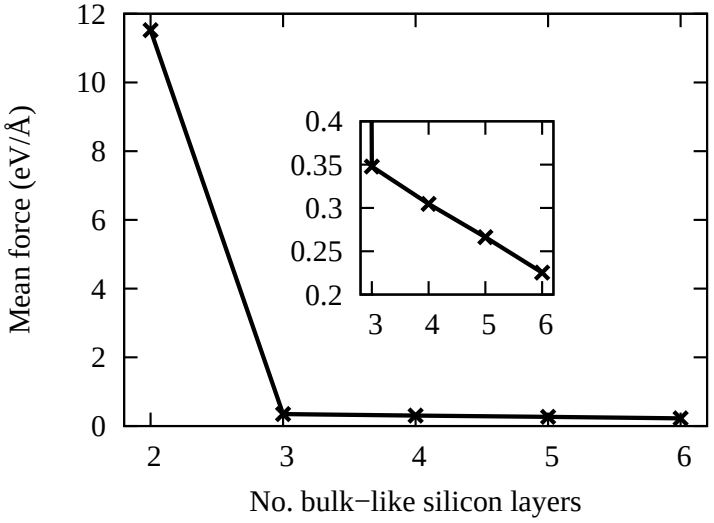

Figure 4.3: The variation of the mean force with the number of bulk-like silicon layers for the Si(111)-1×1-Ho system.

4.2.2 The effect of spin polarisation

This system contains an even number of electrons and we are not forced to consider spin polarisation. Moreover, the Curie temperature of bulk Ho is 10 K (and magnetic properties have not been observed in the silicide) and spin polarisation of the electrons cannot be expected to have an effect upon the atomic geometry for any material studied in an experiment conducted at room temperature. Nevertheless, the effect shall be investigated.

For a given atomic configuration and basis set and with a fixed number of layers in the slab and a fixed vacuum gap thickness the total energy has been calculated for a variety of different spin states. Figure 4.4 compares the convergence of the electronic structure optimisation for the cases where effects of spin polarisation have been included and ignored. In the spin polarised calculation the spin was not specified and the system was allowed to relax into the nearest local energy minimum spin state. There is a clear reduction in the total energy when the electrons are allowed to become spin polarised.

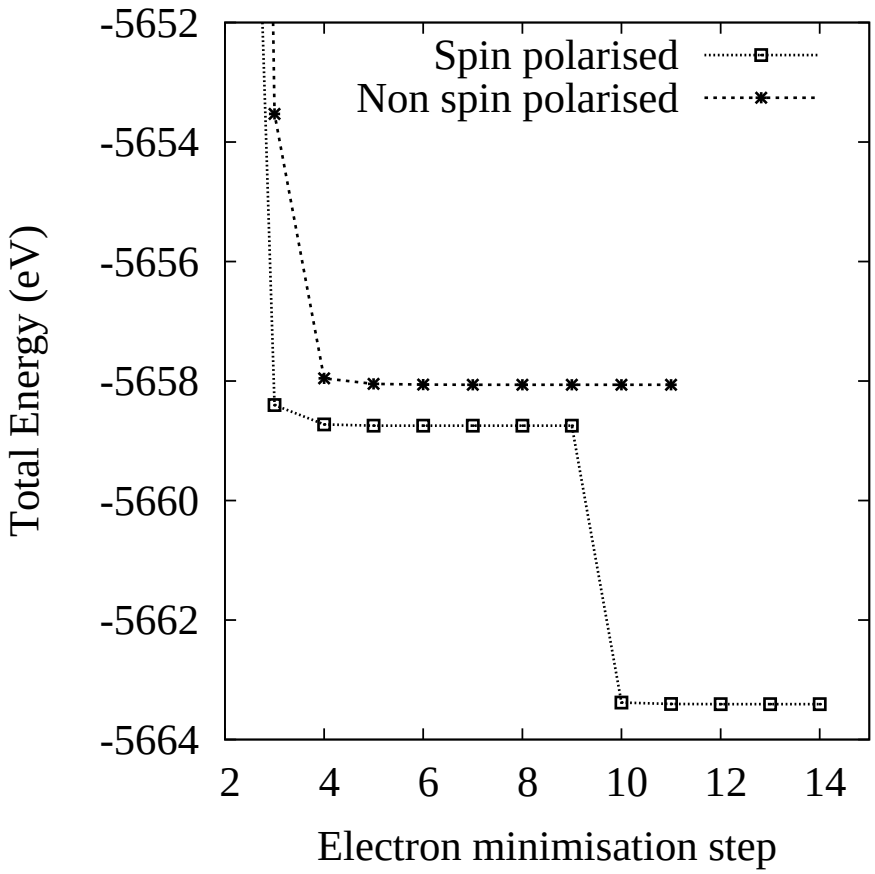

Figure 4.4: Variation of the total energy of a Si(111)-1×1-Ho supercell during electronic minimisation compared for the spin polarised and the non-spin polarised case.

For each spin state on the surface there might exist a different energy landscape. If the electronic structure calculation for the system is allowed to start in some random configuration then it is entirely possible that it will become trapped in the local minimum for some spin state when there could be a different spin state for which the optimised electronic structure leads to a lower total energy. To explore this possibility it is possible to fix the net spin of the electrons at an integer value during the calculation. When the singlepoint calculations are repeated with constrained spin states of 0,2,4,6 and 8 the minimisation fails to converge. This suggests that the imposed spin state is not energetically viable. These calculations were repeated but the spin state was allowed to relax after 8 iterations when the local energy minimum for that spin state had been located. The results of these calculations are shown in figure 4.4 below. For each spin state the electronic structure was relaxed into the local energy minimum in less than 6 iteration steps. However, when the spin state was allowed to relax at 8 iterations all of the local minimum electronic configurations relaxed into a new energy minimum, that of the 'spin free' state. This is the spin state that the system spontaneously adopts when no constraints are placed upon the net spin and it is clearly the lowest energy spin state. No initial constraints were placed upon the spin in any of the spin polarised calculations in this work since the algorithm will naturally find the energy minimum spin state without outside intervention.

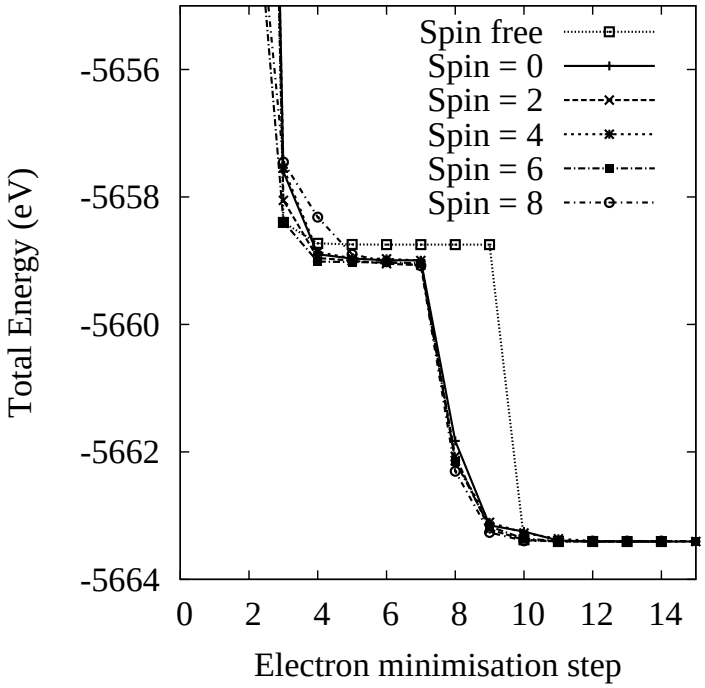

Figure 4.5: Variation of the total energy of a Si(111)-1×1-Ho supercell during electronic minimisation compared for various initial spin states. All spin states were allowed to relax after 8 steps except the spin free state which was relaxed after 9 steps.

4.2.3 Geometry optimisation

The Si(111)-1×1-Ho system was geometry optimised using the structure suggested by LEED as an initial atomic configuration [36]. The calculation was performed twice; with spin polarisation and with no spin polarisation. The structures were allowed to relax until the forces were either below the predefined tolerance of $5 \times 10^{-2} eV/\text{Å}$ or were as converged as possible. Figure 6.11 shows the convergence of the total energy and the maximum force on any atom as the geometry optimisation proceeds for the two structures.

The calculation performed with spin polarisation produces a structure with a converged total energy that is lower than that for the calculation where spin polarisation was not considered. However, the maximum force on any atom is not converged for this supercell. Analysis of the individual force components reveals that it is the atoms in the bottom layer of the supercell whose positions are constrained to bulk values that have large forces. This would suggest that the calculation should be repeated with more bulk layers to try to accommodate these forces. However, the atoms in the top three or four surface layers all have forces that are converged and whose values are comparable to those in the non-spin polarised calculation. For this reason the two calculations can be compared.

The optimised structural parameters for the two supercells are compared to experiment in table 5.9 below. The structural parameters were defined in figure 1.4 in the introductory chapter.

	LEED [36]	LEED	MEIS [32]	DFT	SP DFT
R1	0.82	0.82 ± 0.06	0.88 ± 0.03	0.62	0.72
L1	2.29	2.26 ± 0.06	2.24 ± 0.03	2.31	2.24
R2	1.01	0.98 ± 0.08	0.90 ± 0.06	0.88	0.89
L2	2.54	2.50 ± 0.05	2.55 ± 0.06	2.61	2.51
R3	0.78	0.78*	0.78*	0.78	0.76
L3	3.20	3.14*	3.14*	3.16	3.15
Rp	0.37 ± 0.03	0.29 ± 0.02	0.40 ± 0.04	0.85 ± 0.03	0.47 ± 0.05

Table 4.1: Interlayer spacings (L) and rumpling amplitudes (R) in the Si(111)-1×1-Ho system determined by LEED and DFT in this work compared with the results from other studies. The parameters were defined in figure 1.4 in Chapter 1 and those marked with an asterisk have not been optimised.

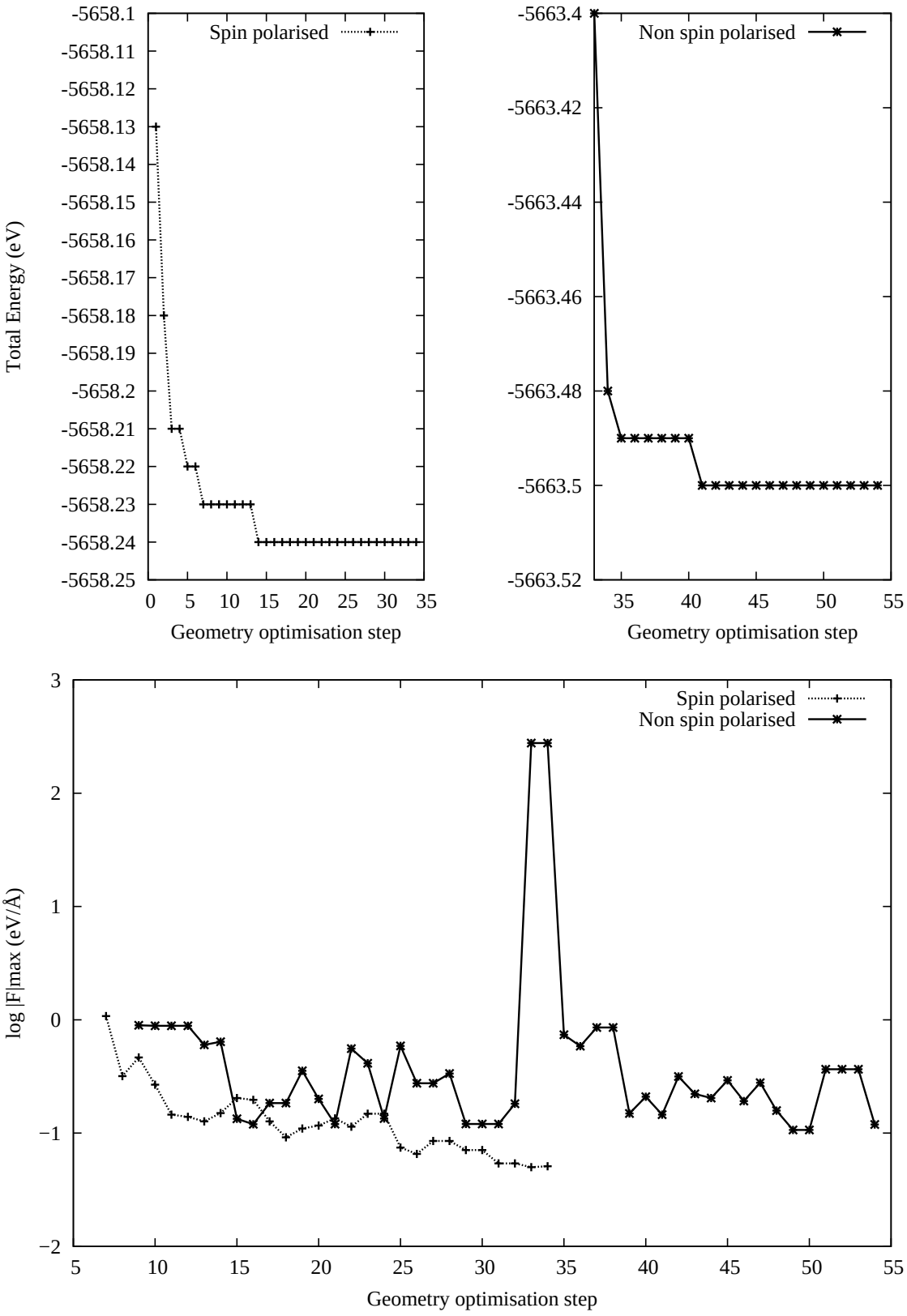

Figure 4.6: Convergence of the total energy (top) and logarithmic convergence of the forces (bottom) during the geometry optimisation of the Si(111)-1×1-Ho supercell for the spin polarised and non spin polarised cases. Only the last few steps are shown in the energy convergence for the spin polarised case since the relative energy of earlier steps would dominate the figure.

4.2.4 Investigation of the top silicon bilayer

As a further investigation of this 2D silicide structure an attempt has been made to understand why the top silicon overlayer adopts a reverse buckling when compared to the bulk layers. Three different configurations have been considered for the Si(111)-1×1-Ho system with the holmium atom in the T4 site in each case. These are shown in figure 4.7 and they correspond three different orientations of the top bilayer of silicon; reverse buckling (RB) and two forms of bulk-like buckling (BB and BS). These initial structures were geometry optimised using optimum values for all of the basis set and supercell input parameters. The effect of spin polarisation was not included. The right column of figure 4.7 shows the geometry optimised structures and 4.8 compares the convergence of the geometry optimisation for all three supercells.

The structure with the reverse buckled top bilayer is clearly lower in energy (by 0.7 eV) than the two structures with bulk-like buckling in the top bilayer. Both structures that initially had bulk buckling in the top bilayer have both adopted a reverse buckled top bilayer that is laterally shifted with respect to that in the 2D silicides. A large energy barrier must be present that has prevented these bulk buckled structures from a reconstruction into the full 2D reverse buckled structure. This shifted reverse buckled structure must have formed in order to satisfy the bonding requirements of both the 'up' and the 'down' atom in the top silicon bilayer. In the BB structure the 'down' silicon atom is presumably too close to the holmium atom and electrostatic repulsion means that this is a high energy configuration. This atom has been moved to become an 'up' atom. In the BS structure the 'up' atom is presumably too far away from the holmium atom to receive adequate charge transfer to quench its dangling bond and it has moved laterally across to be directly above the holmium atom.

The question that now remains is how the bonding environment differs in the two final structures; what charge transfer arrangement makes the reverse buckled structure more stable than the reverse buckled and shifted structure. This is discussed in the next section.

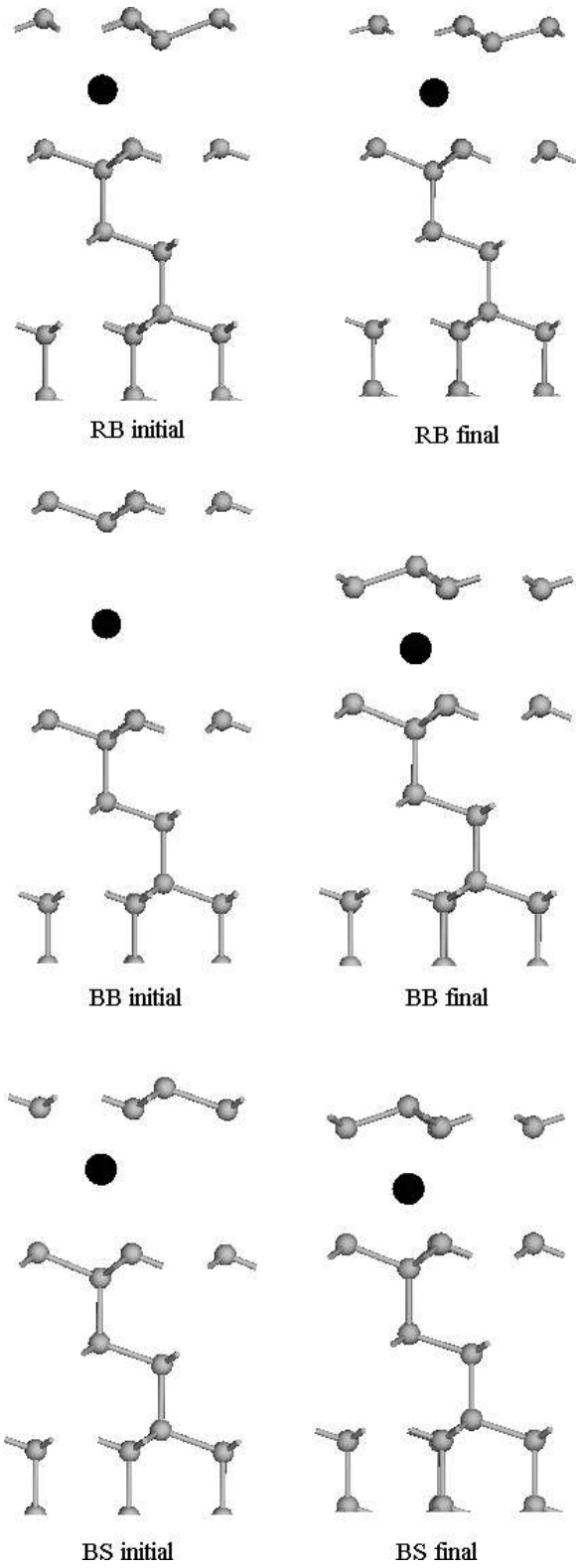

Figure 4.7: Initial (left) and final (right) atomic configurations of three structures for the Si(111)-1×1-Ho surface that have been geometry optimised. The shortened names are defined in the text.

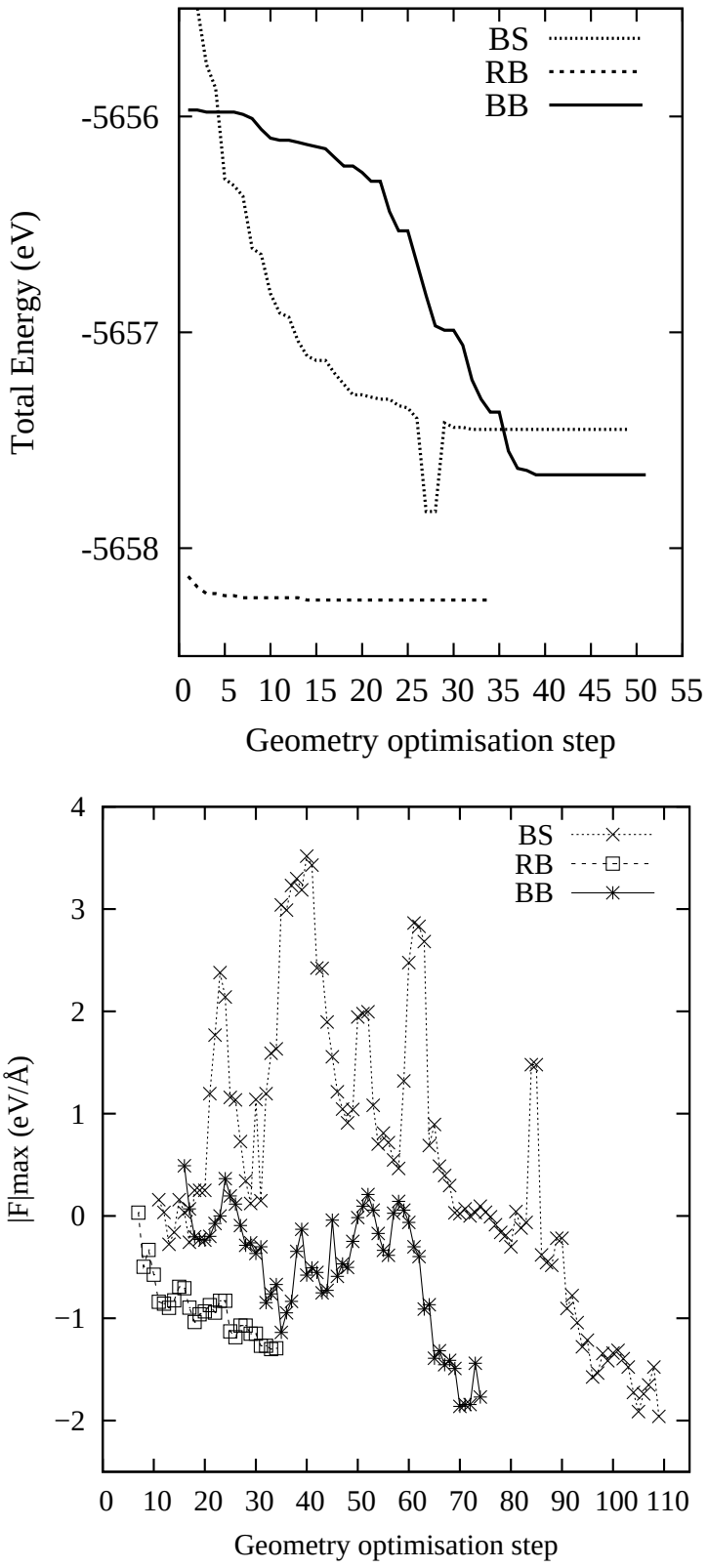

Figure 4.8: Convergence of the total energy and the maximum force on any atom during the geometry optimisation of Si(111)-1×1 supercells with three different top bilayer structures. RS is a reverse buckled 2D silicide that is observed during experiment. BB has buckling in the same sense as in the bulk and BS is BB but with the top bilayer laterally shifted.

4.2.5 Electronic Structure of 2D Si(111)-1×1-Ho

The electronic structure of 2D Si(111)-1×1-Ho reveals that there is charge transfer onto the silicon bilayers immediately above and below the holmium atom. Figure 4.10 shows the electron density difference for the two geometry optimised configurations that were discussed in the last section. This is the difference between the pure atomic density of the atoms treated as isolated objects and the final density after the electronic minimisation. There are two pockets of charge (marked 1 and 2) that represent charge that has been transferred from the holmium atom to saturate the dangling bonds of the silicon atoms closest to it in the silicon layers above and below. There is also a smaller degree of charge transfer into the second nearest neighbours in each layer, that is, the 'up' atom in the top silicon layer and the 'down' atom in the silicon layer below the holmium layer. This acts to partially hybridise the covalent bonds in each silicon bilayer and to further passivate each layer.

The reason for the stability of the 2D reverse buckled structure is now readily apparent. The configuration of the silicon atoms in the first two silicon bilayers is such that it presents the maximum number of silicon atoms as nearest neighbours to the holmium atom; three in the layer above and three in the layer below. These nearest neighbours are passivated by a partial quenching of their dangling bond. This is shown in figure 4.9 below. By contrast, the reverse buckled structure with the 'up' atom above the holmium atom presents a difficulty in saturation of its dangling bonds. The nearest neighbour in the layer above is now directly above the nearest neighbour in the layer below and it is difficult to distribute the dangling bonds without interaction between them.

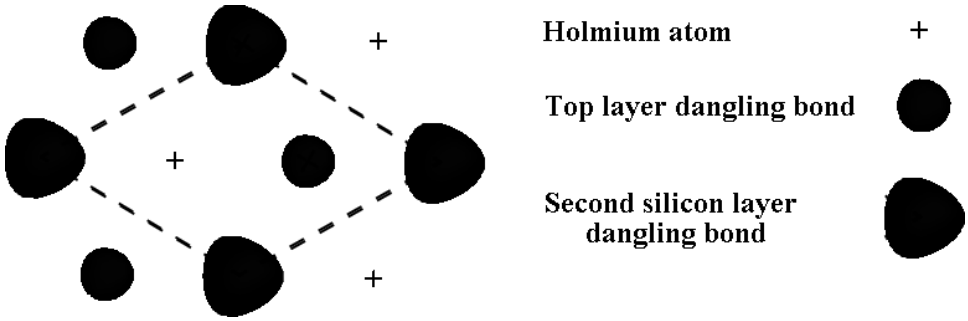

Figure 4.9: 3D isosurface plot showing those regions that have a density difference of 0.44 (e) near to the holmium atom in 2D reverse buckled holmium silicide. The unit cell is shown in a dashed outline. The holmium atom sits at the centre of a triangle formed by both the three dangling bonds in the layers above and below it. These triangles of dangling bonds are rotated 180° with respect to one another to prevent their interaction. This dictates the orientation of the top bilayer.

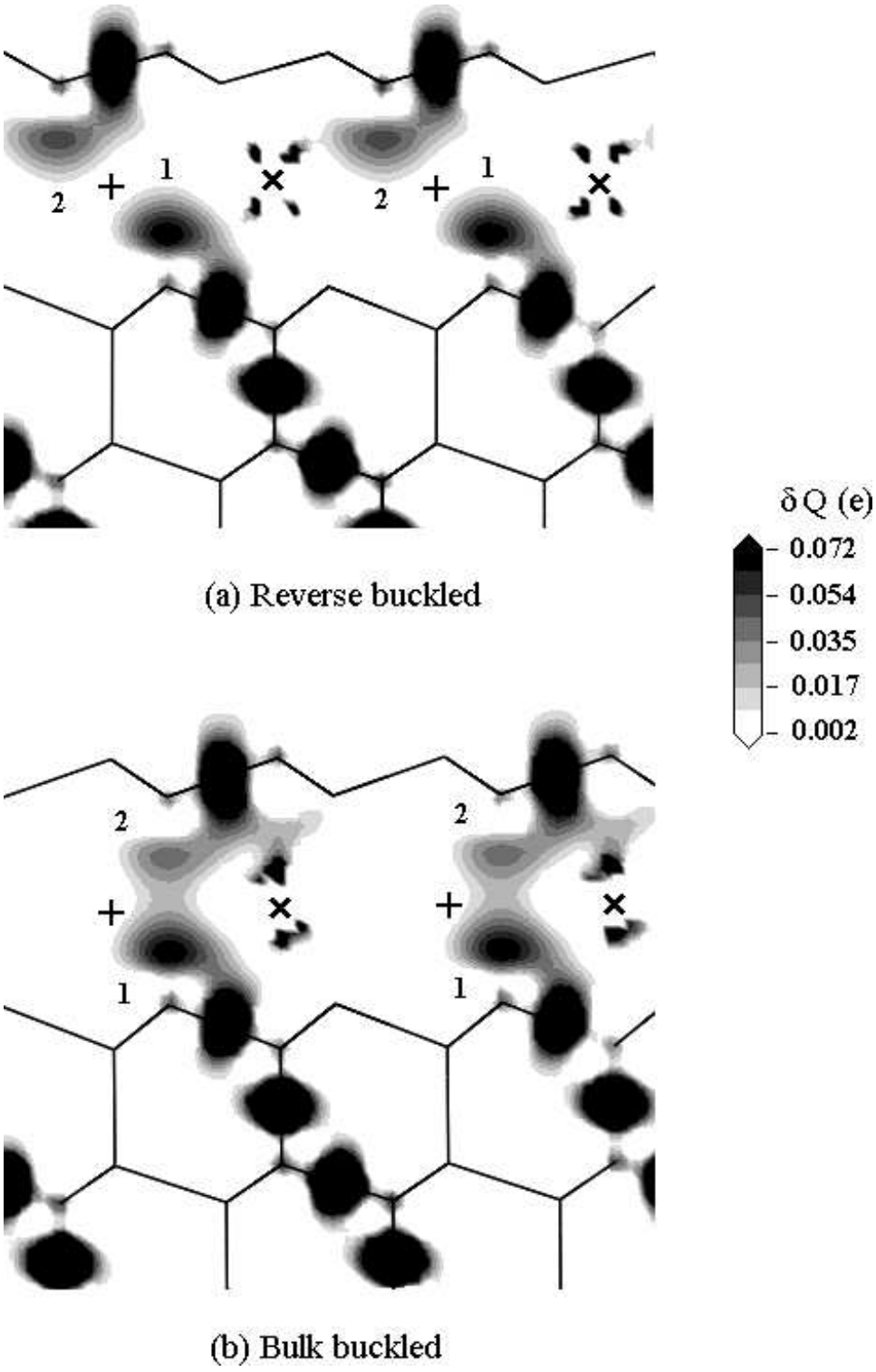

Figure 4.10: Electron density difference (δQ) plot along a vertical slice through the supercell showing the regions that have gained charge during electronic minimisation. In plane holmium atoms are marked + and those out of plane $\times$. Most of the deep black areas are covalent bonds between silicon atoms but there are two regions, marked 1 and 2, that represent charge transfer to saturate dangling bonds in the silicon layers immediately above and below the holmium layer.

4.2.6 Discussion

The structure that was geometry optimised with the effects of spin polarisation included is a better match with experiment than that calculated without spin polarisation. The main difference between the two calculated structures is in the top layer rumpling amplitude (to which LEED is very sensitive). The RE silicides are not known to be magnetic at any experimentally accessible temperature but these calculations do not take temperature into account and the magnetic state that is suggested might be viable near to absolute zero. Cooperative magnetism between atoms is known to depend upon the interatomic spacings and it is possible that the small energy gain from changing some of the interatomic spacings in 2D holmium silicide and inducing a magnetic state is greater than the energetic cost of a small modification to the structure. This might also suggest that the RE silicides are magnetic in the bulk at very low temperature. If this is the case then it means that the improved agreement with experiment for the spin polarised case is random; the change in the interatomic spacings caused by the formation of a low temperature magnetic state in the *ab initio* calculations could just as easily have caused a decrease in the top layer rumpling amplitude. Another factor is therefore responsible for the fact that the top layer rumpling amplitude is greater in the structures observed during the experiments performed at room temperature than in the theoretical calculations.

The total energy calculations and the charge density difference plots suggest that the precise orientation of the top silicon overlayer with respect to the silicon layer below the holmium layer is dictated by the need to laterally space out the dangling bonds that point towards the holmium layer from both directions. What is not clear is why the holmium layer sits subsurface and it is interesting to speculate. What is clear is that this must relate to the bonding requirements of the holmium atoms. It could be that the presence of silicon layers both above *and* below the holmium atom allow it to transfer charge and saturate dangling bonds whilst maintaining a symmetric local charge distribution. The answer probably lies in the complex hybridisation of the atomic orbitals of the holmium atom as it redistributes charge after having transferred some of it to the silicon atoms. Further spectroscopic work is needed to resolve the electronic structure of the holmium atom and how this changes during silicide formation. Such work might be able to link changes in the electronic structure of the holmium atom with the point at which it starts to go subsurface.

4.3 Holmium nanowires on Ge(111)

When one monolayer (ML) of holmium is deposited onto the Ge(111) surface a two-dimensional 1×1 structure is formed after annealing at ≈ 500 °C for 15-20 minutes [32]. A similar structure is formed in Si(111)1×1 RE systems ([35] and therein). Pelletier et al. [119] briefly noted the formation of metastable rod-like structures on the Er/Ge(111)-c(2×8) coexisting with the 1×1 structure.

Workers in the Surface Physics Group at York (namely, E. Perkins and Dr. C. Bonet) have observed isolated rod-like structures on the Ge(111) surface using STM. These are a true isolated nanostructure because they are not part of a periodic reconstruction or rectangular islands. The nanorods have a constant width that is very narrow compared to other nanorod structures and they do not require step edges or patterning in order to form. When the experiment is repeated using a higher Ho coverage the nanorods exist as part of a periodic 5×1 structure. Bonet has used the results of a medium energy ion scattering (MEIS) study in conjunction with the STM data to parameterise the structure to the extent that he has been able to suggest a quantitative model for the 5×1 unit cell.

In the remainder of this chapter the Ge(111)-5×1-Ho unit cell has been investigated using an *ab initio* density functional theory calculation. Simulated STM for the model structure is qualitatively compared to the STM images obtained in the laboratory and the comparisons are favourable. The electronic structure and the stability of the system are discussed in detail and the electronic properties are compared with experiment to show that the nanorod is metallic and that it can be considered as a nanowire.

In the next section the STM experiments performed by C. Bonet and E. Perkins are summarised together with the arguments that lead to the suggestion of the structural model which is the starting point for the *ab initio* calculations whose results form the rest of this chapter.

4.3.1 Experimental STM observations

The STM experiments were performed by E. Perkins and C. Bonet using an Omicron Nanotechnology GmbH microscope at a typical UHV base pressure of $\leq 2 \times 10^{-10}$ mbar. The germanium substrate was cleaned by argon ion bombardment followed by annealing at $\approx 500\,^{\circ}\mathrm{C}$ for about 15 minutes and *in-situ* low-energy electron diffraction (LEED) was used to check that a clean Ge(111)-c(2×8) surface had been made.

The sample was prepared by depositing 0.1 ML of Ho from a quartz crystal calibrated evaporation source onto a clean Ge(111)-c(2×8) surface held at a temperature of $\approx 250\,^{\circ}\mathrm{C}$ that was monitored using a k-type thermocouple attached to the sample stage. Figure 4.11 shows an STM image of a large area on the surface. Isolated and well defined nanorods have formed on flat regions clear of step edges on a surface that was not patterned or pre-structured in any way. The rods typically extend for $\approx 40\,\mathrm{nm}$ and they have a constant width. The structures have been reproduced in several experiments.

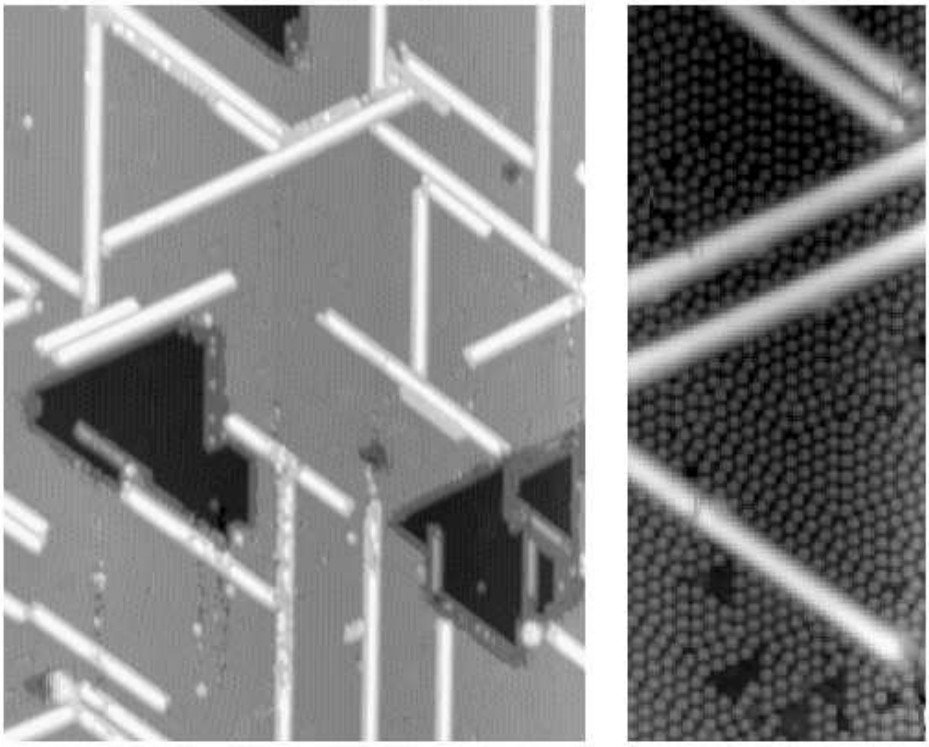

Figure 4.11: Two overview experimental STM images of the nanorods formed with a low (0.1 ML) coverage of Ho. (Left) Large area (59 × 75 nm) filled states image taken with a sample bias of $-2.0\,\mathrm{V}$ and a tunneling current of 2 nA. (Right) 14 × 33 nm empty states image taken with sample bias $+2.0\,\mathrm{V}$ and a tunneling current of 2 nA showing the surrounding clean Ge(111)-c(2×8) substrate. Reproduced with the permission of C. Bonet.

At a higher Ho coverage of 0.25 ML the rods stack in close parallel proximity and a periodic 5×1 structure is formed. Figure 4.12(a) shows a filled states image of a region 4.2 × 3.3 nm in size that contains two nanorods separated by a small gap. The atoms within each nanorod appear to occupy two distinct levels. With respect to the Ge rest atom of the surrounding c(2×8) reconstruction the height of the lower level is 2.1 Å and that of the nanorod peak is 3.9 Å. The width of the lower layer is 1.7 nm.

Figure 4.12(a) shows an empty states STM image of a region 4.2 × 3.3 nm in extent. Features within the top layer of the nanorod can now be resolved, especially when the image contrast is adjusted as in the left half of the figure. In the empty states STM images the top layer of the nanorod was measured as being 3.1 Å above the germanium adatom layer (and thus 3.8 Å above the rest atom layer since the adatom layer is known to be 0.66 Å above the rest atom layer [120]).

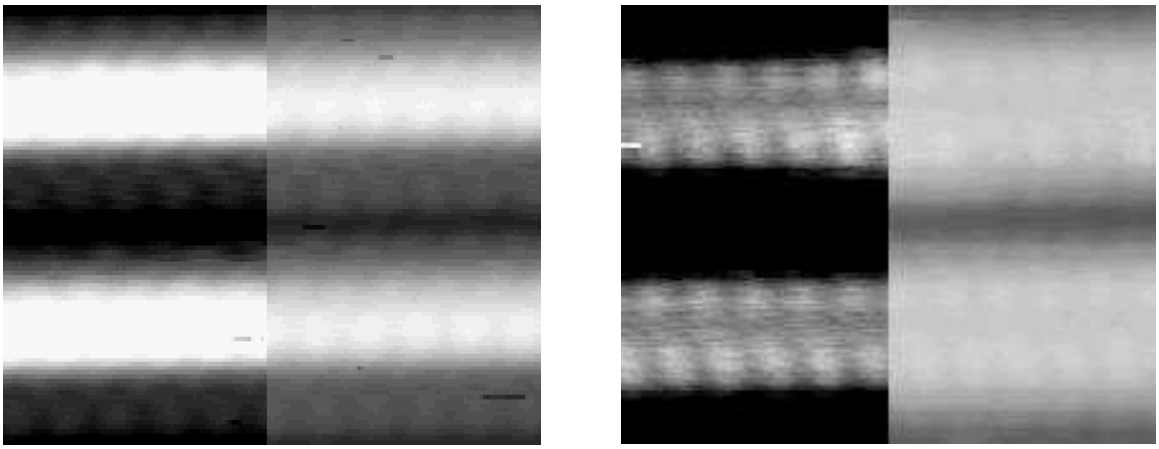

(a) Filled states experiment. (b) Empty states experiment.

Figure 4.12: Filled states (a) and empty states (b) experimental STM images for the Ge(111)-5×1-Ho system. The tunneling current in both images was 2 nA. In the filled states image the sample bias was − 2.0 V and in the empty states image it was + 1.50 V. The dimensions of both images are 4.2 × 3.3 nm. The left half of both images has been contrast adjusted to determine of the holmium atoms within the top layer of the nanorod can be more clearly discerned. Reproduced with the permission of C. Bonet.

Whilst it cannot be claimed that these layer height measurements correspond to pure topography with no contribution from electronic effects, the consistency of the filled and empty states measurements and the large height difference of 3.8-3.9 Å from the nanorod peak to the Ge rest atoms have allowed the conclusion that any model of the nanorod should involve a two-layer structure.

A MEIS experiment in which incident H^+ ions were strongly scattered in all directions by the Ho atoms was carried out at the CCLRC Daresbury UK MEIS facility by C. Bonet. The ion flux scattered from the holmium atoms did not show any dips at any emergent angle which might indicate blocking by germanium atoms in a layer

above the holmium atoms. The two 'bright' features per 5×1 unit cell in the empty states STM images have thus been interpreted as being associated with holmium atoms forming the upper layer of the nanorod.

The Ge atoms in the lower level of the nanorod, 2.1 Å above the rest atoms of the c(2×8) reconstruction, appear to be too low to be a full Ge bilayer (which would have a 3.27 Å step height [120]) and an STM image (not shown) in which nanorods can be seen on adjacent terraces separated by a monoatomic step supports this conclusion. Consideration of the bonding requirements of the two trivalent Ho atoms per 5×1 unit cell also leads to the conclusion that Ho atoms cannot be adsorbed atop a simple bulk-terminated Ge surface since in such a situation the Ge surface would provide only 5 dangling bonds to be quenched by the two trivalent Ho atoms.

On the other hand, the lower layer of the nanorod is too high above the rest atoms of the Ge substrate to be a simple adatom layer (0.66 Å above the rest atoms in clean Ge(111)-c(2×8) [120]). A visual comparison with surrounding areas of the c(2×8) reconstruction in the empty states STM images suggests an atomic density in the lower nanorod layer which is greater than that of a dilute (e.g. 2×2) adatom layer. Further information was obtained from our STM observations of occasional faulted nanowire growth in which the topmost Ho layer was sometimes absent from the nanorod over a small region. Under these conditions the Ge layer was found to be continuous across the width of the nanorod, extending across the area that would normally be covered by the upper Ho layer. The lower level of the nanorod was therefore identified as consisting of a single layer of additional Ge atoms (with density around one monolayer) atop the first bulk-like Ge bilayer.

Given these considerations Bonet has proposed the structure that is shown in Figure 4.13 in which there is a holmium nanorod atop an almost flat germanium layer atop a bulk-like germanium substrate. The structural parameters of the 5×1 supercell are summarised later.

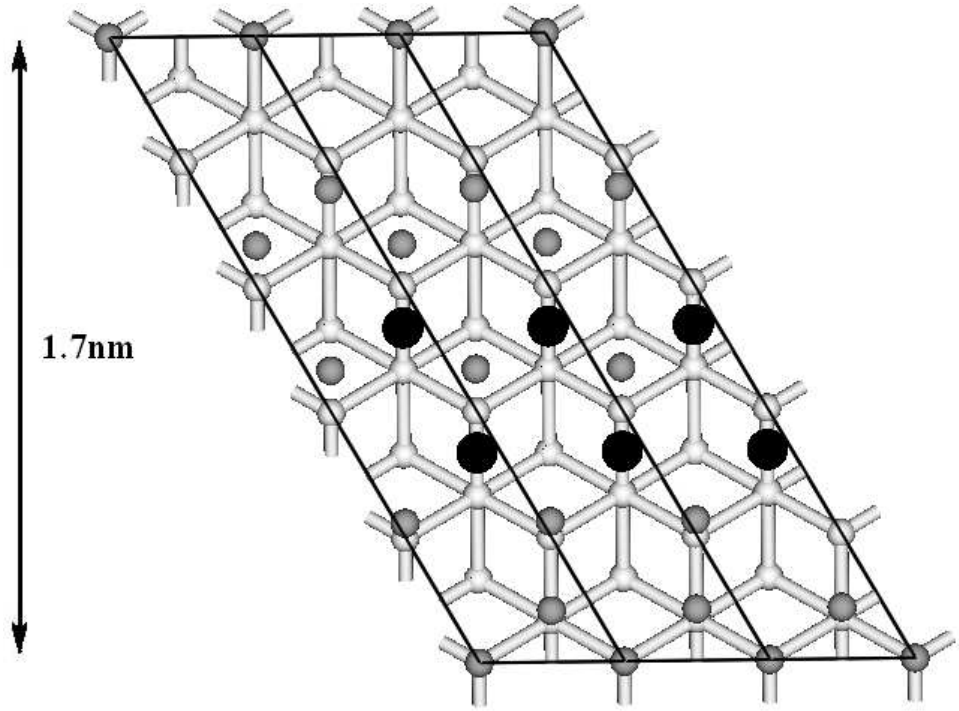

(a) Top view.

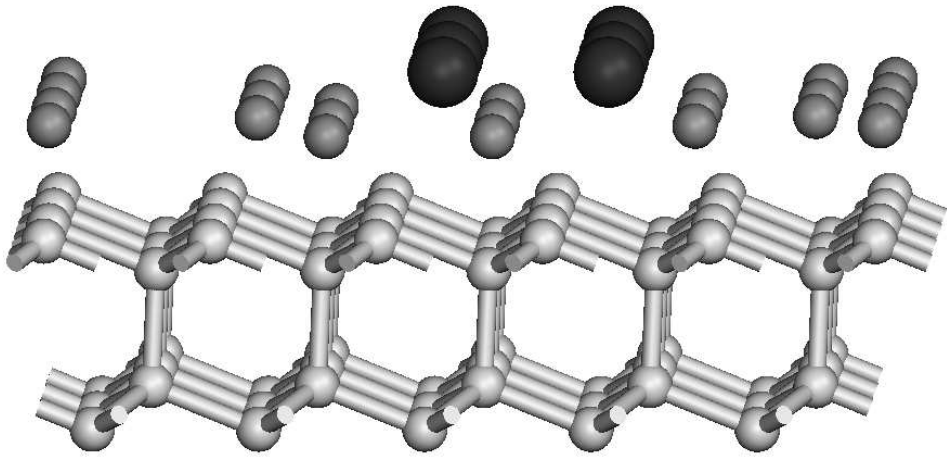

(b) Side view.

Figure 4.13: Two views of the Ge(111)5×1-Ho system whose structure has been suggested by C. Bonet; (a) top view in which the 5×1 unit cell is outlined in black (b) side view. Holmium atoms are large and black, reconstructed germanium atoms are coloured dark grey and bulk-like germanium atoms are light grey.

4.3.2 *Ab initio* Validation of the Structural Model

To validate the structural model the STM image that it would be expected to produce has been calculated using the `CASTEP` *ab initio* density functional theory based code ([9] and see Chapter 3). The generalised gradient approximation was used to model exchange and correlation effects. In the supercell (see figure 4.13) there are 2 holmium atoms, 26 germanium atoms and 5 hydrogen atoms used for passivation. This means that there are 151 valence electrons to account for in the electronic minimisation process, a formidable computational effort. The code was run on 128 processors in a parallel computing environment at the HPCx High Performance Computing facility located at the CCLRC Daresbury laboratory in the UK. It was not possible to optimise the basis set since this would require many singlepoint energy calculations. Instead, the settings for the basis set parameters that are recommended by the author of the pseudopotential were used as a guide. These take the form of a coarse, medium, fine and ultra-fine cutoff energy for the pseudopotential of each atomic species. For the holmium atom the cutoff energies for coarse, medium, fine and ultra-fine accuracy are 260 eV, 290eV, 320eV and 360 eV respectively. In this work a cutoff energy of 360 eV was used with a reciprocal space sampling grid containing 4 k-points, which is of reasonable density for such a large supercell. Resources have not permitted the geometry optimisation of this structure whilst taking account of the infulence of spin polarisation of the electrons.

The supercell contains four layers of atoms; a top reconstructed holmium/germanium nanorod, a bulk-like germanium layer, a second germanium layer in which the atoms are constrained into bulk positions and a final layer of hydrogen atoms used for passivation of dangling bonds on the underside of the supercell. The vacuum gap was 10 Å thick which was the value obtained in the course of the *ab initio* studies of 2D Si(111)-1×1-Ho in section 4.2 of this chapter.

The atomic positions in the experimentally suggested model were varied until the point in the local energy landscape at which the energy and the forces were at their lowest was located and at which the structure was as converged as possible. This required relatively few steps and the forces at this point were higher than other geometry optimisation calculations in this thesis in which the energy and the forces have been fully converged. The coordinates of the atoms in the optimised supercell are listed in table 4.2 below together with the force on each atom and details of the electronic structure of each atom which is to be discussed later. The numbering scheme used to label the atoms in table 4.2 is defined in figure 4.14.

Atom	x	y	z	$\|\boldsymbol{F}\|$ (eV/Å)	s	p	d	f	Q (e)	δ Q (e)
Ho1	2.89	5.01	9.84	1.49	2.54	6.28	1.00	10.78	20.61	-0.39
Ho2	2.89	9.00	9.84	0.55	2.43	6.14	1.30	10.96	20.83	-0.17
Ge1	0.00	0.00	8.98	0.46	1.70	2.35	0.00	0.00	4.05	+0.05
Ge2	2.44	0.23	8.95	0.32	1.78	2.32	0.00	0.00	4.09	+0.09
Ge3	0.20	4.35	8.95	0.19	1.54	2.71	0.00	0.00	4.25	+0.25
Ge4	0.58	9.01	8.69	0.22	1.23	2.80	0.00	0.00	4.03	+0.03
Ge5	0.58	13.00	8.69	0.17	1.65	2.60	0.00	0.00	4.26	+0.26
Ge6	3.07	13.32	8.85	1.44	1.74	2.30	0.00	0.00	4.04	+0.04
Ge7	0.00	0.00	6.53	1.54	1.49	2.51	0.00	0.00	4.00	0.00
Ge8	2.31	0.00	5.72	0.31	1.31	2.53	0.00	0.00	3.84	+0.16
Ge9	3.47	2.00	6.53	0.83	1.32	2.51	0.00	0.00	3.83	+0.17
Ge10	0.00	4.00	6.53	1.64	1.41	2.50	0.00	0.00	3.92	+0.08
Ge11	2.31	4.00	5.72	0.41	1.32	2.55	0.00	0.00	3.87	+0.13
Ge12	3.47	6.00	6.53	0.36	1.37	2.49	0.00	0.00	3.86	+0.14
Ge13	0.00	8.00	6.53	0.16	1.37	2.58	0.00	0.00	3.96	+0.04
Ge14	2.31	8.00	5.72	0.52	1.33	2.49	0.00	0.00	3.82	+0.18
Ge15	3.47	10.00	6.53	1.43	1.53	2.53	0.00	0.00	4.06	-0.06
Ge16	0.00	12.00	6.53	1.53	1.36	2.52	0.00	0.00	3.87	+0.13

Table 4.2: Tabulated atomic coordinates (in Å), forces ($|\boldsymbol{F}|$), electronic configuration, total charge (Q) and charge depletion δ Q of each atom in the geometry optimised Ge(111)5×1-Ho supercell. The lattice parameters are $\boldsymbol{a}$=4.000457 Å, $\boldsymbol{b}$=20.002283 Å, $\boldsymbol{c}$=26.532718 Å with $\alpha = \beta = 90°$ and $\gamma = 120°$.

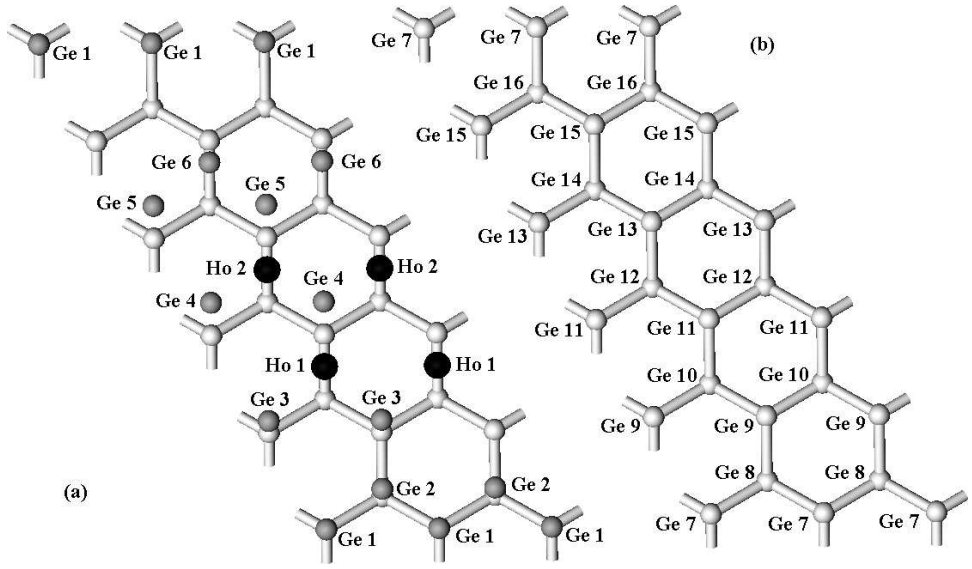

Figure 4.14: Labelling of the top two layers in the optimised Ge(111)5×1-Ho structure. The holmium and germanium atoms in the top nanorod layer are labelled in figure (a) and in (b) the germanium atoms in the second layer, that is bulk-like, are labelled.

Having obtained a stable atomic structure the associated electronic structure was used

to determine the expected constant current STM profile using the Tersoff-Hamann scheme [114]. Figure 4.15(b) shows the filled states image so obtained at a sample bias of $-2.0\,\mathrm{V}$. The image dimensions are 4.2×3.3 nm and it can be directly compared with the experimental result in figure 4.15(a). The dominance of Ho in the nanorod is evident in the modelled system as it was in the experimental images. There are many filled electronic states around the high-valency holmium atoms that have a favourable probability for tunneling into the tip. The trench structure between the nanorods does indeed seem to be formed by the arrangement of germanium that has been suggested.

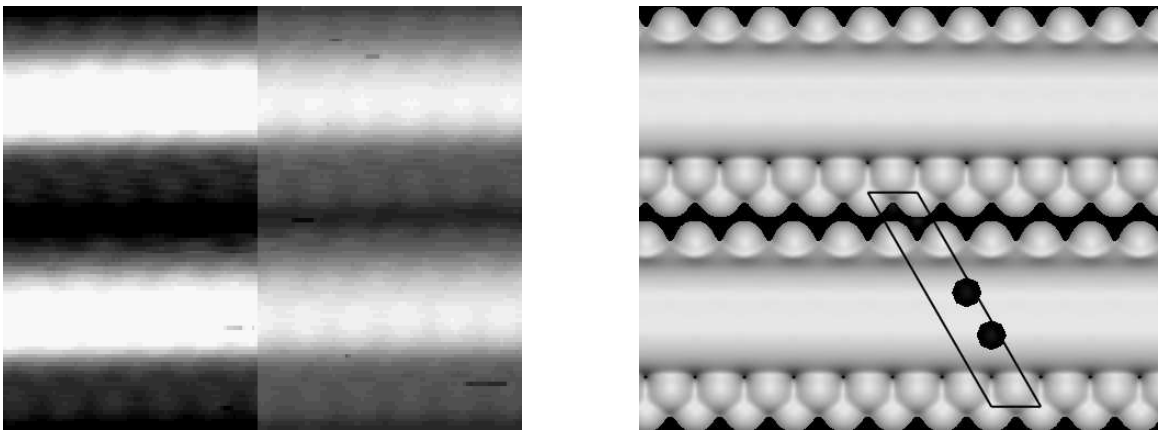

(a) Filled states experiment.

(b) Filled states theory.

Figure 4.15: Measured (a) and simulated (b) filled states STM images for the Ge(111)5×1-Ho system. Both images correspond to a sample bias of $-2.0\,\mathrm{V}$ and have dimensions of 4.2×3.3 nm.

Figure 4.16(b) shows the empty states image calculated with a sample bias of $+1.5\,\mathrm{V}$. The image dimensions are 4.2×3.3 nm and it can be directly compared with the experimental result in figure 4.16(a). Atomic resolution within the nanorod is apparent in the theoretical image as it was in the experiment. Between the nanorods we see the structure in the germanium underlayers that was not accessible in the experiment.

The electronic structure can be used in conjunction with the population analysis in table 4.2 to determine the bonding environment responsible for the nanorod structure. Figure 4.17 shows three slices through the electronic density, one in the plane of the Ge flat layer and two vertical slices through the two holmium atoms. In general, there is a mixture of covalent and ionic bonding within the nanorod reflecting the large contribution of electron transfer from the Ho atoms.

In figure 4.17 germanium atom 4 is covalently bonded to the two holmium atoms and to the germanium atom in the layer below in a tetrahedral arrangement and this atom has negligible extra charge transferred from either Ho atom and a relatively low

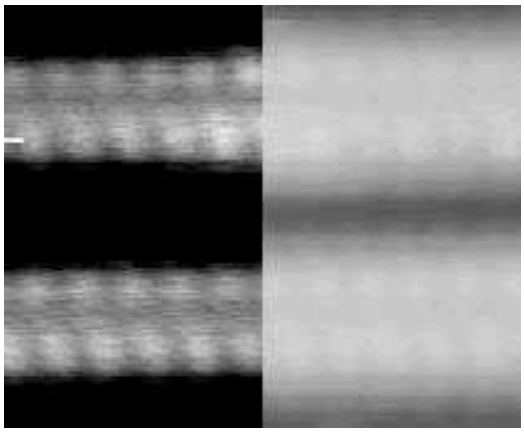

(a) Empty states experiment.

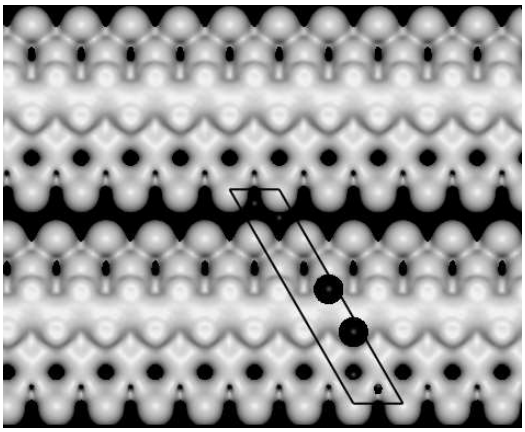

(b) Empty states theory.

Figure 4.16: Measured (a) and simulated (b) empty states STM images for the Ge(111) 5×1 Ho system. Both images correspond to a sample bias of + 1.50 V and have dimensions of 4.2 × 3.3 nm. The left half of (a) has been contrast adjusted so that the Ho atoms within the top layer of the nanorod can be more clearly discerned.

force acting upon it. There is a significant amount of charge transfer from holmium 1 to germanium 3 and to a lesser extent to germanium 2 and germanium 1 near to the edge of the shelf. Germanium 2 is sp^2 hybridised and we can see three planar trigonal bonds in the overhead view and no bonds to the layer below in the side view. There is also a significant amount of charge transfer from holmium 2 to germanium 5 and to a lesser extent to germanium 6. Germanium 1 and germanium 6 are partially sp^2 hybridised with some remainder of tetrahedral bonding. The main residual forces in the system are on the atoms in and around the trench, that is germanium 1, germanium 6, germanium 7, germanium 15 and germanium 16.

The atoms in the first bulk like germanium layer have all gained electric charge. This is not charge transferred from the holmium or germanium atoms in the layers above. In table 4.2 we can see that the values in the charge transfer column (δ Q, final column) do not sum to zero. That is, there must be net charge transfer from outside of these top layers. Population analysis of the layer below (not shown) reveals that this layer is charge depleted.

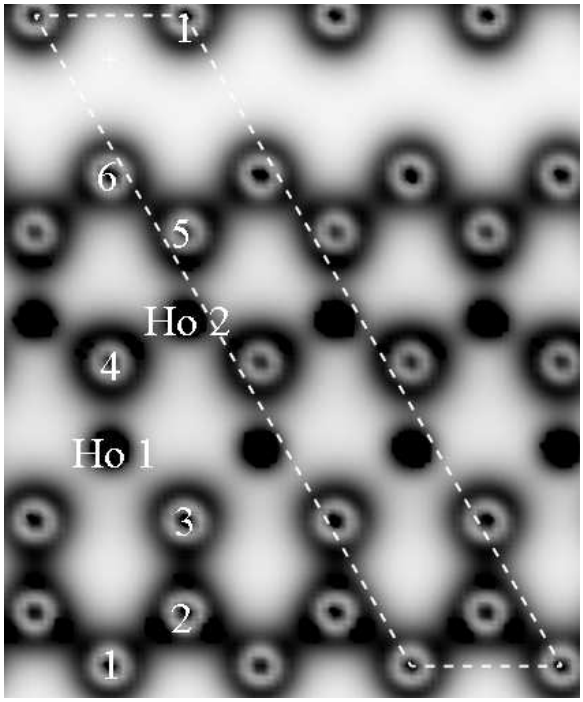

(a)

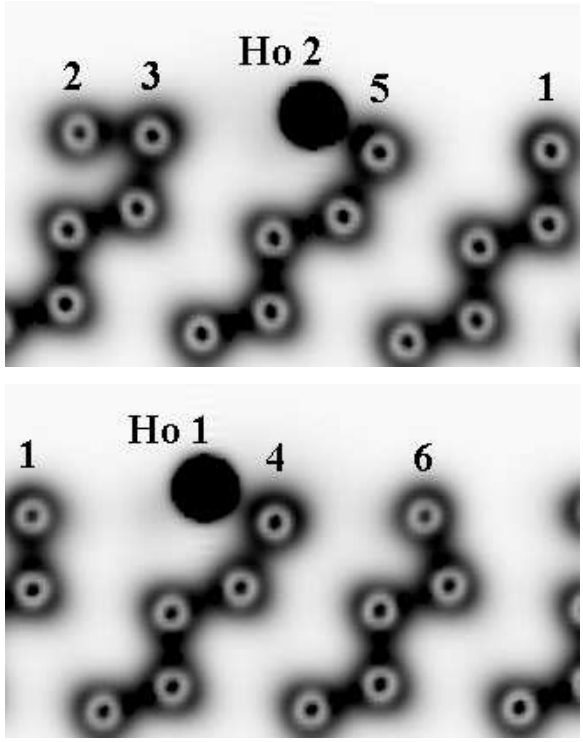

Figure 4.17: Electron density within a slice taken (a) horizontally in the plane of the surface through the flat layer of germanium atoms labelled 1-6 and (b)/(c) vertically through the two holmium atoms (labelled Ho 1 and Ho 2) to show the bonding to the layer below.

The electronic properties of the nanorods can be predicted from the results of the *ab initio* calculation. In figure 4.18 the local density of states within the nanorod is shown. The spike in the electronic population at energies close to the Fermi level indicates the metallic character of the nanorod and confirms the decoupling of its electronic states from those in the semiconducting germanium bulk.

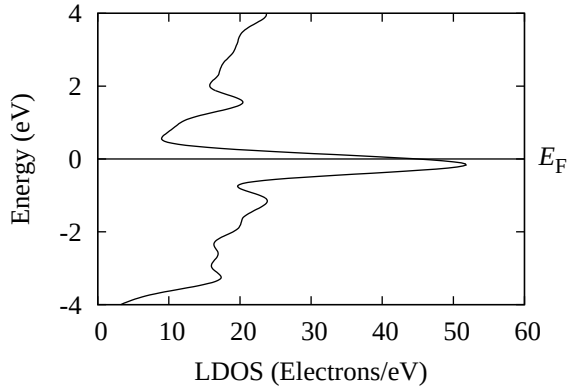

Figure 4.18: Calculated local density of states for the Ge(111)-5×1-Ho structure.

Figure 4.19 shows tunneling current measurements taken from the nanorod and from the surrounding Ge substrate for reference by Dr. C. Bonet. The nanorod clearly has conducting states at the Fermi level whereas the bandgap of the Ge substrate means that it has no conducting states at the Fermi level. This would suggest that some of the electron states at the fermi level identified in the theoretical calculation correspond to mobile electrons.

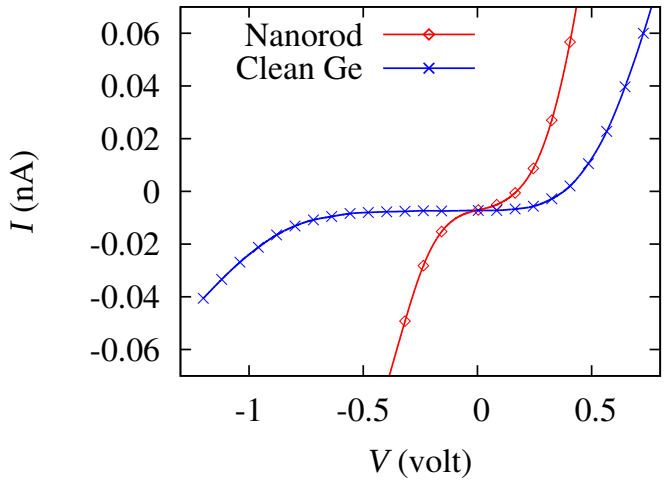

Figure 4.19: (Original in colour) Experimental Scanning Tunneling Spectroscopy data showing the conducting properties of the nanorod. Data taken from the germanium substrate, with its large bandgap at the Fermi level, is included for reference. Reproduced with permission of Dr. C. Bonet

4.3.3 Discussion

The main observation in this section is that the STM profile of the model structure is in good qualitative agreement with experiment. This would suggest that the atomic and electronic structure of the model system are in good qualitative agreement with that observed in the experiment.

The nature of the convergence of the geometry optimisation of this system would suggest that the system is metastable. After some slight relaxation (mainly in the vertical position of the holmium atoms) the geometry optimiser could find no direction in which to reduce the forces and energy further and it was forced to suggest that this system was as 'converged as possible'. This could be an indication that there is noise in the hessian matrix that is distorting the energy landscape but this is unlikely to have accumulated in so few geometry optimisation steps and their associated hessian updates.

That this is a metastable system is supported by the observations made during experiment. First, the structure was formed using a very low temperature ($\approx 250\,^{\circ}\mathrm{C}$) and it is tempting to speculate that at this temperature there is not enough energy in the system for any major reconstruction. The second experimental observation that supports the idea that this system is metastable is the fact that when this system is annealed at a higher temperature ($\approx 500\,^{\circ}\mathrm{C}$) regions of the surface form a 2D RE germanide. This suggests that the 2D RE germanide is of lower energy than the nanorod but that the annealing temperature must be sufficiently high to overcome local energy barriers in order to form this lower energy structure. It is not possible to perform two *ab initio* calculations to directly compare the energies of the two reconstructions. The unit cell of the 2D RE germanide contains a different ratio of each atomic species to that in the nanorod unit cell.

The structure as observed would appear to be a very delicate balance of the forces and the bonding requirements of the atoms within the nanorod. The main feature of the structure is of charge transfer from the holmium atoms to form a charge envelope over the flat germanium atoms in the layer below which adopt varying degrees of sp^2 charge hybridisation. The atoms that are too far from the holmium atoms to receive excess charge to saturate dangling bonds and to allow partial hybridisation of their bonds exist in a highly strained tetrahedral bonding environment which has consequent effects upon the forces on the germanium atoms at the edges of the nanorod and in the trench. A major open question is why the holmium atoms form such a one dimensional chain structure and why simple electrostatic repulsion does not cause them to be more evenly spaced out in both dimensions.

Further work is needed to quantitatively validate the atomic structure suggested here but this structure forms at low coverage and is very dilute and most of this surface seems to be unreconstructed Ge(111)-c(2×8). This would make a LEED investigation very difficult and has restricted the cursory MEIS investigation that was carried out to be limited in scope to merely showing that the holmium atoms sit atop the surface. The electronic structure also requires validation. Surface spectroscopy experiments would be very useful in determining the bonding environment within the nanorod. The population analysis reveals that the top germanium layer and the first germanium bulk like layer contain excess charge and that the layer immediately below is charge depleted. Spectroscopy would be of use in investigating the nature any excess charge that has accumulated in the top germanium layers and the charge that has been delocalised from the holmium atoms.

A question remains to be answered about the nature of the electrons that reside close to the Fermi level. The four k-points used to sample the many body wavefunction in reciprocal space do not permit the full resolution of the electronic states of the holmium atom from those of the germanium atoms in the nanorod. However, we would expect the holmium atoms, which each contain more than 20 valence electrons, to dominate the density of states and it is a reasonable assumption that the density of states, as calculated, represents that of the local density of states of the holmium atoms. If the electronic population near to the Fermi level comprises solely of electrons in the holmium f shell then it is unlikely that these electrons would be mobile since the f shell is highly localised. However, the density of states presented in figure 4.18 has not been resolved into angular momentum channels for the electrons and it could be that there are mobile s states or hybridised sp states at the Fermi level. Experiment would seem to support this idea since in figure 4.19 we can see that there are mobile electrons at the Fermi level. A further *ab initio* calculation with angular momentum resolved local density of states would clarify this matter somewhat. If a very dense k-point grid was used it would also allow the unambiguous resolution of the germanium substrate density of states from that of the holmium atoms.

4.4 Chapter 4 Conclusions

In conclusion, the structure of 2D holmium silicide has been quantitatively investigated using `CASTEP`. Spin polarisation has been shown to have an influence upon the structure when the effects of temperature are not included. These effects improve the agreement of the calculated structure with experiment but this is likely to be related to other factors. The structure of the top bilayer has been investigated using the nature of the calculated dangling bonds. The structure in the top bilayer has been shown to be dictated by the need to space out the dangling bonds that point towards the holmium layer.

The structural model for a rod-like formation that has been formed by other workers by depositing a low coverage of Ho on the Ge(111) surface has been qualitatively verified using *ab initio* geometry optimisation. It has been shown that the structure is stable and that in both filled and empty states imaging the calculated STM profile for this model is in good qualitative agreement with experiment. The calculated electronic structure supports the experimental conductivity measurements which suggest that the nanorod is metallic in character and can be termed a nanowire.

Chapter 5

LEED and Ab-Initio Study of Iron and Holmium on Si(111)

5.1 Introduction: The Interface of Iron and Silicon

Interest in the Fe/Si interface has been due to the potential for application in electronics [121], spin electronics [122] and optoelectronics [123, 124]. Unfortunately, the iron silicides have poor epitaxy when grown on the Si(111) surface. As a result many metastable phases have been observed that are not seen in bulk FeSi. The interface is rough and the reconstructions formed are very sensitive to the formation conditions.

In 1987 Urano et al. [125] used LEED I-V to investigate Fe films of varying thickness deposited onto Si(111)-7×7. A phase diagram was generated that shows how the Fe/Si(111) structure that is formed depends on the amount of material deposited and the annealing temperature used. When a 1ML deposit of Fe on Si(111)-7x7 is annealed below 350^{o}C a 1x1 structure is produced. Above around 400^{o}C a 2x2 structure results and for an annealing temperature above about 600^{o}C the substrate 7x7 structure begins to emerge. The authors obtained experimental I-V curves for a 1ML deposit of Fe and compared them with theoretically generated I-V curves for three different sites for the Fe atoms but were unable to obtain a full structural model.

Subsequent investigations revealed the presence of a number of different phases and a sensitive dependence upon the exact amount of Fe deposited (see [126] and therein). This was placed into sharp focus by a study in 2002 by Starke et al. [127]. They compared the I-V curves for the (1,0) LEED spot for a variety of annealing temperatures. It was shown that a change in the annealing temperature of just 50^{o}C can result in marked changes in the I-V curve. Also, these I-V curves do not agree well with those obtained by Urano et al. The conclusion is that the precise structure formed depends very sensitively upon the preparation conditions and the repeated preparation

of a given phase will be very difficult to achieve.

A great deal of effort has gone into investigating the growth conditions of iron on silicon and there been have attempts using a variety of growth techniques to construct a clean ordered interface (see [128] and therein for an exhaustive list of references). Another approach has been taken during the initial stages of interface formation. The Si(111) surface has been prepatterned by the deposition of another material first and then Fe has been deposited atop this ordered surface layer. Castrucci et al. [129, 130] have used Auger electron diffraction and STM to study the behaviour of Fe when it is deposited onto a thick (15ML) buffer layer of Cu on the Si(111) surface. They have shown that for Fe coverages $>$ 3ML an ordered Fe phase is formed but they have also found evidence that there is a degree of order for coverages less than this at which they assume that the Fe forms small islands. They have not been able to conclusively determine the degree of intermixing between the Fe overlayer and the Cu buffer layer below. They have not attempted to investigate the effect of reducing the thickness of the Cu buffer layer; the nominal thickness of 15 ML that was used was that at which the Auger signal from the underlying silicon substrate was not detectable. Galkin et al. [131] have used conductivity measurements to characterise the iron silicide surface. They have then shown that with a 3 ML buffer of Cr atop the Si(111) substrate the characteristic conductivity profile of iron silicide is not seen when Fe is deposited, which implies that the Cr buffer acts as a barrier to the formation of iron silicide. They have also shown that the metallic conductivity profile of bulk Fe is not apparent until around 8.5 ML of Fe are deposited atop Si(111)-Cr and they have suggested that at lower coverages the deposited Fe forms small 3D islands.

Thus Cr and Cu form an unreactive barrier to the formation of iron silicides. Xi et al. [132] have used the $\sqrt{3} \times \sqrt{3}$-Al/Si(111) surface as a patterned template on which to grow Fe. They have shown using STM that deposition of $>$ 0.1ML of Fe at room temperature results in small clusters of Fe atop the Al adlayer with some evidence of incorporation. Growth at 100°C results in larger clusters with no internal crystal structure apparent. Growth at 400°C (or after post deposition annealing) of 0.3ML Fe results in the formation near to step edges of small islands of ordered 2×2 Fe in the CsCl structure. At higher coverages (but still $<$ 1ML) islands of Fe grow in the terrace regions. The presence of the Al atoms has thus enabled the 2×2 structure to grow at lower coverage and temperature than on the Si(111)-7×7 surface.

The rare earth silicides are known to have good epitaxy with the Si(111) surface and they produce well ordered reconstructions (see chapter 1). Bonet [92] has conducted a LEED I-V investigation of the growth of Ho on Si(111) with Ag or Pb. When 1ML of Pb or Ag are deposited onto Si(111)-1×1-Ho at room temperature and annealed at $<$ 500°C the LEED I-V curves show a great deal of similarity with those of Si(111)-

1×1-Ho. The implication is that the 2D RE silicide surface is relatively passive and any deposited material forms small islands which leave the 2D silicide exposed. When 1ML of Ho was deposited onto the Si(111)–Pb surface a $\sqrt{3} \times \sqrt{3}$ LEED pattern was observed and this, together with STM observations allowed a tentative structural model to be suggested in which Ho forms an overlayer atop a flat layer of Pb atoms. No evidence for intermixing was found. When 1ML of Ho was deposited onto Si(111)-($\sqrt{3} \times \sqrt{3}$)R30°-Ag the LEED I-V curves were found to be very similar to those for Si(111)-($\sqrt{3} \times \sqrt{3}$)R30°-Ag if annealing was performed at $\sim$ 500°C. Annealing at $\sim$ 700°C changed the LEED pattern from a $\sqrt{3} \times \sqrt{3}$ into a 1×1 periodicity. The I-V curves for this new surface show some common peaks with the I-V curves for both the Si(111)-1×1-Ho and Si(111)-($\sqrt{3} \times \sqrt{3}$)R30°-Ag surfaces but there are also some extra features corresponding to some new intermixed phase and a tentative model has been proposed.

In the first half of this chapter an attempt to grow a mixed phase of Fe and Ho atop the Si(111) surface is described. A 1 ML amount of each material has been deposited both by depositing the Fe first and the Ho first. A 1×1 phase has been observed and this has been characterised using LEED I-V and STM. The effect of increased Fe coverage has also been characterised.

5.2 Iron and Holmium on Si(111)

5.2.1 Low Energy Electron Diffraction Experiments

In this section the LEED experiments are discussed. These were done using the York LEED instrument that was described in chapter 2 of this thesis. The first step in each experiment was to clean the silicon substrate by flashing it to $\approx 1200\,^{\circ}\mathrm{C}$ using an electron beam heater and then the sample was slowly cooled through the $\approx 900 - 700\,^{\circ}\mathrm{C}$ region over a period of 15 minutes. All temperatures were monitored using an infra-red pyrometer. The LEED pattern was then checked and a sharp 7×7 LEED pattern was taken as evidence that a clean, well ordered Si(111)-7×7 surface was present. Holmium was deposited from a tungsten basket source and iron was deposited from a nugget of iron inside a coil of tantalum that was used to heat it. All sources were calibrated prior to each separate deposition episode.

Holmium on the Si(111)-1×1-Fe Surface

One monolayer of iron was deposited from a pre-calibrated source onto the clean Si(111)-7×7 substrate which was not held at an elevated temperature. The sample was annealed at ≈ 400 °C for 15 minutes. A diffuse 1×1 LEED pattern resulted (see figure 5.6). 1ML of holmium was then deposited onto this surface which was then annealed at ≈ 400 °C for 15 minutes. A streaky 1×1 LEED pattern resulted and images of this are shown in figure 5.8 for two different experimental runs. During some experiments it was necessary to repeat the latter anneal in order to sharpen the 1×1 LEED pattern.

Images of this diffraction pattern were acquired over a 40-300 eV range of primary electron energies in steps of 2 eV using a CCD camera and stored on an instrument dedicated computer. For each spot in the LEED pattern the variation in its intensity with primary electron energy was recorded which resulted in a set of 17 I-V curves. Degenerate beams were averaged together to reduce the signal to noise ratio and also to reduce any small errors that may have occurred in setting up normal beam incidence.

The experiment was repeated several times and the I-V curves obtained during different experiments are shown in figure 5.2. These curves were compared using the Pendry R-factor [93] and these R-factors are shown in table 5.1. These interrun R-factors are not as low as we would expect for an experiment-experiment comparison if the surface was repeatedly preperable. This would suggest that although it is possible to repeatedly prepare a similar surface there is some variability in the surface structure. This is usually indicative of disorder and/or variable domains on the surface. To further reduce noise the I-V curves from three separate experiments were averaged together and a three point smooth was applied.

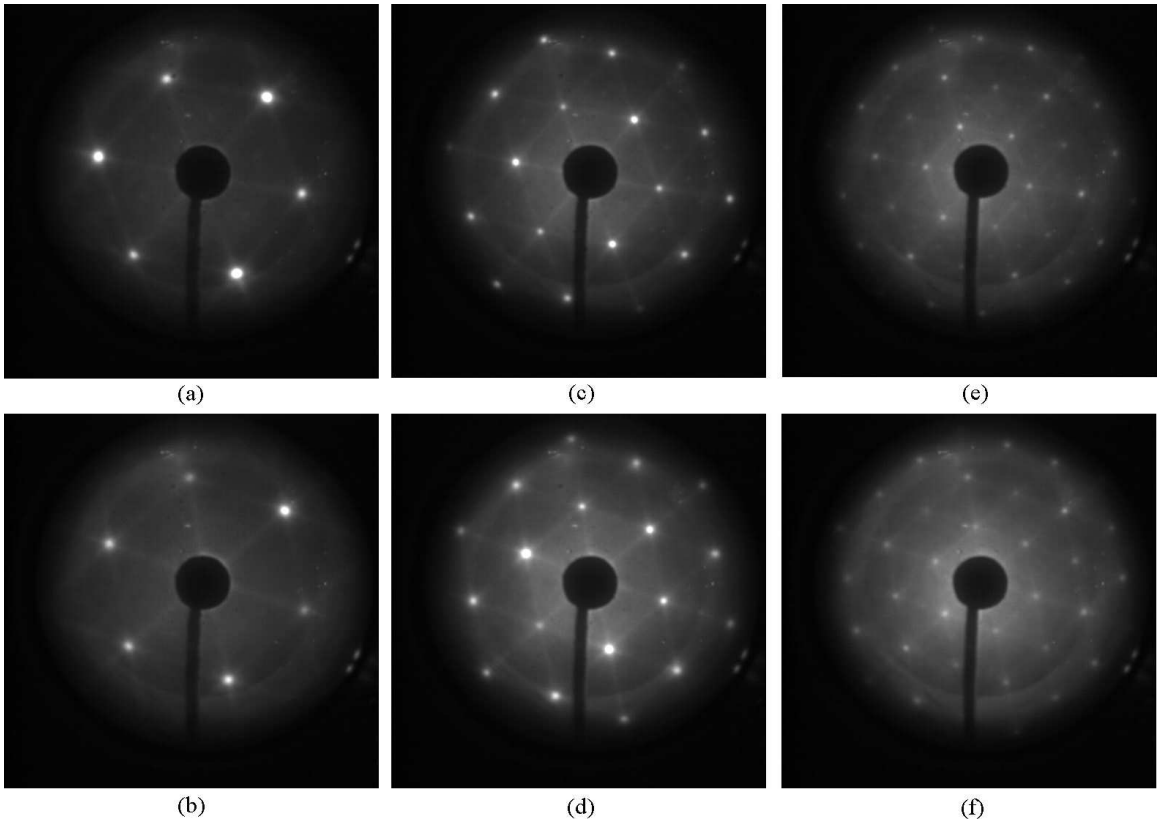

Figure 5.1: Experimental LEED spot pattern formed by Ho on the Si(111)-1×1-Fe surface shown at (a), (b) 40 eV and (c), (d) 80 eV and (e), (f) 150 eV for two separate experiments.

LEED Spot	Range of interrun R-factors
(1,0)	0.19 - 0.27
(0,1)	0.19 - 0.32
(2,0)	0.22 - 0.36
(0,2)	0.21 - 0.37
(1,1)	0.38 - 0.50

Table 5.1: The range of interrun R-factors for each spot in the 1×1 LEED pattern of the surface formed by Ho on Si(111)-1×1-Fe.

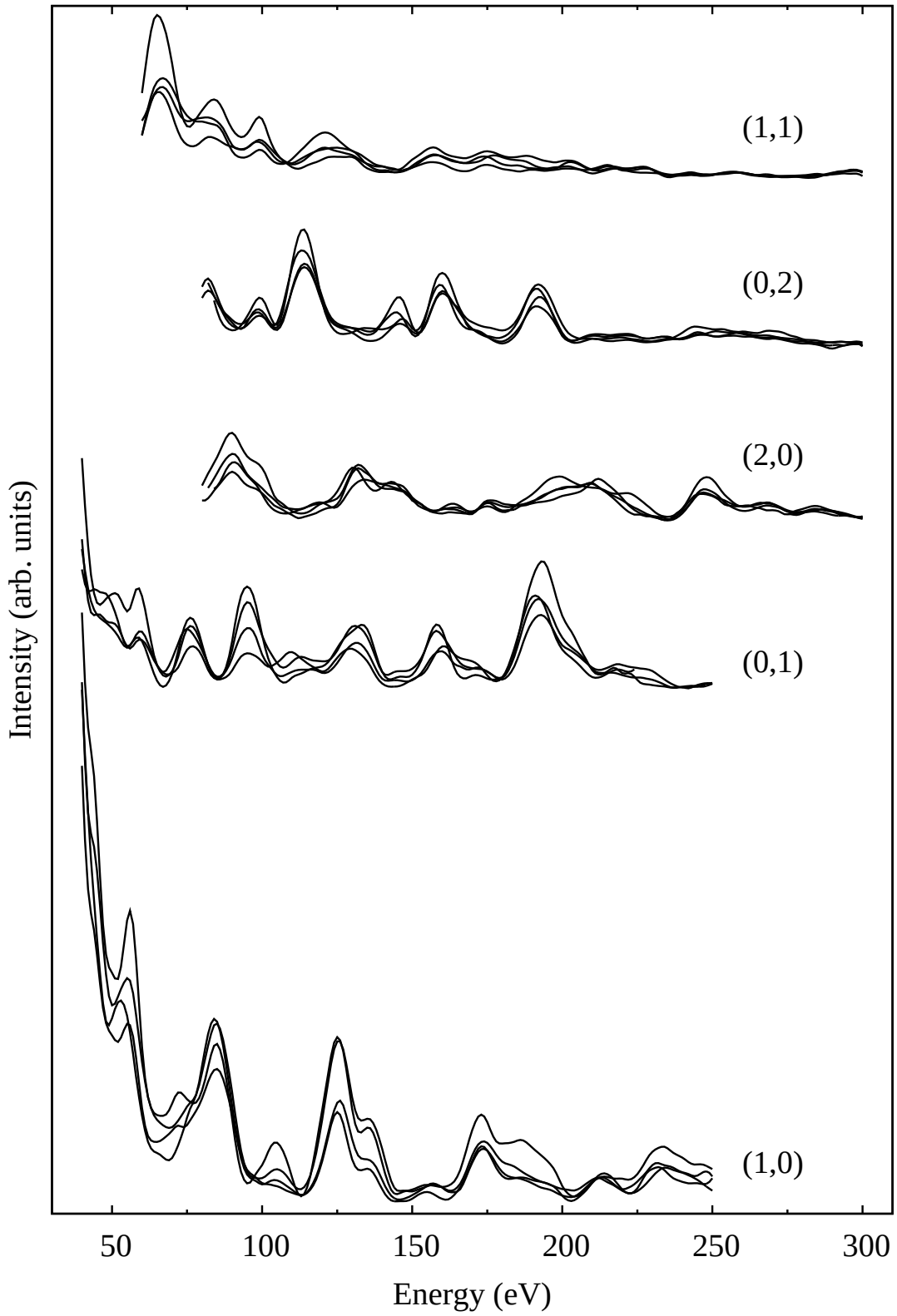

Figure 5.2: Experimental LEED I-V curves for the 1×1 surface formed by Ho on Si(111)-1×1-Fe for all five degenerate spot groups. For a given spot group experiments performed on different days starting from a clean substrate are compared.

Iron on the Si(111)-1×1-Ho Surface

One monolayer of holmium was deposited from a pre-calibrated source onto the clean Si(111)-7×7 substrate which was not held at an elevated temperature. The sample was annealed at ≈ 400°C for 15 minutes. A sharp 1×1 LEED pattern resulted with a low background intensity (see figure 5.8). 1ML of iron was then deposited onto this surface which was then annealed at ≈ 400°C for 15 minutes. A 1×1 LEED pattern resulted and images of this are shown in figure 5.3. During some experiments it was necessary to repeat the latter anneal in order to sharpen the 1×1 LEED pattern.

Images of this diffraction pattern were acquired over a 40-300 eV range of primary electron energies in steps of 2 eV using a CCD camera and stored on an instrument dedicated computer. For each spot in the LEED pattern the variation in its intensity with primary electron energy was recorded which resulted in a set of 17 I-V curves. Degenerate beams were averaged together to reduce the signal to noise ratio and also to reduce any small errors that may have occurred in setting up normal beam incidence.

The experiment was repeated several times and the I-V curves obtained during different experiments are shown in figure 5.4. These curves were compared using the Pendry R-factor [93] and these R-factors are shown in table 5.2. These interrun R-factors are not as low as we would expect for an experiment-experiment comparison if the surface was repeatedly preperable. This would suggest that although it is possible to repeatedly prepare a similar surface there is some variability in the surface structure. This is usually indicative of disorder and/or variable domains on the surface. To further reduce noise the I-V curves from three separate experiments were averaged together and a three point smooth was applied.

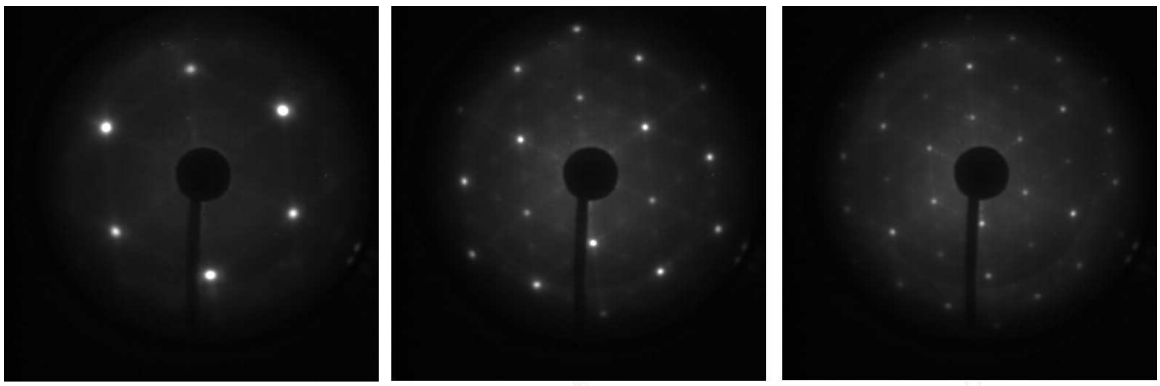

Figure 5.3: Experimental LEED spot pattern formed by Fe on the Si(111)-1×1-Ho surface shown at (a) 40 eV and (b) 80 eV and (c) 150 eV.

LEED Spot	Range of interrun R-factors
(1,0)	0.20 - 0.28
(0,1)	0.18 - 0.36
(2,0)	0.22 - 0.39
(0,2)	0.23 - 0.41
(1,1)	0.40 - 0.53

Table 5.2: The range of interrun R-factors for each spot in the 1×1 LEED pattern of the surface formed by Fe on Si(111)-1×1-Ho.

Comparison of averaged data

When iron is deposited onto the Si(111) surface it forms ordered regions with a 1×1 periodicity with respect to the substrate as evidenced by the 1×1 LEED pattern. When holmium is deposited atop this Si(111)-1×1-Fe surface a 1×1 LEED pattern is again evident after annealing and this surface appears to posses slight variability in its composition as evidenced by the interrun R-factors. The same behaviour occurs when it is holmium that is deposited first and followed by iron. Figure 5.5 compares the averaged LEED I-V curves for Fe on Si(111)-1×1-Ho and Ho on Si(111)-1×1-Fe. The R-factors indicate that there is a good degree of similarity between the two structures that have been formed in reverse order to one another.

One can imagine two scenarios for the type of surface that might be responsible for the similar 1×1 LEED pattern that results in both cases. The first scenario is that there is a previously unseen reconstruction in which holmium and iron mix evenly to form a reasonably well ordered phase. The second scenario is that there are domains of Si(111)-1×1-Fe or Si(111)-1×1-Ho or both upon the surface and that these are responsible for the 1×1 reconstruction. The latter possibility must be investigated before the former possibility can be considered.

To that end I-V curves for the Si(111)-1×1-Fe surface and the Si(111)-1×1-Ho surface are required. In the next two subsections experimental efforts to obtain these are reported.

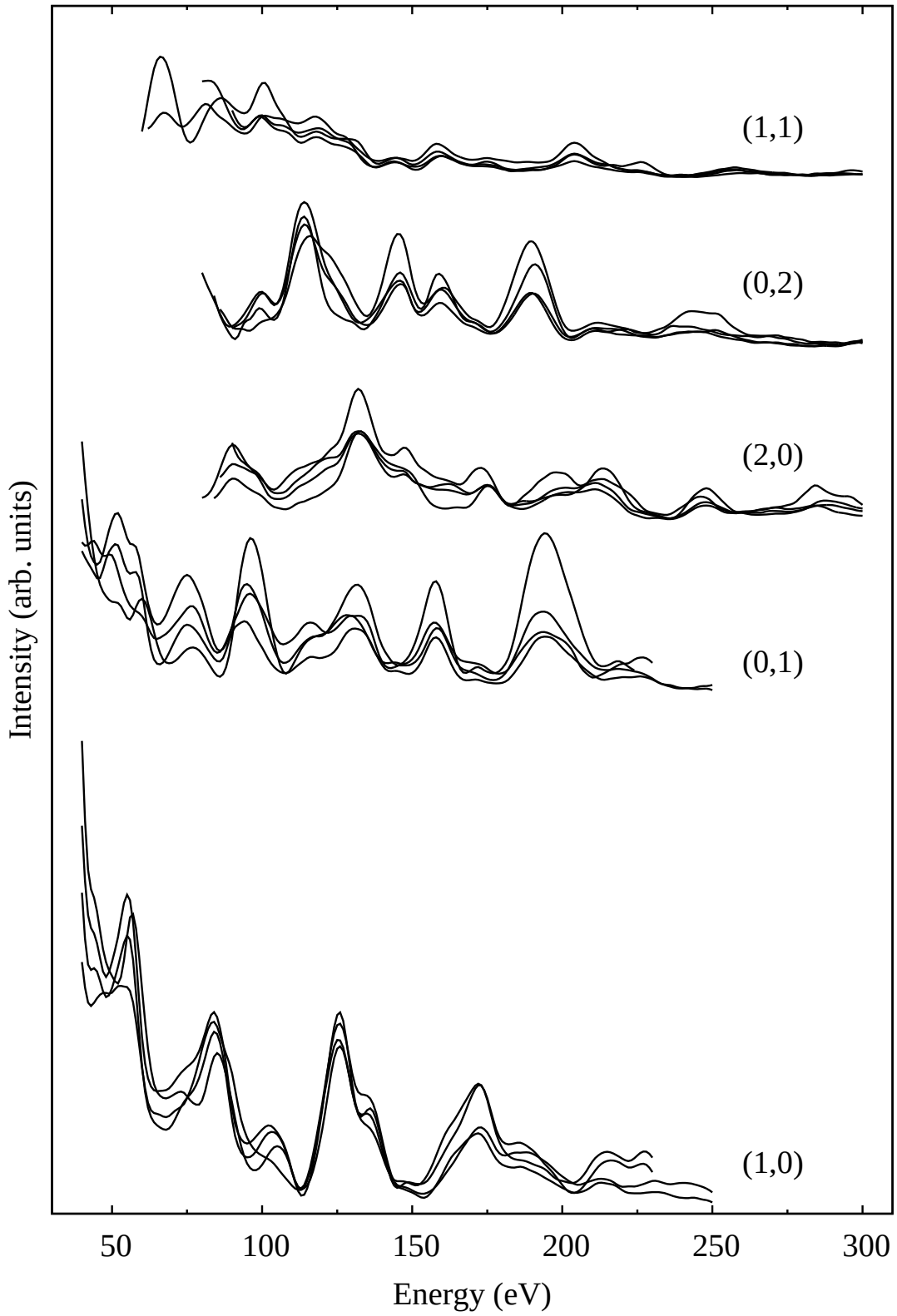

Figure 5.4: Experimental LEED I-V curves for the 1×1 surface formed by Fe on Si(111)-1×1-Ho for all five degenerate spot groups. For a given spot group experiments performed on different days starting from a clean substrate are compared.

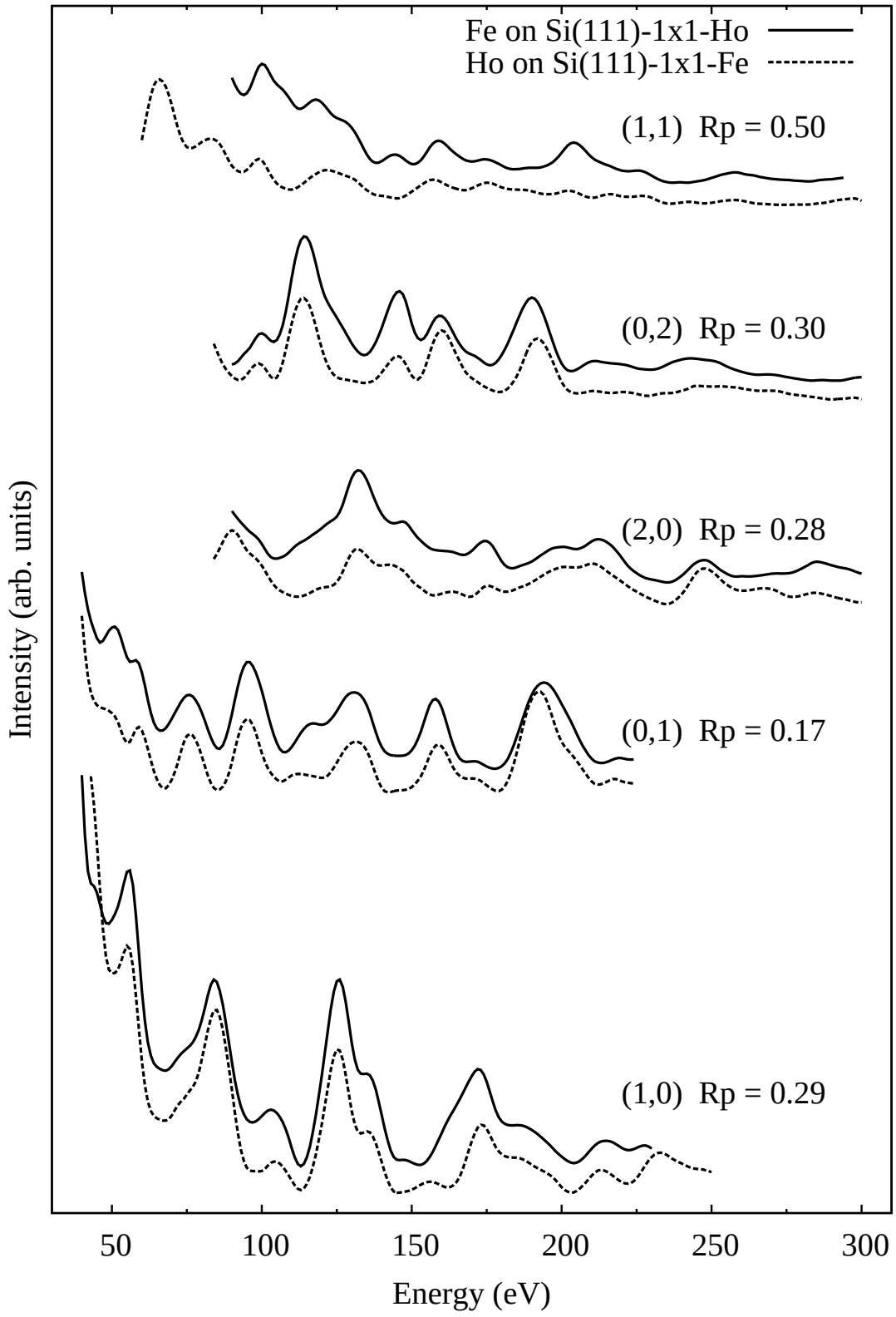

Figure 5.5: A comparison of the averaged experimental LEED I-V curves for the surface formed by Fe on Si(111)-1×1-Ho with those for the surface formed by Ho on Si(111)-1×1-Fe. The R-factor beside each curve indicates the level of agreement.

I-V curves for the Si(111)-1x1-Fe surface

The preparation conditions for the Si(111)-1×1-Fe surface have been described in the subsection concerning Ho on Si(111)-1×1-Fe. Images of the diffuse 1×1 LEED pattern produced by this surface are shown in figure 5.6. A full set of images of this diffraction pattern were acquired and the 17 I-V curves were produced and deegerate beams were averaged together.

The experiment was repeated several times and the I-V curves obtained during different experiments are shown in figure 5.7. The interrun R-factors are shown in table 5.3. Although these are a little high they are consistently better than those for the Fe on Si(111)-1×1-Ho surface and the Ho on Si(111)-1×1-Fe surface. On the other hand the background intensity in the LEED patterns for the Si(111)-1×1-Fe surface is higher than that in the surfaces with two metal adsorbates. This would suggest that there is more disorder upon the Si(111)-1×1-Fe surface but that the structure that is responsible for the spots in the LEED pattern is more consistent across runs. The I-V curves from three separate experiments were averaged together and a three point smooth was applied.

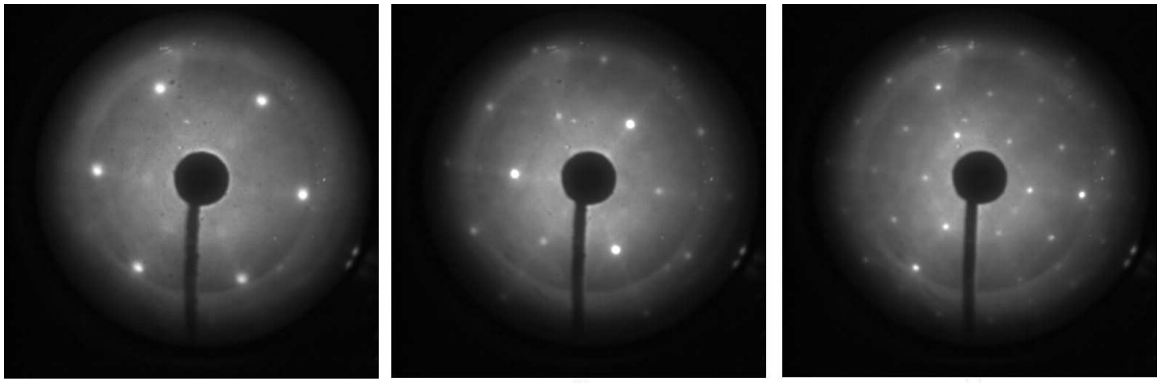

Figure 5.6: Experimental LEED spot pattern for the Si(111)-1×1-Fe surface shown at (a) 40 eV and (b) 80 eV and (c) 150 eV.

LEED Spot	Range of interrun R-factors
(1,0)	0.08 - 0.13
(0,1)	0.12 - 0.28
(2,0)	0.28 - 0.37
(0,2)	0.09 - 0.21
(1,1)	0.27 - 0.40

Table 5.3: The range of interrun R-factors for each spot in the 1×1 LEED pattern of the Si(111)-1×1-Fe surface.

I-V curves for the Si(111)-1x1 Ho surface

The preparation conditions for the Si(111)-1×1-Ho surface have been described in the subsection concerning Fe on Si(111)-1×1-Ho. Images of the clean and sharp 1×1 LEED pattern produced by this surface are shown in figure 5.8. A full set of images of this diffraction pattern were acquired and the 17 I-V curves were produced and degenerate beams were averaged together.

The experiment was repeated several times and the I-V curves obtained during different experiments are shown in figure 5.9. The interrun R-factors (shown in table 5.4) indicate that this surface is well ordered and repeatedly preparable. To further reduce noise the I-V curves from three separate experiments were averaged together and a three point smooth was applied.

LEED Spot	Range of interrun R-factors
(1,0)	0.09 - 0.17
(0,1)	0.07 - 0.15
(2,0)	0.07 - 0.18
(0,2)	0.05 - 0.31
(1,1)	0.07 - 0.17

Table 5.4: The range of interrun R-factors for each spot in the 1×1 LEED pattern of the Si(111)-1×1-Ho surface.

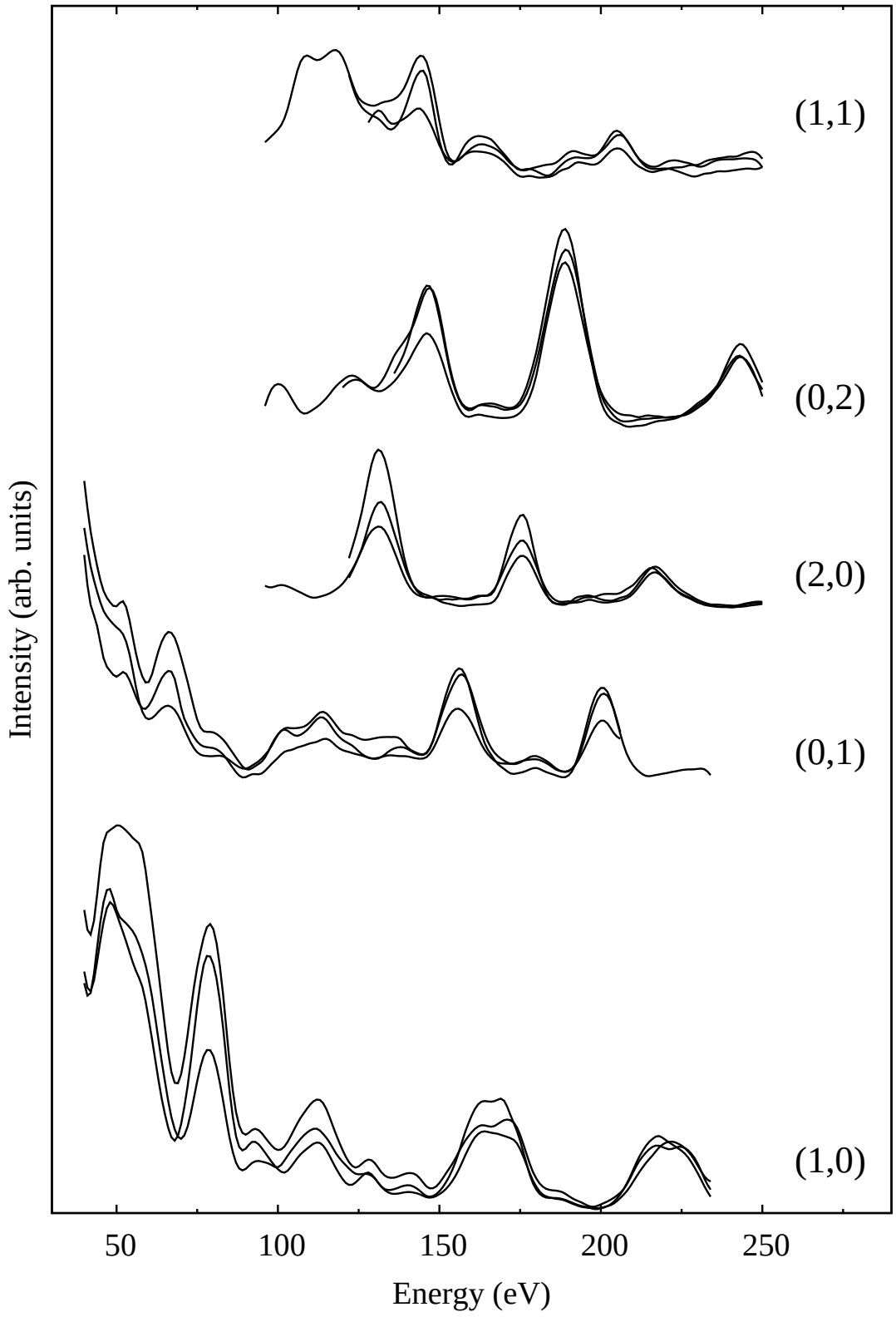

Figure 5.7: Experimental LEED I-V curves for the Si(111)-1×1-Fe for all five degenerate spot groups. For a given spot group experiments performed on different days starting from a clean substrate are compared.

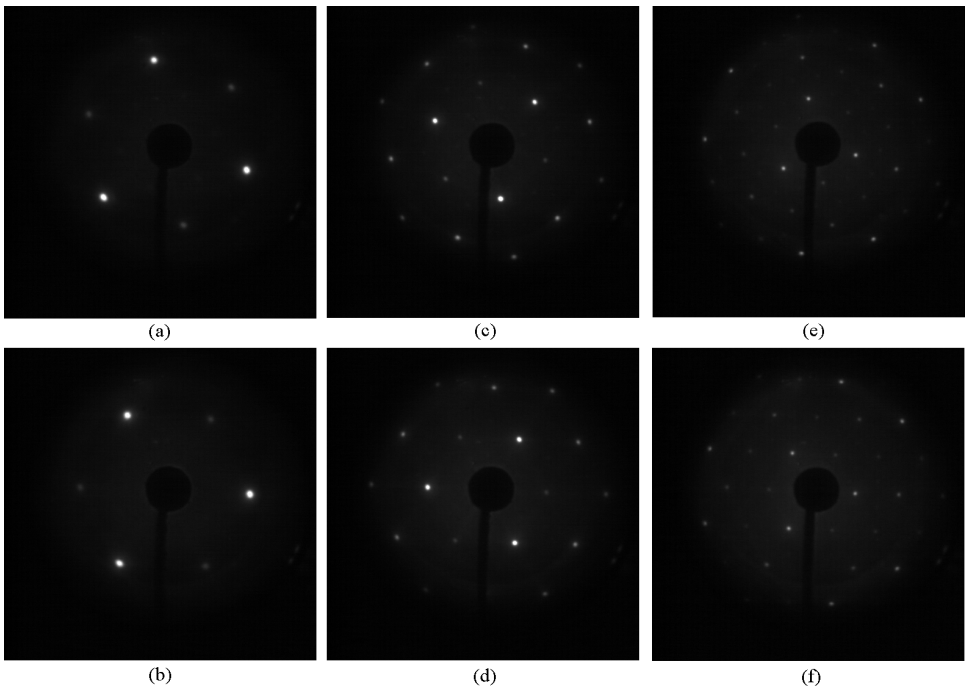

Figure 5.8: Experimental LEED spot pattern for the Si(111)-1×1-Ho surface shown at (a), (b) 40 eV and (c), (d) 80 eV and (e), (f) 150 eV for two separate experiments.

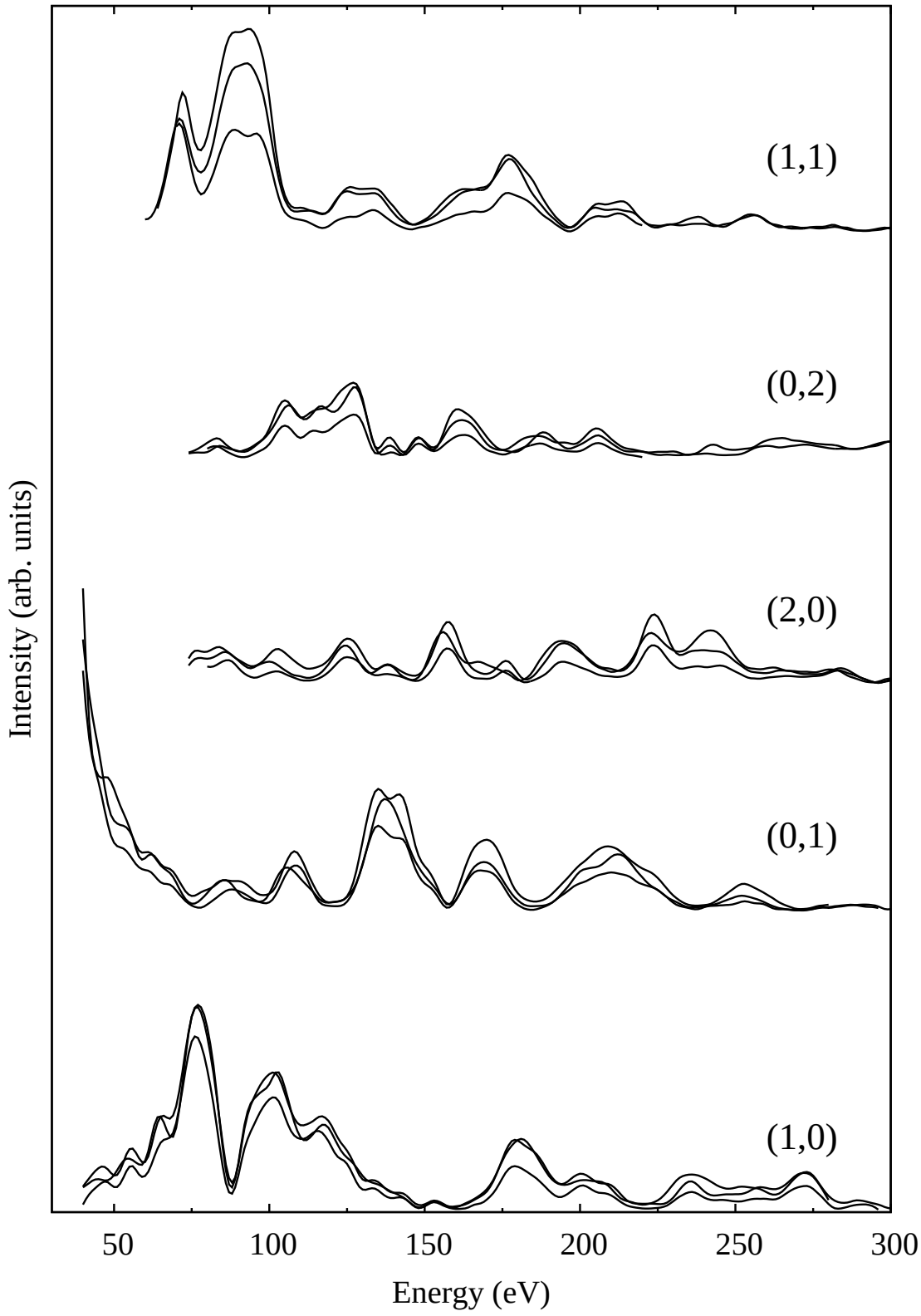

Figure 5.9: Experimental LEED I-V curves for the Si(111)-1×1-Ho for all five degenerate spot groups. For a given spot group experiments performed on different days starting from a clean substrate are compared.

5.2.2 Mixed phase investigation

Figures 5.10 and 5.11 compare the averaged I-V curves for Si(111)-1×1-Fe and Si(111)-1×1-Ho with those for the composite surfaces. There are some features of both structures that are visible in the I-V curves for the composite surfaces. This would suggest that an overlaid LEED pattern from separate domains of the two structures might be responsible for the composite I-V curves. To quantify this a comparison of a linear combination of these two sets of I-V curves has been compared against those for the composite surfaces.

For each spot in the LEED pattern the intensities from the I-V curves obtained for the Si(111)-1×1-Ho and the Si(111)-1×1-Fe structures have been combined in various ratios. The addition of the intensities is a means of simulating large and separate domains of the two structures. If the real surface is comprised of a random arrangement of small domains of the two structures then the amplitudes of the scattered electrons might coherently combine and cause the resulting I-V curves to be different to those that are obtained from the addition of intensities. Figure 5.12 shows a series of plots in which the Pendry R-factor has been obtained when the I-V curves from Si(111)-1×1-Ho and Si(111)-1×1-Fe are combined in various ratios for each LEED spot and compared with the composite surfaces.

The first observation is that there is no unique ratio for which there is a minimum in the R-factor for all of the spots. Some spots suggest an Fe rich surface and other spots suggest the opposite. It could be that for some spots features from the I-V curves from the Fe rich surface dominate and give good agreement with those for the composite surface and for other spots it is features from the I-V curves from the Ho rich surface that dominate. A visual inspection of the I-V curves for the four structures shows that there are some features in the I-V curves of the composite structures that are not present in either set of curves for the single deposit surfaces. This would suggest either that the structure of the single deposit surfaces has been modified when they form the composite surface or that there is a 1×1 phase present that has not yet been considered.

For the Fe on Si(111)-1×1-Ho surface the minimum R-factors for a comparison with the composite surface range from around 0.2 - 0.6 but for three out of the five spots they have a value of around 0.4. These are comparable with the interrun R-factors for both of the multideposit surfaces. This indicates that the best fit composite structures for each spot are a reasonable match with the averaged experimental data with its inherent variability. This is not by any means conclusive proof that this surface is a composite of the Si(111)-1×1-Ho and/or the Si(111)-1×1-Fe surfaces in a pure or modified form. The Ho on Si(111)-1×1-Fe surface shows similar behaviour to that of its sister composite surface but the minima are less well defined and the R-factors are higher.

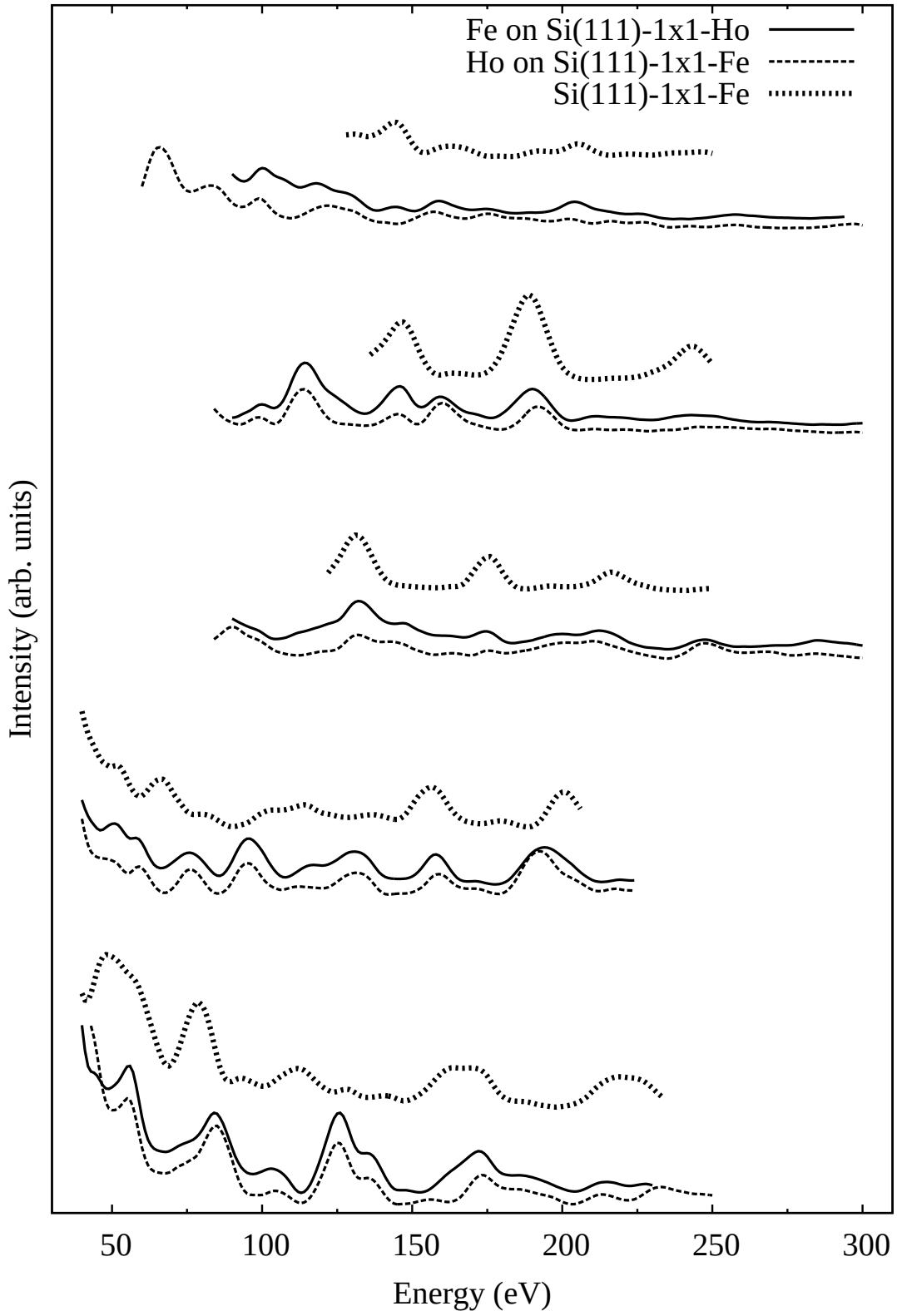

Figure 5.10: A comparison of the averaged experimental LEED I-V curves for the Si(111)-1×1-Fe surface with those for the surface formed by Fe on Si(111)-1×1-Ho and the surface formed by Ho on Si(111)-1×1-Fe.

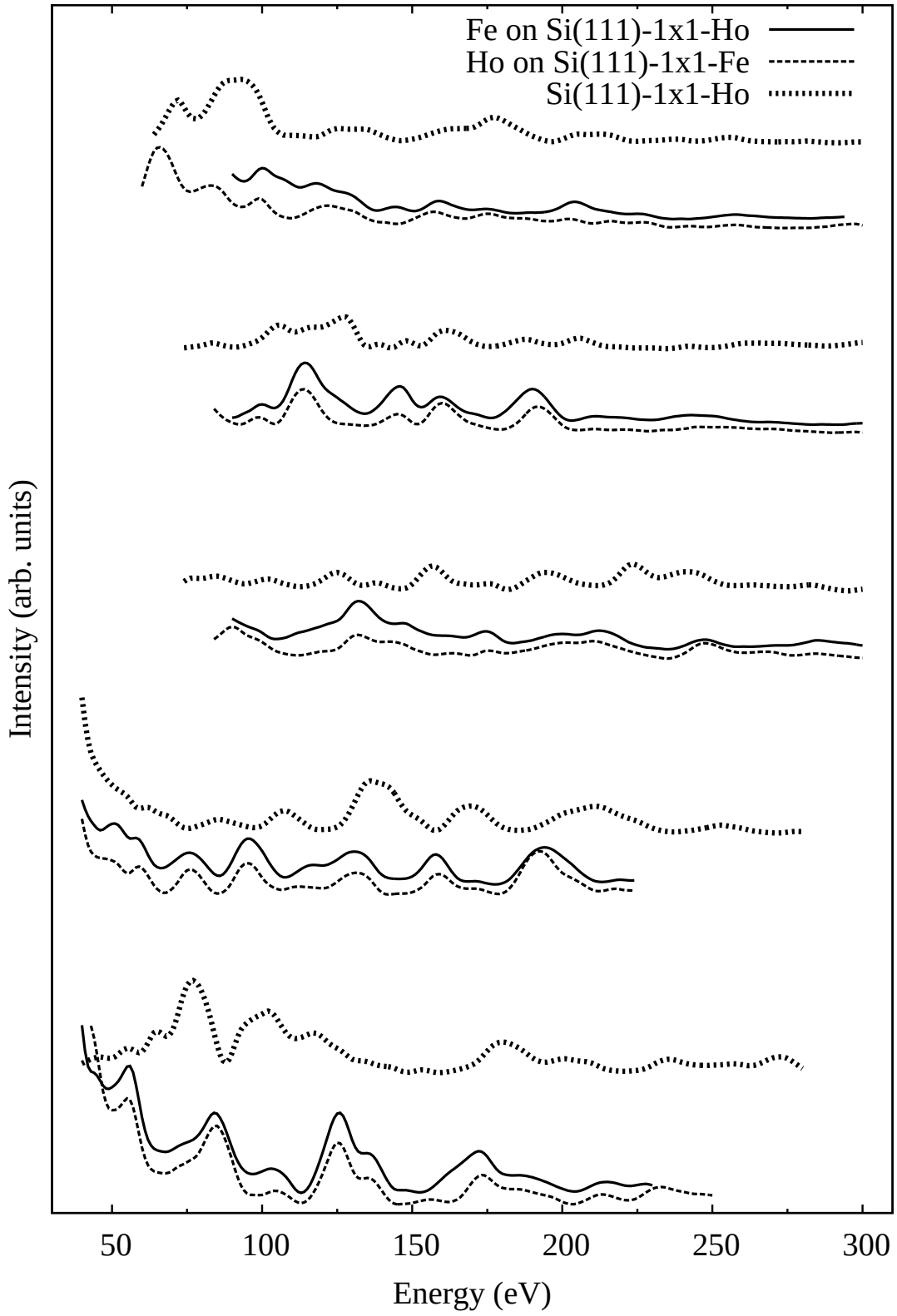

Figure 5.11: A comparison of the averaged experimental LEED I-V curves for the Si(111)-1×1-Ho surface with those for the surface formed by Fe on Si(111)-1×1-Ho and the surface formed by Ho on Si(111)-1×1-Fe.

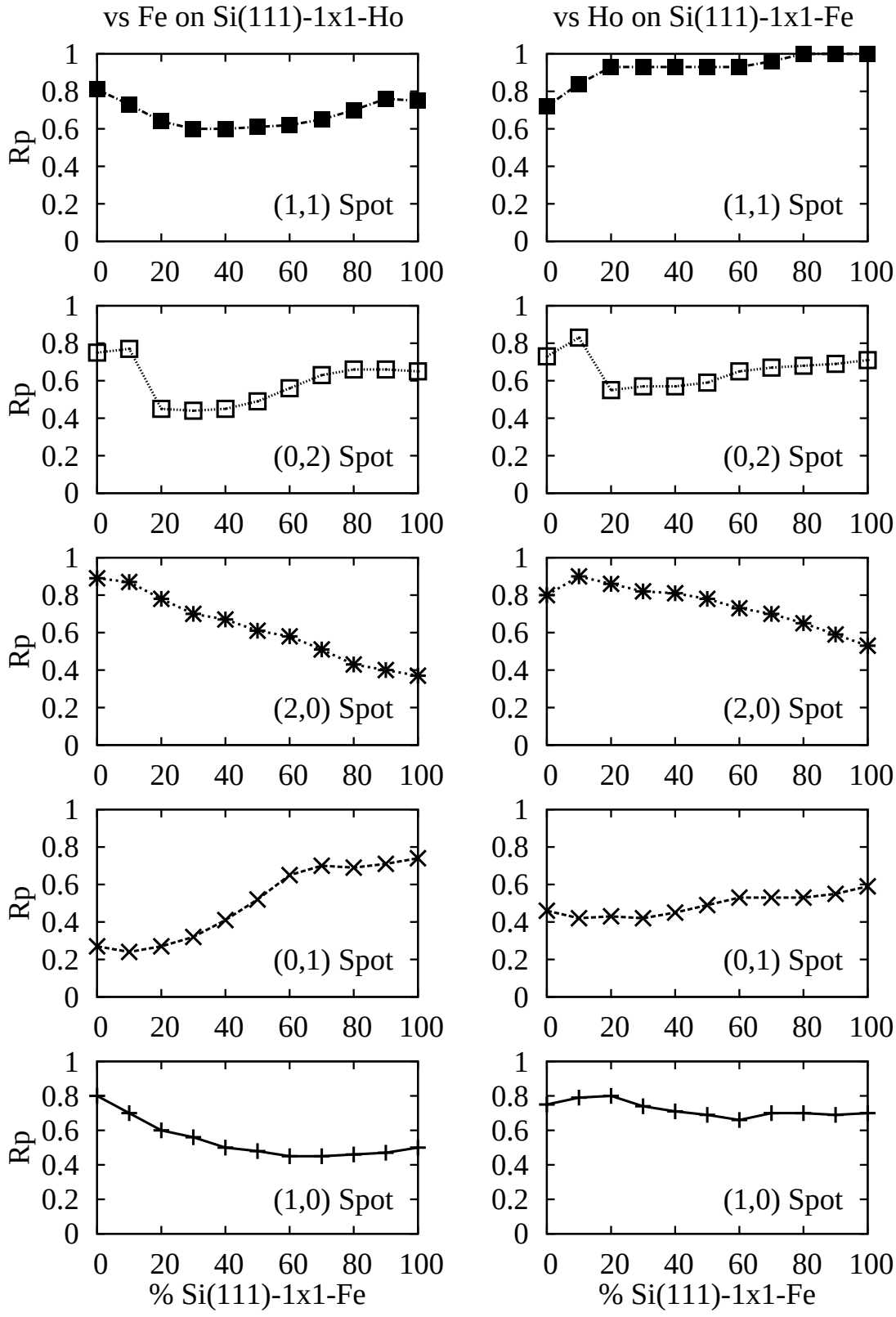

Figure 5.12: Pendry R-factors for linear combinations of the Si(111)-1×1-Fe and Si(111)-1×1-Ho experimental I-V curves when compared with (left) the averaged experimental LEED I-V curves for the Fe on Si(111)-1×1-Ho surface and (right) the averaged experimental LEED I-V curves for the Ho on Si(111)-1×1-Fe surface.

Higher coverage of Fe on Si(111)-1×1-Ho

Several experiments were performed in which the Fe on Si(111)-1×1-Ho surface was prepared with an increased coverage of Fe, namely 1.5 ML. The other preparation conditions were unchanged. A 1×1 LEED pattern was again observed 5.13 that is similar in quality to that produced when just 1 ML of Fe is used (see figure 5.3). I-V curves were again obtained from separate experiment runs and these are compared in figure 5.14 and the interrun R-factors are shown in table 5.5 below. There is again variability in the structure formed during separate experiments and the interrun R-factors are slightly higher than those for the 1 ML Fe on Si(111)-1×1-Ho surface. The I-V curves for the separate runs have been averaged and these are compared with those for the 1 ML Fe on Si(111)-1×1-Ho surface and the Ho on Si(111)-1×1-Fe surface in figure 5.14. The surface formed when 1.5 ML of Fe is deposited on Si(111)-1×1-Ho produces essentially the same I-V curves as when just 1 ML of Fe is deposited.

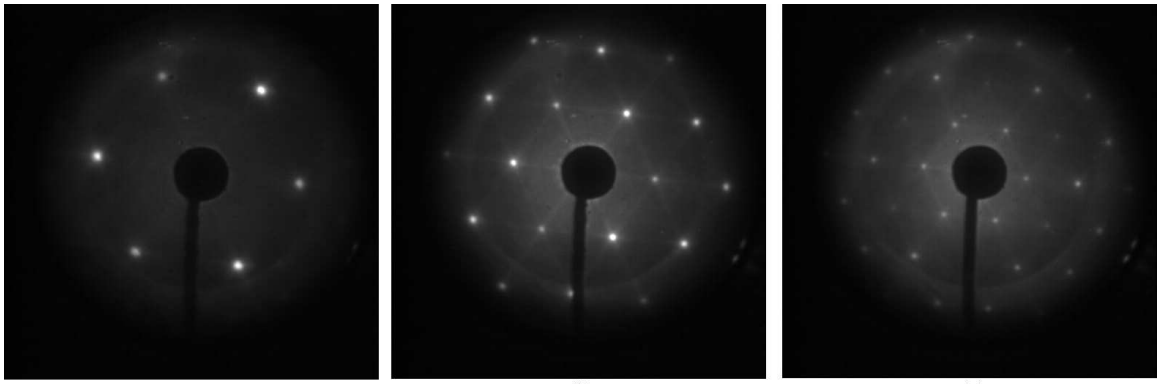

Figure 5.13: Experimental LEED spot pattern for the Si(111)-1×1-Ho surface shown at (a), (b) 40 eV and (c), (d) 80 eV and (e), (f) 150 eV for two separate experiments.

LEED Spot	Range of interrun R-factors
(1,0)	0.17 - 0.46
(0,1)	0.21 - 0.51
(2,0)	0.34 - 0.58
(0,2)	0.38 - 0.57
(1,1)	0.42 - 0.61

Table 5.5: The range of interrun R-factors for each spot in the 1×1 LEED pattern of the surface formed by 1.5 ML of Fe on Si(111)-1×1-Ho.

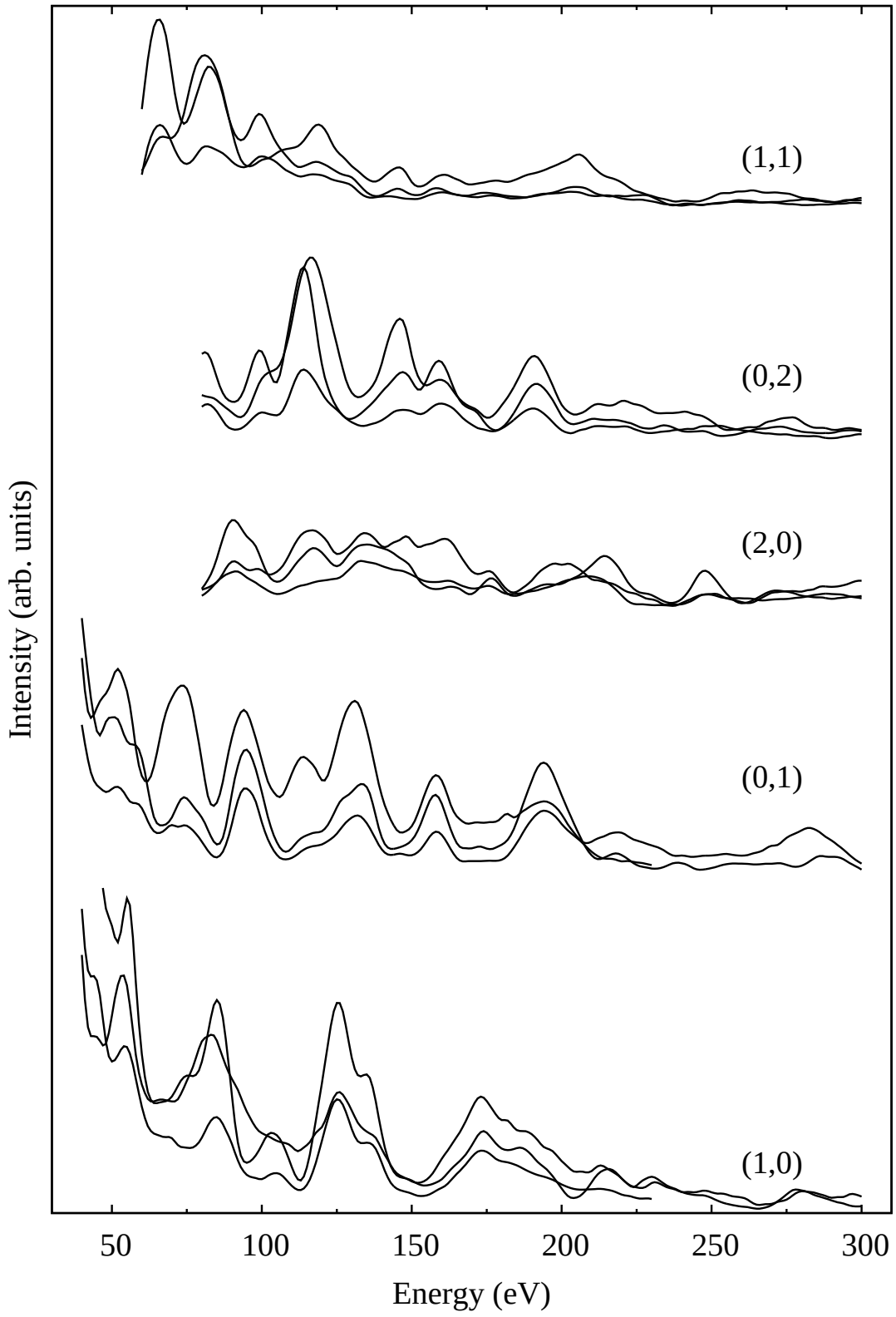

Figure 5.14: Experimental LEED I-V curves for the surface formed by 1.5 ML of Fe on Si(111)-1×1-Ho for all five degenerate spot groups. For a given spot group experiments performed on different days starting from a clean substrate are compared.

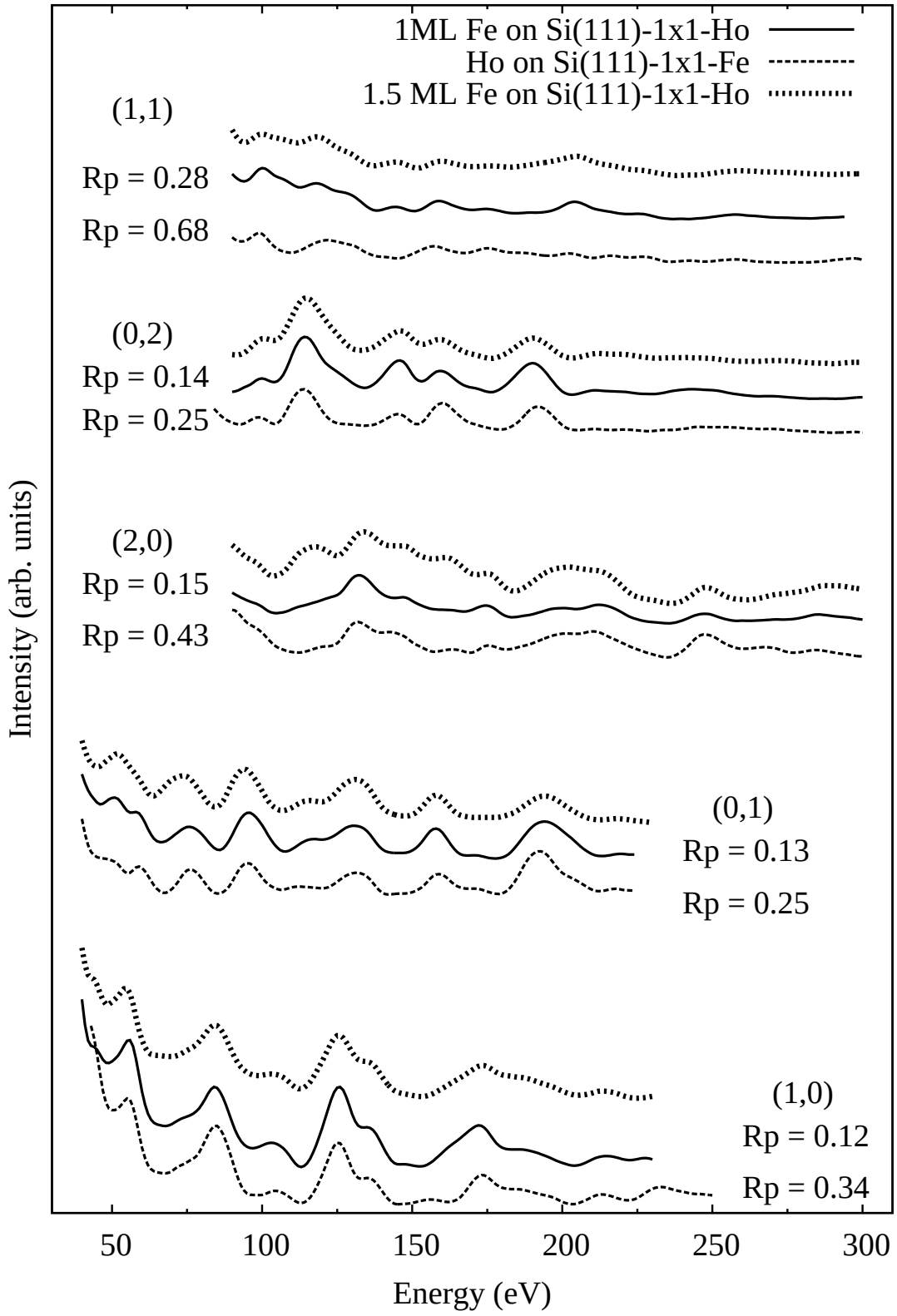

Figure 5.15: A comparison of the averaged experimental LEED I-V curves for the Si(111)-1×1-Ho surface with those for the surface formed by 1.5 ML Fe on Si(111)-1×1-Ho and the surface formed by Ho on Si(111)-1×1-Fe.

5.2.3 STM study of 1ML Fe on Si(111)-1×1-Ho

A cursory STM investigation has been carried out by C. Bonet with the author in attendance. Experiments were performed using the York STM instrument which is an Omicron Nanotechnology GmbH microscope that operates at a typical UHV base pressure of $\leq 2 \times 10^{-10}$ mbar. Samples were prepared using a similar method to that used in the LEED experiments. The principal difference is that direct current is used to heat the samples whereas in the LEED system electron beam heating is used. Holmium was first deposited and annealed into an ordered 1×1 structure. 1ML of Fe was then deposited atop this surface and several annealing cycles were carried out at increasing temperature until a 1×1 LEED pattern resulted and until this pattern became sharp. Figure 5.16 shows two STM images of this surface.

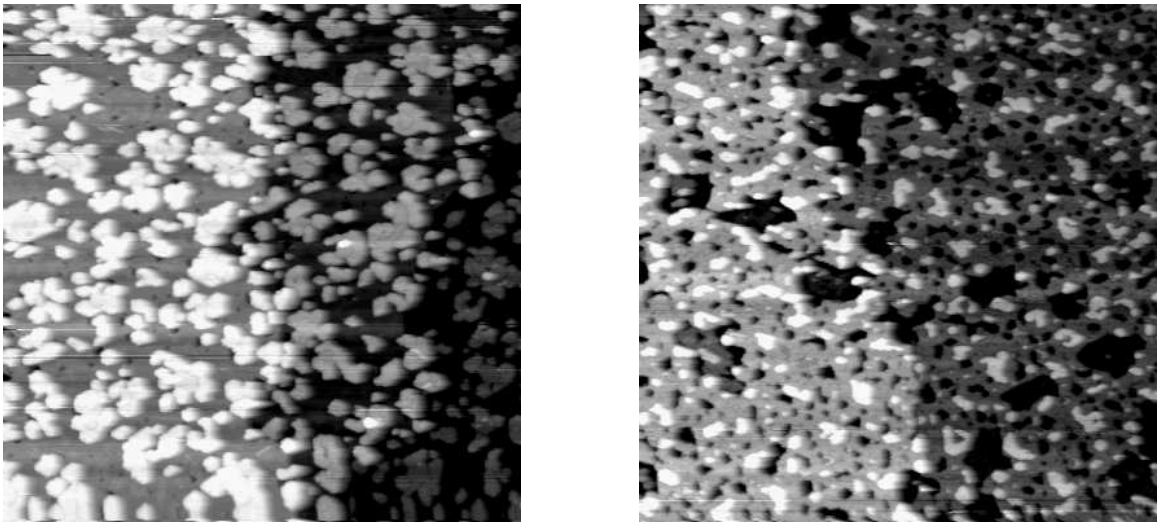

(a) (b)

Figure 5.16: Two 200 × 200 nm^2 STM images of the surface formed by 1ML of Fe on Si(111)-1×1-Ho taken during different experiments.

Islands of some material (presumably iron) have formed atop a 1×1 surface. It was not possible to resolve features within these island structures but if they are composed of Fe then this would suggest that these are disordered islands of unreacted Fe. Another feature of note is the difference between the two surface regions observed during different experiments. Subtle differences in the preparation conditions would seem to have conspired to produce smaller islands and a more pitted underlying 1×1 layer. The difference could have been in the annealing conditions but is probably caused by temperature gradients across the sample: figure 5.16(b) could correspond to a hotter part of the sample plate than figure 5.16(a).

5.2.4 Discussion

The structures formed by Fe on Si(111)-1×1-Ho and Ho on Si(111)-1×1-Fe show a great deal of similarity and it is clear that Ho does not form a barrier to prevent the formation of iron silicides and vice-versa. The I-V curves for the composite structures show some common features with those for Si(111)-1×1-Ho and for Si(111)-1×1-Fe which suggests that both are present to some degree in the mixed deposit surface. However, the extra features in the I-V curves for the composite surface show that there is an extra phase present. STM observations show that there are small islands atop a flat 1×1 surface whose composition has not been determined. At higher temperatures there are fewer and smaller islands and the underlying 1×1 surface is pitted.

Given the evidence from LEED and STM one can tentatively suggest that the surface comprises of regions of ordered Si(111)-1×1-Ho and Si(111)-1×1-Fe with unreacted Fe islands sitting atop these. A good degree of intermixing and/or incorporation are expected in order to account for the extra features in the composite I-V curves. Another possibility is that as Fe reacts with the Si(111)-1×1-Ho surface in order to access the substrate silicon the defects and pitting that it creates in this layer cause a distortion of the Si(111)-1×1-Ho structure and a modification of the I-V curves that it produces.

The order of deposition of Fe and Ho would seem to be important in this intermixed/composite phase since the averaged I-V curves for 1.5 ML of Fe on Si(111)-1×1-Ho show much greater similarity with those from 1 ML of Fe on Si(111)-1×1-Ho than with those from 1 ML of Ho on Si(111)-1×1-Fe; as Fe is deposited it is incorporated/mixed into the holmium layer up to some saturation amount above which it sits atop the surface in reacted islands. When the order of deposition is reversed it is holmium that is incorporated/mixed into the Si(111)-1×1-Fe surface to form a similar structure. The difference in the I-V curves might be caused by the relative layer ordering of the two materials.

It was hoped that by intermixing iron with holmium a new ordered phase would result on the Si(111) surface. Some evidence for such an intermixed phase has been found but there remains much to be done to fully characterise this surface. Simultaneous deposition of Fe and Ho onto a hot sample might increase intermixing. A systematic investigation of different relative coverages of the two deposited materials and of the effect of varying the annealing temperatures is needed. The STM experiments reported here need to be expanded upon and an STM investigation into Ho on Si(111)-1×1-Fe and its differences with Ho on Si(111)-1×1-Fe are needed. Auger electron spectroscopy might be able to detect the formation of Fe-Ho bonds as an intermixed phase is formed. Another interesting line of study might be to attempt to form a surface using cobalt and the rare earth silicides.

5.3 Re-evaluation of Si(111)-1×1-Ho

The LEED I-V curves for the Si(111)-1×1-Ho surface that were displayed in the last section show a marked similarity to those obtained by Bonet et al. [37] in a study of Si(111)-1×1-Dy that was made using the LEED chamber at York. Moreover, these experimental curves differ from those obtained for the Si(111)-1×1-Ho surface by Kitayama et al. [36], again using the York LEED instrument. The Pendry R-factor in this latter study was 0.42.

In the rest of this section a new structural fit is obtained for the Si(111)-1×1-Ho surface. The purposes of this are threefold. The structure is to be fitted to the refined experimental data presented earlier in this chapter. The effects of enhanced vibrations are to be included in order to attempt a reduction of the R-factors. Finally, the optimised structural parameters for this surface can be compared against those obtained in the *ab initio* studies of this surface that were discussed in the previous chapter.

5.3.1 LEED I-V Structure fit

Kitayama et al. [36] have used LEED I-V to eliminate many structural models of the Si(111)-1×1-Ho surface. They have shown that this surface adopts a 2D RE silicide structure with the holmium atom located in the T4 site with respect to the underlying substrate and with the top silicon bilayer buckled in the opposite sense to that in the bulk (this structure was discussed in the introductory chapter). A later MEIS study has confirmed the validity of this model structure [32]. This 2D Si(111)-1×1-Ho structure was taken as the model starting structure and the parameters were varied around these values. Four structural parameters were varied; the rumpling amplitude in the top silicon bilayer and the first bulk-like silicon bilayer and the first and second interlayer spacings. These parameters are labelled in figure 1.4 from chapter 1.

LEED I-V curves were calculated using the `CAVLEED` code [87] for each model structure and compared against the experimental data using the Pendry R-factor [93]. A full set of phase shifts were generated for the initial model structure using the `DLPHASE` code [86]. The bulk value of the Debye temperature (T_D) was used for each atomic species (that is $T_D = 645K$ for silicon and $T_D = K$ for samarium) except in the top bilayer and the RE layer, where the vibrations were enhanced by a factor of $\sqrt{2}$. An initial coarse search was first carried out over a wide range of values for each parameter and with a large step size in order to observe a large region of the R-factor landscape. The details of this coarse search are shown in table 5.6.

This coarse search over 8712 different structures produced an R-factor of 0.42 and

Parameter	Range (Å)	Step size (Å)
$R1$	0.54 - 1.08	0.11
$R2$	0.54 - 1.08	0.11
$L1$	2.17 - 2.72	0.05
$L2$	2.17 - 2.72	0.05

Table 5.6: The range of values and the step sizes for each parameter that was varied in the coarse structural fit for the Si(111)-1×1-Ho system.

it identified a clear minimum in the many parameter R-factor landscape. In figure 5.17 the variation in the R-factor with each parameter is plotted with all other parameters being fixed at their optimum values for each case.

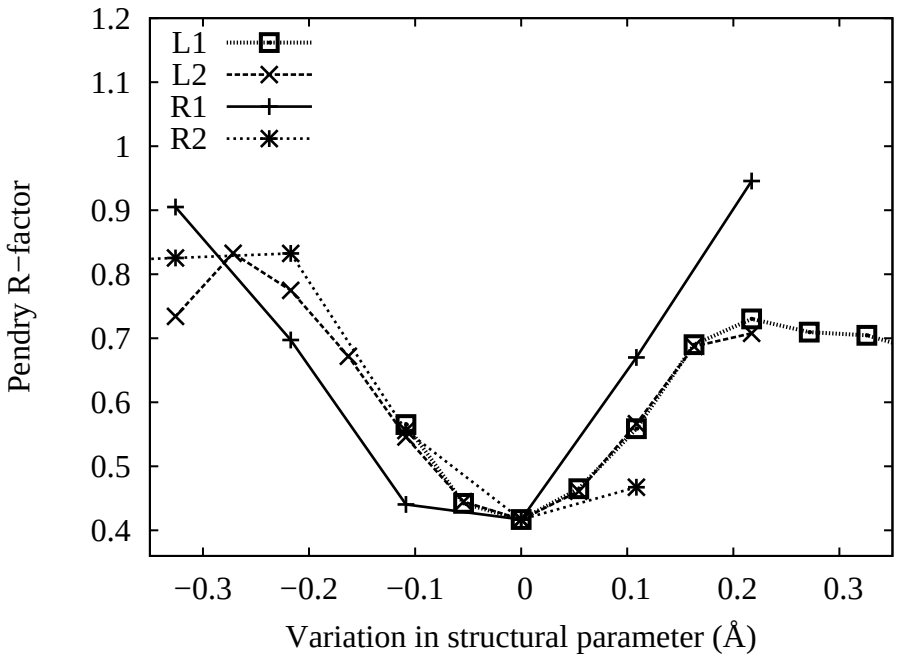

Figure 5.17: The effect upon the r-factor of the variation of each structural parameter in the coarse search. For each curve one parameter only is varied and the other parameters are fixed at their optimum values.

There is a clear minimum for all of the structural parameters and the minima for each independent parameter coincide. The match with experiment is not more sensitive to any particular structural parameter. Having identified the approximate location of the R-factor minimum a fine search was performed over a narrow range of values about this minimum and with small step sizes. The parameters in this search are shown in table 5.7.

This fine search over 13195 different structures produced an R-factor of 0.37. In figure 5.18 the variation in the R-factor with each parameter is plotted with all other

Parameter	Range (Å)	Step size (Å)
$R1$	0.739 - 0.891	0.005
$R2$	0.96 - 1.00	0.01
$L1$	2.22 - 2.35	0.01
$L2$	2.416 - 2.580	0.027

Table 5.7: The range of values and the step sizes for each parameter that was varied in the fine structural fit for the Si(111)-1×1-Ho system.

parameters being fixed at their optimum values for each case. There is again evident a clear minimum for all of the structural parameters and the minima for each independent parameter coincide.

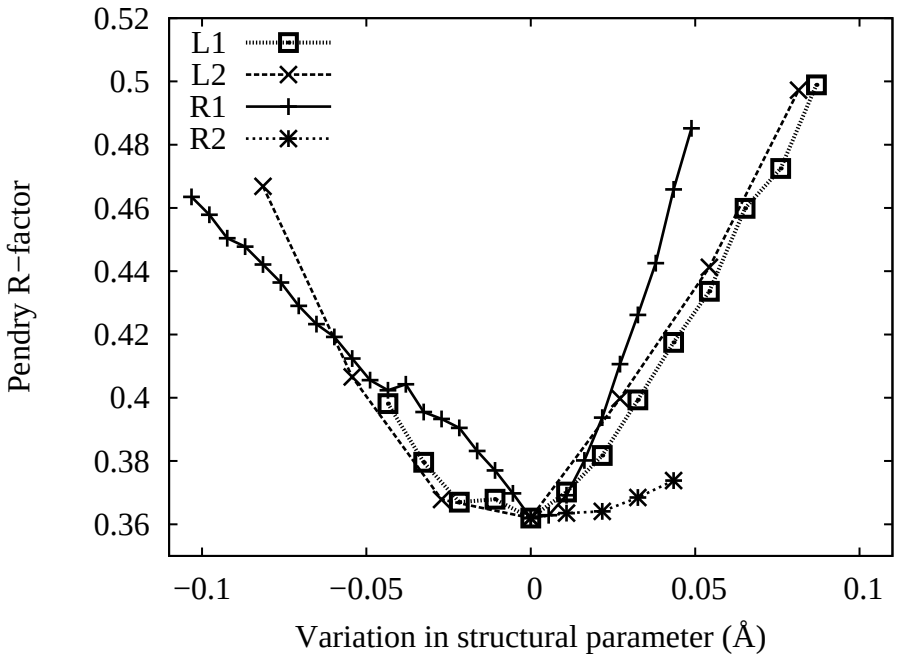

Figure 5.18: The effect upon the r-factor of the variation of each structural parameter in the fine search. For each curve one parameter only is varied and the other parameters are fixed at their optimum values.

Error analysis

The total R-factor is an average over those for the individual spots. The standard error in this R-factor can be used to estimate the error in each of the interlayer spacings. Figure 5.21 shows the variation of the R-factor with the variation of one parameter with the others kept fixed at their optimum valuee. The standard error in the Pendry R-factor has been used to estimate the error in each structural parameter that has been allowed to vary. The results are summarised in table 5.8.

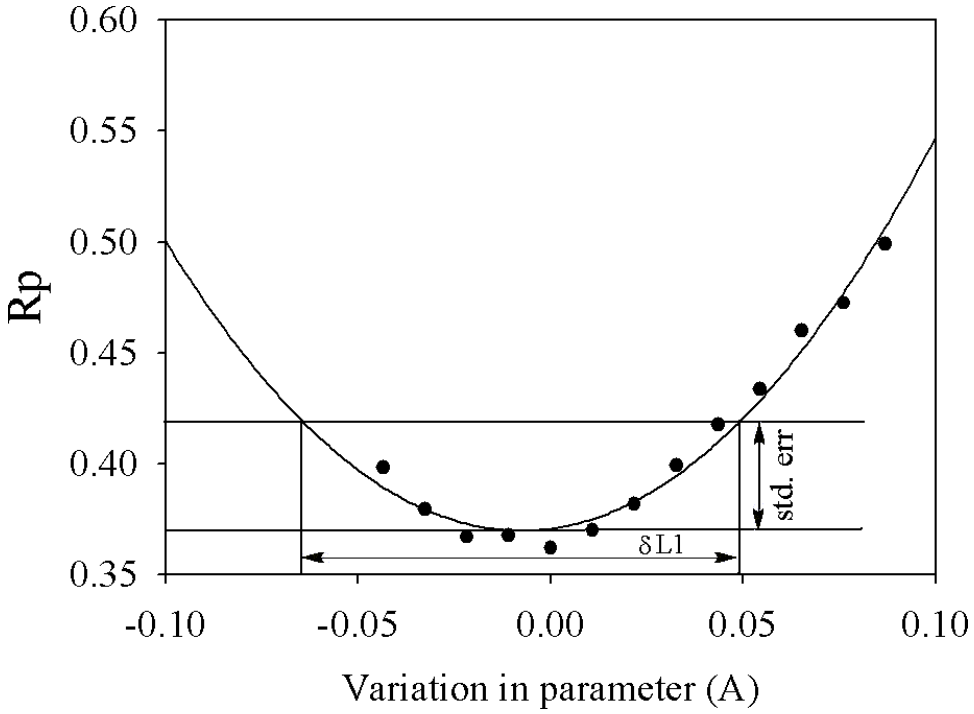

Figure 5.19: Variation of the Pendry R-factor with interlayer spacing 2 showing how the standard error was used to determine the error in the structural parameter.

Parameter	Optimised value (Å)	Error (Å)
$R1$	0.82	± 0.06
$R2$	0.98	± 0.08
$L1$	2.26	± 0.06
$L2$	2.50	± 0.05

Table 5.8: Errors in the four structural parameters that have been optimised for the Si(111)-1×1-Ho system. The method shown in figure 5.21 for interlayer spacing 2 was repeated for each parameter.

5.3.2 Thermal vibrations

The structural parameters that have been varied for the Si(111)-1×1-Ho have yielded a structure that is in good agreement with experiment and the best fit R-factor of 0.37 represents an improvement of the value of 0.42 that was obtained in the previous LEED study by Kitayama et al. [36]. In this previous LEED study the effect of an enhancement of the vibrations beyond their bulk values was not considered. However, in other experimental work the effect of enhanced vibrations has been included to great effect. In the MEIS study of Ge(111)-1×1-Dy by Spence et al. [51] and in the MEIS study of Si(111)-1×1-Y by Wood et al. [34] it was shown that an enhancement of the vibrations in the top two layers by a factor of $\sqrt{2}$ produced an improvement in the fit with experimental data. In a LEED I-V study by Rogero et al. [38] it was shown that if the vibrations in the top layer of Si(111)-1×1-Y are enhanced beyond their bulk values (they do not quote the exact enhancement factor) then there is an improvement of their overall r-factor from 0.46 to 0.21.

These effects have been investigated for the Si(111)-1×1-Ho structure. For the optimal set of structural parameters whose determination has just been described the phase shifts were re-calculated using a range of values for the Debye temperatures in each of the top three layers. These I-V curves, that correspond to every independent combination of available Debye temperatures, were then compared with experiment. The optimal set of Debye temperatures were; top silicon bilayer 258 K, holmium layer 127 K, first silicon bulk like layer 645 K. The Debye temperatures of deeper silicon layers were not enhanced beyond their bulk value of 645 K (the Debye temperature for bulk holmium is 190 K). For these optimal Debye temperatures the effects of the varying the Debye temperature for one layer only at a time is shown in figure 5.20 for each of the top three layers. The optimal Debye temperature for each layer is readily apparent.

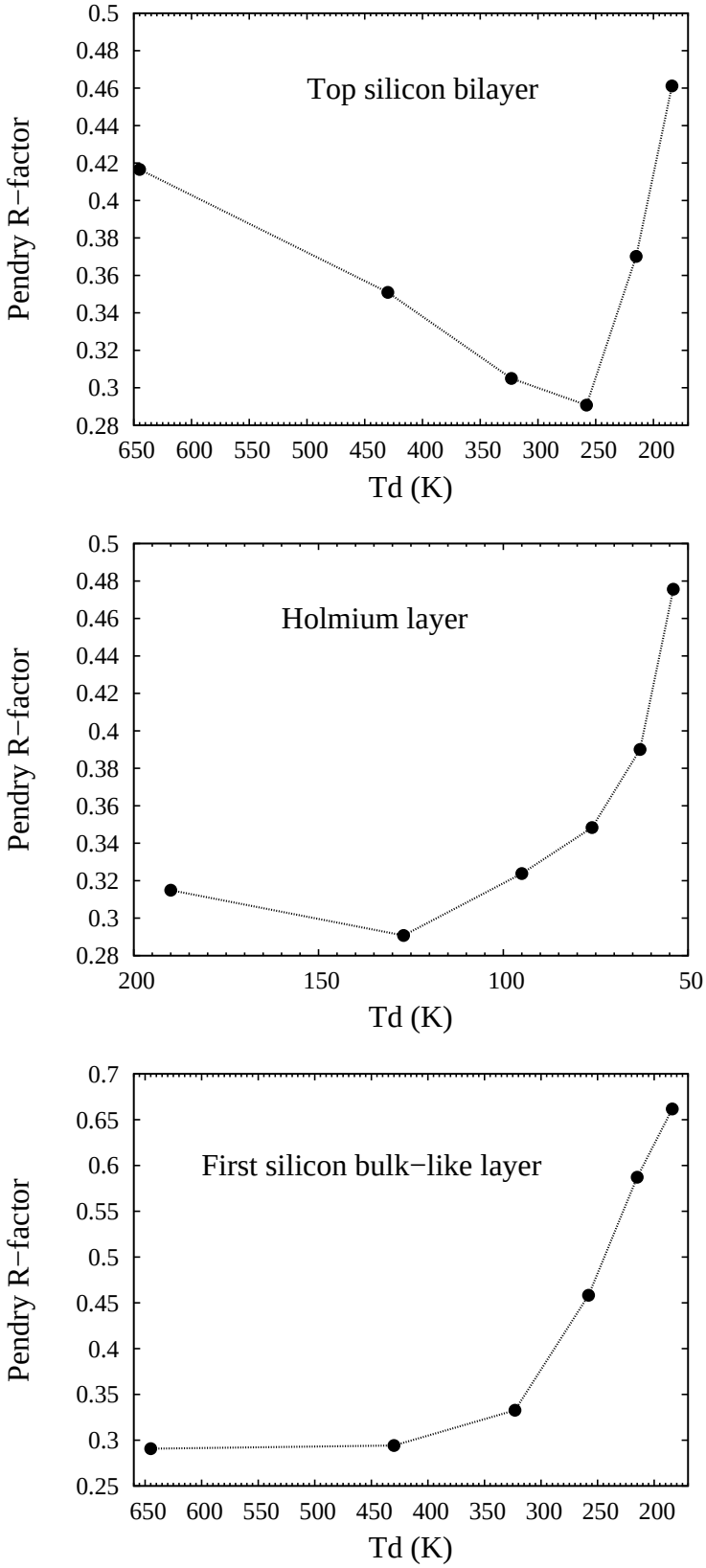

Figure 5.20: Variation of the Pendry R-factor with the Debye temperature for the atomic species in each of the three top layers. The bulk Debye temperatures for silicon and holmium are 645K and 190K respectively.

5.3.3 Comparison of Experimental and Ab-initio Structures.

The final best fit structural parameters are listed in table 5.9 below where they are compared with those obtained in other experimental studies and with the *ab initio* studies in chapter 5 of this work.

	LEED [36]	LEED	MEIS [32]	DFT	SP DFT
R1	0.82	0.82 ± 0.06	0.88 ± 0.03	0.62	
L1	2.29	2.26 ± 0.06	2.24 ± 0.03	2.31	
R2	1.01	0.98 ± 0.08	0.90 ± 0.06	0.88	
L2	2.54	2.50 ± 0.05	2.55 ± 0.06	2.61	
R3	0.78	0.78*	0.78*	0.78	
L3	3.20	3.14*	3.14*	3.16	
Rp	0.37 ± 0.03	0.29 ± 0.02	0.40 ± 0.04	0.85 ± 0.03	0.47 ± 0.05

Table 5.9: Interlayer spacings (L) and rumpling amplitudes (R) in the Si(111)-1×1-Ho system determined by LEED and DFT in this work compared with the results from other studies. The parameters were defined in figure 1.4 in Chapter 1 and those marked with an asterisk have not been optimised.

The Pendry R-factors that are listed in table 5.9 have all been calculated afresh by the author. They represent a comparison with the experimental data described earlier in this chapter and the calculated curves include the optimum set of vibrationally enhanced phase shifts so as to allow a fair comparison of each model in pure structural terms. It is clear that the structural parameters obtained in this work represent a better fit with the experimental data that was also obtained in this work. The r-factor obtained in this study was 0.29 which is a significant improvement over the value of 0.42 obtained in the previous LEED study. The best fit I-V curves that were obtained in this study are shown alongside those obtained by experiment in figure 5.21 overleaf.

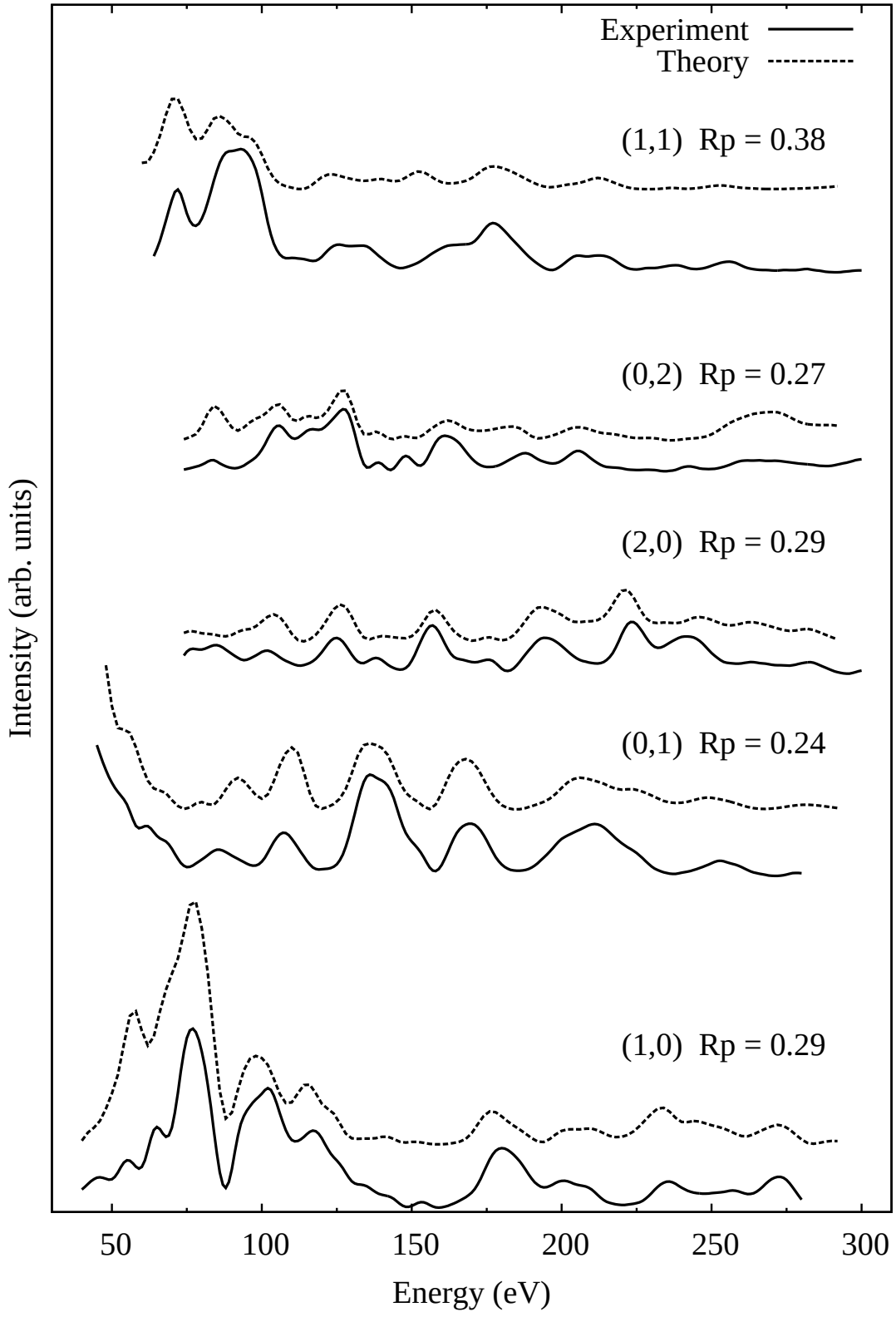

Figure 5.21: Best fit theoretical I-V curves for the five degenerate spots groups in the LEED pattern of Si(111)-1×1-Ho compared with experiment. The effects of enhanced vibrations are included in the calculated curves. The Pendry R-factor that was used to compare each pair of curves is included. The overall R-factor was 0.29 ± 0.02.

5.3.4 Discussion

In summary, the structural parameters of the Si(111)-1×1-Ho system have been refined. Using a fine search technique covering a large range of each structural parameter the Pendry R-factor for the best fit structure of 0.36 ± 0.05 has been obtained. An independent investigation of the vibrational parameters of each of the top three layers has further reduced this R-factor to 0.29 ± 0.03. The third interlayer spacing and rumpling amplitude have not been varied in this study. However, the earlier LEED study and the *ab initio* study in this work both reveal that there is a slight expansion of the third interlayer spacing relative to that in the bulk and it is anticipated that the Pendry R-factor of 0.29 might be improved further. Another potential source of improvement would be a more detailed study of the vibrations within the top few layers using a smaller step size in the Debye temperatures used.

This structure obtained in this work by quantitative LEED has been compared to that obtained in the theoretical work in this thesis and to other experimental studies. The refined structure in this work is a better match to the experimental data obtained in this work than that of the earlier LEED study by Kitayama et al. which was in turn a refinement of the earlier MEIS work by Spence et al. The structure as predicted by density functional theory is a poor match to experiment. The main discrepancy is in the top bilayer rumpling amplitude, to which LEED is very sensitive. It has been shown that there is a significant enhancement of the vibrations in this top layer with respect to those for bulk silicon; the effect of temperature on this top bilayer is very pronounced. The *ab initio* calculation does not take temperature into account and the top bilayer is more flat than the structure obtained at finite temperature in the experiments. We might expect that at finite temperature there is excited a vibrational mode of the top layer in the surface normal direction that increases the mean rumpling amplitude of this bilayer.

Several experimental studies have noted that enhanced vibrations, particularly in the top bilayer, are apparent in the 2D rare earth silicides. There has been no theoretical work to confirm this. A molecular dynamics or a finite displacements phonon study using the geometry optimised structure from this work or from those obtained for other 2D RE silicides by other workers might indicate the effect of finite temperature upon the static structure. Further experiments conducted below room temperature might confirm that the top bilayer becomes flatter if less thermal energy is available to excite vibrational modes.

5.4 Chapter 5 Conclusions

The possibility of growing a mixed phase of holmium and iron atop the Si(111) surface has been investigated. It has been shown that a 1×1 phase is formed by the two materials but that this has a variable composition. Further quantitative LEED I-V studies have not been able to conclusively determine if this phase is a mixed one or if it comprises separate domains of Si(111)-1×1-Ho and Si(111)-1×1-Fe whose structure has been modified. A cursory STM investigation has shown that when Fe is deposited atop Si(111)-1×1-Ho it forms unreacted islands atop a pitted 1×1 phase that has not been identified. The prospect of creating an ordered 1×1 mixed phase on this surface does not appear to be very great based upon the observations made with the preparation conditions used. Other workers might exploit different regimes of growth using different relative amounts of the two deposited materials to obtain more success.

The Si(111)-1×1-Ho structure has been refined using quantitative LEED I-V and a fine parameter search. The structure was fitted to the experimental data obtained in the first half of this chapter. Computational resources have permitted a large number of trial models to be investigated and the degree of agreement with experiment has been improved over that obtained in previous attempts using MEIS and LEED. Following suggestions by other workers in the literature the effect of thermal vibrations upon the R-factors has been investigated. Enhancement of the vibrations in the top layer by a factor of 2.5 and the vibrations of the holmium layer by a factor of 1.5 have improved the level of agreement with experiment. The theoretical work has shown that this structure is stable and the structural parameters obtained are in reasonable agreement with experiment. The major discrepancy is in the top bilayer rumpling amplitude and this study has highlighted the need for an investigation of the effects of finite temperature upon the 2D rare earth silicides, particularly in the top layer.

Chapter 6

LEED and ab initio Study of Samarium Silicide on Si(111)

6.1 Introduction

Samarium is of particular interest to spectroscopists since in bulk samarium metal the atoms exhibit a 3^+ valency with a $4f^5(5d^16s^2)$ electron configuration whereas in rarefied environments samarium retains the 2^+ valency of the isolated atom with a $4f^6(6s^2)$ electronic configuration. The energy difference between these two valence states has been estimated at 0.3 eV [133, 134] which suggests that it is energetically inexpensive to change the valency of a samarium atom to accomodate the needs of the local chemical environment. At the elemental metal surface it has been shown that the samarium atoms have a 2^+ valency [133, 135–137] but there have been no structural studies to determine the precise bonding arrangement of the surface atoms.

When samarium is deposited on the (100) surface of silicon at room temperature there is a valence change from around 2.4^+ to around 2.8^+ as the coverage is increased from < 1ML to 5 ML and the valence remains at this saturation value for higher metal coverages [138–140]. The structural phase diagram of samarium on Si(100) has been mapped out as a function of coverage and substrate temperature during deposition by Godowski et al. [141]. They have identified a 3×2 phase at low coverage (<0.25ML) and a 2×1 phase when the coverage is between 0.25 ML and 0.5 ML and they suggest possible structures for these two reconstructions. A recent STM study by Ohbuchi and Nogami [142] has largely confirmed the phase diagram that was generated by LEED. They have described a low coverage (<0.2 ML) 3×2 phase and they show that at higher coverage the 2×1 phase that is visible in LEED is the Si(100) 2×1 substrate in a distorted form in which the top layer dimer atoms form a zigzag chain. At higher coverages they note that the samarium atoms form 3D islands.

On the silicon (111) surface there is also evidence for mixed valency. When $<$ 1ML of samarium is deposited at room temperature it exists in a purely divalent state and as the coverage is increased towards 1 ML a mixed valence state is observed which becomes purely trivalent at coverages $>$ 1ML [143–145]. There is no reaction between samarium and the substrate at this temperature [146] and the valency change has been attributed to the buildup of a disordered samarium overlayer with a bulk-like 3^+ signature.

When samarium is deposited onto a heated ($T \sim 500°C$) Si(111) substrate a series of ordered $n\times2$ phases ($n = 3, 5, 7$) are observed with coverages of $\frac{1}{6}$, $\frac{2}{5}$ and $\frac{3}{7}$ ML respectively and the samarium atoms in these structures have been found to be divalent [145–152]. At a saturation coverage of $\frac{1}{3}$ ML a $\sqrt{3} \times \sqrt{3}\,R30°$ phase is observed and it has been shown that the samarium atoms in this structure are trivalent [145–152]. A 1x1 phase has also been observed by Wigren et al. [150] after growth at $400°C$. They note a high background intensity and large spots in the LEED pattern and they suggest that there are small ordered domains on the surface surrounded by disordered regions.

Of the structures formed by samarium on the Si(111) surface the 3×2 phase has attracted the most interest because it adopts the Honeycomb-Chain Channel (HCC) structure that is common to the reconstructions formed by alkali, alkali-earth and rare-earth metals on the (111) surface of silicon (see §1.2.3 in the introductory chapter). Palmino et al. [151,152] have used qualitative LEED to generate the phase diagram and they have characterised the various phases using STM. They have also used the `VASP` *ab initio* code to geometry optimise the HCC structure for two different configurations with the samarium atom in the T4 and H3 sites and they found that the latter structure was 0.07 eV/Sm atom higher in energy. Theoretical STM images for this structure were then compared with experiment. The bias voltage dependence of features in the surface allowed the isolation of specific features and the theoretical and experimental images are in excellent qualitative agreement. The same group have subsequently used this surface as a template on which to grow Pb nanorods [153].

It has been suggested that the HCC structure is responsible for many reconstructions formed by metal atoms on Si(111) and there is a good deal of indirect and qualitative evidence to support this. A fully quantitative comparison is needed between the structural parameters as suggested by experiment and those offered by the model structure. In this chapter LEED I-V analysis and *ab initio* calculations have been used to quantitatively investigate both the Si(111)-1×1-Sm phase and the Si(111)-3×2-Sm phase. Evidence is presented for a disordered multidomain structure in the 1×1 phase. For the 3×2 phase a full structural fit and an R-factor analysis have been used to quantitatively confirm the validity of the HCC model and to resolve the discrepancy between the 3×2 unit cell and its 3×1 periodicity in reciprocal space.

6.2 Experimental Preparation of Samarium Overlayer Structures

The silicon substrate was cleaned by flashing to $\approx 1200\,^{\circ}\mathrm{C}$ using an electron beam heater and then the sample was slowly cooled through the $\approx 900 - 700\,^{\circ}\mathrm{C}$ region over a period of 15 minutes. All temperatures were monitored using an infra-red pyrometer. The LEED pattern was then checked and a sharp 7×7 LEED pattern was taken as evidence that a clean, well ordered Si(111)-7×7 surface was present.

In the literature other workers [151] have formed the Si(111)-3×2-Sm structure by depositing $\frac{1}{6}$ ML onto a clean silicon sample held at a temperature of around $500\,^{\circ}\mathrm{C}$ followed by annealing at this temperature for 20 minutes. In this work the sample was prepared by depositing 1 ML of Sm from a quartz crystal calibrated evaporation source onto the clean Si(111)-7×7 surface which was not at elevated temperature. The deposition period was about ten minutes. This was followed by annealing at $\approx 500\,^{\circ}\mathrm{C}$ for 15 minutes. A 1×1 LEED pattern was observed and images of this are shown in figure 6.2.

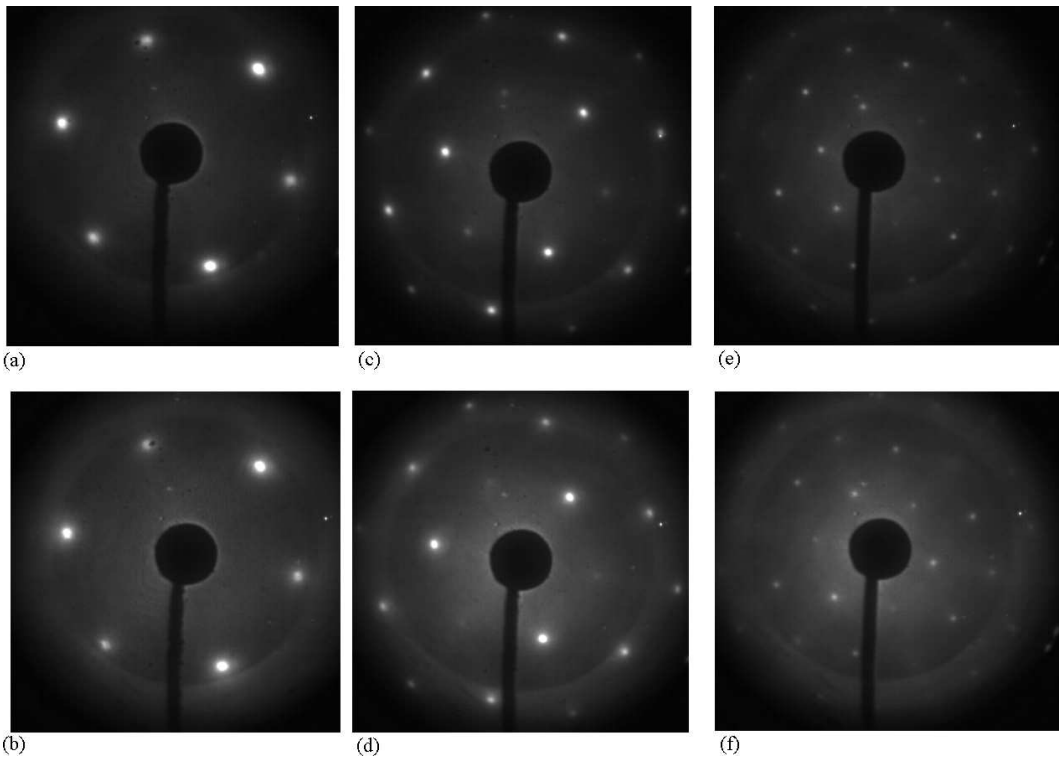

Figure 6.1: Experimental LEED spot pattern for the Si(111)-1×1-Sm surface shown at (a), (b) 40 eV and (c), (d) 80 eV and (e), (f) 150 eV for two separate experiments.

Images of this diffraction pattern were acquired over a 40-300 eV range of primary electron energies in steps of 2 eV using a CCD camera and stored on an instrument dedicated computer. For each spot in the LEED pattern the variation in its intensity with primary electron energy was recorded which resulted in a set of 17 I-V curves. Degenerate beams were averaged together to reduce the signal to noise ratio and also to reduce any small errors that may have occurred in setting up normal beam incidence.

The experiment was repeated several times and the I-V curves obtained during different experiments were compared using the Pendry R-factor [93] (see figure 6.4). Inter-experiment R-factors are in the range from 0.19 for the (0,2) spot to 0.38 for the (1,1) spot. This would suggest that although it is possible to repeatedly prepare a similar surface there is some variability in the surface composition. This is usually indicative of disorder and domains on the surface. To further reduce noise the I-V curves from three separate experiments were averaged together and a three point smooth was applied.

The 1×1 structure was annealed at a higher temperature of $\approx 700\,^{\circ}\mathrm{C}$ for 15 minutes and a sharp 3×1 LEED pattern resulted (see figure 6.2). There is some variability in the annealing temperature that can be used and temperatures in the range $\approx 700 - 900\,^{\circ}\mathrm{C}$ all gave a sharp diffraction pattern. It is at around $1000\,^{\circ}\mathrm{C}$ that the pattern begins to degrade, presumably as the samarium begins to desorb.

Images of this diffraction pattern were acquired over a 40-300 eV range of primary electron energies in steps of 2 eV using a CCD camera and stored on an instrument dedicated computer. For each spot in the LEED pattern the variation in its intensity with primary electron energy was recorded which resulted in a set of 70 I-V curves. Degenerate beams were averaged together to reduce the signal to noise ratio and also to reduce any small errors that may have occurred in setting up normal beam incidence. Figure 6.3 below defines the spot labelling system and the degenerate beams.

The experiment was repeated several times and the I-V curves obtained during different experiments were compared using the Pendry R-factor [93] (see figure 6.5). The R-factor for I-V curves obtained on different days was typically 0.1 or less which indicates that the surface is repeatedly preparable and well ordered. To further reduce noise the I-V curves from three separate experiments were averaged together and a three point smooth was applied.

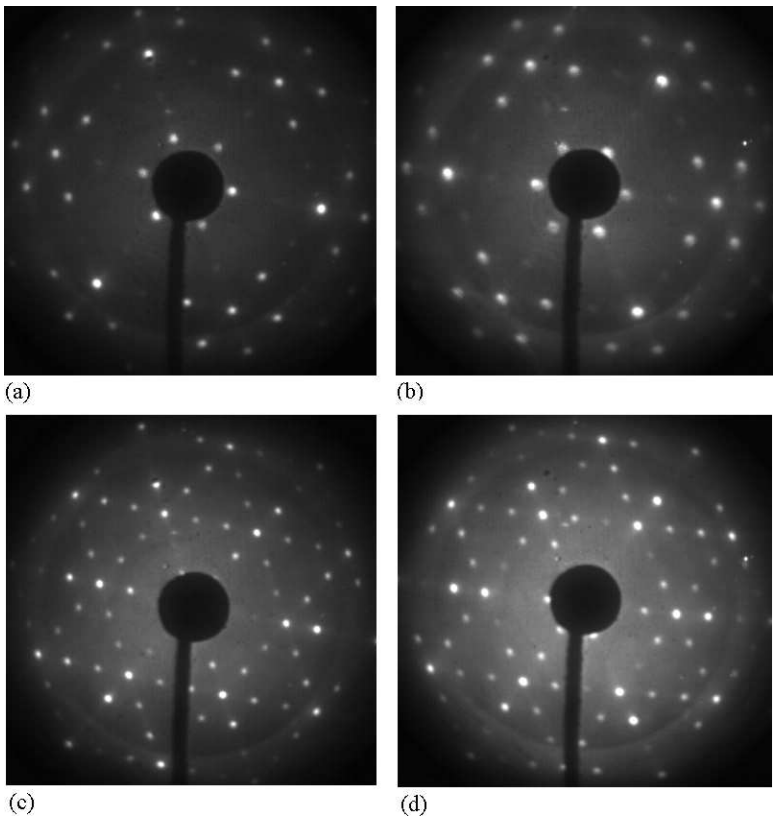

Figure 6.2: Experimental 3×1 LEED spot pattern for the Si(111)-3×2-Sm surface shown at (a), (b) 40 eV and (c), (d) 80 eV for two separate experiments.

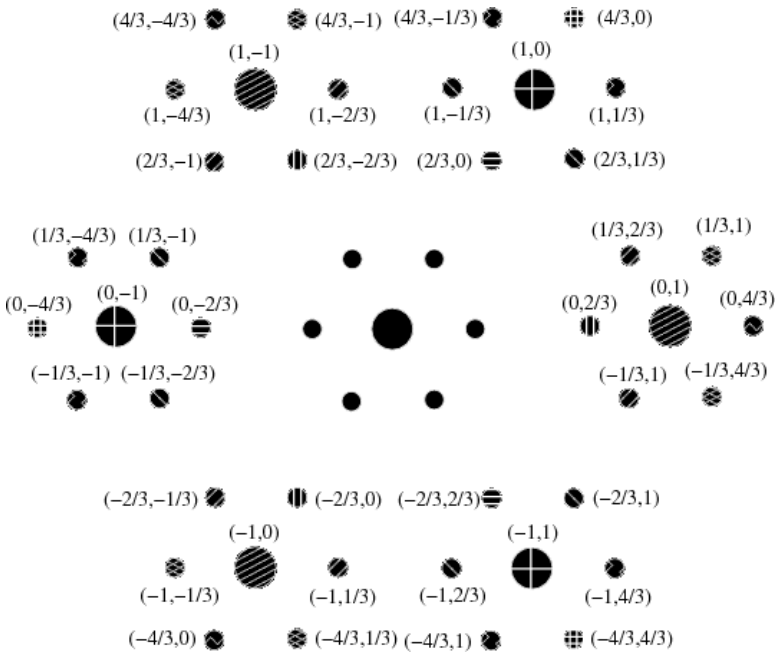

Figure 6.3: Labelled spots in the 3×1 LEED pattern produced by the Si(111)-3×2-Sm surface as it appears at 40 eV. The degeneracies of the spots are indicated by the pattern used to fill each spot.

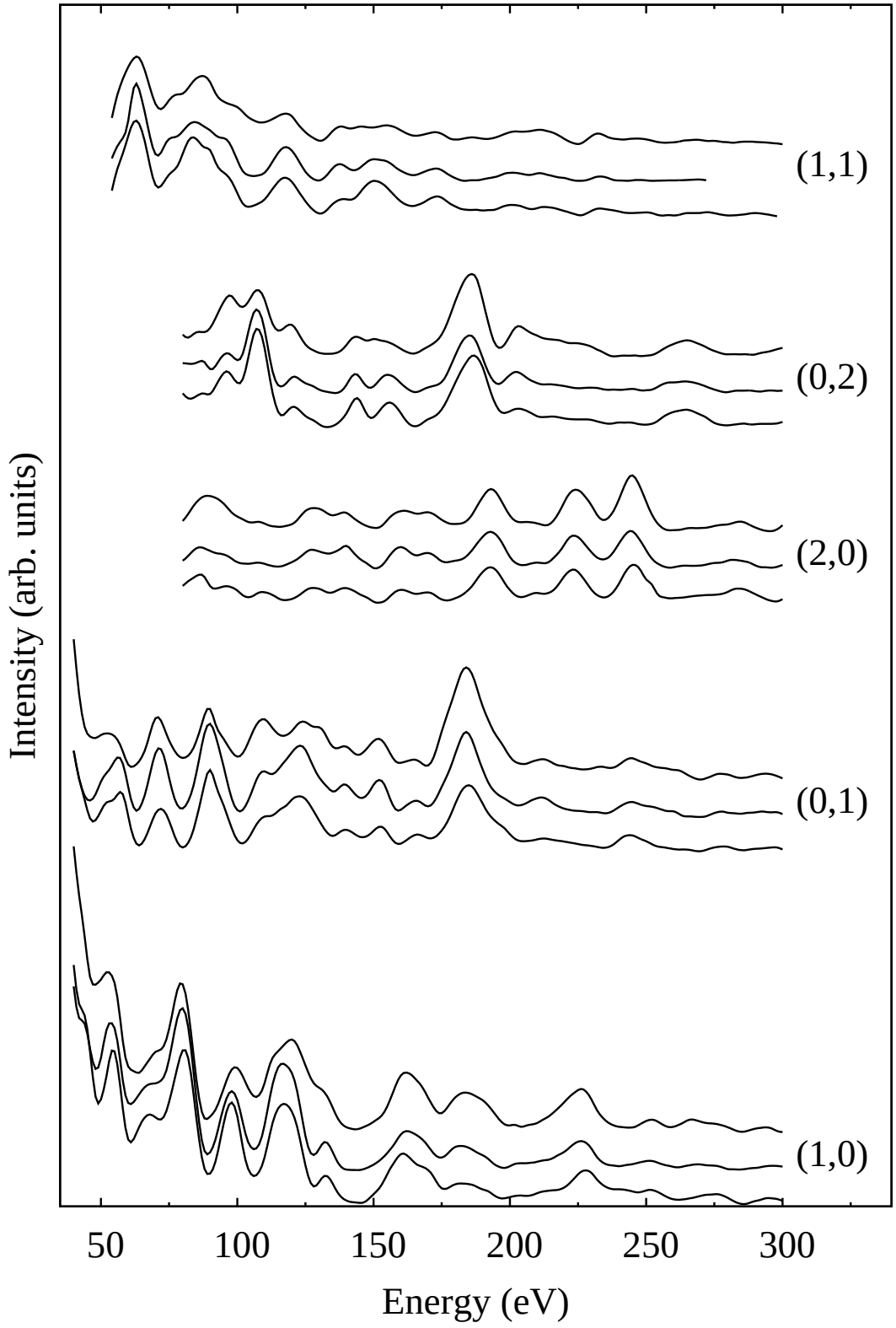

Figure 6.4: Experimental LEED I-V curves for the Si(111)-1×1-Sm surface for all five degenerate spot groups. For a given spot group experiments performed on different days starting from a clean substrate are compared.

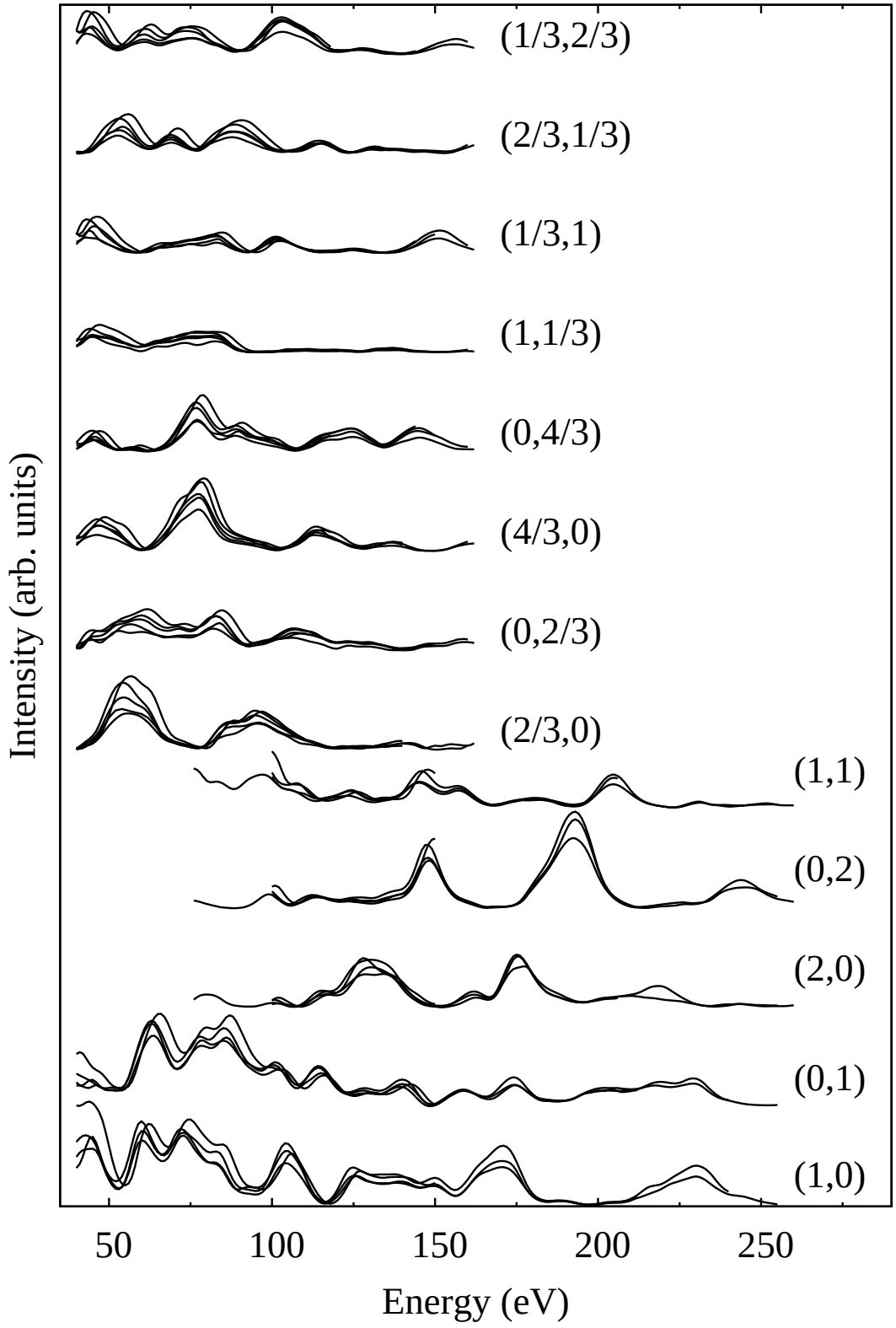

Figure 6.5: Experimental LEED I-V curves for the Si(111)-3×2-Sm surface for all thirteen degenerate spot groups. For a given spot group experiments performed on different days starting from a clean substrate are compared.

6.3 LEED I-V and *ab initio* Study of the Si(111)-1x1-Sm Phase

Although an observation of the 1×1 phase has been reported in the literature there have been no detailed studies that parameterise any structural model. This is a fundamental problem that faces any LEED investigation into a virgin surface. A wide range of candidate structures must be compared with the experimental data that was presented in the previous section. The possible structures that will be investigated here are;

Bulk-terminated Si(111) The poor inter-experiment R-factors suggest disorder and variable composition on this surface. The samarium atoms might form a disordered overlayer atop a bulk terminated Si(111) surface.

T1 atop The samarium atoms sit in T1 sites atop a bulk terminated Si(111) surface.

T4 atop The samarium atoms sit in T4 sites atop a bulk terminated Si(111) surface.

H3 atop The samarium atoms sit in H3 sites atop a bulk terminated Si(111) surface.

2D H3 site bulk buckled The samarium atoms form a 2D RE silicide and occupy H3 sites but with the top silicon bilayer buckled in the same sense as in the bulk.

2D T4 site The samarium atoms form a 2D RE silicide and occupy T4 sites.

2D T4 site bulk buckled The samarium atoms form a 2D RE silicide and occupy H3 sites but with the top silicon bilayer buckled in the same sense as in the bulk.

In this section efforts to determine if any of these candidate structures are responsible for the experimental 1×1 LEED pattern and its fingerprint I-V curves are described. The candidate structures have been geometry optimised using an *ab initio* method and their energies have been compared. This information has been used to suggest if any of these structures are stable and to indicate which of the structures are the most energetically favourable. The LEED I-V curves of the optimised structures have been compared with experiment using the Pendry R-factor.

Ab initio comparison of candidate structures

The *ab initio* geometry optimisation calculations were performed using the `CASTEP` code [9]. The code was run in a parallel computing environment on a Beowulf cluster of 33 machines, each with dual Intel Pentium 4 Xeon processors running at 1.7 GHz in the Department of Physics at York. A typical geometry optimisation calculation used 18 processors and required around 200 hours.

Before proceeding the input parameters in the calculation were carefully checked (see [118] and Chapter 3 of this work for a discussion of the importance of this). Figure 6.6 shows how the calculated energy varies with the number of plane waves included in the calculation as the cutoff energy is raised for three increasingly dense Monkhorst-Pack [108] reciprocal space sampling grids. A cutoff energy of 420 eV yields a total energy near to the variational minimum and will allow accurate calculation of the energy and the forces within the system. A reciprocal space sampling grid with 18 k-points was used in the geometry optimisation since in figure 6.6 it is apparent that increasing the sampling grid to size to 32 k-points does not significantly change the energy. The Perdew-Burke-Ernzerhof [99] generalised gradient approximation was used to represent exchange and correlation effects.

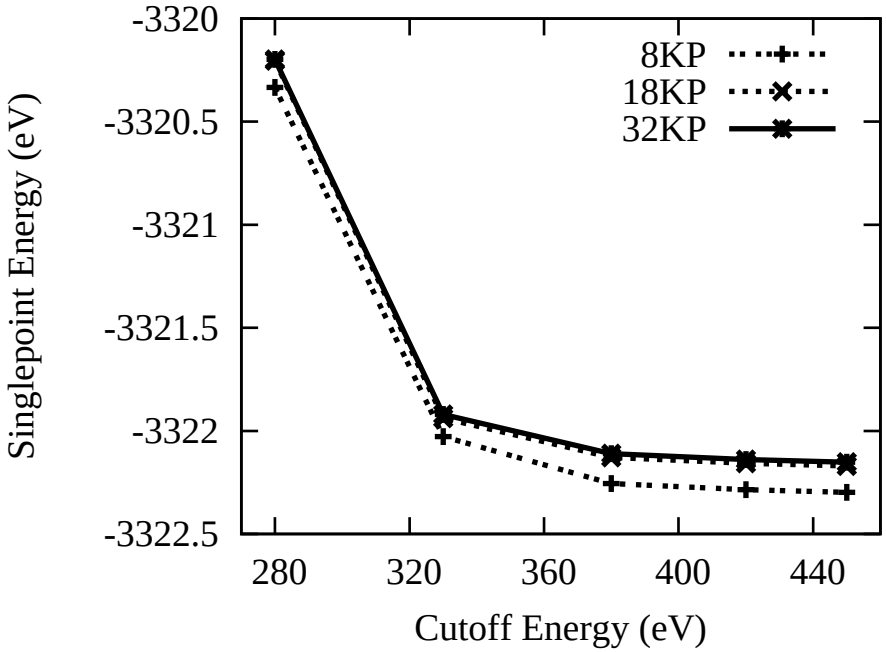

Figure 6.6: Variation of the singlepoint energy, which is the calculated energy for a given configuration of the atomic positions, with the cutoff energy and with the number of k-points at which the wavefunction is sampled in reciprocal space for the Si(111)-1×1-Sm system.

The vacuum gap that was used to prevent interaction between the top surface in one supercell and the bottom surface in the supercell above was 9 Å thick which was optimised during the course of the *ab initio* studies of 2D Si(111)-1x1-Ho in Chapter 5 of this work. For the same reason four bulk-like silicon layers were included below the samarium layer. To prevent interactions through the supercell between uncompensated charge in the top and bottom layers and to fully replicate the transition to the bulk silicon crystal the deepest bulk-like silicon layer has been hydrogen passivated and the coordinates of the silicon atoms in this layer have been fixed so that they are not free to move from their bulk positions.

This system contains an odd number of electrons and we must consider the effects of spin polarisation. For a given atomic configuration the total energy has been calculated for a variety of different spin states. During each of these calculations the spin was constrained to remain at a fixed value during the electronic minimisation which allows the energy of different spin states to be directly compared. Figure 6.7 shows the convergence of the electronic minimisation for several possible spin states.

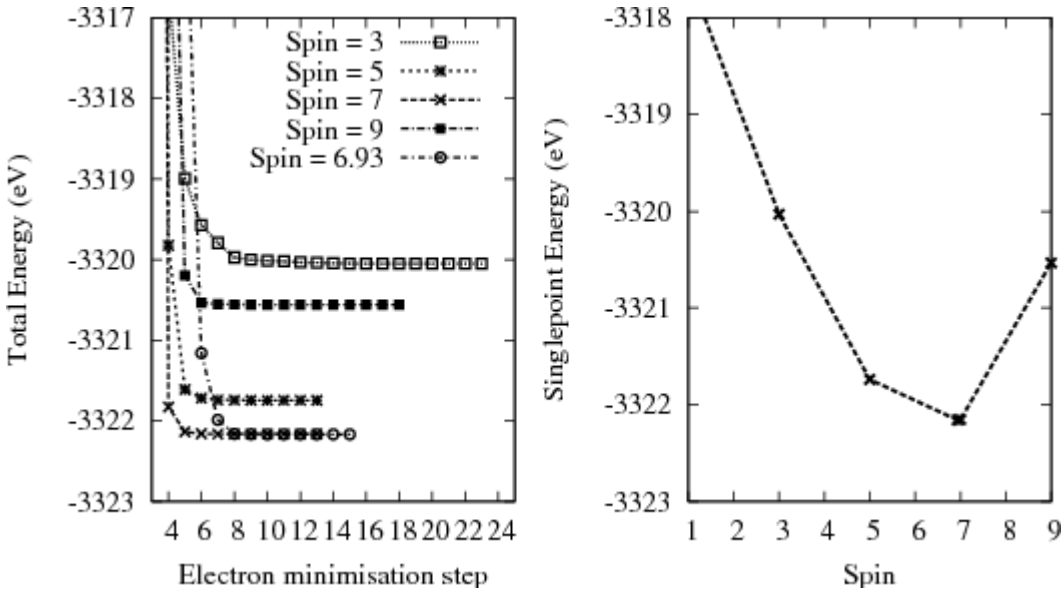

Figure 6.7: Variation of the energy with the total spin for the Si(111)-1×1-Sm system. The figure on the left shows the convergence of the electronic minimisation for each spin state and the figure on the right shows the final singlepoint energy as a function of the net spin state imposed on the system.

The lowest energy spin configuration occurs when the net spin is equal to 7. If the calculation is repeated with no constraints upon the net spin then the system evolves into a state with a net spin of 6.93 and with an energy slightly lower than that of the state with a net spin of 7. This would suggest that during the electronic minimisation the calculation will automatically fall into the energy minimum defined by the spin state

with the minimum energy and we need not worry about training the system into the energy basin of this spin state. In all of the geometry optimisation calculations involving Si(111)-1×1-Sm the spin was allowed to vary freely and to reduce the calculation time the electronic minimisation was begun using an initial spin state of 7.

Figure 6.8 shows the top few surface layers of each of the six structures that have been investigated. The bulk terminated silicon (111) surface has not been geometry optimised. Each supercell was geometry optimised until the maximum force on any atom was less than $5 \times 10^{-2}\,\mathrm{eV/\AA}$ and the change in the energy between geometry optimisation steps was less than 5×10^{-6} eV. The final energies and forces for each optimised structure are shown in table 6.1 below.

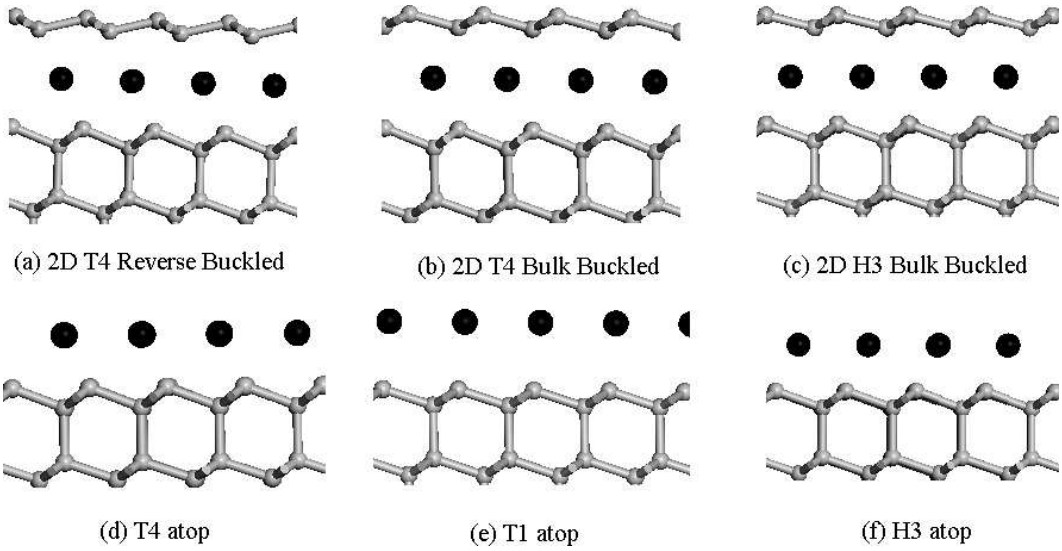

Figure 6.8: Showing the structure of the surface layers of each of the Si(111)-1×1-Sm structures that have been geometry optimised.

Structure	Final energy (eV)	$\lvert\boldsymbol{F}\rvert$max (eV/Å)
T1 atop	-3321.28	0.017
T4 atop	-3322.28	0.015
H3 atop	-3322.22	0.036
2D H3 site bulk buckled	-3322.49	0.040
2D T4 site	-3322.48	0.009
2D T4 site bulk buckled	-3322.45	0.012

Table 6.1: The energy and the maximum force on any atom tabulated for all of the Si(111)-1×1-Sm structures that have been geometry optimised.

Comparison of experimental and calculated LEED I-V curves

The `CAVLEED` [87] code was used to calculate LEED I-V curves for the seven candidate structures. A full set of phase shifts was generated using the `DLPHASE` code [86] for each individual structure using the bulk value of the Debye temperature (T_D) for each atomic species (that is $T_D = 645K$ for silicon and $T_D = 169K$ for samarium). The calculated I-V curves for all six geometry optimised structures and for the bulk-terminated Si(111) surface have been compared against the experimental I-V curves and the Pendry R-factor was used to indicate the level of agreement. These R-factors are listed in table 6.2.

Structure	R_P
Bulk-terminated Si(111)	0.70
T1 atop	0.80
T4 atop	0.88
H3 atop	0.78
2D H3 site bulk buckled	0.83
2D T4 site	0.91
2D T4 site bulk buckled	–

Table 6.2: Pendry R-factors resulting from a comparison of the candidate structures for the Si(111)-1×1-Sm surface with averaged experimental data.

These R-factors are all very poor. However, in Chapter 5 it was shown that poor R-factors result when the *ab initio* geometry optimised Si(111)-1×1-Ho structure is compared against experiment. Subsequent variation of the interlayer spacings to allow outward expansion of the top surface layer improved the R-factor considerably. This possiblity must be considered here. In the next section the interlayer spacings and the rumpling amplitudes are varied for the Si(111)-1×1-Sm trial structures.

Variation of interlayer spacings and rumpling amplitudes

The calculation of the I-V curves was repeated using a wide range of values for the first two interlayer spacings with a step size of 0.16 Å which was around 7% of the total value. The buckling amplitude in the silicon overlayer for the 2D structures and the buckling amplitude in the top silicon layer for the bulk terminated surface were also varied in steps of 0.03 Å which was typically around 7% of the total value. The R-factor for each trial structure was determined and the R-factors of the best fit structures that were obtained in this coarse search are shown in table 6.3.

Model	R_P
Bulk-terminated Si(111)	0.59
T1 atop	0.70
T4 atop	0.67
H3 atop	0.66
2D H3 site bulk buckled	0.64
2D T4 site	0.65
2D T4 site bulk buckled	–

Table 6.3: Pendry R-factors resulting from a comparison of a coarse fit of the seven candidate structures for the Si(111)-1×1-Sm surface with averaged experimental data.

There has been a modest improvement in the R-factors by around 0.1 - 0.15. The I-V curves for two of the best-fit structures in table 6.3 are plotted against the experimental I-V curves in figure 6.9.

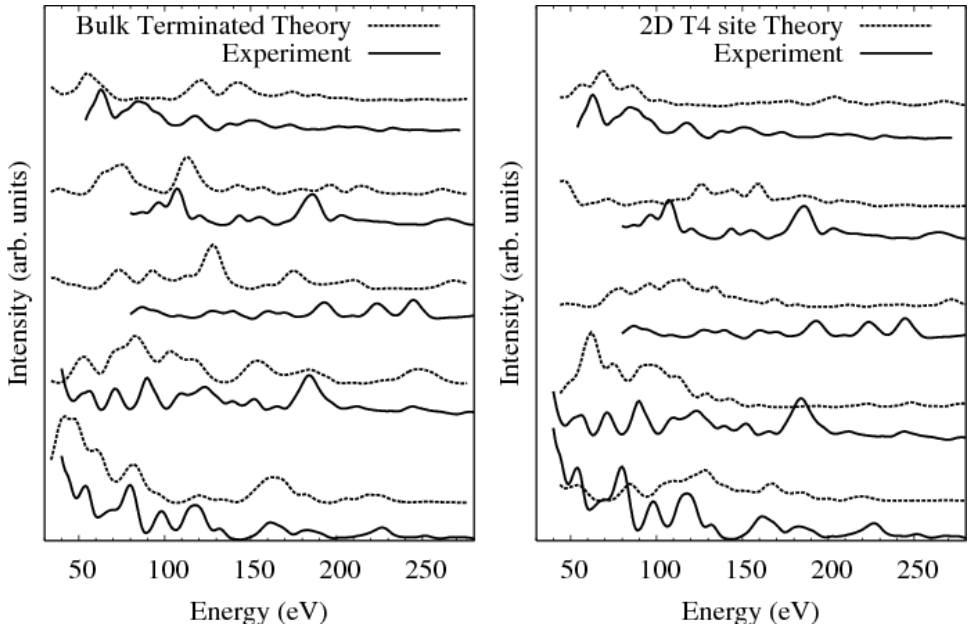

Figure 6.9: Calculated coarse-fit LEED I-V curves for the bulk terminated silicon (111) surface (left) and the 2D silicide with the samarium atoms in a T4 site (right) compared with experiment for the Si(111)-1×1-Sm surface.

We can see that for certain spots in these LEED patterns there is a semblance of good agreement in the peak positions over some energy ranges. For the sake of brevity only two sets of I-V curves are shown in figure 6.9 but partial agreement of the I-V curves is apparent for all of the candidate structures and not just the two shown here.

Summary and Discussion

Several candidate structures have been compared with experiment. Each of these is stable and physically reasonable; the forces within the supercell and the interlayer spacings are similar to those calculated for other surface structures elsewhere in this thesis. However, the poor R-factors obtained when the candidate structures were compared with experiment indicate that none of them can be considered as being individually responsible for the experimental observations. It might be possible to improve these R-factors by using a fine search of the parameter space spanned by the rumpling amplitudes and the interlayer spacings and by optimising the thermal vibrations. In the last chapter it was shown that for the Si(111)-1×1-Ho surface this process of correcting the structure suggested by the *ab initio* calculation by optimising the main features to which LEED is sensitive improved the R-factor by around 0.4. However, the R-factor after a coarse parameter search was found to be 0.42 in that work which was a good indication that the trial structure was viable. In this work the coarse search failed to produce an R-factor that was better than 0.64 for any of the ordered structures.

The *ab initio* calculations suggest that the 2D RE silicide structures are the most energetically favourable atomic configuration when a single unit cell is considered but these structures produce only a slightly improved match to experiment than any model that involves samarium atop the substrate. The I-V curves obtained during the LEED experiments do not resemble those for other 2D rare earth silicides, which are known to be mutually similar (see chapter 5). The annealing temperature used here was typical of that required to form the other 2D RE silicides.

It is clear from a visible inspection of the I-V curves that all of the structures have features that match well with experiment over a narrow energy range for a given spot. For each structure the R-factor for each individual LEED spot was near to the value of the total R-factor which would suggest that there is a consistent and non-random level of agreement with experiment across the whole calculated LEED pattern. Of the structures compared with experiment it was the bulk terminated Si(111) surface that provided the most favourable comparison, producing an R-factor of 0.58. This is a model in which ordered samarium is not present. This would suggest that the surface comprises a disordered samarium layer atop bulk-terminated silicon with perhaps pockets of ordered regions of some or all of the candidate structures that contribute in unison to the observed I-V curves. The variability between the I-V curves produced in different experimental runs also strongly suggests that there is some variability in the composition or the structure of the surface. LEED can provide no more information about this and an STM observation of this surface phase would perhaps provide a much clearer insight.

6.4 LEED I-V and *ab initio* Study of the Si(111)-3×2-Sm Phase

Ab initio Geometry Optimisation of Si(111)-3×2-Sm

The *ab initio* calculations were performed using the `CASTEP` code [9]. The code was run on 30 processors in a parallel computing environment at the HPCx High Performance Computing facility located at the CCLRC Daresbury laboratory in the UK and a typical geometry optimisation calculation required around 4 hours. Two different unit cells for the HCC structure have been geometry optimised (see figure 6.12 for details of these). In the first unit cell the samarium atom is located in the T4 site with respect to the first bulk-like silicon layer and in the other unit cell the samarium atom is situated in a H3 site. We will refer to the two structures as 'T4' and 'H3'. The initial atomic positions were those that were obtained in the *ab initio* study by Palmino et al. [151] and these were were very kindly provided by F. Palmino.

Before proceeding the input parameters in the calculation were carefully checked (see [118] and Chapter 3 of this work for a discussion of the importance of this). Figure 6.10 shows how the calculated energy varies with the number of plane waves included in the calculation as the cutoff energy is raised for three increasingly dense Monkhorst-Pack [108] reciprocal space sampling grids. A cutoff energy of 380 eV yields a total energy near to the variational minimum and will allow accurate calculation of the energy and the forces within the system. A sampling grid with 3 k-points in reciprocal space was used since an increase to 6 k-points does not significantly change the energy. Finally, the Perdew-Burke-Ernzerhof [99] generalised gradient approximation was used to represent exchange and correlation effects.

The vacuum gap that was used to prevent interaction between the top surface in one supercell and the bottom surface in the supercell above was 9 Å thick which was optimised during the course of the *ab initio* studies of 2D Si(111)-1x1-Ho that are included in Chapter 4 of this work. Two bulk-like silicon layers were included below the top layer that contains the samarium atom and the honeycomb chain structure. To prevent interactions through the supercell between uncompensated charge in the top and bottom layers and to fully replicate the transition to the bulk silicon crystal the deepest bulk-like silicon layer has been hydrogen passivated and the coordinates of the silicon atoms in this layer have been fixed so that they are not free to move from their bulk positions. The geometry optimisation of the unit cells was repeated without passivation and positional constraints. The final positions of the silicon atoms in this bottom layer were not drastically altered and the total energy was not significantly different which suggests that using so few bulk-like layers is reasonable.

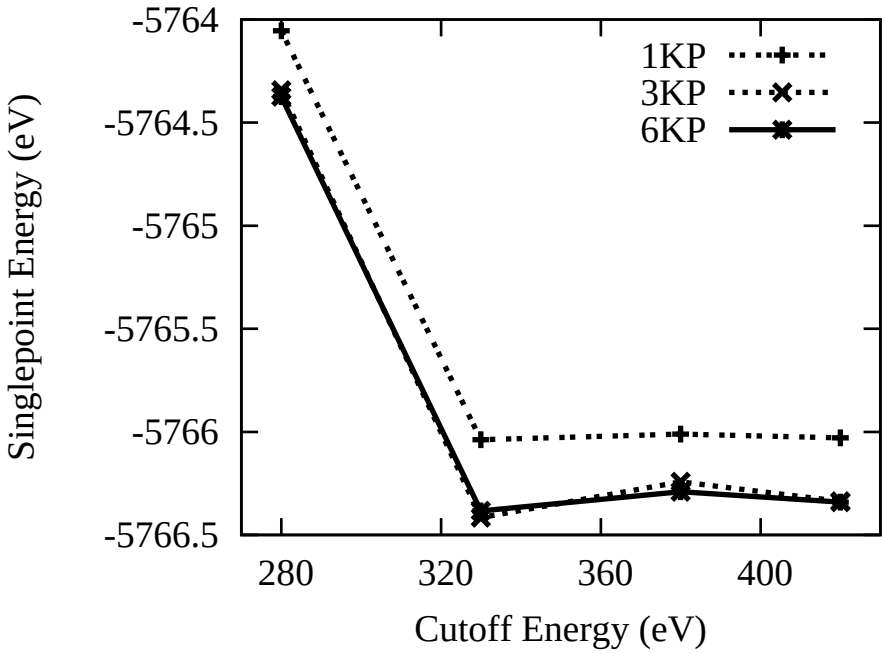

Figure 6.10: Variation of the singlepoint energy, which is the calculated energy for a given configuration of the atomic positions, with the cutoff energy and with the number of k-points at which the wavefunction is sampled in reciprocal space.

The structures were allowed to relax until the forces were below the predefined tolerance of 5×10^{-2} eV/Å. Figure 6.11 shows the convergence of the total energy and the maximum force on any atom as the geometry optimisation proceeds for the two structures. The T4 structure has a slightly lower energy than that of the H3 structure and the maximum force in the system is slightly lower. The final optimised structures are shown in figure 6.12 below. The interlayer spacings (ignoring the samarium atom for now) in both structures are almost identical.

The major difference between this calculated structure and that in Ref. [67] is in the interlayer spacings. In this study the spacing between the top layer and the first bulk-like layer (L1 in figure 6.12) is approximately 8% greater than that in Ref. [67] and the spacing between the first bulk-like layer the the second bulk-like layer (L2 in figure 6.12) is about 4% greater. There are also some minor differences in the position of the silicon atoms in the honeycomb chain.

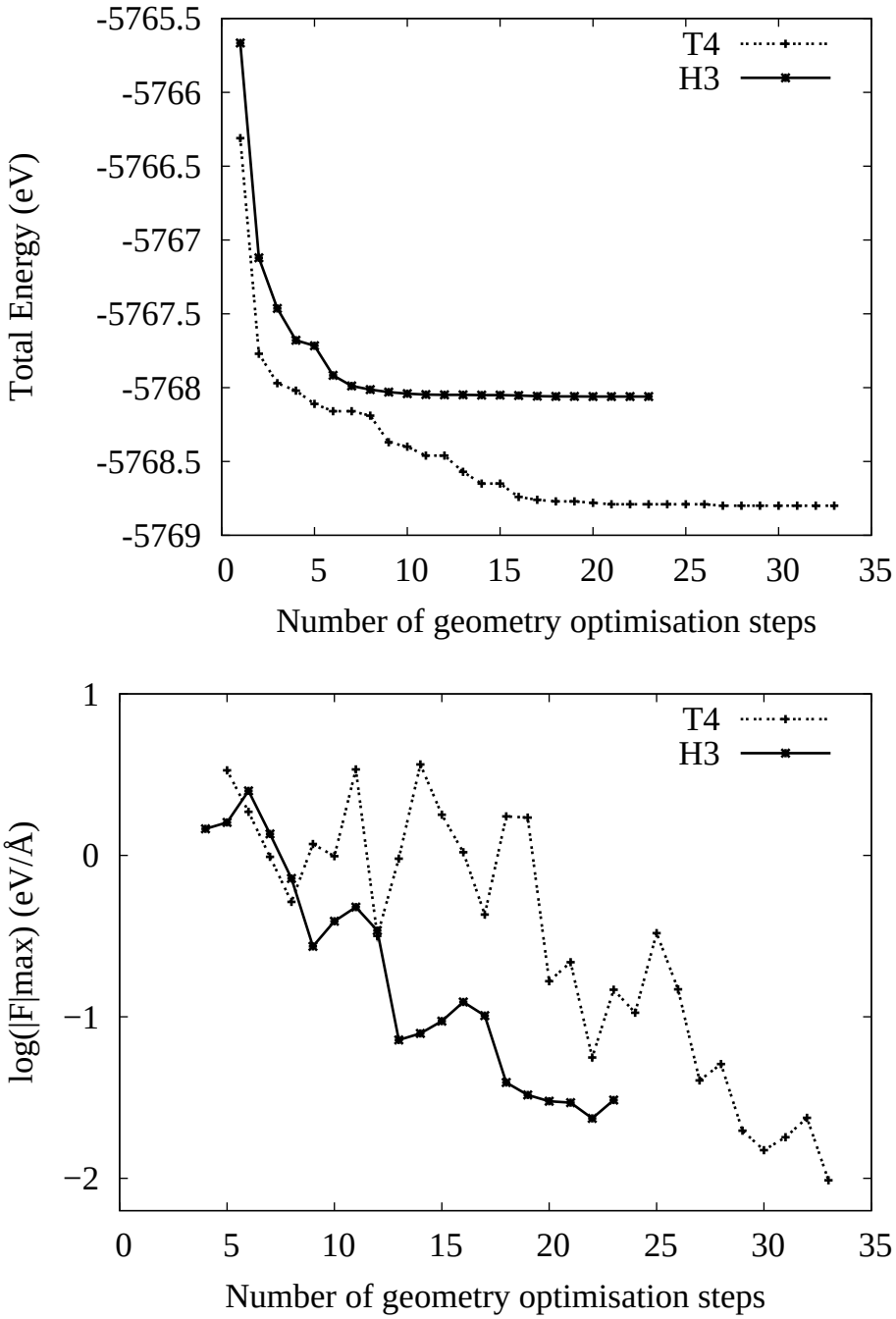

Figure 6.11: Convergence of the total energy (top) and logarithmic convergence of the forces (bottom) during the geometry optimisation of the T4 and H3 structures. The T4 structure has a lower energy than the H3 structure and the maximum force on any atom is lower.

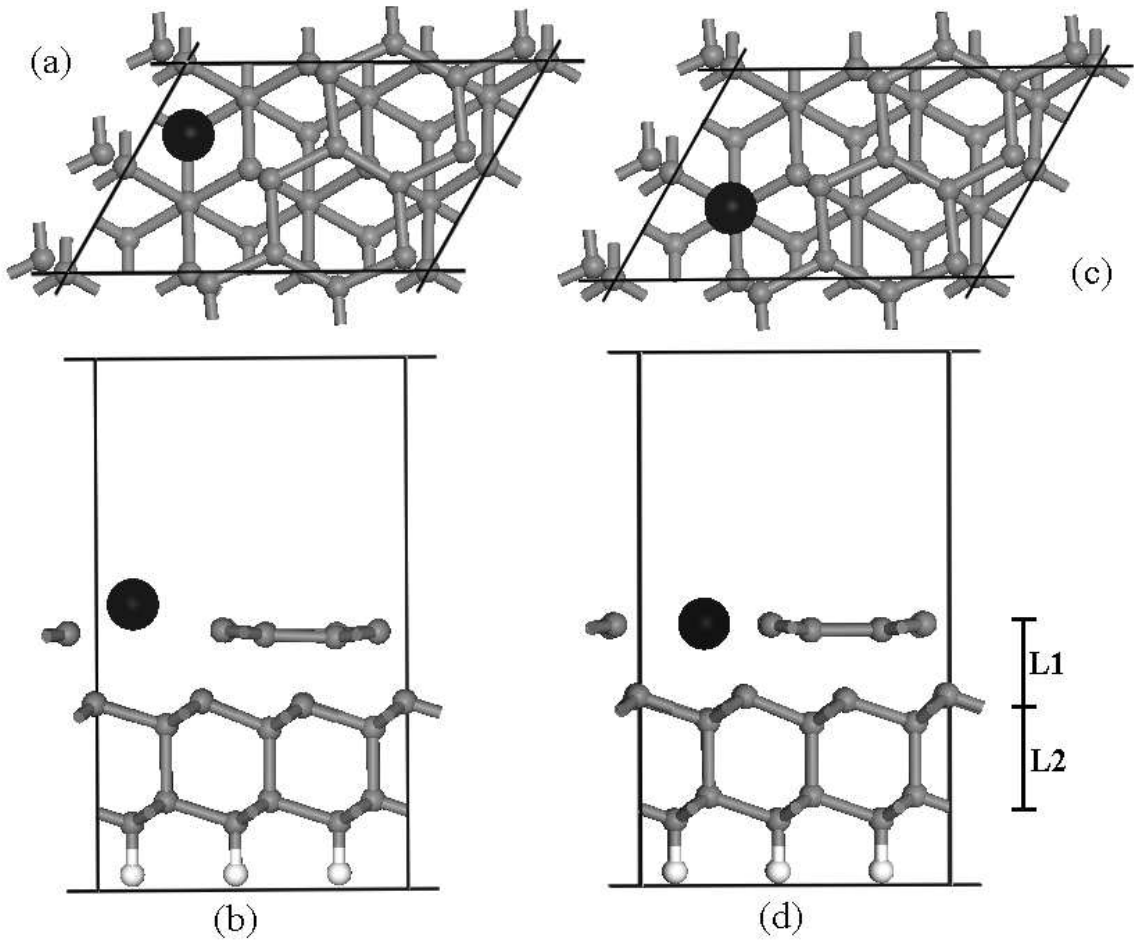

Figure 6.12: Optimised structures for the HCC model showing the H3 model from above (a) and in side view (b) and the T4 model from above (c) and in side view. Silicon atoms here are grey, samarium is black and the hydrogen atoms are white. The first and second interlayer spacings are labelled L1 and L2 respectively.

Comparison of experimental and calculated LEED I-V curves

The `CAVLEED` [87] code was used to calculate LEED I-V curves for the optimised atomic configurations of the two unit cells in this work and for the unit cell that was determined by other workers. A full set of phase shifts were generated using the `DLPHASE` code [86] for each individual structure using the bulk value of the Debye temperature for each atomic species (that is 645 K for silicon and 169 K for samarium). The I-V curves of the integer spots for all three structures are compared against experiment in figure 6.13.

The first thing to note is that the I-V curves of the T4 and the H3 site from this study are very similar and we cannot discard either structure (the calculated energies and atomic positions are also similar). The structures obtained from these two *ab initio* calculations are a consistently better match to experiment than that in ref. [67]. This suggests that the interlayer spacings obtained in this study, to which LEED is very sensitive, are closer to those present in the real surface. The improvement in the geometry optimisation could be due to the use of a higher cutoff energy or more rigorous convergence parameters in the electronic minimisation and/or the geometry optimisation or in the use of more accurate pseudopotentials. Theirs was a comparison against STM data for which the lateral dimensions were much more important than the vertical spacings, to which STM is not directly sensitive.

We can divide the spots in the LEED pattern into two groups. The integer spots ((1,0), (2,0), (1,1) etc) contain a large contribution from the bulk and are sensitive to the top few layers. The fractional spots ((1,3,0), (-4/3,1) etc) are extremely sensitive to the top layer reconstruction and only mildy sensitive to deeper layers through multiple scattering.

The poor Pendry R-factors (that is >0.7 in this context where enhanced vibrations have not been applied) for some of the integer spots in figure 6.13 indicate that further structural optimisation is needed. It is apparent that for some curves the right peaks are present but that their energy is slightly wrong (see the (0,2) and (2,0) spots in figure 6.13 for example). The fractional spots have much better R-factors (see figure 6.14) which indicates that the structure of the top layer is in good agreement with experiment. The natural way to proceed is to vary the interlayer spacings to attempt an improvement in the match with experiment, particularly for the integer spots. In the next section this is attempted.

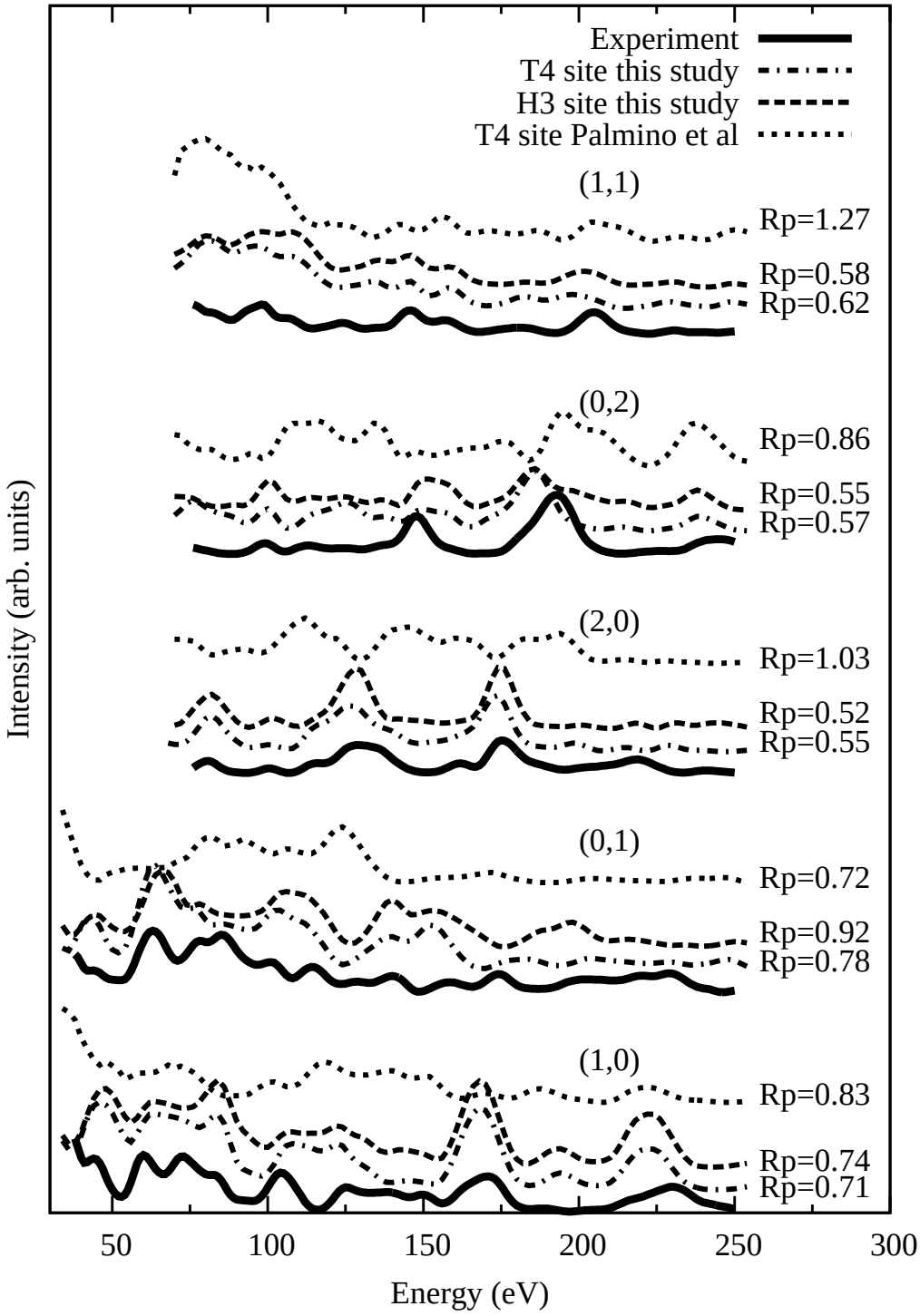

Figure 6.13: A comparison of the I-V curves calculated for the integer spots for the structures suggested by the *ab initio* calculations in this study and elsewhere with those obtained experimentally. The R-factor beside each curve indicates the level of agreement with experiment.

Variation of the interlayer spacings

The calculation of the I-V curves was repeated using various values for the first two interlayer spacings and the R-factors were determined. An initial coarse search was carried out over a wide range of values for the interlayer spacings and with a large step size of 0.05Å which is around 2 % of the typical value of the total spacing. Figure 6.14 shows the R-factor landscape obtained in this manner for the fractional spots. There is a clear minimum in both cases and the position of this minima does not change if we consider the fractional spots, the integer spots or all of the spots.

In figure 6.14 the samarium atom has been considered in determining the midpoint of the top layer which is why the minima do not coincide in the two coarse searches; the samarium atom sits proud of the honeycomb layer in the H3 structure and it is much lower in the T4 structure. This skews the layer midpoints away from one another when infact the spacing between the honeycomb layer and the first silicon bulk-like layer was almost identical in both cases.

In the *ab initio* calculations in this study the interlayer spacings were approximately 3.06, 3.10Å for the H3 structure and 2.65, 3.14 Å for the T4 structure which places the *ab initio* energy minimum (indicated by a cross in figure 6.14) very close to that of the `CAVLEED` I-V R-factor minimum. Two independent techniques are thus suggesting very similar best fit structures.

Having identified the minima a fine search over a smaller range of interlayer spacings was carried out using a smaller step size of 0.005 Å. The results of this are shown for the fractional spots in figure 6.15. The minima in each case are very flat and the fine search has achieved only a modest improvement in the R-factor of 0.01 in each case. Further searches using a finer grid of values for the interlayer spacings were not performed.

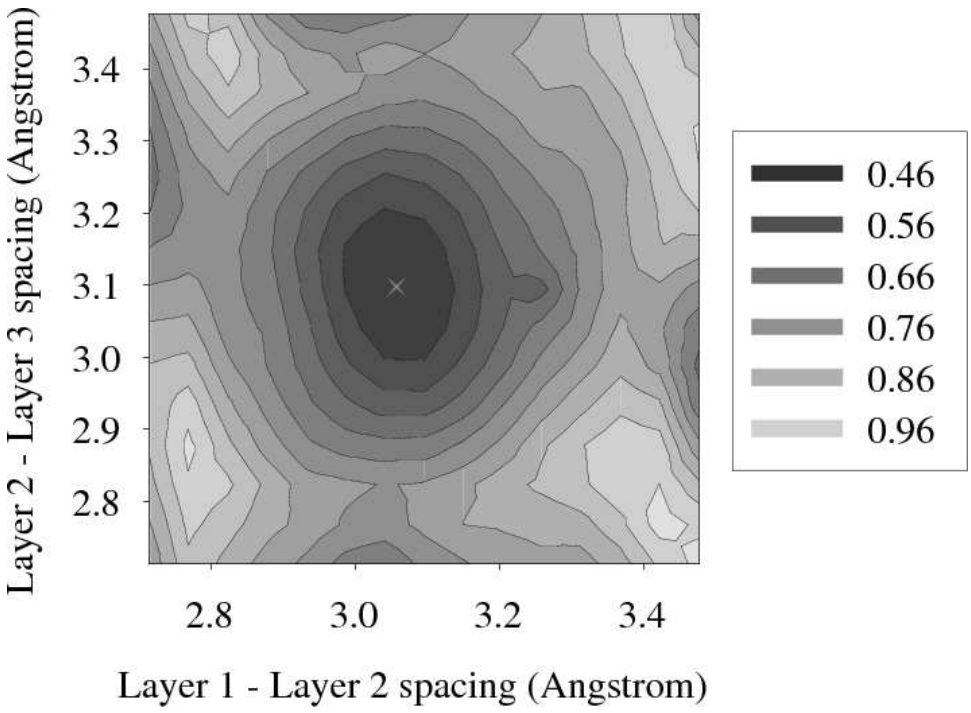

(a) H3 site coarse search

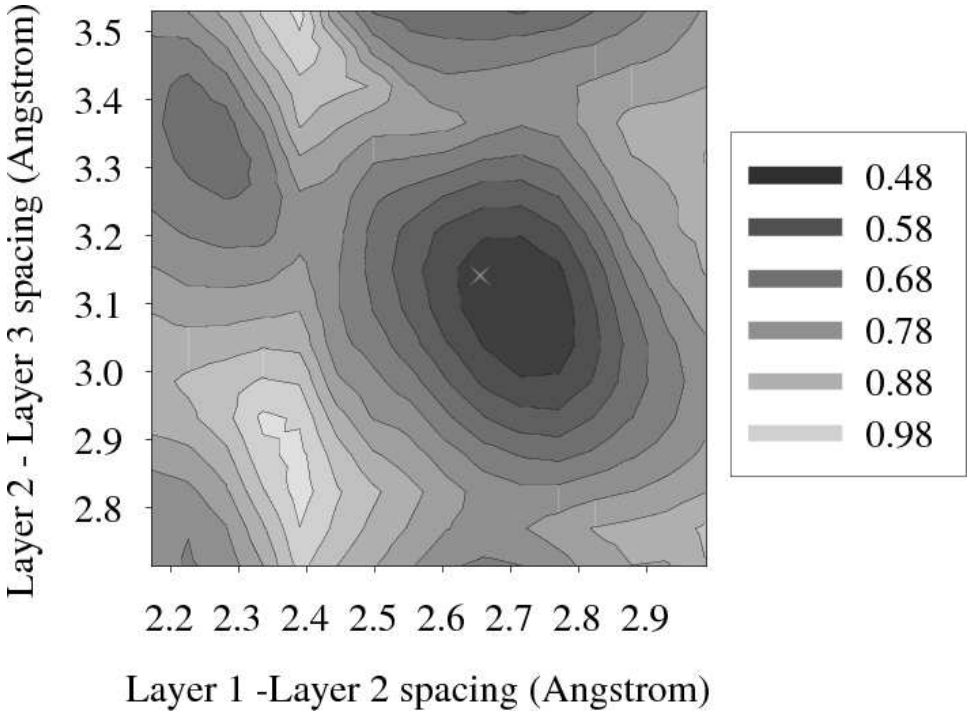

(b) T4 site coarse search

Figure 6.14: Coarse search Pendry R-factor landscape for a range of values of the interlayer spacings in the (a) H3 and (b) T4 structure for the fractional spots. The step size was 0.05 Å. The cross indicates the *ab initio* energy minimum.

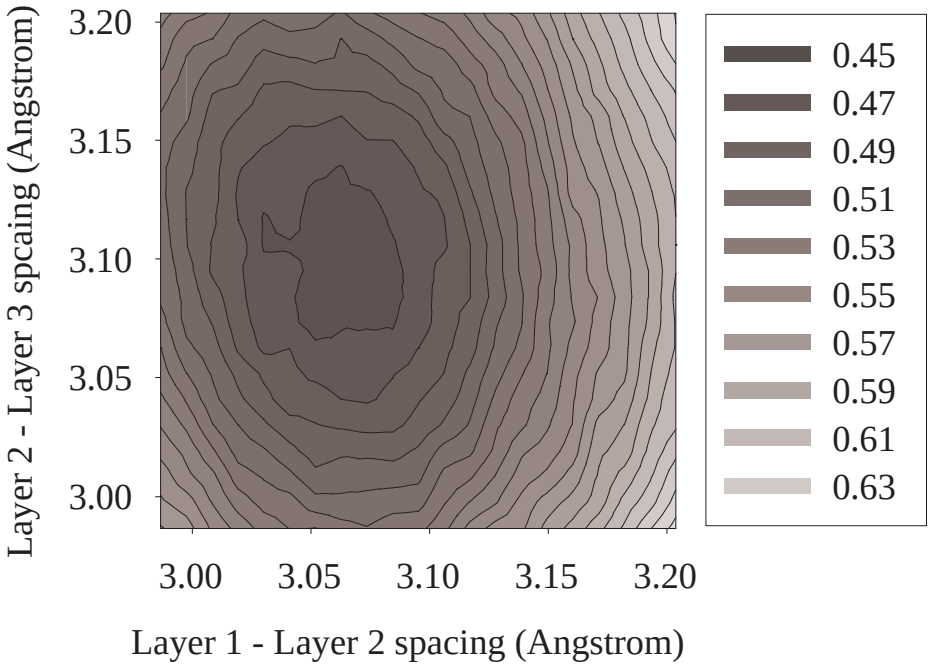

(a) H3 site fine search

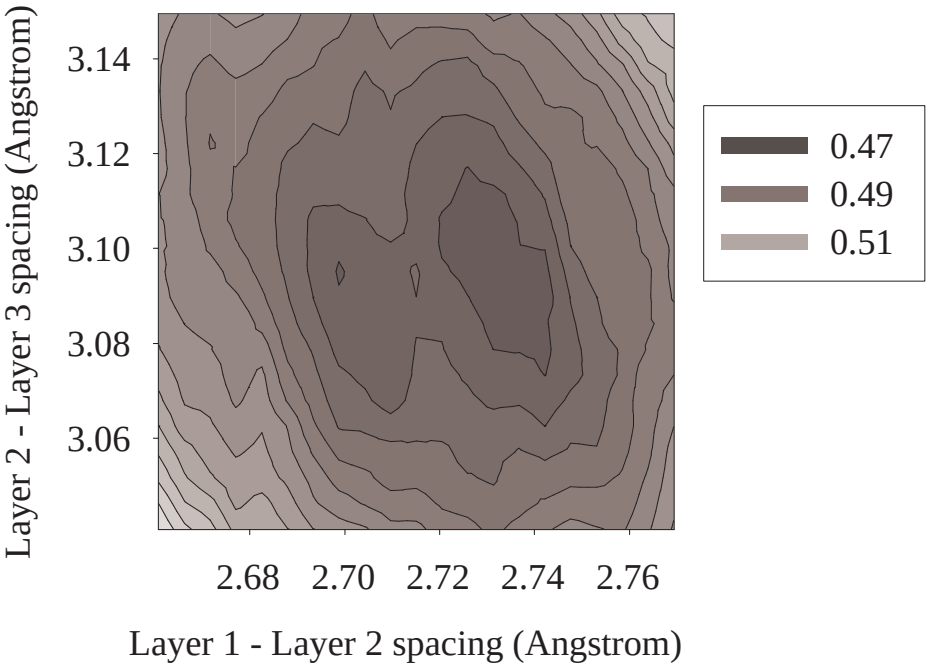

(b) T4 site fine search

Figure 6.15: Fine search Pendry R-factor landscape for a range of values of the interlayer spacings in the (a) H3 and (b) T4 structure for the fractional spots. The step size was 0.005 Å.

Error analysis

The total R-factor is an average over those for the individual spots. The standard error in this R-factor can be used to estimate the error in each of the interlayer spacings. Figures 6.16 and 6.17 each show the variation of the R-factor with one of the interlayer spacings with the other kept fixed at its optimum value for the H3 structure. The standard error in the Pendry R-factor has been used to determine an error in the first interlayer spacing of approximately δ L1 = $\pm$ 0.1 Å and in the second interlayer spacing the error is approximately δ L2 = $\pm$ 0.1 Å.

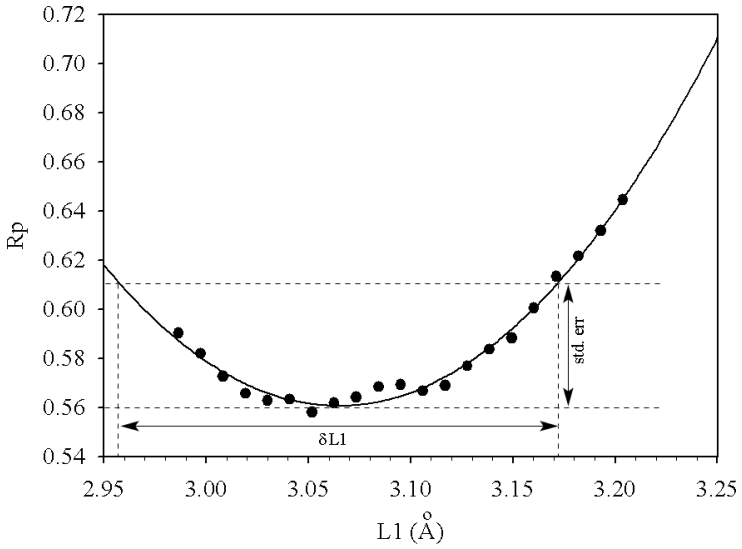

Figure 6.16: Variation of the Pendry R-factor with interlayer spacing 1 showing how the standard error was used to determine the error in the structural parameter.

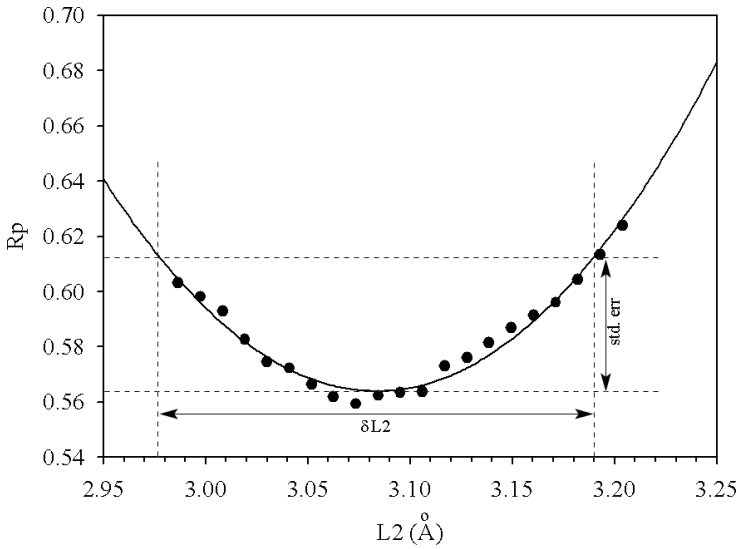

Figure 6.17: Variation of the Pendry R-factor with interlayer spacing 2 showing how the standard error was used to determine the error in the structural parameter.

Variation of the third interlayer spacing

There is another interlayer spacing deeper into the bulk that we might try to vary. Computational resources do not permit an independent variation of this spacing along with those between the top three layers. Figure 6.18 shows the variation of the Pendry R-factor as the spacing between layers three and four is changed with the first and second interlayer spacings fixed at their optimum value.

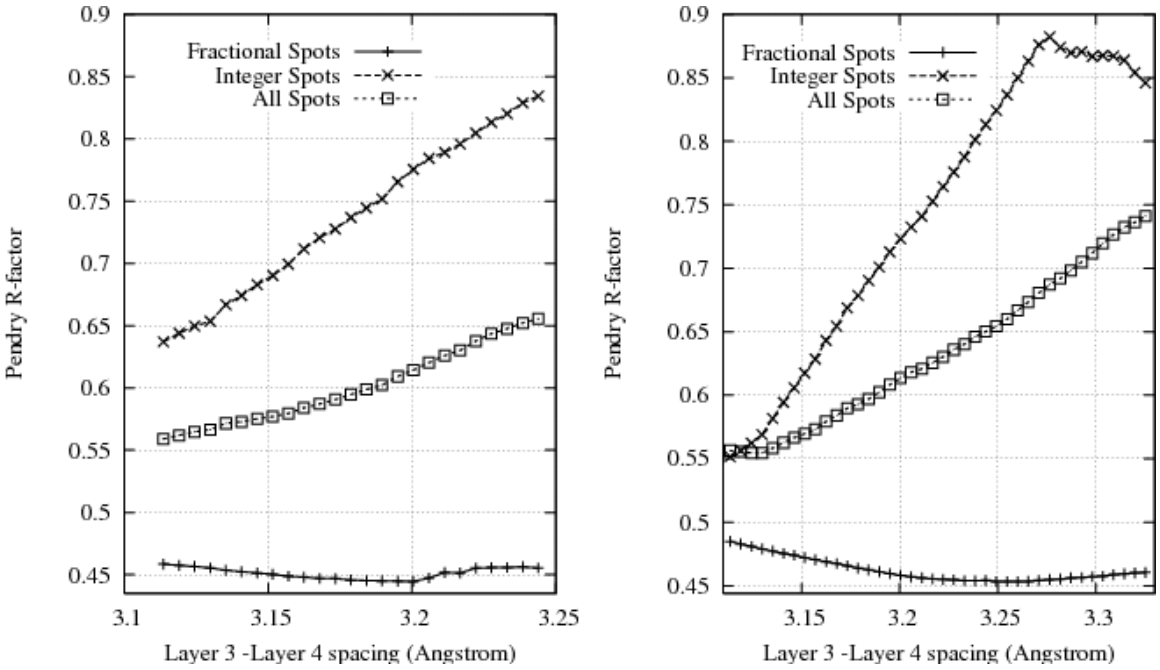

Figure 6.18: Variation of the spacing between layers three and four in the Si(111)-3x2-Sm H3 (left) and T4 (right) structures. The bulk value for this interlayer spacing is 3.14 Å

There is a small improvement in the R-factor for the fractional spots at the expense of a large worsening of the R-factor for the integer spots which are more sensitive to structure in the near bulk. From the trend in the graph for the H3 structure which is on the left in figure 6.18 it appears that further reduction of this interlayer spacing might continue to improve the overall R-factor. However, the optimised vibrations, which are discussed in the next section, do not improve upon the R-factor of the integer spots for this reduced interlayer spacing as much as when this spacing remains at its bulk value. We therefore reject any variation of this spacing and retain the bulk value.

Optimisation of the thermal vibrations

The effect of thermal vibrations within the system has also been investigated. The Debye temperature T_D of the samarium atom, the silicon atoms in the honeycomb layer and the silicon atoms in the first bulk-like layer have each been independently reduced by factors of $\sqrt{2}, 2$ and 3 from their bulk values. The effects of these enhanced vibrations for the two most effective combinations are shown in table 6.4 alongside the R-factors obtained with no enhanced vibrations.

Sm T_D	Si1 T_D	Si2 T_D	R_P^{FRAC}	R_P^{INT}	R_P^{ALL}
B	B	B	0.49	0.72	0.63
$B/\sqrt{2}$	$B/3$	$B/2$	0.48	0.46	0.48
$B/2$	$B/3$	$B/2$	0.45	0.44	0.45

Table 6.4: Variation of the Debye temperature for the samarium atom, silicon honeycomb layer and first bulk like layer and the effect upon the Pendry R-factors for the H3 structure. The naming scheme here is Sm=samarium atom, Si1=silicon honeycomb atoms, Si2=first silicon bulk-like layer. A Debye temperature of B indicates the bulk unoptimised value for that atomic species. Similar data is available for the T4 structure.

Further enhancement of the Debye temperature of the samarium atom (that is, to $B/3$) increased the R-factor. The two schemes of enhanced vibrations both reduce the overall R-factor by around 0.2 and this significant improvement is mainly due to the improvement in the R-factors of all the integer spots (and not just a significant improvement in one or two integer spots that skews the mean R-factor). This suggests that thermal vibrations are as important in this structure as in the 2D Si(111)-1x1-Y structure where Rogero et al. found an improvement of 0.2 in the R-factor upon optimisation of the vibrations and in Chapter 5 of this thesis it was shown that a similar improvement was made for the 2D Si(111)-1x1-Ho structure.

Linear combination of the T4 and H3 structures

The H3 and T4 structures have similar energies, similar structures (ignoring the position of the samarium atom) and similar LEED I-V curves. It is reasonable to suggest that both structures might co-exist upon the surface. Linear combinations of the best fit H3 and T4 structures are shown in figure 6.19 for the two regimes of optimal enhanced vibration shown in table 6.4. The H3 and T4 structures are considered as being separated by a distance greater than the coherence length of the LEED beam. To simulate large and separate domains of the two structures in this way the LEED spot

intensities have been combined and not the amplitudes. Each linear combination is a weighted sum of the I-V curves from both structures.

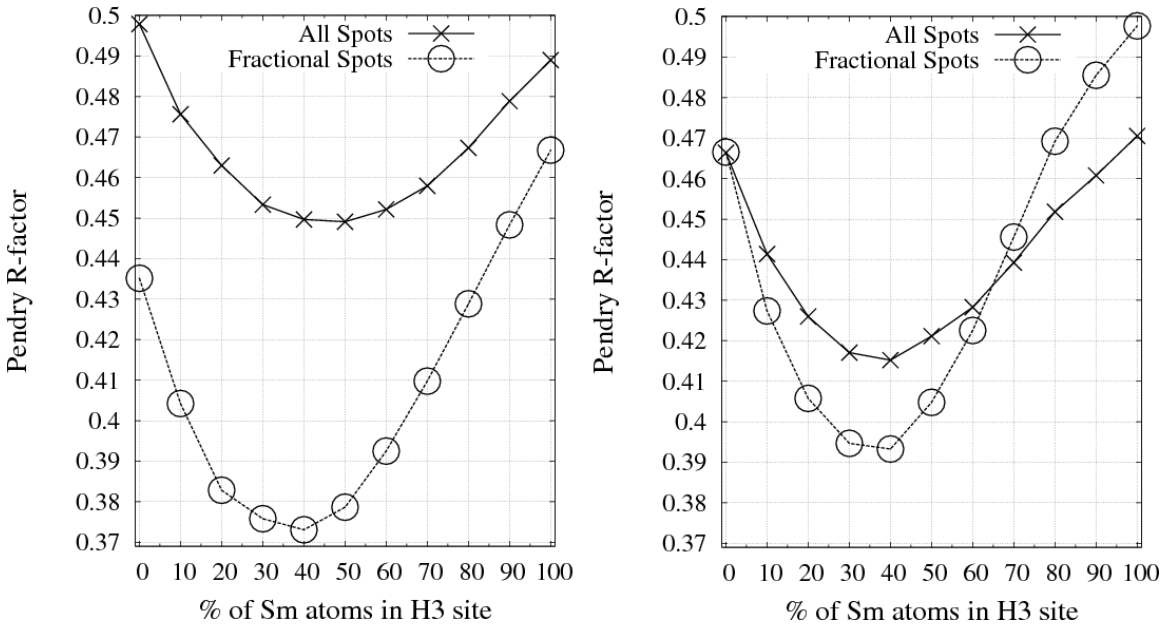

Figure 6.19: Pendry R-factors for various linear combinations of the H3 and T4 structures in various mixing ratios for two different vibrational regimes. In the figure on the left the Debye temperature for the samarium atom is $119K$ and in the figure on the right it is $84K$. In both cases the Debye temperatures of the top silicon honeycomb layer, the first silicon bulk-like layer and the repeated bulk layer are $215K$, $323K$ and $645K$ respectively.

The vibrational regime with a Debye temperature for the samarium atom of 119 K ($B/\sqrt{2}$ in table 6.4) gives a lower R-factor for the fractional order spots but it gives a worse overall R-factor. The vibrational regime with a Debye temperature for the samarium atom of 84 K ($B/2$ in table 6.4) gives a better overall R-factor and the minima for both the fractional and the integer spots coincide. The final ratio of H3 40:60 T4 is in favour of the structure that is lower in energy which is what we would expect.

This average composition has been determined with respect to the averaged experimental data obtained from four similar experimental runs. To determine whether the composition of T4 60 : 40 H3 is present each time the above composition comparison would need to be repeated against each individual experimental run. There are two reasons why this was not carried out; first, the individual experimental runs were very similar to one another and differences in composition would be expected to give higher interrun R-factors than those observed. Second, the noise level in the individual unsmoothed experimental datasets would introduce error that would be greater than the difference between the interrun I-V curves.

The production of a 3×1 LEED pattern from a 3×2 unit cell

The silicon honeycomb layer is almost mirror symmetric about a plane perpendicular to the ×2 direction. It is the location of the samarium atom that breaks this mirror symmetry and renders a quasi 3×1 unit cell into a 3×2 unit cell. It is natural to attempt the calculation of the I-V curves without the samarium atom in place. Figure 6.20 shows calculated I-V curves for the H3 structure for the fractional and integer spots compared with those for the same structure with the samarium atom removed.

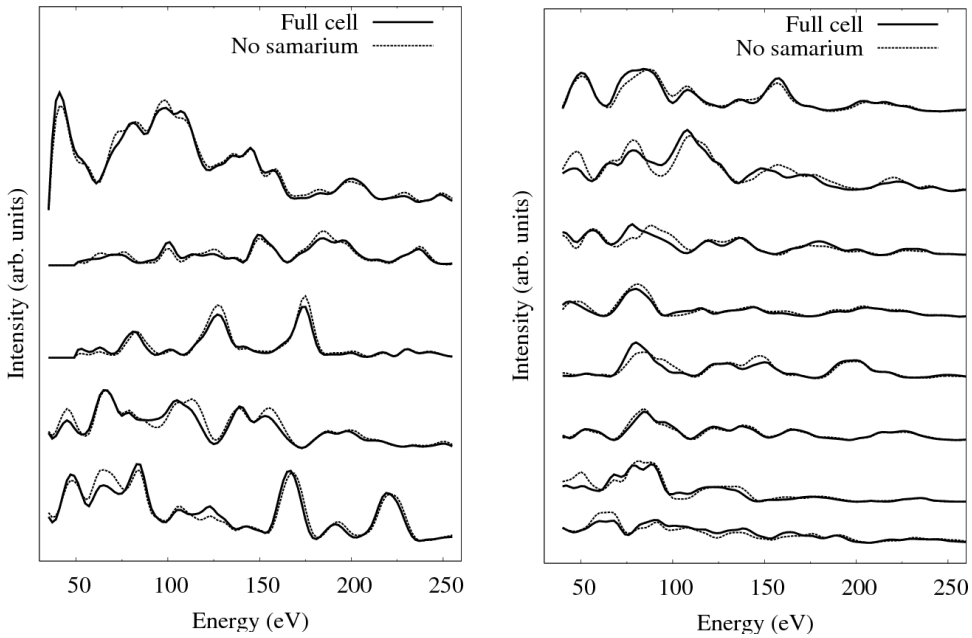

Figure 6.20: Calculated LEED I-V curves for the integer spots (left) and fractional spots (right) of the H3 unit cell with and without the samarium atom in place. Bulk Debye temperatures were used throughout.

It would appear that the I-V curves are insensitive to the presence of the samarium atom and that this atom has only an indirect effect upon the I-V curves via the honeycomb chain of silicon atoms whose structure it dictates. This is not to say that the samarium atom is not a strong scatterer. It would appear that the silicon honeycomb layer as a scattering unit of 8 atoms contributes much more to the I-V curves than the lone samarium atom. The curves in figure 6.20 were calculated using the bulk Debye temperature and this effect is not due to enhanced vibrations.

The silicon honeycomb layer is not perfectly symmetrical about the mirror plane perpendicular to the ×2 direction. The half order spots that are apparently missing from the experimental 3×2 LEED pattern should produce a small but finite intensity. Figure 6.21 shows the calculated I-V curves of the half order spots compared to that of the (1,0) spot. The half order spots in the 3×2 LEED pattern are so weak in intensity that they fall below the background intensity leaving only a 3×1 LEED pattern visible.

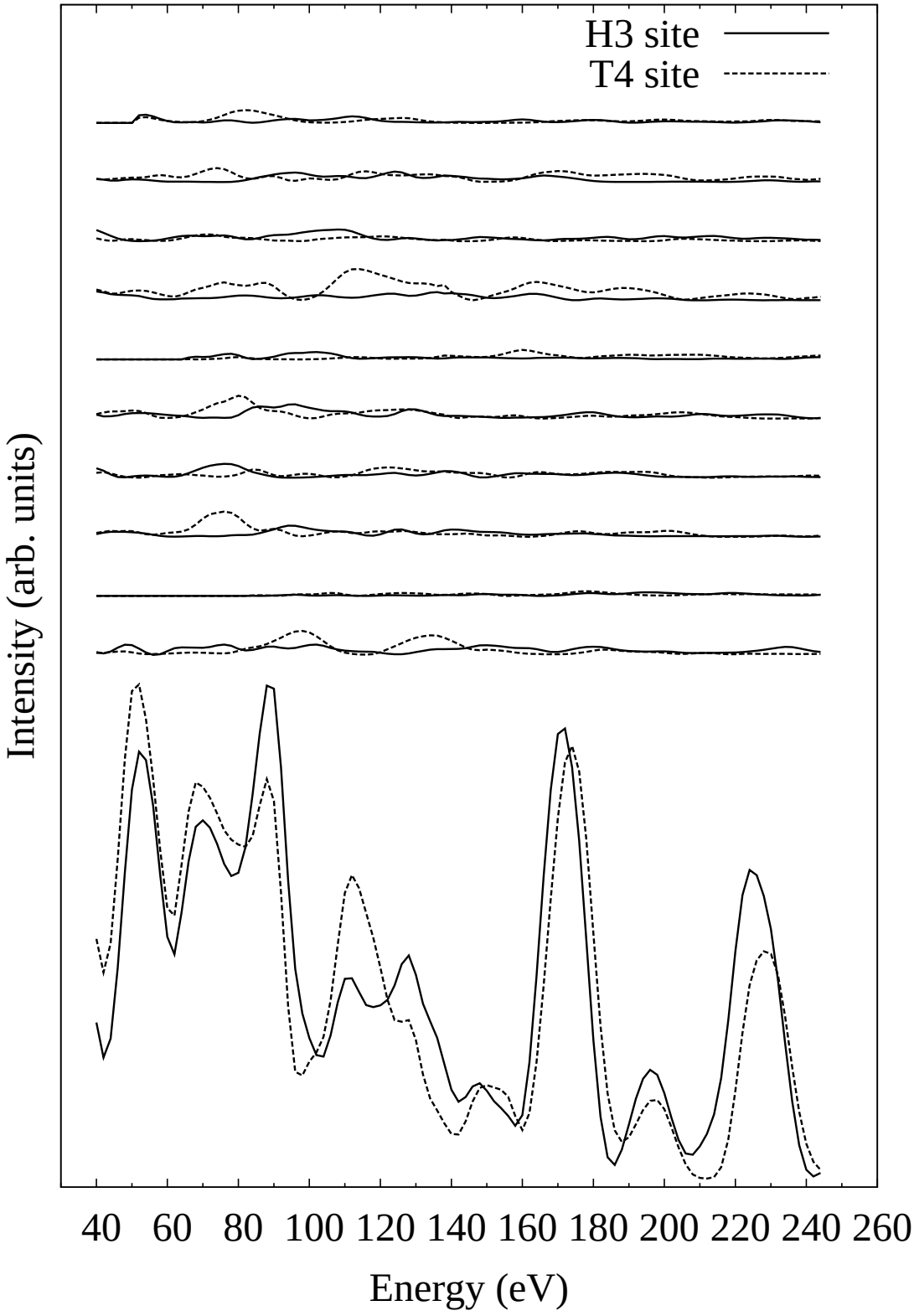

Figure 6.21: Calculated I-V curves for the HCC structure showing the difference in the intensity (typically an order of magnitude) between the half order spots and a representative spot that is visible in the LEED pattern during an experiment.

Summary and Discussion

Table 6.5 contains a summary of the Pendry R-factors obtained from a comparison with experiment of the structures obtained in the *ab initio* calculations and from the `CAVLEED` LEED I-V structure fit. The error quoted with each R-factor is the standard error in the choice of a mean R-factor to represent all of the spot R-factors. The final optimised and linearly combined LEED I-V curves are compared with experiment for the integer spots in figure 6.22 and for the fractional spots in figure 6.23. Finally, the optimised atomic coordinates are listed in table 6.6.

Structure	R_P^{FRAC}	R_P^{INT}	R_P^{ALL}	L1 (Å $\pm$ 0.1)	L2 (Å $\pm$ 0.1)
T4 (ref. [151])	0.87 ± 0.06	0.88 ± 0.07	0.92 ± 0.07	2.42	3.02
T4 `CASTEP`	0.44 ± 0.04	0.46 ± 0.08	0.46 ± 0.05	2.64	3.14
H3 `CASTEP`	0.47 ± 0.08	0.43 ± 0.04	0.45 ± 0.05	2.62	3.10
T4 `CAVLEED`	0.48 ± 0.07	0.41 ± 0.07	0.46 ± 0.05	2.72	3.10
H3 `CAVLEED`	0.45 ± 0.06	0.44 ± 0.08	0.45 ± 0.05	2.65	3.11
Combination	0.39 ± 0.07	0.42 ± 0.08	0.42 ± 0.05	2.69	3.10

Table 6.5: Pendry R-factors for the fractional spots (R_P^{FRAC}), integer spots (R_P^{INT}) and for all spots (R_P^{ALL}) for the various optimised structures in this work. All of the calculated I-V curves used optimised vibrations. The interlayer spacings are shown in columns five and six and the midpoint of layer 1 is defined as the midpoint of the honeycomb layer; for this table only the height of the samarium atom has not been included to determine the midpoint.

The Pendry R-factors obtained upon comparison of the *ab initio* calculations with experiment are not as low as we would expect. We can see that for some spots the I-V curves are visually very similar to those obtained experimentally (see the I-V curves for the (-4/3,1) and (2,0) spots for example) but they have a poor R-factor. This suggests that the structure is very nearly right and the minor discrepancy could be a result of not including enough bulk like silicon layers in the bottom of the supercell with consequent effects upon the reconstruction within the top honeycomb layer. Computational resources prohibit a repeat of the *ab initio* calculation with more silicon layers included. Some simple variation in the top layer structure has been attempted, for example flattening the layer, but this drastically worsens the R-factor. Perhaps a study using a LEED I-V genetic algorithmn search might optimise this structure further. The moderate R-factors are offset by the fact that two independent techniques both show optimum structural fits for almost identical interlayer spacings.

The lateral atomic structure was freely varied in the *ab initio* calculations in this work and the lateral atomic positions agree well with those found by Palmino et al. [151]

Atom	T4			H3		
	x	y	z	x	y	z
Sm	4.4560	-0.0908	5.8200	2.3052	0.1015	6.3278
Si	0.5246	4.6622	5.7745	0.5302	8.6449	5.4884
Si	0.5265	8.7543	5.6117	2.6963	4.7995	5.2425
Si	2.8342	4.8407	5.6212	2.8725	8.8656	5.3529
Si	2.8648	8.8751	5.7302	3.8813	6.7565	5.3864
Si	3.7821	2.7298	5.7798	3.7429	2.7074	5.3314
Si	3.9458	6.8101	5.6120	6.2206	6.9457	5.4747
Si	6.1180	2.9175	5.5986	6.0799	2.8190	5.4051
Si	6.2624	7.0453	5.7947	0.3739	4.5405	5.3248
Si	0.0000	0.0000	3.5161	0.0000	0.0000	3.1445
Si	0.0796	3.9443	3.4835	0.0529	3.9455	3.2037
Si	6.6813	3.8794	3.3539	0.0221	7.7093	3.0346
Si	1.1233	9.6836	2.6037	1.1166	9.6682	2.2829
Si	1.1354	5.8248	2.5887	1.1439	5.8010	2.2943
Si	1.1432	1.9616	2.7279	1.1331	1.9875	2.4160
Si	3.3018	9.5475	3.4438	3.2893	9.5989	3.1315
Si	3.3957	2.0357	3.4807	4.4639	0.0620	2.4343
Si	3.3458	5.7837	3.3691	3.3757	2.0353	3.1927
Si	4.4727	0.0459	2.6891	3.3462	5.8008	3.0829
Si	4.4896	3.8935	2.5911	4.4643	3.9001	2.2990
Si	4.4973	7.7254	2.6050	4.4672	7.7474	2.3037
Si	1.1445	1.9792	0.2812	1.1445	1.9792	0.2812
Si	2.2530	3.8992	-0.5026	2.2530	3.8992	-0.5026

Table 6.6: Tabulated atomic coordinates (in Å) for each atom in the top three layers in the geometry optimised Si(111)-3×2-Sm supercells in the T4 and H3 arrangements. The deepest layer is bulk-like silicon and the coordinates of two atoms are listed. The lattice parameters are $\boldsymbol{a}$=7.68 Å, $\boldsymbol{b}$=11.52 Å, $\boldsymbol{c}$=17.096832 Å with $\alpha = 120°$ and $\beta = \gamma = 90°$.

which they have shown to be in good qualitative agreement with experimental STM images. In this work the focus has been upon the optimisation of the vertical spacings, to which LEED is particularly sensitive.

The R-factors for the integer spots are consistently worse than those for the fractional spots. There is the possibility that there are some regions in which there is a disordered overlayer of samarium atop a bulk terminated Si(111)-1×1 surface. Such a phase has been reported by Wigren et al. [150] and was investigated in the first half of this chapter. The integer spots from such regions might contribute to the overall integer spots for the surface and reduce the level of agreement with the calculated I-V curves for the pure 3×2 surface.

It has not been possible to determine the long range order in the system. We might expect that simple electrostatic repulsion along the 1D chain would space out the metal atoms and provide large separate domains of the H3 and the T4 structures. However,

the two sites are almost degenerate and there would be an entropic gain from disorder. In the literature one can find evidence for both order and disorder in the long range positions of the metal atoms. In this study the improvement in the Pendry R-factor when the T4 and H3 structures are considered together on the surface suggests that both sites are occupied within the surface. It has also been shown that more than one unit cell is not required to explain the missing half order spots in the LEED pattern and the experimentally observed LEED patterns show a low background due to good order on the surface. It could be that there is long range disorder on the surface and that the coupling between many adjacent H3 and T4 unit cells and matching of the interlayer spacings introduces a slight strain that changes the structure in the honeycomb layer and the first bulk-like layer enough to account for the R-factors. If this is the case then it would be impossible to obtain the structure to a high degree of accuracy without an *ab initio* calculation using a supercell that comprises several thousand unit cells of the H3 and T4 structures randomly tesselated in both directions.

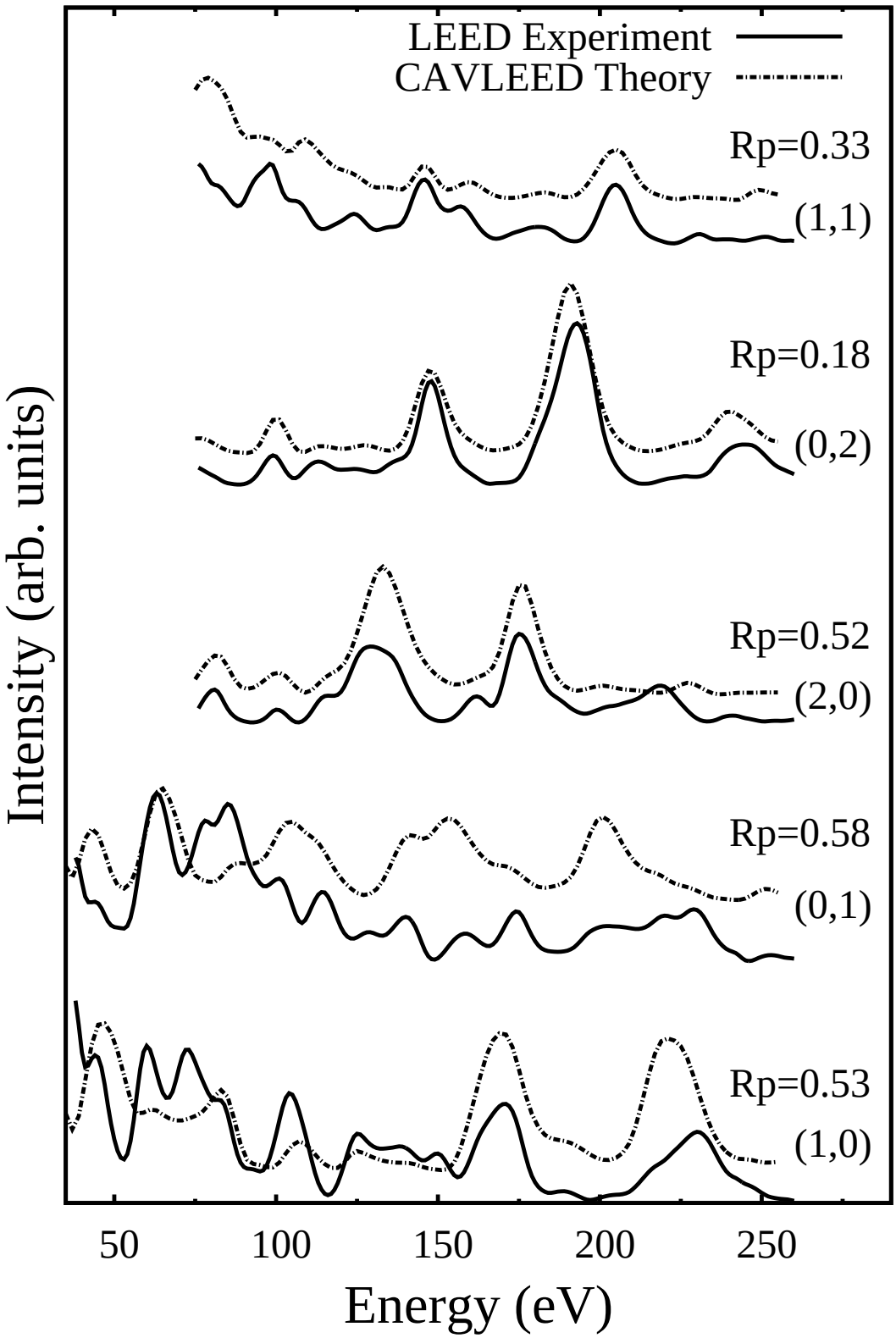

Figure 6.22: Best fit I-V curves for the integer LEED spots produced by a linear combination of the H3 and the T4 structures in a 40: 60 ratio.

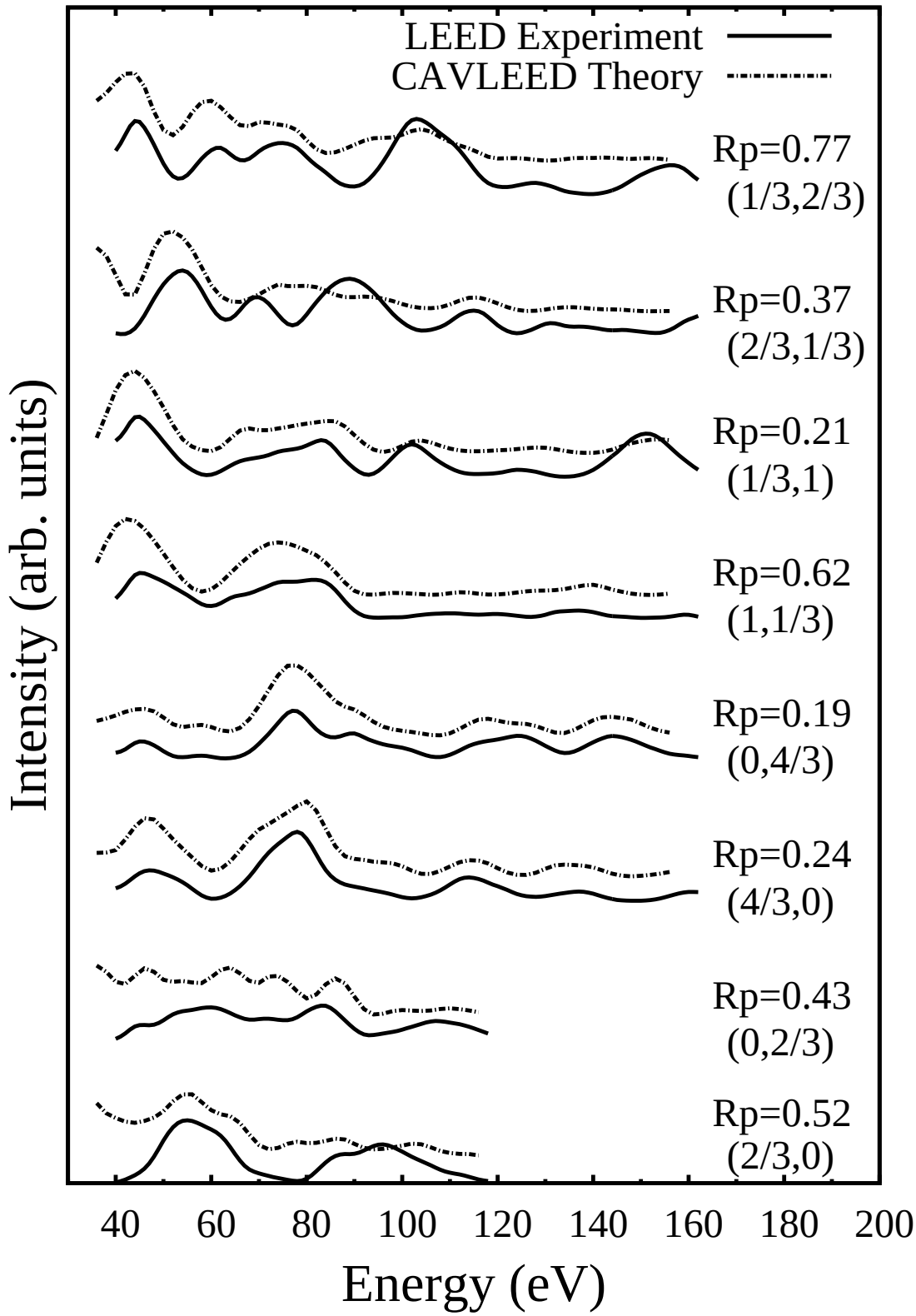

Figure 6.23: Best fit I-V curves for the fractional spots produced by a linear combination of the H3 and the T4 structures in a 40: 60 ratio.

6.5 Chapter 6 Conclusions

A 1×1 phase that was observed on the Si(111)-1×1-Sm surface has been investigated with LEED I-V and several *ab initio* geometry optimisation calculations. LEED I-V curves were first obtained in order to fingerprint the surface structure. Several candidate structures were suggested and these were geometry optimised and their energies compared using the `CASTEP` code. For an isolated 1×1 unit cell this suggested that it was energetically more favourable for the samarium overlayer to sit subsurface. However, a comparison of the model structures with experiment via LEED I-V curves has shown that none of the model structures produce a good match with the experimental data. Moreover, the structure that is in best agreement with experiment is the bulk terminated Si(111) surface. This behaviour persists even when the first few interlayer spacings and rumpling amplitudes are varied for each structure. It would appear that the 1×1 phase that has been observed in this work and reported in the literature by other workers is a disordered phase of samarium atop a bulk terminated Si(111) surface. No conclusions can be drawn as to which sites are occupied upon the surface and an STM investigation is needed to determine the degree of disorder and the size of any small ordered domains that might exist.

A quantitative validation of the honeycomb-chain channel model common to the 3×1 and 3×2 structures formed by alkali, alkali-earth and rare-earth metals on Si(111) has been carried out. Several I-V datasets were obtained from LEED experiments and used to fingerprint the surface. The atomic structure suggested by two *ab initio* calculations is in reasonable agreement with this experimental data. Further structural optimisation and mapping of the R-factor landscape have shown that a slight outward expansion of the top layer improves the fit somewhat but increasing the vibrations in the top two layers gives a significant improvement. A linear combination of the two HCC structures has been shown to improve the fit still further with the ratio being slightly in favour of the structure with the lower energy of the two. Finally, the intensities of the half order spots have been calculated and it was shown that these spots are sufficiently dim to fall below the background intensity in a LEED experiment. Little change in the calculated I-V curves results from removing the samarium atom which supports the idea that as a scattering unit the silicon honeycomb layer dominates the unit cell and makes LEED insensitive to the metal atom in these 3× systems.

References

[1] M. H. Hablanian, J. Vac. Sci. Tech. A. **2**, 118 (1982).

[2] J. H. Singleton, J. Vac. Sci. Tech. A. **2**, 126 (1982).

[3] P. A. Redhead, J. Vac. Sci. Tech. A. **2**, 132 (1982).

[4] N. W. Ashcroft and N. D. Mermin, *Solid State Physics* (Thomson Learning, United States, 1976).

[5] R. Car and M. Parrinello, Phys. Rev. Lett. **55**, 2471 (1985).

[6] J. M. Soler *et al.*, J. Phys.: Cond. Matt. **14**, 2745 (2002).

[7] J. P. LaFemina, Surf. Sci. **16**, 137 (1992).

[8] R. M. Martin, *Electronic Structure - Basic Theory and Practical Methods* (Cambridge University Press, Cambridge, 2004).

[9] M. D. Segall *et al.*, J. Phys.: Cond. Matt. **14**, 2717 (2002).

[10] G. Kresse and J. Furthmuller, Phys. Rev. B. **54**, 11169 (1996).

[11] I. Štich *et al.*, Phys. Rev. Lett **68**, 1351 (1992).

[12] K. D. Brommer, M. Needels, B. E. Larson, and J. D. Joannopoulos, Phys. Rev. Lett **68**, 1355 (1992).

[13] W. Foulkes, L. Mitas, R. Needs, and G. Rajagopal, Rev. Mod. Phys. **73**, 33 (2001).

[14] W. Schattke, R. Bahnsen, and R. Redmer, Prog. Surf. Sci. **72**, 87 (2003).

[15] K. N. Tu, R. D. Thompson, and B. Y. Tsaur, Appl. Phys. Lett. **38**, 626 (1981).

[16] S. Vandre *et al.*, Appl. Surf. Sci. **123**, 100 (1998).

[17] H. Norde *et al.*, Appl. Phys. Lett. **38**, 626 (1981).

[18] M. H. Unewisse and J. W. V. Storey, J. Appl. Phys. **73**, 3873 (1992).

[19] L. Pahun, Y. Campidelli, F. A. dAvitaya, and P. A. Badoz, Appl. Phys. Lett. **60**, 1166 (1991).

[20] S. Zhu *et al.*, IEEE Elec. Device Lett. **25**, 565 (2004).

[21] S. Y. Zhu *et al.*, IEEE Elec. Device Lett. **25**, 268 (2004).

[22] M. Jang *et al.*, Appl. Phys. Lett. **83**, 2611 (2003).

[23] P. Muret, T. A. N. Tan, N. Frangis, and J. van Landuyt, Phys. Rev. B. **56**, 9286 (1997).

[24] M. Q. Huda and K. Sakamoto, Mater. Sci. Eng. **B89**, 378 (2002).

[25] F. P. Netzer, J. Phys.: Cond. Matt. **7**, 991 (1995).

[26] J. A. Knapp and S. T. Picraux, Appl. Phys. Lett. **48**, 466 (1985).

[27] *Properties of Metal Silicides*, edited by K. Maex and M. van Rossum (INSPEC, London, 1995).

[28] R. Baptist, S. Ferrer, G. Grenet, and H. C. Poon, Phys. Rev. Lett. **64**, 311 (1990).

[29] M. H. Tuilier *et al.*, Surf. Sci. **307**, 710 (1994).

[30] T. Wood *et al.*, Phys. Rev. B. **73**, 235405 (2006).

[31] L. et al, Phys. Rev. B. **54**, 2004 (1996).

[32] D. J. Spence, S. P. Tear, T. C. Q. Noakes, and P. Bailey, Phys. Rev. B. **61**, 57075713 (2000).

[33] D. J. Spence, T. C. Q. Noakes, P. Bailey, and S. P. Tear, Surf. Sci. **512**, 61 (2002).

[34] T. Wood *et al.*, Surf. Sci. **598**, 120 (2005).

[35] C. Bonet *et al.*, Phys. Rev. B. **72**, 165407 (2005).

[36] H. Kitayama, S. P. Tear, D. J. Spence, and T. Urano, Surf. Sci. **482-485**, 1481 (2001).

[37] C. Bonet, D. J. Spence, and S. P. Tear, Surf. Sci. **504**, 183 (2002).

[38] C. Rogero *et al.*, Phys. Rev. B **66**, 235421 (2002).

[39] P. Wetzel *et al.*, Solid State Comm. **82**, 235 (1992).

[40] P. Paki *et al.*, Phys. Rev. B **45**, 8490 (1992).

[41] P. Wetzel *et al.*, Phys. Rev. B **47**, 3677 (1993).

[42] C. Rogero *et al.*, Phys. Rev. B **69**, 54312 (2004).

[43] L. Stauffer *et al.*, Phys. Rev. B **47**, 10555 (1993).

[44] W. A. Henle *et al.*, Solid State Comm. **71**, 657 (1989).

[45] J. A. Martín-Gago, J. M. Gómez-Rodríguez, and J. Y. Veuillen, Phys. Rev. B **55**, 5136 (1997).

[46] T. P. Roge *et al.*, Surf. Sci. **352**, 622 (1996).

[47] P. Wetzel *et al.*, Surf. Sci. **355**, 13 (1996).

[48] J. A. Martin-Gago, J. M. Gomez-Rodroguez, and J. Y. Veuillen, Surf. Sci. **366**, 491 (1996).

[49] C. Polop, C. Rogero, J. L. Sacedon, and J. A. Martin-Gago, Surf. Sci. **482**, 1337 (2001).

[50] E. Duverger, F. Palmino, E. Ehret, and J.-C. Labrune, Surf. Sci. **595**, 40 (2005).

[51] D. J. Spence, T. C. Q. Noakes, P. Bailey, and S. P. Tear, Phys. Rev. B **62**, 5016 (2000).

[52] H. W. Yeom *et al.*, Phys. Rev. Lett. **82**, 4898 (1999).

[53] P. Segovia, D. Purdie, M. Hengsberger, and Y. Baer, Nature **402**, 504 (1999).

[54] R. Losio, K. N. Altmann, and F. J. Himpsel, Phys. Rev. Lett. **85**, 808 (2000).

[55] J.-Z. Wang *et al.*, Phys. Rev. B. **65**, 235303 (2002).

[56] B. Z. Liu and J. Nogami, Nanotechnology **14**, 873 (2003).

[57] R. Ragan *et al.*, J. Crys. Growth **251**, 657 (2003).

[58] M. Kuzmin *et al.*, Appl. Surf. Sci. **222**, 394 (2004).

[59] C. J. Chen, Phys. Rev. B. **42**, 8841 (1990).

[60] A. Kirakosian *et al.*, Surf. Sci. **498**, L109 (2002).

[61] E. Hoque, A. Petkova, and M. Henzler, Surf. Sci. **515**, 312 (2002).

[62] F. Palmino *et al.*, Surf. Sci. **586**, 56 (2005).

[63] A. A. Saranin *et al.*, Phys. Rev. B. **58**, 7059 (1998).

[64] H. H. Weitering, X. Shi, and S. C. Erwin, Phys. Rev. B. **54**, 10585 (1996).

[65] K. Sakamoto, W. Takeyama, H. M. Zhang, and R. I. G. Uhrberg, Phys. Rev. B. **66**, 165319 (2002).

[66] G. Lee *et al.*, Phys. Rev. Lett. **87**, 56104 (2001).

[67] F. Palmino *et al.*, Phys. Rev. B. **67**, 195413 (2003).

[68] M. Kuzmin *et al.*, Surf. Sci. **538**, 124 (2003).

[69] H. Weitering, Surf. Sci. Lett. **355**, 271 (1996).

[70] D. Jeon, T. Hashizume, T. Sakurai, and R. Willis, Phys. Rev. B. **69**, 1419 (1992).

[71] C. Wigren *et al.*, Phys. Rev. B **48**, 1993 (1993).

[72] J. Quinn and F. Jona, Surf. Sci. **249**, L307 (1991).

[73] W. Fan and A. Ignatiev, Phys. Rev. B. **41**, 3592 (1990).

[74] C. Collazo-Davila, D. Grozea, and L. D. Marks, Phys. Rev. Lett. **80**, 1678 (1998).

[75] L. Lottermoser *et al.*, Phys. Rev. Lett. **80**, 3980 (98).

[76] S. C. Erwin and H. H. Weitering, Phys. Rev. Lett. **81**, 2296 (98).

[77] H. Over *et al.*, Surf. Sci. **314**, 243 (1994).

[78] W. H. Cropper, *Great Physicists,* (Oxford University Press, New York, 2001).

[79] C. Davisson and L. H. Germer, Physical Review, **30**, (1927).

[80] G. P. Thomson, Proc. Royal Soc. London, Series A, **117**, (1928).

[81] M. H. Hablanian, J. Vac. Sci. Tech. A, **2**, (1983).

[82] P. A. Redhead, J. Vac. Sci. Tech. A, **2**, 132 (1983).

[83] J. H. Singleton, J. Vac. Sci. Tech. A, **2**, 126 (1983).

[84] J. Pendry, *Low Energy Electron Diffraction* (Academic Press, London, 1974).

[85] M. A. V. Hove and S. Y. Tong, *Surface Crystallography by LEED* (Springer-Verlag, New York, 1979).

[86] *A CCP3 Library Code*, CLRC, Daresbury Laboratory, UK.

[87] D. J. Titterington and C. G. Kinniburgh, Comput. Phys. Commun., **20**, 237 (1980).

[88] J. B. Pendry, J. Phys. C: Solid State Phys., **4**, 3095 (1971).

[89] V. E. de Carvalho *et al.*, Vacuum, **34**, 893 (1984).

[90] P. G. Cowell, J. Phys. E: Sci. Instrum., **15**, 993 (1982).

[91] P. G. Cowell, Ph.D. thesis, University of York, Department of Physics, 1983.

[92] C. Bonet, Ph.D. thesis, University of York, Department of Physics, 2003.

[93] J. B. Pendry, J. Phys. C. Solid St. Phys., **13**, 937 (1980).

[94] L. H. Thomas, Proc. Cambridge Philos. Soc. **23**, 542 (1927).

[95] E. Fermi, Z. Phys. **48**, 73 (1928).

[96] P. Hohenberg and W. Kohn, Phys. Rev. **136**, B864 (1964).

[97] R. O. Jones and O. Gunnarsson, Rev. Mod. Phys. **61**, 689 (1989).

[98] J. P. Perdew *et al.*, Phys. Rev. B. **46**, 6671 (1992).

[99] J. P. Perdew, K. Burke, and M. Ernzerhof, Phys. Rev. Lett. **77**, 3865 (1996).

[100] B. Hammer, L. B. Hansen, and J. K. Norskov., Phys. Rev. B **59**, 7413 (1999).

[101] M. Marlo and V. Milman, Phys. Rev. B. **62**, 1337 (2000).

[102] W. Kohn and L. J. Sham, Phys. Rev. **140**, 1133 (1965).

[103] P. Gill, *Practical Optimization* (Academic Press Inc., U.S., 1982), Vol. 1.

[104] R. Fletcher, *Practical Methods of Optimization* (John Wiley and Sons Ltd, U.S., 2000).

[105] N. Marzari, D. Vanderbilt, and M. C. Payne, Phys. Rev. Lett. **79**, 1337 (1997).

[106] N. D. Mermin, Phys. Rev. **137**, A1441 (1965).

[107] R. O. Jones and O. Gunnarsson, Rev. Mod. Phys. **61**, 689 (1989).

[108] H. J. Monkhorst and J. D. Pack., Phys. Rev. B. **13**, 5188 (1976).

[109] R. P. Feynman, Phys. Rev. **56**, 340 (1939).

[110] B. G. Pfrommer, M. Côté, S. G. Louie, and M. L. Cohen, J. Comp. Phys. **131**, 233 (1997).

[111] M. D. Segall, C. J. Pickard, R. Shah, and M. C. Payne, Mol. Phys. **89**, 571 (1996).

[112] E. Kaxiras, *Atomic and Electronic Structure of Solids* (Cambridge University Press, Cambridge, 2003).

[113] A. D. Gottlieb and L. Wesoloski, Nanotechnology **17**, R57 (2006).

[114] J. Tersoff and D. R. Hamann, Phys. Rev. B. **31**, 805 (1985).

[115] J. Bardeen, Phys. Rev. Lett. **6**, 57 (1961).

[116] *Materials Studio*, Accelrys Inc., San Diego, CA.

[117] E. Duverger, F. Palmino, E. Ehret, and J.-C. Labrune, Surf. Sci. **595**, 40 (2005).

[118] M. I. J. Probert and M. C. Payne, Phys. Rev. B. **67**, (2003).

[119] S. Pelletier *et al.*, J. Vac. Sci. Technol. A. **18**, 2738 (2000).

[120] R. G. van Silfhout, J. F. van der Veen, C. Norris, and J. E. Macdonald, Faraday. Discuss. Chem. Soc. **89**, 169 (1990).

[121] C. A. Dimitradis *et al.*, J. Appl. Phys. **68**, 1726 (1990).

[122] R. P. Borges *et al.*, J. Phys. D: Appl. Phys. **35**, 186191 (2002).

[123] D. Leong, M. Harry, K. J. Reeson, and K. P. Homewood, Nature **387**, 686 (1997).

[124] M. C. Bost and J. E. Mahan, J. Appl. Phys. **58**, 2696 (1985).

[125] S. H. T. Urano, M. Kaburagi and T. Kanaji, Appl. Surf. Sci. **41-42**, 103 (1989).

[126] S. Hajjar *et al.*, Phys. Rev. B. **68**, 033302 (2003).

[127] U. S. et al, J. Appl. Phys. **91**, 6154 (2002).

[128] A. Wawro, S. Suto, R. Czajka, and A. Kasuya, Phys. Rev. B. **67**, 195401 (2002).

[129] P. Castrucci *et al.*, Surf. Sci. **482-485**, 916 (2001).

[130] P. Castrucci *et al.*, Phys. Rev. B. **65**, 235435 (2002).

[131] N. G. Galkin *et al.*, Thin SOlid Films **464-465**, 18 (2004).

[132] L. Xi *et al.*, Surf. Sci. **600**, 3072 (2006).

[133] B. Johansson, Phys. Rev. B **20**, 1315 (1978).

[134] B. Johansson, Phys. Rev. B **25**, 3374 (1979).

[135] G. K. Wertheim and G. Crecelius, Phys. Rev. Lett. **40**, 813 (1978).

[136] E. Bertel, G. Strasser, F. P. Netzer, and J. A. D. Matthew, Phys. Rev. B. **25**, 3374 (1982).

[137] A. Rosengren and B. Johansson, Phys. Rev. B **26**, 30683078 (1982).

[138] J. Onsgaard, M. Christiansen, F. Orskov, and P. J. Godowski, Surf. Sci. **247**, 208 (1991).

[139] A. Faldt and H. P. Myers, Phys. Rev. B **33**, 1424 (1986).

[140] S. H. Xu *et al.*, J. Elec. Spec. Rel. Phen. **80**, 189 (1996).

[141] J. Onsgaard, M. Christiansen, F. Orskov, and P. J. Godowski, J. Mat. Sci. Lett. **9**, 989 (1990).

[142] C. Ohbuchi and J. Nogami, Surf. Sci. **579**, 157 (2005).

[143] A. Franciosi *et al.*, Solid State Comm. **47**, 427 (1983).

[144] A. Franciosi *et al.*, Phys. Rev. B. **29**, 5611 (1984).

[145] T. V. Krachino, M. V. Kuz'min, M. V. Loginov, and M. A. Mittsev, Physics of the Solid State **40**, 371 (1998).

[146] T. V. Krachino, M. V. Kuz'min, M. V. Loginov, and M. A. Mittsev, Physics of the Solid State **40**, 1758 (1998).

[147] O. Sakho *et al.*, Applied Surf. Sci. **65/66**, 729 (1993).

[148] O. Sakho, M. Sacchi, F. Sirotti, and G. Rossi, Phys. Rev. B. **47**, 3797 (1993).

[149] C. Wigren *et al.*, Phys. Rev. B. **48**, 11014 (1993).

[150] C. Wigren, J. N. Andersen, R. Nyholm, and U. O. Karlsson, Surf. Sci. **293**, 254 (1993).

[151] F. Palmino *et al.*, Phys. Rev. B. **67**, 195413 (2003).

[152] E. Ehret *et al.*, Surf. Sci. **569**, 23 (2004).

[153] F. Palmino *et al.*, Surf. Sci. **586**, 56 (2005).